

Developing Modular Protein Therapeutics as Alternatives to Monoclonal Antibodies for
Cancer Immunotherapy

by

Junseon Min

Department of Biomedical Engineering
Duke University

Date: _____

Approved:

Dr. Ashutosh Chilkoti, Supervisor

Dr. Joel Collier

Dr. Charles Gersbach

Dr. Smita Nair

Dr. Kris Wood

Dissertation submitted in partial fulfillment of
the requirements for the degree of Doctor
of Philosophy in the Department of
Biomedical Engineering in the Graduate School
of Duke University

2021

ABSTRACT

Developing Modular Protein Therapeutics as Alternatives to Monoclonal Antibodies for
Cancer Immunotherapy

by

Junseon Min

Department of Biomedical Engineering
Duke University

Date: _____

Approved:

Dr. Ashutosh Chilkoti, Supervisor

Dr. Joel Collier

Dr. Charles Gersbach

Dr. Smita Nair

Dr. Kris Wood

An abstract of a dissertation submitted in partial
fulfillment of the requirements for the degree
of Doctor of Philosophy in the Department of
Biomedical Engineering in the Graduate School of
Duke University

2021

Copyright by
Junseon Min
2021

Abstract

Monoclonal antibodies have been successfully developed as PD-L1 antagonists, showing unprecedented anti-cancer immune response and efficacy with their high affinity and exquisite specificity. Despite its substantial success, the development of antibody drugs is approaching an asymptote because their structural inflexibility limits the ability to tune their valency, receptor accessibility, and blood circulation duration. Their efficacy in treating solid tumors is also limited by low tumor penetration due to their large size and structural inflexibility. These inherent challenges to utilizing antibodies as therapeutics confine their further improvements.

To address these limitations, we have developed a modular protein therapeutic with rationally tunable valency, affinity, pharmacokinetics, and tumor penetration. In modular protein therapeutics, we can independently tune their affinity and valency for any given target, as well as modulate their pharmacokinetics and tumor penetration. To create a modular PD-L1 antagonist, we chose the human tenth fibronectin type III domain (FN3) as the “affinity module” because it is a small (~10 kDa), structurally robust protein domain that has six disordered loops that are similar to the complementarity-determining regions (CDRs) of antibodies. We then oligomerized the affinity module to enhance its binding to PDL1 via the avidity. To optimize pharmacokinetics, we fused the oligomerized affinity module with a “half-life module”:

1) an elastin-like polypeptide (ELP) that is injectable as a solution at room temperature but forms a gel-like depot at 37 °C and provides sustained, the zero-order release of the fusion; or 2) an albumin-binding domain that binds to and exploits the endogenous albumin to significantly extend the plasma half-life. The fusion with a “half-life module” would enable our modular protein therapeutics to rival the pharmacokinetics of antibodies.

In this thesis, we discovered PD-L1-binding FN3 proteins (aPDL1-FN3) using phage display and modulated their valency and affinity for their equilibrium dissociation constants (K_D) in the picomolar range. Unlike bivalent antibodies, the multivalency of FN3 is not restricted, and tetra-valency was chosen because (aPDL1-FN3)₄ reached a plateau in terms of binding ability to PD-L1, measured by surface plasmon resonance (SPR), *in vitro* PD-L1 neutralization assay, and flow cytometry. To overcome glomerular filtration cutoff (~50 kDa) and improve pharmacokinetics, we genetically fused the (aPDL1-FN3)₄ protein with either elastin-like polypeptides (ELPs) or albumin-binding proteins (ABDs). Using these fusions, we studied pharmacokinetics, biodistribution, and tumor uptake as compared to anti-PD-L1 antibodies. Also, we validated *in vivo* preclinical efficacy using three different immunocompetent mice models: 1) B16.F10 melanoma model; 2) CT26 colon cancer model; and 3) MC38 colon cancer model. These results demonstrated that our modular protein therapeutics successfully mimic antibodies as alternative therapeutics and have the potential to

outperform antibodies regarding multivalency and cellular and tumor penetration. We believe that this research project serves as a proof-of-concept for modular protein therapeutics where tunable efficacy and pharmacokinetics can lead to a clinical utility that can eventually overcome the hurdles of traditional antibody-based therapy.

Dedication

To my family that I can always count on.

Contents

Abstract.....	iv
List of Tables.....	xvi
List of Figures.....	xvii
Acknowledgements	xxii
1. Introduction.....	1
1.1 Monoclonal antibodies	1
1.1.1 The types of antibodies.....	2
1.1.2 The structure of an antibody	4
1.1.3 Advantages and limitations	6
1.2 Target-binding scaffolds.....	8
1.2.1 Ig-like scaffolds	9
1.2.2 Non-Ig scaffolds	11
1.2.2.1 Anticalins.....	12
1.2.2.2 DARPins	13
1.2.2.3 Avimers.....	14
1.3 Human fibronectin type III domain	15
1.3.1 Properties.....	15
1.3.2 Applications.....	16
1.3.3 Advantages and limitations	17
1.4 Biopolymers for recombinant fusion.....	19

1.4.1 Elastin-like polypeptides	19
1.4.2 Albumin-binding domain.....	21
2. Developing phage-displayed FN3 library.....	22
2.1 Introduction and motivation.....	23
2.1.1 M13 filamentous phage	24
2.1.2 Low valency display	26
2.1.3 Phage library construction	29
2.2 Materials and methods	30
2.2.1 FN3 variants library	30
2.2.2 Phage-displayed FN3 library	32
2.2.2.1 Electroporation.....	33
2.2.2.2 Purification	34
2.2.2.3 Characterization.....	35
2.3 Results and discussion.....	36
2.3.1 Construction of FN3 variants library.....	36
2.3.2 Construction of phage-displayed FN3 library	37
2.4 Conclusion and future direction	38
3. Discovering PDL1-binding FN3.....	40
3.1 Introduction and motivation.....	40
3.1.1 Immune checkpoints.....	40
3.1.2 Immune checkpoint inhibitors	42
3.1.3 PDL1-binding scaffolds	44

3.2 Materials and methods	46
3.2.1 Panning against PDL1.....	46
3.2.2 Identifying sequences and phage ELISA.....	49
3.2.3 Affinity maturation.....	51
3.2.3.1 Construction of gene ibrary.....	51
3.2.3.2 Construction of phage library	52
3.2.3.3 Panning.....	53
3.2.3.4 Next generation sequencing.....	54
3.2.4 PDL1-binding FN3 protein.....	55
3.2.4.1 Molecular cloning	55
3.2.4.2 Protein expression and purification	55
3.2.4.3 Surface plasmon resonance	57
3.3 Results and discussion.....	59
3.3.1 Optimizing panning system against PDL1	59
3.3.2 Discovering FN3 sequences that bind to PDL1.....	60
3.3.3 Affinity maturation.....	63
3.3.4 Characterization of PDL1-binding FN3 protein	64
3.4 Conclusoin and future directions	66
4. Optimizing the valency of aPDL1-FN3	69
4.1 Introduction and motivation.....	69
4.1.1 Modularity and multivalency	69
4.1.2 Multivalency and therapeutic effects	71

4.2 Materials and methods	71
4.2.1 Construction of (aPDL1-FN3) _n	71
4.2.2 Expression and purification of (aPDL1-FN3) _n	72
4.2.3 Biophysical characterization.....	73
4.2.3.1 Mass spectrometry	73
4.2.3.2 Dynamic light scattering	74
4.2.3.3 Surface plasmon resonance	74
4.2.3.4 Fluorescent dye labeling and confirmation.....	75
4.2.4 <i>In vitro</i> characterization	76
4.2.4.1 PDL1-blockade assay	76
4.2.4.2 Flow cytometry	78
4.2.4.3 3D spheroids and confocal imaging	79
4.3 Results and discussion.....	80
4.3.1 Qualitative characterization of (aPDL1-FN3) _n with gel electrophoresis	80
4.3.2 Biophysical characterization of (aPDL1-FN3) _n	82
4.3.3 Characterization of the binding kinetics of (aPDL1-FN3) _n	84
4.3.4 Characterization after fluorescence conjugation.....	85
4.3.5 Characterization of the potency of (aPDL1-FN3) _n	87
4.3.6 Quantifying the effect of multivalency on <i>in vitro</i> PDL1-binding with flow cytometry.....	89
4.3.7 <i>In vitro</i> characterization of tumor spheroids uptake and penetration	90
4.4 Conclusion and future directions	92

5. Developing the fusion between (aPDL1-FN3) ₄ and ELP.....	94
5.1 Introduction and motivation.....	94
5.1.1 Recombinant fusion with ELP.....	94
5.1.2 Sustained and localized release of ELPs.....	95
5.2 Materials and methods	97
5.2.1 Construct design and synthesis	97
5.2.2 Protein expression and purification.....	98
5.2.3 Biophysical characterization.....	99
5.2.3.1 Dynamic light scattering	99
5.2.3.2 UV/vis spectroscopy	99
5.2.3.3 Surface plasmon resonance	99
5.2.3.4 Fluorescent dye labeling and confirmation.....	100
5.2.4 <i>In vitro</i> characterization	101
5.2.4.1 Cell culture	101
5.2.4.2 PD1/PDL1 blockade assay.....	102
5.2.4.3 Flow cytometry	103
5.2.4.4 3D spheroids and confocal imaging	104
5.2.5 <i>In vivo</i> studies	106
5.2.5.1 Pharmacokinetics	106
5.2.5.2 Efficacy.....	107
5.2.5.3 Rechallenge.....	109
5.2.5.4 Biodistribution.....	110

5.2.5.5 Immunomodulation profiles.....	111
5.3 Results and discussion.....	112
5.3.1 Depot vs Soluble ELP for (aPDL1-FN3) ₄ fusion.....	112
5.3.1.1 (aPDL1-FN3) ₄ -ELP _{depot} is tuned for its Tt below 37 °C	112
5.3.1.2 (aPDL1-FN3) ₄ -ELP _{depot} shows strong PDL1 antagonism.....	114
5.3.1.3 (aPDL1-FN3) ₄ -ELP _{soluble} shows better <i>in vivo</i> tumor efficacy than (aPDL1-FN3) ₄ -ELP _{depot} at their equimolar doses	114
5.3.2 Qualitative characterization with gel electrophoresis.....	117
5.3.3 Biophysical characterization of (aPDL1-FN3) ₄ -ELP	119
5.3.4 Characterization of the binding kinetics of (aPDL1-FN3) ₄ -ELP	120
5.3.5 Characterization after fluorescence conjugation.....	121
5.3.6 Characterization of the potency of (aPDL1-FN3) ₄ -ELP	123
5.3.7 <i>In vitro</i> quantifying specific PDL1-binding of (aPDL1-FN3) ₄ -ELP with flow cytometry.....	126
5.3.8 <i>In vitro</i> characterization of 3D tumor spheroids uptake and penetration of (aPDL1-FN3) ₄ -ELP	130
5.3.9 Pharmacokinetics of (aPDL1-FN3) ₄ -ELP	133
5.3.10 Evaluating <i>in vivo</i> efficacy of (aPDL1-FN3) ₄ -ELP	137
5.3.10.1 Primary tumor growth.....	137
5.3.10.2 Tumor rechallenge	142
5.3.11 <i>In vivo</i> biodistribution of (aPDL1-FN3) ₄ -ELP	145
5.3.12 Tumor immunomodulation profiles of (aPDL1-FN3) ₄ -ELP.....	148
5.4 Conclusion and future directions	152

6. Developing the fusion between (aPDL1-FN3) ₄ and ABD.....	155
6.1 Introduction and motivation.....	155
6.1.1 Recombinant fusion with ABD	155
6.1.2 Advantages over the fusion with ELP	157
6.2 Materials and methods	158
6.2.1 Construct design and synthesis	158
6.2.2 Protein expression and purification.....	159
6.2.3 Biophysical characterization.....	160
6.2.3.1 Mass spectrometry	160
6.2.3.2 Dynamic light scattering	161
6.2.3.3 Surface plasmon resonance	161
6.2.4 <i>In vitro</i> potency	162
6.3 Results and discussion.....	163
6.3.1 Qualitative characterization with gel electrophoresis.....	163
6.3.2 Biophysical characterization.....	164
6.3.3 PDL1 antagonism.....	166
6.3.4 Binding affinity to PDL1 and albumin	167
6.4 Conclusion and future directions	169
7. Concluding remarks	171
7.1 Summary of works.....	171
7.2 Future directions	174
Appendix A.....	176

Appendix B.....	180
References.....	184
Biography	203

List of Tables

Table 1: FDA-approved antibodies therapeutics.....	3
Table 2: Overview of commonly used non-Ig scaffolds.....	12
Table 3: Overview of M13 coat proteins.....	25
Table 4: Overview of constructed phage-displayed FN3 libraries.....	38
Table 5: Examples of scaffold proteins that target PDL1	46
Table 6: Degenerate base for encoding certain nucleotides	52
Table 7: Primers for next-generation sequencing	54
Table 8: The sequences and binding affinities of five clones	61
Table 9: The binding kinetics of aPDL1-FN3	65
Table 10: The binding kinetics of (aPDL1-FN3) _n oligomers.....	85
Table 11: The IC ₅₀ of (aPDL1-FN3) _n oligomers.....	88
Table 12: Pharmacokinetics parameters	135
Table 13: Pharmacokinetics parameters as compared to anti-PDL1 antibodies.....	137
Table 14: The IC ₅₀ of (aPDL1-FN3) ₄ -ABD proteins	167
Table 15: The binding kinetics of (aPDL1-FN3) ₄ -EH-ABD proteins.....	169
Table 16: The reagents and materials used in this thesis	176
Table 17: The recipes for buffers and media used in this thesis	177
Table 18: The antibodies used in this thesis	178
Table 19: The reagents for cell cultures	179
Table 20: The sequences of all protein constructs used in this thesis.....	180

List of Figures

Figure 1: Schematic overview of human IgG1.....	5
Figure 2: Graphical representation of different Ig-like scaffold structures	10
Figure 3: Structures of non-Ig scaffolds.....	13
Figure 4: Schematic for the formation of ELP depot structures.....	20
Figure 5: Schematic for the <i>in vivo</i> approach of using ABD.....	22
Figure 6: Structural illustration of M13 filamentous phage.....	25
Figure 7: Schematic for phagemid vector.....	28
Figure 8: Schematic overview for gene assembly	31
Figure 9: Schematic overview for generating phage-displayed FN3 libraries.	32
Figure 10: Agarose gel electrophoresis for the FN3-inserted phagemid.	36
Figure 11: Structure of synthetic gene-coding for FN3	37
Figure 12: Graphical representation showing immune checkpoints.....	41
Figure 13: Therapeutic strategy for anti-PDL1 binders.....	45
Figure 14: Schematic diagrams showing the experimental panning procedures.	48
Figure 15: Schematic showing the experimental process for identifying sequences and their binding affinities.	49
Figure 16: Schematic showing the structures of phage ELISA.....	50
Figure 17: Schematic for gene assembly and protein expression.....	55
Figure 18: Schematic showing the structures of SPR for binding kinetics.....	58
Figure 19: Paper-based ELISA showing the successful enrichment and panning against PDL1.....	60

Figure 20: Phage ELISA of five sequences from naïve libraries	61
Figure 21: Synthetic gene-coding for second-generation libraries	62
Figure 22: Phage ELISA of final five hits for their binding affinity to PDL1 and their sequences.....	64
Figure 23: SDS-PAGE showing the successful expression and purification of His-tag-fused FN3.....	65
Figure 24: The binding kinetic profiles of the FN3 by the SPR.....	66
Figure 25: Schematic for the construction of aPDL1-FN3 oligomers.. ..	70
Figure 26: Representation of the PD1/PDL1 blockade assay.	78
Figure 27: Agarose gel image of the genes of aPDL1-FN3 oligomers.....	81
Figure 28: SDS-PAGE and WB images of multivalent (aPDL1-FN3) _n proteins	82
Figure 29: (aPDL1-FN3) _n are characterized for their molecular weights	83
Figure 30: (aPDL1-FN3) _n are characterized for their hydrodynamic radius (R _h).....	84
Figure 31: SPR sensorgrams of (aPDL1-FN3) _n oligomers	85
Figure 32: Characterization of Alexafluor488-conjugated (aPDL1-FN3) _n proteins.....	86
Figure 33: A PDL1 blockade assay was used to characterize the IC ₅₀ values of (aPDL1-FN3) _n proteins (n=1-5).....	88
Figure 34: Flow cytometry was performed using CHO-hPDL1 cells to characterize the <i>in vitro</i> PDL1 binding of (aPDL1-FN3) _n proteins (n=1-5).....	89
Figure 35: Montage of Z-stack images of (A) (aPDL1-FN3) ₁ and (B) (aPDL1-FN3) ₄ proteins	91
Figure 36: The schematic shows the modular design of (aPDL1-FN3) ₄ fused with ELP ...	96
Figure 37: The schematic shows a plasmid reconstruction for FN3-ELP fusion by recursive directional ligation (PRe-RDL)	97

Figure 38: The schematic shows the methodology.....	111
Figure 39: SPR determines the C-terminus fusion of ELP	113
Figure 40: (aPDL1-FN3) ₄ -ELP _{depot} is tuned for Tt below 37 °C.....	113
Figure 41: PDL1 blockade assay shows that (aPDL1-FN3) ₄ -ELP _{depot} antagonizes PDL1 signaling, with an IC ₅₀ of 250 pM.	114
Figure 42: <i>In vivo</i> anti-cancer efficacy in a CT26 syngeneic mouse model.	115
Figure 43: <i>In vivo</i> efficacy with three injections in CT26 model	116
Figure 44: Characterization of fusion proteins using an agarose gel	117
Figure 45: Characterization of fusion proteins using SDS-PAGE and WB.....	118
Figure 46: Biophysical characterization of (aPDL1-FN3) ₄ -ELP fusion protein.....	119
Figure 47: Characterization of the specific PDL1 binding kinetics of (aPDL1-FN3) ₄ -ELP using SPR.....	120
Figure 48: Successful conjugation of (aPDL1-FN3) ₄ -ELP with Alexafluor488	121
Figure 49: Biophysical characterization of (aPDL1-FN3) ₄ -ELP conjugated with Alexafluor488	122
Figure 50: Schematic showing the mechanism of AlphaLISA assay for mouse PDL1 antagonism	123
Figure 51: Characterization of IC ₅₀ of (aPDL1-FN3) ₄ -ELP as compared to anti-PDL1 antibodies	125
Figure 52: AlphaLISA for murine PDL1 binding showing the normalized AlphaLISA signal as a function of protein concentration of the Alexafluor488- conjugated, iodine-conjugated and unconjugated (aPDL1-FN3) ₄ -ELP	126
Figure 53: Flow cytometry data analysis using Jurkat/PD1 cells	127
Figure 54: Flow cytometry data analysis using CHO-hPDL1 cells	128

Figure 55: Flow cytometry data analysis of binding of (NonsenseFN3) ₄ -ELP and (aPDL1-FN3) ₄ -ELP to PDL1 receptors on CT26.WT, MC38, and CHO-hPDL1 cells	129
Figure 56: Montage of Z-stack images of (NonsenseFN3) ₄ -ELP using CT26 spheroids..	131
Figure 57: Montage of Z-stack images of (aPDL1-FN3) ₄ -ELP using CT26 spheroids.....	131
Figure 58: Montage of Z-stack images of Bioxcell's anti-PDL1 antibody using CT26 spheroids	132
Figure 59: Montage of Z-stack images of Invivogen's anti-PDL1 antibody using CT26 spheroids on ELP	132
Figure 60: Tumor penetration depth for (aPDL1-FN3) ₄ -ELP and antibodies.....	133
Figure 61: Pharmacokinetics show circulating proteins in plasma as a function of time following a single injection of (A) <i>i.p.</i> (aPDL1-FN3) ₄ , (B) <i>i.p.</i> (aPDL1-FN3) ₄ -ELP, and (C) <i>i.v.</i> (aPDL1-FN3) ₄ -ELP	134
Figure 62: Pharmacokinetics of (aPDL1-FN3) ₄ -ELP and anti-PDL1 antibodies	136
Figure 63: <i>In vivo</i> anti-cancer efficacy in a B16.F10 syngeneic mouse model	139
Figure 64: <i>In vivo</i> anti-cancer efficacy in an MC38 syngeneic mouse model.....	140
Figure 65: <i>In vivo</i> anti-cancer efficacy in a CT26.WT syngeneic mouse model	141
Figure 66: <i>In vivo</i> anti-cancer efficacy in an MC38 syngeneic mouse model showing some tumor-free mice.....	143
Figure 67: <i>In vivo</i> rechallenge experiment in an MC38 syngeneic mouse model.....	144
Figure 68: <i>In vivo</i> re-rechallenge experiment in an MC38 syngeneic mouse model	145
Figure 69: Biodistribution profiles of (aPDL1-FN3) ₄ -ELP compared to anti-PDL1 antibodies and (NonsenseFN3) ₄ -ELP scaffold control	147
Figure 70: Tumor immunomodulation profile study using a CT26 mouse model.....	149
Figure 71: Flow cytometry data analysis for quantification of tumor-infiltrating T lymphocytes	151

Figure 72: Schematic for the construction of (aPDL1-FN3) ₄ -ABD protein.....	156
Figure 73: SDS-PAGE images of (aPDL1-FN3) ₄ -ABD proteins	164
Figure 74: Purified (aPDL1-FN3) ₄ -ABD proteins are characterized for their molecular weights.....	165
Figure 75: Purified (aPDL1-FN3) ₄ -ABD proteins are characterized for their hydrodynamic radius	166
Figure 76: Characterization of the PDL1 antagonism of (aPDL1-FN3) ₄ -ABD proteins using <i>in vitro</i> PDL1 blockade assay	167
Figure 77: Characterization of the specific PDL1 and albumin binding kinetics of (aPDL1-FN3) ₄ -EH-ABD using SPR.....	168

Acknowledgments

First, I would like to thank my Ph.D. advisor, Dr. Ashutosh Chilkoti. Without his guidance and mentoring, I would not be able to achieve my research goals. His insightful suggestions and constructive feedback are very much appreciated. His understanding and encouragement have helped me throughout the challenges I faced throughout my research.

Secondly, I thank Dr. Smita Nair, who endlessly provides brilliant insight and guidance to my research, especially for *in vivo* experiments. With her extensive research experience in immune-oncology, she has greatly helped me design most of my *in vivo* work based on my preliminary data. Her discussion and feedback were highly informative and useful in determining my research direction.

Also, I am appreciative of my preliminary examination and dissertation committee members: Dr. Joel Collier, Dr. Charles Gersbach, Dr. Xilling Shen, and Dr. Kris Wood. I am thankful for their contribution of time and constructive feedback towards my presentation, documents, and overall research goals. I am also thankful to Dr. Michael Zalutsky and Dr. Zhengyuan Zhou for their collaboration that was instrumental in performing biodistribution studies using a gamma counter.

I am deeply grateful to the members of the Duke shared facilities who helped me to conduct significant experiments in my research: Dr. Nicolas Devos from GCB for next-generation sequencing, Dr. Brian Watts from DHVI for surface plasmon resonance,

and Dr. Michael Cook from FCSR for flow cytometry. I am also appreciative to Dr. Don Siegel and Dr. Gregg Silverman from Cold Spring Harbor Phage Display course. Thanks to their kind teaching and mentoring, I was able to achieve my Ph.D. research goals.

I am forever indebted to my intelligent and diligent colleagues in the Chilkoti lab. I learned a lot of techniques and helpful tips from them. Their discussion and advice were very thoughtful and insightful, their help with experiments was invaluable, and their passion for science has always motivated me to work hard towards my research goals. I am so lucky to have them in my life.

Last, but not least, I thank my family and friends for their love and support. They are the reasons that I have been persistent. They have always believed in me and encouraged me whenever I needed it.

1. Introduction

One way that our body fights against foreign molecules is by producing antibodies. Antibodies are proteins that recognize specific molecules called antigens. Once antibodies bind to antigens, they induce a series of downstream processes that activate immune cells and destroy antigen-containing cells. Since our body elaborately creates antibodies that strongly bind to antigens for various diseases, many scientists have enthusiastically identified and developed antibodies to be used as therapeutics (1). As of 2021, there are more than 100 therapeutic antibodies approved by FDA on the market (2), and around 830 are currently being evaluated in clinical trials (3). The general strategy is to develop antibodies that bind therapeutically relevant targets for diseases (4). These therapeutic antibodies are commonly monoclonal antibodies produced by plasma B cells to bind to specific cells or targets.

1.1 Monoclonal antibodies

There are two types of developed antibodies (5): 1) polyclonal antibodies that are usually generated by different B cell clones in the body; 2) monoclonal antibodies that are produced by identical B cells whose clones are from a single parent cell. Monoclonal antibodies only recognize the same epitope of an antigen with high specificity, while polyclonal antibodies are heterogeneous, binding to different epitopes of a single antigen. As therapeutics, monoclonal antibodies indicate higher specificity and lower cross-reactivity (5). Therefore, monoclonal antibodies are preferred for targeting highly

specific molecules in the body, such as surface components or markers overexpressed on cancer cells (6).

While the use of monoclonal antibodies to selectively target cancer cells is referred to as targeted therapy, the use of monoclonal antibodies to activate the immune system against cancer is called immunotherapy. In immunotherapy, antibodies agonize or antagonize receptors that modulate immune cells so that targeted immune cells recognize and attack cancer cells. In this thesis, monoclonal antibodies used in immunotherapy are generally covered.

1.1.1 The types of antibodies

Monoclonal antibodies are man-made proteins acting like natural antibodies in the immune system. Based on their protein composition, these antibodies have the following naming conventions (4). Names ending in -omab refer to murine antibodies and are completely made from mouse proteins. Names ending with -ximab refer to chimeric antibodies and are a combination of mouse and human protein. Names ending in -zumab refer to humanized antibodies and are made from small proportions of mouse proteins combined with human proteins. Names ending in -umab refer to human antibodies fully made from human proteins.

In the treatments of cancer, there are three different types of monoclonal antibodies. Pure antibodies, also known as naked antibodies, are antibodies without drug or radioactive material attached to them. They bind to antigens on cancer cells or

even free-floating proteins and are the most common type of monoclonal antibodies used as cancer therapeutics (6). Conjugated antibodies are combined with a chemotherapy drug or a radioactive particle (7). These antibodies are used as a homing molecule to deliver their attached partner directly to cancer cells. While monoclonal antibodies circulate throughout the body, they bind to their target antigens. Their attached toxic substances are delivered usually to tumor microenvironments. This targeted delivery is expected to reduce off-target toxicity in the body. Bi-specific antibodies are drugs composed of parts of two different antibodies that can bind to two different antigens simultaneously (8). By binding both antigens, these antibodies are designed to bring two different cells together, usually engaging both cancer cells and immune cells, to activate host immunity to destroy nearby cancer cells. **Table 1** shows a few examples of different types of monoclonal antibodies that are FDA-approved and currently commercially used.

Table 1: FDA-approved antibodies therapeutics

Type	Name	Target	Label	Approval	Reference
Pure	Alemtuzumab	CD52	N/A	2014	(9)
	Nivolumab	PD1		2014	(10)
	Durvalumab	PDL1		2017	(11)
Conjugated	Ibritumomab tiuxetan	CD20	Yttrium-90	2002	(12)
	Brentuximab vedotin	CD30	Monomethyl auristatin E	2011	(13)
	loncastuximab tesirine-lpyl	CD19	Pyrrlobenzo-diazepine	2021	(14)
Bispecific	Blinatumomab	CD3/CD19	N/A	2014	(15)

1.1.2 The structure of an antibody

An antibody molecule is the secretion form of B cell receptors (BCR) produced by activated B cells. For BCR, the C-terminus is a hydrophobic membrane-anchoring region, while for antibodies, the C-terminus is a hydrophilic heavy-chain constant region. This water-solubility allows antibodies to readily circulate throughout the body.

There are five different classes of immunoglobulins (IgM, IgD, IgG, IgA, and IgE), and all of them are composed of heavy and light polypeptide chains. Since the most abundant antibody in serum is IgG, in this section, we use the IgG antibody as an example to describe the general structure of an antibody.

IgG antibodies are large molecules, with a molecular weight of around 150 kDa, made of two different kinds of polypeptide chains (16). One is termed a heavy (H) chain, around 50kDa, and the other is termed a light (L) chain, around 25kDa. An IgG antibody possesses a Y shape that consists of a total of four polypeptides chains - two identical heavy chains and two identical light chains. The two heavy chains are connected by disulfide bonds, and each heavy chain is bound to a light chain by many noncovalent bonds and disulfide bonds. The schematic representation of antibody structure is illustrated in **Figure 1**. Each tip of the “Y” contains a paratope (a structure analogous to a lock) that is specific for one specific epitope (analogous to a key) on an antigen (16). The interaction between a paratope and an epitope allows both antibody and antigen to bind together precisely.

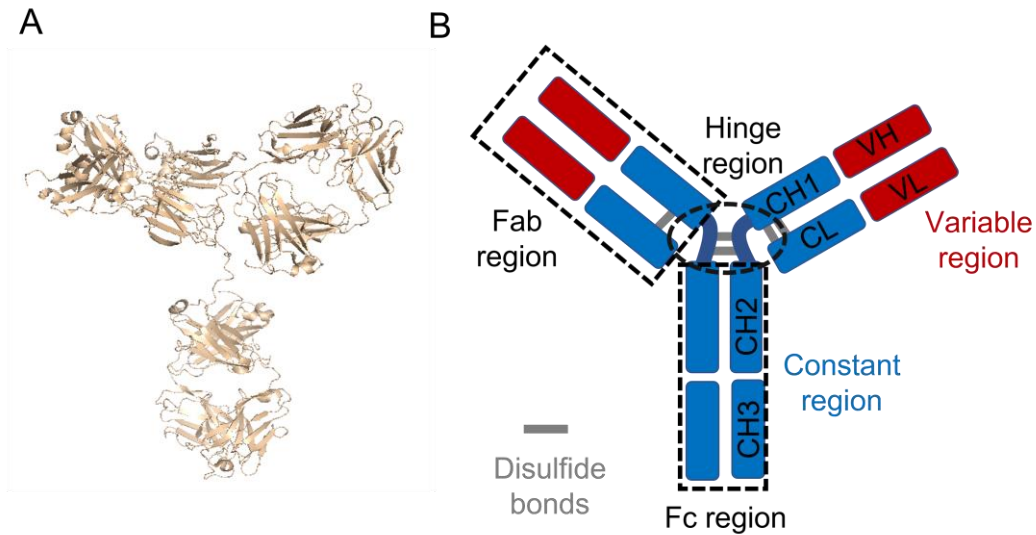


Figure 1: Schematic overview of human IgG1. (A) Secondary β barrel structures are illustrated by PyMol (PDB:1HZH). (B) The heavy chain (HC) contains three constant domains (CH1-CH3) and a variable domain (VH), whereas the light chain (LC) has only one constant domain (CL) and a variable domain (VL). The Fab consists of VH, CH1, and LC. CH2 and CH3 of the two heavy chains compose the fragment crystallizable (Fc). Between the CH1 and CH2 of the heavy chains is a mostly flexible hinge region and the four chains are covalently connected via disulfide bridges.

Antibodies bind to various antigens, and a limited number of effector molecules and cells (16). The two tips of the Y structure vary between different antibody molecules and are called the variable (V) region. This region contributes to antigen binding. The overall arms of this region are termed fragment antigen-binding (Fab). Antibodies have two Fab regions that provide more stable antigen-binding through bivalency (17). The stem of the Y structure, called a constant (C) region, is less variable among antibodies. The bottom trunk of the Y structure is termed fragment crystallizable (Fc). Flexible hinge regions join the arms of the Y structure to the bottom trunk. The Fc and hinge regions

determine the isotypes of antibodies based on which effector molecules and cells they interact with (16).

The human IgG has four subclasses, based on their CH2 domains and hinges, IgG1, IgG2, IgG3, and IgG4 (18). These regions can bind to both IgG-Fc receptors (Fc γ R) and C1q, which are parts of signaling proteins on different immune effector mechanisms. Once antibodies bind to both antigens and these proteins, antigens are tagged by Fc γ R-expressing cells, leading to the destruction of antigens by phagocytosis, antibody-dependent cell-mediated cytotoxicity (ADCC), and complement-dependent cytotoxicity (CDC) (18). The Fc region also contains a binding epitope for the neonatal Fc receptor (FcRn), responsible for extended serum half-life, placental delivery, and bidirectional transport of antibodies to mucosal surfaces (18).

The hinge region that links the Fc and Fab is a loosely connected tether, providing flexible and independent movement of two Fab regions. Some flexibility also exists at the junction between V and C domains. The flexibility of the antibody provides its molecular bending, rotation, and stretching to allow for its target binding easily at various distances apart as well as mediating effector functions simultaneously (8).

1.1.3 Advantages and limitations of using antibodies

Antibodies are a rapidly growing class of therapeutics that have shown unprecedented clinical success rates (19). This great success is mainly because of four reasons: 1) their exceptional binding affinities and exquisite specificities to their

antigens. These allow them to effectively bind to their targets with limited off-target effects, which greatly improved the efficacy and safety of treatments; 2) their large sizes and Fc regions allow for very long serum half-life, providing sufficient time for antibodies to bind their targets, accumulating in their target tissues, while circulating throughout the body; 3) their relatively low immunogenicity because most antibodies are human originated (20), and producing adaptive antibodies is a part of natural human immunity to infection; and 4) they are bifunctional that can directly bind to their target, while interacting with Fc receptors to induce effector functions, such as ADCC and CDC.

However, the development of antibody drugs is approaching an asymptote because their structural complexity and inflexibility for engineering provide limited options to improve their clinical utility (21). First, within the large size of 150kDa, antibodies have an Fc region and two Fab arms that show only bivalent binding. To increase their valency and receptor accessibility, genetically engineering one or two more variable regions would reach even larger sizes, which can be very detrimental to their folding, solubility, expression, and yield (22). Also, the large size of antibody and steric hindrance upon tight binding restrict the tumor uptake and penetration of antibody (23). This can be a serious problem, especially for the treatments of solid tumors, because solid tumors are poorly vascularized, unlike liquid tumors. Without efficient access in solid tumors, the efficacy of antibodies can be greatly impaired (24).

To overcome these issues, the desire to develop smaller target-binding scaffolds rises (25). These scaffolds can retain tight and specific binding to targets, like antibodies, but can be faster to discover, less expensive to manufacture, more efficient to penetrate solid tumors (26). They would not exhibit Fc-mediated effector functions, but these functions are not entirely necessary to be used as a simple antagonist or drug delivery vehicle. The most important feature of using smaller protein scaffolds is its modularity: the amenability to various genetic modifications for their different structural orientation, tunable valency, binding affinity, and binding specificities. This modularity can easily generate bi- or multi-specific molecules, which is a very challenging task for traditional, full-length antibodies (22).

1.2 Target-binding scaffolds

In the past decades, approximately 50 different protein scaffolds have been discovered and developed as antibody mimetics for therapeutic and/or diagnostic tools. The 'scaffold' term is used in protein engineering to refer to a single chain polypeptide molecule, typically with a very smaller size (<200 amino acid residues) (26). Also, this scaffold possesses a highly structured core with some flexible regions that can be highly tolerable to genetic modifications, including mutations, insertions, and deletions. This structural flexibility can allow us to tune their valency and binding affinity to targets: we can engineer them to interact with multiple targets or to facilitate their concerted binding to a given target more strongly and tightly via avidity (27). In addition, based

on their engineering purposes, they can potentially provide better solubility in aqueous solution, reversible refolding, higher thermodynamic stability, lack of aggregation, comparatively low costs to manufacture, and better tumor uptake and penetration (25). This scaffold molecule can be based on either a conventional immunoglobulin backbone (Ig-like scaffold) (28) or a derivate of a completely unrelated protein (Non-Ig scaffold) (29).

Many of these novel scaffolds are developed to validate targets in cancer and inflammatory diseases, including vascular endothelial growth factor (VEGF) (30), tumor necrosis factor- α (TNF- α) (31), CD20 (32), and CD19 (33). Currently, some of the promising candidates have reached the stage of development in therapeutics and diagnostics (34). Here, the most clinically advanced binding scaffolds will be covered in terms of cancer immunotherapy.

1.2.1 Ig-like scaffolds

Thorough structural studies of antibodies and advances in genetic engineering techniques allow us to construct and develop a variety of Ig-like scaffolds (28). These Ig-like domains are commonly present in cellular signaling pathways throughout our body, which also can be named the Ig superfamily (35). The principle underlying this molecular development is that many polypeptide chains residing in the C and V domains of IgG are critical to their folding and stability. Thus, proteins whose sequences are similar to those of IgGs are expected to exhibit similar β sheets structures, similar

folding patterns, and thus similar binding affinities, and this has been verified by X-ray crystallography (36).

One type of Ig-like scaffold is the single-chain Fv (scFv, **Figure 2A**), which truncates the Fab region resulting in only the V domain of a heavy chain (VH) linked by a stretch of synthetic peptides to a V domain of light chain (VL) (37). scFv is a genetic fusion protein between the VH and VL of IgGs, connected with a short linker that is comprised of 10 to 25 amino acid residues. The overall size of scFv ranges from 25kDa to 30kDa (37). scFv is a valuable therapeutic molecule because its scaffold still retains its strong binding affinity, similar to that of a full-structure antibody, but with minimal size, so that they may penetrate the target tissue easily.

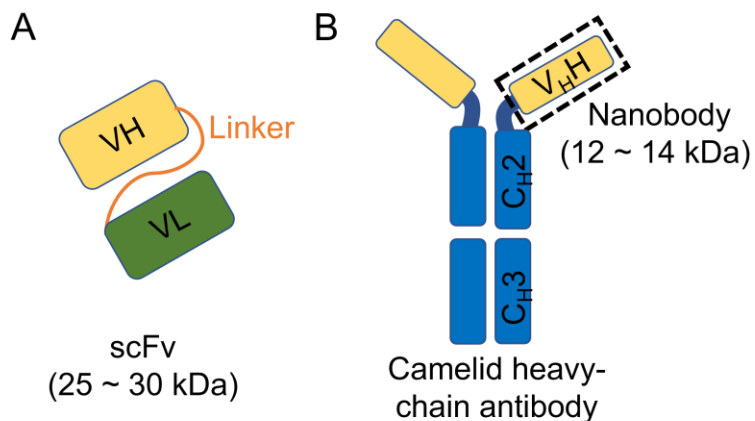


Figure 2: Graphical representation of different Ig-like scaffold structures. (A) An scFv consists of VH and VL connected with a polypeptide linker. (B) A camelid heavy-chain antibody consists of two same heavy chains only for both variable (V_HH) and constant (C_H2 and C_H3) domains. The antigen-binding region consists of a single variable domain V_HH, also called nanobody.

To make the scaffold even smaller, another strategy is to utilize nanobodies, also called V_HH (38), which are the smallest naturally occurring Ig-like protein, (**Figure 2B**). Camelids produce this atypical Ig format, which is very distinct from human IgG, containing only one heavy chain with a single variable domain. After the discovery that camelids have fully functional antibodies without light chains (39), many researchers developed nanobodies that are stable and fully active without the addition of light chains (40). Therefore, nanobodies have extremely minimal size, which can significantly enhance the tissue permeability and receptor accessibility of molecules. However, to reduce the potential immunogenicity of therapeutic candidates, nanobodies should undergo conventional humanization procedures (20). Currently, one nanobody molecule, named caplacizumab, is FDA-approved in 2019 (41), and eight other nanobody candidates are in the clinic (34): one in phase III, four in phase II, and three in phase I. The FDA-approved nanobody drug is a bivalent nanobody targeting von Willebrand Factor (vWF) to treat acute thrombotic thrombocytopenic purpura (aTTP) (42).

1.2.2 Non-Ig scaffolds

Unlike Ig-like scaffolds, non-Ig scaffolds are derived from proteins whose sequences and structures are completely different from those of the Ig superfamily (43). These scaffolds include the Kunitz domain (44), PDZ domains (45), and affibodies

domains (46). Among many of them, in this thesis, the three most well-established platforms are covered. **Table 2** summarizes these scaffolds.

Table 2: Overview of commonly used non-Ig scaffolds

Scaffold	Parental protein	The # of AAs	MW (kDa)	Structure	Reference
Anticalin	Lipocalin	160-180	18-20	β -barrel with 4 loops	(47)
DARPin	Ankyrin repeats	133-199	14-21	α -helical + β -turn	(48)
Avimer	A-domain from LDLR	35	4	Ca ²⁺ binding Disulfide confined	(49)
Affibody	Z-domain from protein A	58	7	α -helical bundles	(50)
Monobody	Human 10 th fibronectin type III	94	10	β -sandwich with 3 loops	(51)

1.2.2.1 Anticalins

Lipocalins have been developed as a promising protein backbone because they possess four-loop regions outside of a β -barrel structure (**Figure 3A**). Many derivative forms of lipocalins have been utilized to randomize 16 amino acid residues on these four-loop regions, including the bilin-binding protein from the cabbage white butterfly and the human tear lipocalin (52). These lipocalin-based structures were named ‘anticalins’, and have been commercially developed by Pieris (Germany) (47). Anticalins are very soluble and stable proteins and can be readily produced in both *E. coli* and yeast. Currently, four anticalins scaffolds are in clinical trials: one in phase II and three in phase I (47). One of the leading candidates is a PEGylated anticalin that targets

hepcidin, named PRS-080, to treat functional iron deficiency (FID) anemia (53). Based on their PK/PD studies, to achieve a low steady-state concentration, 30kDa PEG polymer is most suitable to conjugate the hepcidin-targeting anticalin protein (54). Their clinical phase I study showed that a single intravenous injection with a dose of 16 mg/kg BW was very safe and well-tolerated (53). Notably, the administration of this drug exhibited substantial therapeutic efficacy and duration, leading to a subsequent phase IIa study (NCT03325621).

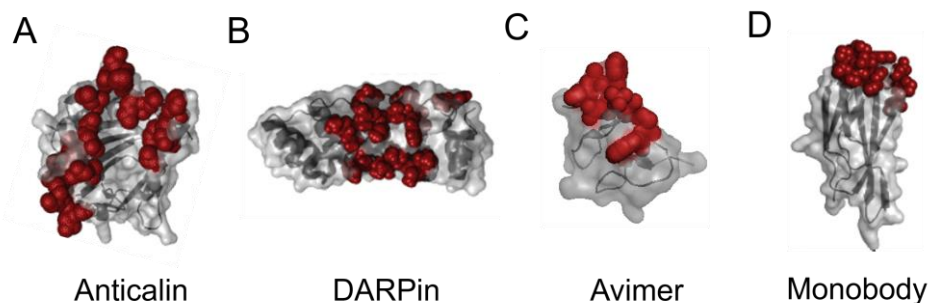


Figure 3: Structures of non-Ig scaffolds: (A) anticalin (5KBN), (B) DARPin (4DUI), (C) avimer (1AJJ), and (D) monobody (5KBN). The figures were generated by PyMoL using the structures in PDB databases. Representative scaffolds are shown in a gray surface with typical diversified binding regions illustrated as red spheres.

1.2.2.2 DARPins

Designed ankyrin repeat proteins (DARPins) are fully engineered protein scaffolds derived from ankyrin repeat (AR) proteins (48). Most natural AR proteins consist of consecutive repeats of AR domains stacked with each other, ranging from four to six domains (55). However, DARPins are usually limited to two to four repeats of these domains and contain N- and C- terminal capping motifs to cover hydrophobic

regions to increase overall solubility (**Figure 3B**) (55). These molecules have been commercially developed by Molecular Partners (Switzerland). DARPins are well produced in *E. coli* and exhibit high thermodynamic stability and low aggregation. One of the most clinically advanced DARPin molecules is a highly specific and potent VEGF-A inhibitor, whose IC₅₀ value is lower than 10 pM (MP0112) (56). To improve the pharmacokinetics of this drug, MP0112 was conjugated to a PEG molecule, and renamed as Abicipar pegol. Although Abicipar pegol was not FDA-approved after clinical phase III, this drug proved a great potential to treat age-related macular degeneration (AMD) and diabetic macular edema (DME) (57).

1.2.2.3 Avimers

The avimer is named after the “avidity multimer”. The rationale of designing avimers is to oligomerize small A-domain scaffolds to increase their binding affinity through the avidity effect. These A-domain scaffolds are commonly present in a wide variety of cell surface receptors, including low-density lipoprotein receptors (**Figure 3C**) (58). Using the universally conserved residues of the A-domain, multiple A-domain scaffolds are genetically fused to form a high-affinity avimer. Notably, avimers even with 24 disulfide bonds can be readily produced in *E. coli* (49). The most clinically advanced avimer is the C326 molecule that targets the cytokine IL-6 (AMG220) (59). This avimer exhibits a very strong binding affinity in a picomolar range for IL-6, measured by

an *in vitro* proliferation assay (58). It is currently in clinical phase I to treat Crohn's disease (NCT00353756).

1.3 Human fibronectin type III domain (FN3)

1.3.1 Properties

The monobody is an engineered target-binding protein scaffold derived from the tenth type III domain of human fibronectin (FN3), one of the human extracellular matrix proteins (60). The original function of FN3 is to bind integrins in fibronectin. This domain consists of 94 amino acid residues and exhibits high thermodynamic stability whose melting temperature is above 80°C (61). The native scaffold forms a β -sandwich with seven β -strands connected by six loops (**Figure 3D**), which are similar to Ig domains without disulfide bonds (62). Every three loops are very flexible, comprised of around 15 amino acid residues (AAs) present at both ends. Therefore, one end can be engineered to have a desired binding function by randomizing its sequences and displaying these diversified proteins on a phage (63), yeast (64), or mRNA (65). Adnexus (USA, now Bristol-Myers-Squibb), translated this discovery and renamed it as an 'adnectin' (60). Usually, target-binding adnectin candidates exhibit their binding affinities in nanomolar to picomolar ranges (66). Other monobody mimetics have been successfully developed as scaffold proteins, such as a human tenascin-C domain (67) and a universal consensus fibronectin domain (68).

1.3.2 Applications

Currently, three different adnectin candidates have been evaluated in clinical trials (43): two in phase II and one in phase I. The most clinically examined adnectin is the PEGylated CT-322 molecule that targets and inhibits the vascular endothelial growth factor (VEGF2) receptor (69). This potential drug has a binding affinity of around 11 nM (70), a serum half-life of 4 days due to a conjugated 40 kDa branched PEG molecule, and a maximum tolerated dose (MTD) of 2 mg/kg to humans administered intravenously (71). Also, in clinical trials, the drug showed clinical therapeutic responses, stabilizing disease conditions by increasing the level of serum VEGF. However, approximately 80% of patients developed anti-drug antibodies, because of engineered loop regions in the binding moiety (71). In the following phase II, although the drug showed low-grade toxicities, it was not as effective as expected (70).

The next drug in the clinical stage is a PEGylated adnectin that binds and inhibits cholesterol regulator proprotein convertase subtilisin/kexin type 9 (PCSK9) (BMS-962476) (72). The PCSK9 is a useful target to decrease low-density lipoprotein (LDL) to treat cardiovascular diseases. This drug has an EC₅₀ value of 31 nmol/L, successfully reducing the level of cholesterol in animal models (72). In a clinical phase I, this drug was well-tolerated at doses up to 1 mg/kg while significantly lowering the levels of free PCSK9 and LDL (73).

The last drug is an adnectin that binds and inhibits myostatin, which negatively regulates skeletal muscle development (BMS-986089) (74). This drug is currently being evaluated in phase II clinical trials to treat Duchenne's muscular dystrophy (DMD), one of the skeletal muscle diseases.

1.3.3 Advantages and limitations

Many FN3-based molecules in preclinical or clinical stages were developed by phage display, yeast display, or mRNA display (60). Through these techniques, the selected FN3 scaffolds' sequences were screened for predicted immunogenicity, favorable biophysical and biochemical properties such as affinity, specificity, stability, and solubility (75). To improve their pharmacokinetics, the original scaffold was modified to conjugate with PEG molecule and characterized for its biological efficacy in both *in vitro* and *in vivo* models (70). The utility of FN3 has already been demonstrated by several studies that have successfully engineered to bind to diverse proteins and receptors, including SH2 domains (51) and epidermal growth factor receptors (EGFR) (76).

There are mainly three reasons why FN3-based monobody has been preferred and explored by many scientists: 1) The structure of this molecule is easily engineered. FN3 has a β -sandwich bundle that provides binding moieties every three loops at both ends, with at least 15 amino acid residues for randomization at each end (77). This offers a powerful diversity of potential binding moieties; 2) Structural stability and plasticity

enable us to robustly develop this molecule as a therapeutic. FN3 has high structural stability attributed to its tight hydrophobic core of β -sheets (78). Thus, it can be stable over a wide range of temperature, pH, and chemical denaturants. It can be refolded to its native conformation after thermal or chemical denaturation. The FN3 molecule is devoid of cysteine residues and independent of any metal ions, bound ligands, or disulfide bonds for stabilization. It can be readily expressed in *E. coli* and is usually soluble. All these factors show that FN3 can be rapidly and inexpensively produced, reducing both manufacturing costs and laborious optimization steps as compared to antibodies; 3) A compact size and simple structure provide modularity (79). To optimize the scaffold for desired functions, including binding affinities, specificities, and pharmacokinetics, genetic modifications are necessary. The well-defined structure of FN3 can make these possible because multiple FN3 proteins can be linearly repeated with flexible linkers to modulate their valency and affinity (80). Unlike bivalent antibodies, the multivalency of FN3 is not restricted. The engineered and optimized FN3 can selectively and efficiently enter target tissue, which can be inaccessible by large molecular weight antibodies.

Although the compact size of the FN3 protein offers many advantages, this can be counterbalanced by a very short serum half-life time due to a glomerular filtration cut-off (50kDa) (81). A rapid renal clearance is desirable for diagnostics tools, but not for therapeutics because this faster clearance would significantly reduce the circulation of

drugs, which eventually reduces the overall uptake of target cancers. To improve its circulation time as well as pharmacokinetic properties, one common approach is to develop a fusion protein with biopolymers (82).

1.4 Biopolymers for recombinant fusions

Biopolymers are a serial chain of biological monomers that are covalently linked together, such as polypeptides, polysaccharides, and nucleic acids. Recombinant biopolymers are designed and engineered by scientists to exhibit desired biophysical properties and/or functions. For example, the recombinant biopolymers can be engineered to have motifs derived from silk (83), collagen (84), and resilin (85), so that they can exhibit the specific properties of their parent protein. The advantages of using biopolymers over synthetic polymers are not only biocompatibility, but also the ability to precisely control their sequences, structures, and sizes, enabling the production of a large quantity of uniform and monodisperse polymers.

1.4.1 Elastin-like polypeptides

Elastin-like polypeptides (ELPs) are polymers with repeat units consisting of the VPGXG amino acid motif (where X can be any amino acid except proline), which is derived from the hydrophobic domain of tropoelastin (86). As ELPs are genetically encoded, they can be readily produced in *E. coli*, are monodisperse, and their sequence and MW can be precisely specified (87). ELPs have been injected into humans in several clinical trials and have shown minimal immunogenicity (88, 89). ELPs are useful as

depot-forming protein modules, as they exhibit reversible lower critical solution temperature (LCST) phase-transition behavior (**Figure 4**) (90), wherein an ELP solution forms an insoluble coacervate upon heating above a critical transition temperature (T_t).

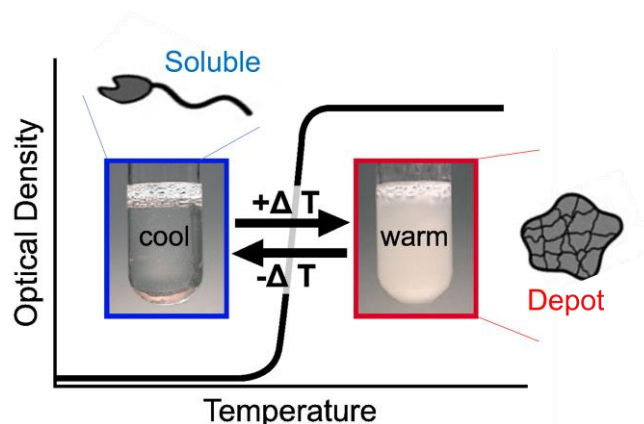


Figure 4: Schematic for the formation of ELP depot structures. Since ELP has LCST behavior at the T_t , soluble ELP forms an insoluble coacervate upon heating above this T_t . This figure is adapted from (96).

The T_t can be precisely tuned by modulating the MW of the ELP and the hydrophobicity of the guest residue (X), enabling the rational design of ELPs that transition from a solution at room temperature in a syringe into an insoluble coacervate upon injection *in vivo* (91). Because the T_t varies as a strong inverse log function of ELP concentration, as ELP at the depot boundary is diluted by interstitial flow, its T_t increases above body temperature and the ELP becomes soluble and is released into circulation with zero-order kinetics (92). The plasma circulation duration of the released ELP fusion can be further tuned by adjusting the MW of the ELP (93). Furthermore, ELPs retain their thermal responsiveness after the genetic fusion while the fusion

partners maintain their bioactivities, making them a promising biopolymer for recombinant fusion to improve pharmacokinetics (94, 95).

1.4.2 Albumin-binding domain

Albumin has served as an ideal drug carrier (97) because it is a natural, biocompatible, and biodegradable transporter and most notably, exhibits an exceptionally long half-life. To exploit this albumin as an *in vivo* drug carrier, drugs can be modified to confer an affinity to albumin, such that after the injection of drugs, they can piggyback onto the albumin in the bloodstream and ride until they arrive at the targets. This strategy can be achieved by the genetic fusion of drugs with albumin-binding domains (**Figure 5**) (98).

Albumin-binding domains are derived from streptococcal protein G (SpG), a bacterial receptor present on the surface of streptococcus strain G148 (99). Since SpG has a binding affinity to both IgG and albumin, scientists separated each binding region that contains three independent folding domains and determined the structure of the albumin-binding domain (ABD) (100). This domain consists of 46 amino acid residues, exhibiting three alpha-helix secondary structures with sub-nanomolar binding affinity to human serum albumin. Based on this sequence, advances in protein engineering and phage display have resulted in the development of artificial variants of ABD to improve their stability and affinities to albumin (99). One of these variants, used in this work, is called ABD094. This specific domain is a deimmunized ABD variant to remove T cell

epitopes while maintaining a high affinity to human serum albumin (101, 102). We expect that this ABD would not possess any significant immunogenicity that could potentially affect our future *in vivo* studies.

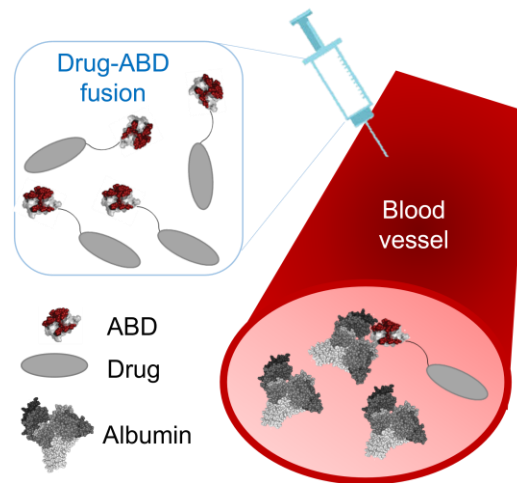


Figure 5: Schematic for the *in vivo* approach of using ABD. After being administered intravenously, ABD-fused drugs bind to albumin in plasma, circulate throughout the blood until drugs find their targets. This approach is expected to greatly prolong the plasma half-life of drugs. This figure is adapted from (103).

2. Developing phage-displayed FN3 library

2.1 Introduction and motivation

To develop an alternative protein drug to a monoclonal antibody, we first determine a type of binding scaffold to be used as an affinity module. Among many candidates, we decided to use non-Ig scaffolds, because they address potential problems associated with the large and complex antibody and simultaneously offer modularity that can engineer multivalent or multi-specific constructs. Specifically, FN3 described in chapter 1.3 was chosen, because it has the most compact size without any cysteine residues.

An FN3 that can bind to a target of choice is created by directed evolution (104). Usually, large combinatorial libraries are generated where the amino acid sequence of an exterior surface on the scaffold is diversified while maintaining its core structure. From these libraries, specific binding proteins are screened by molecular display technologies, including yeast-, mRNA-, or phage- display. We decided to use a phage display because it is easy to generate a library comprising the highest level of diversity (105). Using this highly diverse library, we can readily obtain variants with high specificity and strong affinity in sub-nanomolar ranges (106).

Libraries can be generated from not only natural immune libraries, but also designed universal methods such as sequential cloning, splicing by overlap extension PCR, and using restriction enzymes (107). These genetic modifications allow us to

develop diverse libraries readily and robustly. Since randomized mutations are simultaneously introduced, the total number of diversified sequences usually exceeds the number that is experimentally achieved. Thus, when developing a functional combinatorial library, significant considerations are the proper selection of target residues for randomization as well as the appropriate choice of amino acids to include at each position. In this chapter, I will first outline the basic principles for the use of protein-displayed phage libraries. Next, I describe detailed methods to achieve a wide diversity of FN3-displayed phage libraries. Lastly, I cover library design, construction, and analysis.

2.1.1 M13 filamentous phage display system

One of the most successful technologies for the discovery of binders is phage display because it reflects the natural immune system. At least 100 monoclonal antibodies have been FDA-approved and more than 14 were discovered and engineered by M13 filamentous phage display (108). In addition to the M13 phage display, lambda phage display has been developed, because lambda phage allows for both N-terminal and C-terminal fusions of phage coat proteins (109). However, M13 phage is preferred over lambda, because lambda can promote a lytic infection causing the cytotoxicity of *E. coli*, while M13 provides a lysogenic infection without any cell death. Therefore, lambda phage display is used only when fragment candidates are toxic for the host cell or not

secreted throughout the periplasm (110). Thus, we decided to use M13 filamentous phage display, a more commonly used and well-established approach.

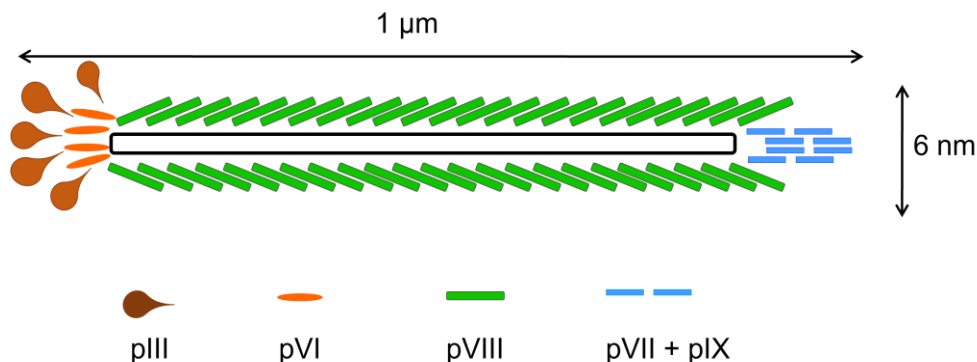


Figure 6: Structural illustration of M13 filamentous phage. The major coat protein pVIII assembles along the phage while four minor coat proteins are capped at both ends. The most exposed pIII protein is commonly used for a fusion partner to incorporate binder candidates.

Table 3: Overview of M13 coat proteins

Coat proteins	pIII	pVI	pVIII	pVII	pIX
The # of AAs	406	112	50	33	32
MW (kDa)	42.5	12.4	5.2	3.6	3.7
Copies/virion	~5	~5	~2,700	~5	~5

M13 filamentous phage display was first developed in 1985, by Dr. George P. Smith who genetically fused short peptides to the pIII minor coat protein of M13 phage (111). M13 is a filamentous bacteriophage that infects bacteria, particularly, the *E. coli* strains that have the F-pilus (male *E. coli*). The structure of this phage has a long rod shape, approximately 1 μm in length and 6 nm in width (Figure 6). It consists of a circular single-stranded DNA (ssDNA) surrounded by different types of capsid proteins (112): 1) Around 2700 copies of major coat proteins (pVIII) that are assembled along the

overall body of the phage; 2) Around five copies of four other minor coat proteins comprised of pIII and pVI on one side at the edge and pVII and pIX on the other edge (**Table 3**). Particularly, pIII coat proteins are commonly exploited, because they have five copies and do not play a role in any infection processes.

Since its first discovery, the M13 phage has been extensively studied to characterize its components and to understand its biological roles and mechanisms of replication (112). Also, the rapid advancement of molecular biology tools has allowed the M13 phage to be a more attractive tool for various applications (113, 114). For example, it can be served as a building block that can be self-assembled to functional materials (115) and devices (116). Most importantly, because the M13 phage can easily display the genetically fused peptides/proteins on its surface, the development of novel molecular diagnostics and therapeutics has become more robust and convenient (117). This feature provides the groundwork to readily identify and discover many interactions between proteins and their targets/ligands (118).

2.1.2 Low valency display

Based on the first developed polypeptides display of M13 phage, three teams have successfully included antibody fragments on M13 phage surfaces: the research groups of McCafferty and Chiswell (Cambridge) (119), Barbas (La Jolla) (120), and Breitling and Dübel (Heidelberg) (121). While the McCafferty group integrated the sequences of antibody fragments into the pIII-encoded gene in the phage genome, the

other two groups developed the phagemid system which is more frequently used these days because of its improved flexibility.

The difference between using the phage genome and the phagemid is the valency of proteins that are displayed on the pIII coat protein of the M13 phage. Once the gene fragments encoding target-binding motifs are directly fused to the phage genome DNA encoding the pIII protein, all five copies of pIII coat proteins would display a diverse set of peptides in a polyvalent format (122). Due to the avidity effects, this penta-valency results in the selection of proteins that have low binding affinities, usually in a high micromolar range. However, the developed phagemid system allows the display of protein in a monovalent format, allowing for the identification of high-affinity binders in the nanomolar ranges (122).

A monovalent display can be achieved by fusing the gene fragment candidate with the gene encoding pIII in a phagemid (**Figure 7**) (122). A phagemid is a plasmid containing sequences necessary for the expression of fusion and packaging proteins. Using this phagemid, the expression of the fusion protein is uncoupled from the original phage replication and phage protein production. Instead, the phagemid contains its origin of replication, a gene conferring resistance to ampicillin and carbenicillin, and the fusion gene under the control of a promoter. In this way, only the phagemid is responsible for the expression of fusion, not other phage proteins. Assembly of functional phage particles is then facilitated by the addition of a helper phage (M13K07

or VCSM13) (123). The helper phage exclusively provides all components for packaging M13 phages. Thus, all new phage particles contain all the viral proteins from the helper phage, including large amounts of the wild type pIII, with a very low proportion of the fusion from the phagemid (124). As the phagemid is more efficiently packaged than the helper phage DNA, most of the phage particles contain phagemid. However, regarding the expression of the fusion, the majority of viral particles do not have the foreign fusion from phagemid, only the wild-type pIII from the helper phage. It is known that 1-10% of the viral particles display foreign fusion, normally in a monovalent way (124). The low abundance of foreign protein is a way to achieve monovalency.

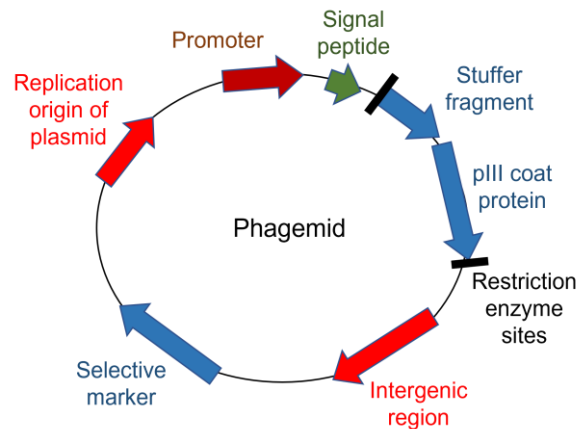


Figure 7: Schematic for phagemid vector. The phagemid only includes the gene encoding pIII coat protein with selective antibiotics marker, signals for DNA replication and packing for M13 phage particles, and restriction enzyme sites to readily incorporate target-binding variants to the N-terminus of the pIII coat protein.

The M13 phages can readily infect the host *E. coli* and robustly utilize its expression system for propagation (125). Thus, once the genes of the M13 phage enter

the *E. coli*, the *E. coli* expresses the M13 phage genes, producing proteins for M13 phages. This relationship establishes a link between phenotype and genotype: proteins displayed on the surface of the phage contain the corresponding gene of those proteins inside the phage. This is very advantageous, because specific phages that bind targets can be isolated from other non-binding phages, and their genes can be analyzed simultaneously to identify the target-specific sequences.

2.1.3 Phage library construction

Based on the system using phagemid vector and helper phage, we can construct diversified phage libraries that display monovalent target-binding proteins. In detail, we can incorporate genes encoding the fusion between target-binding proteins and pIII coat proteins into the phagemid. After the transformation of phagemid into male *E. coli* strains and the addition of helper phages, we can obtain functional phage libraries that display a wide range of target-binding variants on their surfaces.

To accomplish a good quality phage library, it is crucial to produce a large quantity of highly purified M13 phage particles. Currently, the gold-standard method is precipitation with polyethylene glycol (PEG) after the propagation in *E. coli* batch cultures (126). PEG has been widely used for precipitation because of the amphiphilic moieties of PEG. PEG has the external hydroxyl groups and the interior chain groups, which interact with proteins through a variety of non-covalent interactions, including the hydrophobic attraction and multipoint van der Waals contacts (127). These

interactions are between PEG and many chemical groups commonly present in proteins, like aromatic rings, amides, carboxylates, and hydroxyls. However, it is also known that high molecular weights of PEGs (MW > 5kDa) could affect the conformation of proteins that could change their biological activities (114). Thus, it is significant to minimize the presence of PEG as well as to remove any accumulation of contaminant PEG in freshly generated M13 phage libraries.

2.2 Materials and methods

2.2.1 FN3 variants library

The FN3 scaffold (also termed “monobody”) has two β -sheets: one is composed of three β -strands A, B, and E, and the other consists of four β -strands C, D, F, and G. The connecting loops of these two β -sheets are BC, DE, and FG loops, and they are equivalent to the complementarity-determining regions (CDRs) of antibody (63). We decided to diversify these three loops by introducing randomized amino acid sequences because loop-focused mutants would highly probably maintain their original structures and provide sufficient space for loops to recognize targets (76).

A synthetic gene for FN3 was designed based on the amino acid sequences from the previous research. We purchased the oligonucleotides from Integrated DNA Technologies (USA).

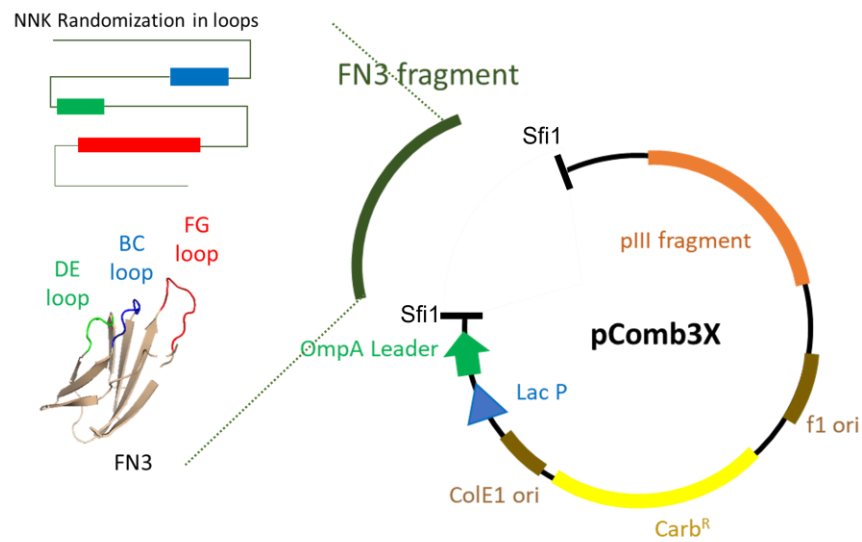


Figure 8: Schematic overview for gene assembly. The NNK randomized loop regions were spliced into a full FN3 sequence and then annealed into the phagemid (pComb3X) to be fused into the N-terminus of the pIII coat protein.

The gene was assembled as follows (**Figure 8**): 1) the gene sequence was divided into three sections for each BC, DE, and FG loop region; 2) for the 5' end of BC and the 3' end of FG loop section, the gene fragments should contain the required complementary region paired with the phagemid gene for fusion later, including restriction enzyme sites (Sfi1); 3) All three genes should begin with 15 base pairs complementary to the region preceding the insertion point and end with 15 base pairs complementary to the region following the insertion point. Any randomization sequence should be inserted between these regions; 4) The loop region was randomized using a degenerated codon NNK, where N is a mixture of all four nucleotides and K is a 1:1 mixture of T and G. This provides all codons for 20 amino acid residues; 5) all three sections were annealed and amplified as double-stranded DNA using both forward and reverse primers by overlap

extension PCR; 6) After the confirmation of amplified FN3 fragments using agarose gel electrophoresis, diversified FN3 fragments were cut, dissolved, and purified by Qiagen gel extraction kits (Qiagen, Germany).

This method is greatly versatile because any template can be used with any randomization as long as the genes contain the required complementary regions for splicing. This method allows for the construction of many diversified libraries from a single template.

2.2.2 Phage-displayed FN3 library

Figure 9 overviews the process to generate combinatorial phage-displayed FN3 libraries and characterize their level of diversity.

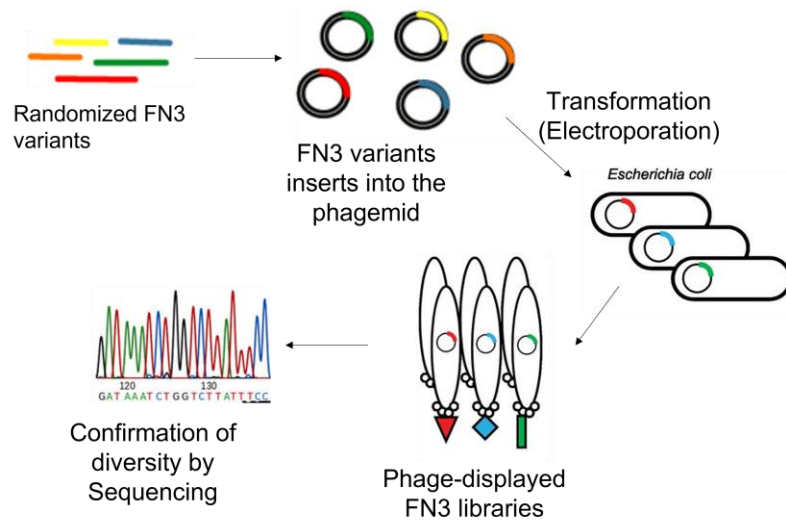


Figure 9: Schematic overview for generating phage-displayed FN3 libraries.

2.2.2.1 Electroporation

The gene encoding the FN3 with randomized loops was inserted into the pComb3X phagemid vector using Gibson assembly (Synthetic Genomics Inc., USA). This phagemid vector was provided by the Antibody Engineering course from Cold Spring Harbor and linearized after restriction enzyme digestion using Sfi1. After the gene assembly between the FN3 with randomized loops and the pComb3x encoding the pIII coat protein of M13 phage, FN3-inserted phagemid was transformed into the male *E. coli* strain ER2738 by electroporation (Lucigen, USA). Since the diversity of phage-displayed libraries is limited by the efficiency of transformation, high-voltage electroporation was used, as it is the most efficient transformation method. Electroporation is a two-component reaction where the electric field is applied to promote the DNA uptake into *E. coli*. This reaction is extremely sensitive to salt concentration and the DNA concentration is limited by the need for low conductance. Thus, ethanol precipitation of FN3-inserted phagemid was performed, and the final DNA solution was recovered in ultrapure DNase/RNase-free water (Invitrogen, USA). Also, the transformation efficiency and yield can be improved by increasing the concentration of DNA. Therefore, the final DNA concentration in water was 500 ng/ μ l.

To achieve at least $\sim 10^9$ of diversity, we calculated the transformation efficiency of single electroporation with its diversity. One electroporation with 500 ng of DNA reliably produces diversities of an average of 1.7×10^7 cfu/ μ l from five trials. Thus, to

cover at least $\sim 10^9$ of diversity, a total of 60 separate electroporation reactions were performed and pooled.

2.2.2.2 Purification

After electroporation, transformed cells were cultured in 2 mL of prewarmed recovery medium at 37°C with shaking at 225 rpm for 1 hour. This culture was transferred to 25 ml of autoclaved LB broth in a 150ml Erlenmeyer flask, tetracycline was added for active ER2738 cells, carbenicillin was added for selecting only phagemid-positive cells, and the flask was shaken again at 37°C for 30mins. A helper phage, M13K07 (New England Biolabs, USA), was introduced for generating M13 phage particles and the flask was shaken again at 37°C at 225 rpm for 1 hour. Kanamycin was treated for helper phage-positive selection, and the flask was shaken at 37°C at 225 rpm for 12 hours. Cells were centrifugated at 15,000g for 10 mins at 4°C, and then, from their pellets, phagemid DNAs were obtained by Qiagen Maxiprep kits (Qiagen, Germany). These genes were analyzed by Sanger sequencing for characterizing the diversity of randomized variants. The supernatant was subjected to PEG precipitation to obtain highly purified phage-displayed FN3 libraries.

For PEG precipitation, first, autoclaved PEG/NaCl (5X) stock solution (PEG-8000 20%, NaCl 2.5 M in ddH₂O) was prepared. A one-to-four volume ratio of PEG/NaCl solution was added to the supernatant, and the mixture was incubated on ice. After a few minutes, the mixture was checked for visible PEG-precipitated phages. If a

precipitate was visible, the incubation time could be as short as 5 min, otherwise, it could be up to an hour. The mixture was centrifuged again for 10 min at 15,000 g at 4°C, and the supernatant was removed carefully. The pellet was centrifuged again for 10 min at 15,000 g at 4°C. The second centrifugation was essential to collect all the phage particles at the bottom of the tube and achieve complete removal of bacterial supernatant. Pellet was resuspended with a 1:10 volume ratio of initial culture volume of TBS (1x) (50 mM Tris-HCl pH 7.5, 150 mM NaCl, sterile) and shaken vigorously to be completely resolubilized on ice for 30 min. Then, the solution was centrifuged for 10 min at 15,000 g at 4°C, followed by supernatant transferred to a clean tube and further characterization.

2.2.2.3 Characterization

To quantify the number of phages in the clean phage solution, UV/vis spectroscopy was used. The phage (virion) concentration was calculated by the equation below.

Equation 1: The formula quantifying the concentration of phage (virion) solution, established by Dr. George Smith (118).

$$\text{virions/ml} = \frac{(A_{269} - A_{320}) \cdot 6 \times 10^{16}}{\text{number of bases/virion}}$$

After the quantification, purified phages were subjected to titration. Phages were added to the ER2738 cells for infection. After 10 min incubation at room temperature,

serially diluted cells were plated onto the LB agar plates treated with tetracycline and carbenicillin. The colonies were counted to confirm the number of phages, and 50 of them were picked up and added into the 3ml of LB-filled autoclaved 12ml culture tubes. After incubating them at 37°C at 225 rpm overnight, from these cultures, phagemid DNAs were extracted and purified by Qiagen miniprep kits (Qiagen, Germany). The sequences of FN3 variants were characterized by Sanger sequencing (Genewiz, USA) and the diversity of phage-displayed FN3 library was determined.

2.3 Results and discussion

2.3.1 Construction of FN3 variants library

Using the degenerate oligonucleotides for randomized BC, DE, and FG loops of FN3, we successfully annealed the full sequence of FN3 using overlap extension PCR and confirmed this by 2% agarose gel electrophoresis (**Figure 10**). This indicated that the FN3 variants library was successfully constructed.

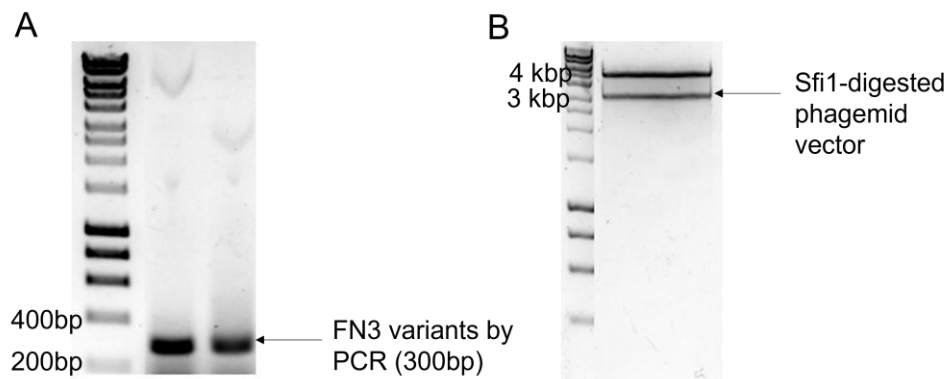


Figure 10: Agarose gel electrophoresis for the FN3-inserted phagemid. (A) FN3 fragments were assembled using overlap extension PCR. The FN3 fragments include randomized amino acid sequences for BC, DE, and FG loops. (B) The phagemid vector

was digested using *Sfi*I restriction enzymes such that this linearized vector can be used for gene assembly with FN3 variants inserts.

2.3.2 Construction of FN3-displayed phage library

The specific amino acid sequence used to construct the FN3 library is shown with the brief structural information of FN3 in **Figure 11**.

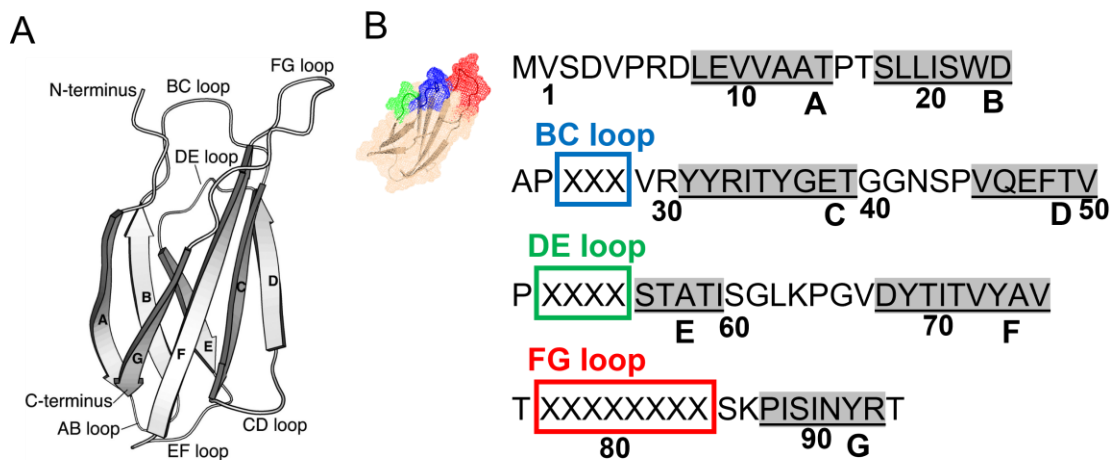


Figure 11: Structure of synthetic gene-coding for FN3. (A) The overall FN3 structure is illustrated and includes the locations of 7 different β -strands (A-G), 6 loops, and N- and C- terminus. **(B)** The amino acid sequences of FN3 are shown with indications of β -strands (A-G) and randomized BC, DE, and FG loop regions

The library developed in this study contains $\sim 10^{13}$ independent clones with around 5×10^9 diversity of FN3 variants sequences. This calculation of diversity was based on two assumptions: 1) Each *E. coli* has no more than one transformed phagemid; 2) If small subsets of colonies on a plate have all different variants confirmed by Sanger sequencing, we hypothesized that every colony contains different variants on the plate. Although both assumptions are not always perfectly true, this is an acceptable measure in practical terms, commonly used to calculate the approximate coverage of constructed

libraries and to determine the overall sizes of libraries before any selection/enrichment (117).

Although our library could not completely cover all possible sequences coded by 15 positions of randomized amino acids, we believe that this size of a starting library of 15-mer peptides should provide some specific binders with reasonable affinities to start with. **Table 4** summarizes the overview of combinatorial phage-displayed FN3 libraries.

Table 4: Overview of constructed phage-displayed FN3 libraries

Library	Randomized positions	Protein diversity (20^n)	Coverage
1	NNK at FG loop (X_8)	2.56×10^{10}	$\sim 5 \times 10^9$
2	NNK at BC (X_4) & FG (X_8) loops	4.10×10^{15}	$\sim 5 \times 10^9$
3	NNK at DE (X_3) & FG (X_8) loops	2.05×10^{14}	$\sim 5 \times 10^9$
4	NNK at BC (X_4) & DE (X_3) & FG (X_8) loops	3.28×10^{19}	$\sim 5 \times 10^9$

2.4 Conclusion and future directions

We have successfully constructed FN3 loop-randomized variants and phage-displayed FN3 libraries. This demonstrated that the FN3 framework can be used as a target-binding scaffold for molecular interactions. The compact size, well-defined structure, and structural stability, and plasticity make FN3 an attractive scaffold. The potential of this scaffold for specific target-binding is covered in the next chapter. Although the focus of this thesis is to develop antibody-inspired, loop-based FN3 libraries, recent structural studies have suggested the possibility of an alternative design (68). This new design includes not only loop regions but also the face of a β -sheet of the

FN3 molecule that provides a concave binding surface. Anticalins, affibodies, and DARPin use non-loop positions for presenting amino acid diversity. These examples show the FN3 does not have to exclusively utilize loop positions for binding surface and suggest the potential for tailoring a new location such as the side-and-loop region of the FN3 scaffold.

3. Discovering PDL1-binding FN3

3.1 Introduction and motivation

With the phage-displayed FN3 libraries developed in chapter 2, we can isolate specific phages from other phages by binding to certain targets of choice. This selection process is called “panning”. The specific phage that can bind to a target is amplified in *E. coli* and subjected to additional several rounds of panning. Through these repetitive procedures, the genes for a specific binding entity are enriched from non-binding or weak-binding and identified for further characterization.

For panning, a specific target should be determined. Since the research topic is to develop antibody mimetics for cancer therapeutics, targets that aid in the treatment of cancer are considered. In recent years, cancer therapeutics have been greatly advanced by the development of immune checkpoint inhibitors, which utilize our immune system to destroy cancers (128-130). As immune checkpoint inhibitors, antibody therapeutics show significant clinical success, but still possess significant shortcomings due to their large sizes and structures, such as limited tumor penetration, fixed two valency, and inflexible modularity (24). Thus, a small FN3 scaffold can be developed as an alternative immune checkpoint inhibitor.

3.1.1 Immune checkpoints

The anti-cancer immunity usually begins with the full activation of T cells. To activate T cells, two different signals should be co-activated (131): 1) the first signal is

derived from the interaction between the T cell receptor (TCR) from T cells and the complex of antigenic peptide and the major histocompatibility complex (MHC) from antigen-presenting cells (APC). Once APCs process antigenic peptides and display these peptides complexed by MHC molecules on their surfaces, T cells recognize these complexes using TCRs. This engagement is the first activation signal; 2) the second signals require antigen-independent co-signaling molecules. In T cells, these co-signaling molecules are either stimulatory or inhibitory, also known as immune checkpoints (132).

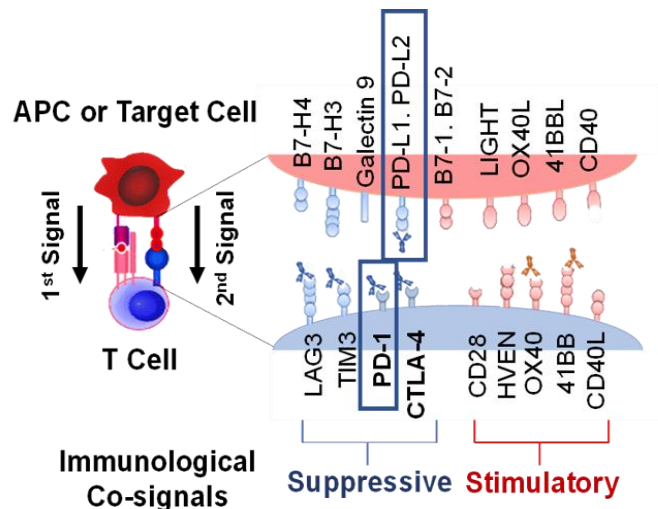


Figure 12: Graphical representation showing immune checkpoints. Upon the binding of TCR and the complex of antigen/MHC, T cell activation is regulated by multiple co-signal molecules. These molecules can negatively (suppressive) or positively (stimulatory) regulate the immune response. This image is extracted from (133).

These immune checkpoints tightly regulate and modulate T cell activation (Figure 12). If the first signal is accompanied by the engagement of co-stimulators such as CD28, T cells are activated and proliferated upon recognizing the specific antigen. On

the other hand, if the first signal is accompanied by the engagement of co-inhibitors such as CTLA4, T cell activation is suppressed. Usually, CTLA4 is not detectable in naïve T cells but is very rapidly induced after T cell activation to regulate the amplitude of T cell activation (131). This regulation mainly occurs during the early priming phase in lymphoid organs. CTLA4 binds to B7 proteins which also bind to CD28, a co-stimulator. This makes the binding of CTLA4 compete with that of CD28, naturally preventing excessive immunity (131).

The purpose of co-inhibitory signals is to prevent excessive immunities and minimize any damage to normal tissues from autoimmunity. However, cancer cells exploit these signals by producing co-inhibitory ligands on their surfaces that can bind to co-inhibitory receptors on T cells (132). This binding prevents T cells activation for anti-tumor immunity and makes cancer evade our normal immune system.

3.1.2 Immune checkpoint inhibitors

Since cancer cells utilize immune checkpoints to escape from the immune system, drugs that target these checkpoints have emerged. These drugs are known as immune checkpoint inhibitors (128). Currently, clinically approved drugs are monoclonal antibodies targeting and inhibiting three different targets: anti-cytotoxic T lymphocyte-associated antigen-4 (CTLA4), anti-programmed cell death protein 1 (PD1), and programmed cell death ligand 1 (PDL1).

CTLA4 is a cell-surface receptor that binds to the ligands CD80 (B7.1) and CD86 (B7.2) (134). This binding negates T cells activation by reducing the availability of CD80/CD86 to CD28. Ipilimumab, the first anti-CTLA4 monoclonal antibody, is used to treat patients with malignant melanoma and continues to be tested for other cancers (135).

In contrast to CTLA4 that negatively regulates pre-existing immune response, PD1 receptors are significantly involved in the maintenance of peripheral immune tolerance (131). To avoid undesired immunity to normal cells, normal cells express the low level of PDL1 on their surfaces and PDL1 binds to PD1 on T cells. This engagement inhibits T cell proliferation and cytokine secretion. To treat cancer cells overexpressing PDL1 to escape from PD1-mediated T cell recognition, drugs that bind either PD1 or PDL1 have been used clinically. The first humanized monoclonal antibody against PD1 is pembrolizumab (136). This drug was first FDA-approved in 2014 for patients with unresectable or metastatic melanoma. Since then, the treatment was expanded to different cancer types, including head and neck squamous cell carcinoma, metastatic urothelial carcinoma, and cervical carcinoma (137). By the end of 2021, 5 more antibody drugs have been approved against PD1 and PDL1: PD1-targeting nivolumab and cemiplimab, and PDL1-targeting atezolizumab, avelumab, and durvalumab (138).

These drugs do not directly kill cancer cells but harness the immune system to invoke endogenous anti-tumor immunity. Although these drugs have shown

compelling clinical efficacy in certain tumor types, around 30% of patients improve their survival with most developing *de novo* or adaptive resistance (139, 140). Since the efficiency remains unsatisfactory, many scientists have explored additional immune checkpoint molecules that agonize T cells (141). Examples of such molecules are OX40 (142) and 4-1BB (143). Additional co-inhibitory molecules, other than PD1 or CTLA4, include mucin-domain containing-3 (TIM-3), lymphocyte activation gene-3 (LAG-3), ITIM domain (TIGIT), and V-domain Ig suppressor of T cell activation (VISTA) (144).

3.1.3 PDL1-binding scaffolds

In our research work, the PDL1 target is specifically chosen for two reasons: 1) PDL1 antagonistic interaction does not require Fc-mediated effector functions that are hard to mimic in our modular protein therapeutics platform. For example, to make anti-CTLA4 drugs efficacious, ADCC from the Fc of antibody is required (145). This is because CTLA4 is mostly expressed on the surface of tumor-infiltrating T regulatory cells (Tregs), and Tregs negatively affect the efficiency of anti-tumor immunity (146). Thus, once the antibody binds to CTLA4 on Tregs, the antibody mediates ADCC to deplete Tregs and induce tumor-reactive T cells. On the contrary, the PD1/PDL1 interaction does not necessitate ADCC, and sometimes prefers to remove any Fc-mediated effector functions, because these functions can deplete antigen-presenting cells which are prerequisites for T cells activation (147); 2) PDL1 is overexpressed on tumor cells and

targeting tumor cells are preferred in our modular protein therapeutics platform because of our delivery formats allow for sustained and localized delivery (148).

Thus, in our modular protein therapeutics, PDL1 is our target. The therapeutics strategy (Figure 13) is to activate T cells using anti-PDL1 binders that antagonize the interaction between PDL1 expressed on tumor cells and PD1 on T cells.

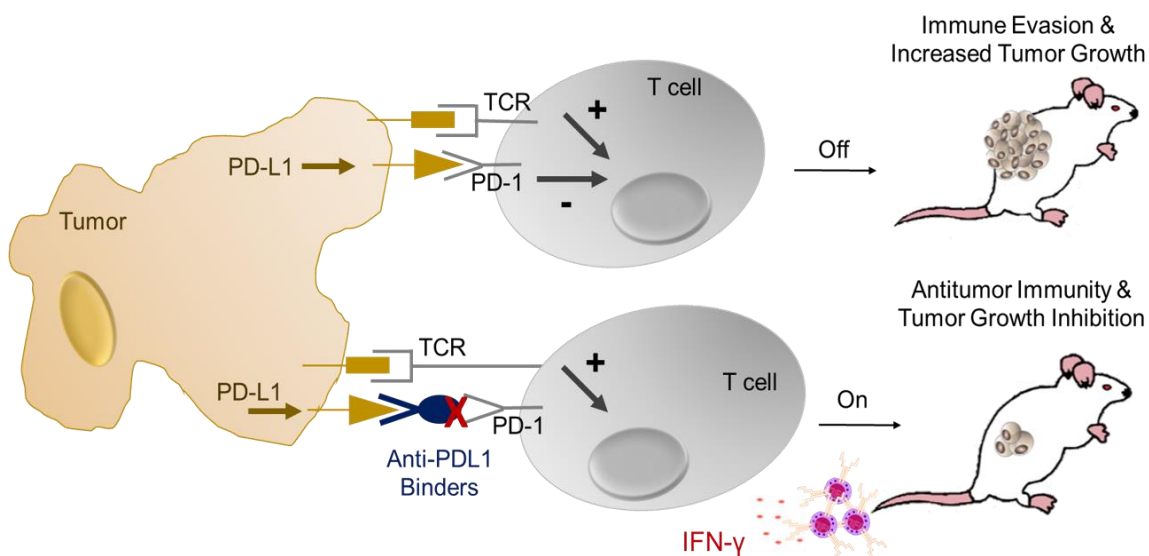


Figure 13: Therapeutic strategy for anti-PDL1 binders. Without anti-PDL1 binders, T cells are not activated, and cancer cells continue to grow. However, with anti-PDL1 binders, they inhibit the interaction between PD1 and PDL1 enabling T cells to be activated, releasing IFN- γ cytokines, and turning on T cell-based anti-tumor immunity.

Many scientists have discovered and engineered small binding scaffolds as PDL1 antagonists, based on the structures of nanobody (149), affibody (150), and monobody (151). Table 5 illustrates some of these molecules. Many have been evaluated for *in vivo* imaging because their small size contributes to short serum half-life and rapid diffusion.

For diagnostics, rapid clearance is desirable for imaging because this reduces any toxic burden to the body from imaging agents, especially if using radiation (152).

Table 5: Examples of scaffold proteins that target PDL1

Scaffold	Target species	Binding affinity	Use	References
Nanobody	Human and monkey	12 nM (K _D by SPR)	<i>In vitro & in situ</i> diagnostics	(149)
Nanobody	Human	5.25 nM (IC ₅₀ by ELISA)	<i>In vivo</i> therapeutics	(153)
Nanobody	Human	0.5 nM (K _D by SPR)	<i>In vivo</i> diagnostics	(154)
Affibody	Human and rhesus monkey	0.07 nM (K _D by SPR)	<i>In vivo</i> diagnostics	(155)
Affimer®	Mouse	0.0361 nM (K _D by SPR)	<i>In vivo</i> therapeutics	(156, 157)
Adnectin	Human and cynomolgus monkey	0.038 nM (K _D by SPR)	<i>In vivo</i> diagnostics	(158)
Monobody	Human	1.4 ± 0.3 nM (IC ₅₀ by ELISA)	<i>In vivo</i> diagnostics	(159)

3.2 Materials and methods

3.2.1 Panning against PDL1

A target protein can be immobilized on a solid surface such as an immunosorbent plastic plate or beads (160). Magnetic beads were chosen to be conjugated with protein G because target immobilization can be achieved via the interaction between protein G and Fc-fused target (161). In this way, the target protein would be completely exposed, providing sufficient space for phage-displayed FN3 libraries. Also, in our modular protein therapeutics, to readily evaluate the therapeutic

efficacy of our FN3 in a preclinical setting, the ability to bind both human and murine PDL1 is desired.

Briefly, our panning procedure is as follows (**Figure 14**): 1) protein G-coated magnetic beads (New England Biolabs, MA) are incubated with Fc protein from human IgG1 (R&D Systems, MN), and the mixtures are washed for 3 times with 1X PBS supplemented with 0.1% tween 20; 2) phages are added and incubated for binding at room temperature for 10 mins; 3) non-bound phages are subjected to the next step. This process is called negative panning, meaning that we isolate the phages that do not bind to the negative target; 4) Protein G-coated magnetic beads are incubated with hIgG1 Fc-fused human PDL1 (R&D Systems, MN) and the mixtures are washed for 3 times with 1X PBS supplemented with 0.1% tween 20; 5) The previous negatively-panned phages are added to the mixture and incubated at room temperature for 15 mins; 6) non-specifically bound phages are removed by washing extensively for 10 times. The washing buffer is 1X PBS supplemented with 0.1% tween 20; 7) the remaining phages are added with acid buffer (10mM Glycine-HCl, pH 1.5), incubated for 7 mins at room temperatures, and then eluted. This selection is called positive panning because we select the phages that bind to the positive target; 8) the eluted phages are neutralized right after the elution using the neutralization buffer (0.1M Tris base, pH 8). These phages are tittered and amplified by passage through an E. coli host using the same culture condition for phage library construction; 9) The amplified phage pool is applied

in 2 more rounds of positive panning step: first positive panning uses murine PDL1 and second uses human PDL1.

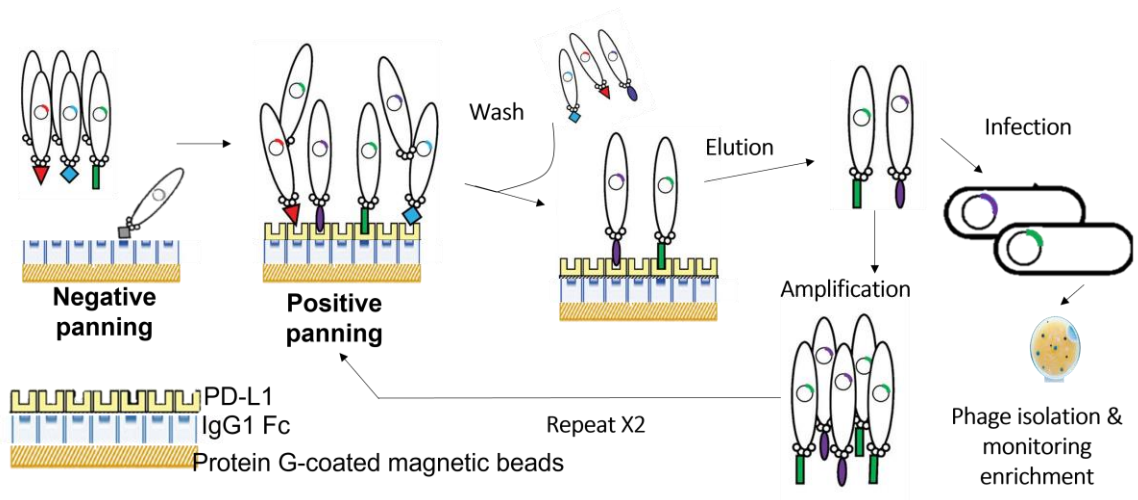


Figure 14: Schematic diagrams showing the experimental panning procedures. A pool of FN3 phage libraries is screened against the immobilized PD-L1. Bound phages are eluted and then amplified for multiple rounds of screening.

Each round of the panning cycle enriches for clones that bind to PDL1, and the final phage pool is eventually dominated by specific PDL1-binders. The progress of this sorting is conveniently monitored by paper-based enzyme-linked immunosorbent assay (ELISA) using tittered plates. LB agar plates are incubated overnight with the *E. coli* cells infected with the serially diluted phages eluted from the last panning. To rigidly fix the colonies, a top agar solution is also applied. After colonies are developed, these colonies on the plate are transferred to a Whatman membrane filter paper (Millipore Sigma, MO). The membrane filter is blocked using 1% skim milk, washed using 1X PBS

supplemented with 0.1% tween 20, and incubated with Fc-PDL1 for 1 hour at room temperature. After washing 3 times using 1X PBS supplemented with 0.1% tween 20, the paper is applied with human IgG1 Fc-specific antibody conjugated with alkaline phosphatase (AP) (Millipore Sigma, MO). After the addition of NBT/BCIP substrates (Thermo Fisher Scientific, MA), PDL1-bound phages are detected as insoluble, purple-colored dots.

3.2.2 Identifying sequences and phage ELISA

After successful panning and monitoring enrichment, we selected several candidates for DNA analysis and their matched approximate binding affinity using phage ELISA (Figure 15).

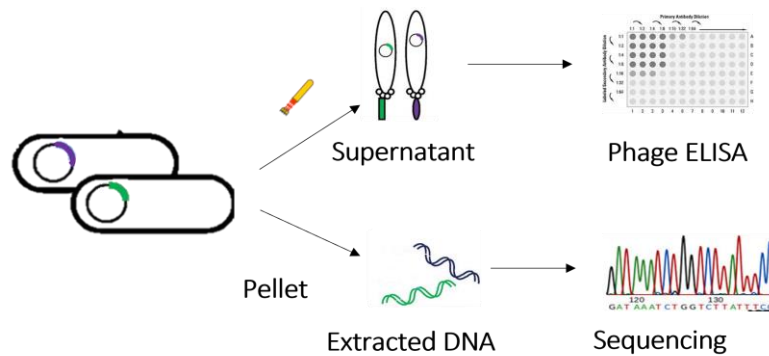


Figure 15: Schematic showing the experimental process for identifying sequences and their binding affinities. After the eluted phages infect *E. coli* cells, they are isolated for multiple single clones. From these clones, genes are extracted for sequencing, and phages are used for phage ELISA for binding affinity to PDL1.

Using the *E. coli* cells infected with the final phage, we placed them on LB agar plates supplemented with carbenicillin and tetracycline and cultured each colony in

each tube filled with LB media and two antibiotics overnight. After centrifugation, their cell pellets are used for DNA extraction using a miniprep kit (Qiagen), and their supernatants are quantified for the phage concentration and analyzed for their binding affinity using phage ELISA.

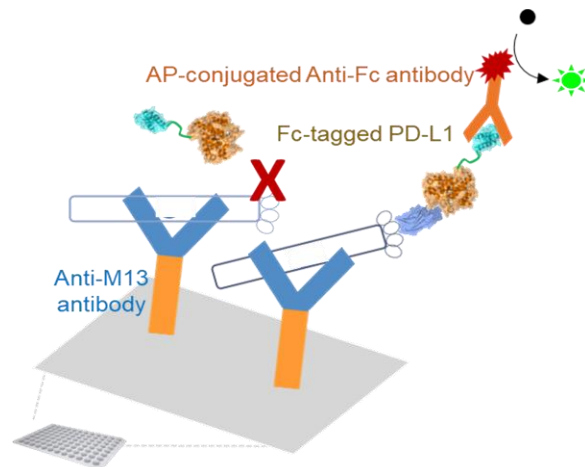


Figure 16: Schematic showing the structures of phage ELISA. Anti-M13 antibody specific to major coat protein immobilizes the phages of choice. Once the phages bind to PDL1, AP-conjugated antibodies can be captured releasing signals, measured at 405 nm absorbance.

Briefly, the phage ELISA is performed as follows (**Figure 16**): 1) supernatants from overnight cultures are purified using PEG precipitation described in the previous chapter; 2) phage concentrations are quantified using UV/vis spectroscopy described in the previous chapter; 3) 96-well Maxisorp immunoplates from Nunc (Roskilde, Denmark) are incubated with M13 pVIII coat protein-specific antibody (clone: RL-ph2, Thermo Fisher Scientific, MA) at 4°C overnight; 4) After 1 hour of blocking at room temperature, serial dilution of quantified phages are added into each well and incubated

at room temperature for 1 hour; 5) After washing 3 times using 1X PBS supplemented with 0.1% tween 20, phages in wells are incubated with Fc-PDL1 for 1 hour at room temperature; 6) After washing 3 times using 1X PBS supplemented with 0.1% tween 20, phages in wells are incubated with human IgG1 Fc-specific antibody conjugated with alkaline phosphatase (AP); 7) If phages are bound to PDL1, the addition of para-Nitrophenylphosphate (pNPP) forms soluble reaction products whose signals are detected at 405 nm of wavelength using a multimode plate reader (Tecan).

3.2.3 Affinity maturation

3.2.3.1 Construction of gene library

Using the consensus sequences of first-generation naïve libraries, we can design second-generation libraries for affinity maturation. To make the pocket bind more tightly to PDL1, we design a randomized sequence covering the sequence space based on the previous binders. When several lead sequences include strong consensus sequences, we fixed their amino acid residues and positions. If they are weak consensus, those spaces are randomized with tailored degenerate codons to encode certain residues with a particular characteristic. For instance, hydrophobic residues can be encoded by an NTC codon, which encodes Phe, Leu, Ile, or Val. The remaining non-consensus positions are hard-randomized using the NNK codon. **Table 6** describes which degenerate base codes should be used to encode certain nucleotides.

Table 6: Degenerate base for encoding certain nucleotides

Degenerate base designation	Actual base coded
N	A, T, G, C
B	T, G, C
D	A, T, G
H	A, T, C
V	A, G, C
K	G, T
M	A, C
R	A, G
S	C, G
W	A, T
Y	C, T

To construct second-generation libraries, we use divergent sequences with homology to the original sequence of strong binders. Some positions are fixed, and other positions are biased to favor binding to PDL1. To extend the binding space for a tight fit, we added two positions on the FG loop region with hard randomization. After the design of new mutations of FN3, we constructed FN3 variants libraries using the same method previously described in chapter 2.

Briefly, three gene fragments for BC, DE, and FG loops are annealed using overlap extension PCR and inserted into the phagemid vector, pComb3x, which encodes the p3 coat protein of M13 filamentous phages, using Gibson assembly.

3.2.3.2 Construction of phage library

As previously described in chapter 2, the FN3-inserted phagemid vectors are transformed into male *E. coli* ER2738 strains by electroporation. To achieve a diversity of

10⁹, we performed a total of 27 transformations based on the calculated transformation efficiency. We selected only phagemid-positive cells using carbenicillin antibiotics, followed by the infection with helper phage, which will help the formation of the overall intact structure of phages. After the selection of only functional helper phages with the addition of kanamycin antibiotics, the phages continue to grow overnight and are subsequently purified by the PEG precipitation method. The final phage concentration is measured by UV/vis spectroscopy and titered using LB agar plates with the serial dilutions of the phages.

3.2.3.3 Panning

With the previously constructed second-generation phage libraries, strong PDL1-binding FN3 molecules can be further discovered by panning. In this panning step, we used the same immobilization methods described previously in chapter 2: PDL1 proteins fused with the Fc domain are captured by protein G-coated magnetic beads. To screen phages more stringently and remove any non-specific binding with serum proteins, we used 1X PBS supplemented with 10% fetal bovine serum (FBS) and 0.1% tween 20. To prevent any potential binding to the Fc fusion tag, we firstly negatively screen our phage-displayed FN3 libraries against Fc-captured protein G magnetic beads and collect unbound phages. Then, these unbound phages are screened against Fc-PDL1-captured protein G magnetic beads. After washing steps to remove weakly or non-specifically bound phages, only specifically and strongly bound phages are eluted.

After the amplification of the phages, two more rounds of selection are used. We used murine PDL1 for the first and third positive panning and human PDL1 for the second positive panning.

3.2.3.4 Next-generation sequencing

After the last round of panning, the final eluted phages infect *E. coli* cells, and from those cells, phagemid genes are extracted. We decided to use next-generation sequencing to discover the sequences that have strong binding to targets and analyze the frequency of amino acid residues in a whole population. Since our FN3 proteins consist of around 300 base pairs of DNA, we utilize Miseq pair-end 250 base pairs by Illumina. To prepare the gene library for next-generation sequencing, four forward primers starting with A-, T-, G-, and C- are designed to equally distribute them on microchip channels, which affect the efficiency of sequencing. **Table 7** illustrates the sequences of these primers. The library is amplified with those primers and the universal reverse primer with PCR, and the amplified DNA is submitted to Duke Center for Genomic and Computational Biology (Duke GCB). The sequencing results are processed by Matlab.

Table 7: Primers for next generation sequencing

Primer	Sequence
Forward 1	5'- A NNNN ATGGTTAGCGATGTTTCCT - 3'
Forward 2	5'- T NNNN ATGGTTAGCGATGTTTCCT - 3'
Forward 3	5'- G NNNN ATGGTTAGCGATGTTTCCT - 3'
Forward 4	5'- C NNNN ATGGTTAGCGATGTTTCCT - 3'
Reverse	5'- GGT GCG GTA GTT AAT CG - 3'

3.2.4 PDL1-binding FN3

3.2.4.1 Molecular cloning

After identifying the DNA sequence of FN3 that binds to PDL1 most strongly, the oligonucleotide encoding this sequence was purchased from Integrated DNA Technologies (Coralville, IA). For ease of purification, we also inserted the genes encoding a Histidine-tag (His8) on the C-terminus of the FN3 gene. This gene was inserted downstream of the T7 promoter in the expression pET24 vector (**Figure 17**) using Gibson assembly. After the confirmation of successful gene assembly by Sanger sequencing, the plasmid was transformed into the BL21(DE3) expression strain of *E. coli* (New England Biolabs, MA). Aliquots of the DNA stocks were stored at $-20\text{ }^{\circ}\text{C}$ and transformed cell stocks with glycerol were stored at $-80\text{ }^{\circ}\text{C}$.

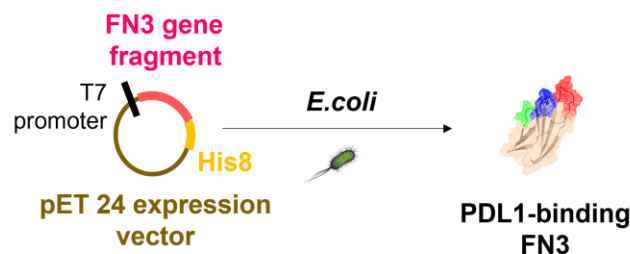


Figure 17: Schematic for gene assembly and protein expression. After the FN3 sequence binding to PDL1 is discovered, the gene with a histidine tag is inserted into the expression vector under the T7 promoter, and FN3 proteins are produced by the *E. coli* expression system.

3.2.4.2 Protein expression and purification

The PDL1-binding FN3 (aPDL1-FN3) was expressed in BL21(DE3) *E. coli* using a previously published protocol. We used autoclaved 2xYT media (16 g of tryptone, 10 g

of yeast extract, 5 g of NaCl, and pH 7.0 in 1L of distilled H₂O) for bacterial cultures. From the frozen glycerol stocks, small starters (50 ml) were grown overnight and used to inoculate 6 of 1 L flasks of 2xYT media supplemented with kanamycin (45 µg/ml). After the flasks were incubated in a shaker at 37°C and 200 rpm for 3 hours, the final concentration of 0.5mM of isopropyl-β-d thiogalactoside (IPTG, Gold Biotechnology) was added per flask. Then, all flasks were incubated in a shaker at 18°C and 200 rpm for 24 hours.

The aPDL1-FN3 protein was purified by immobilized metal affinity chromatography (IMAC), due to the interaction between metal ions and a poly-histidine tag. Briefly, the bacterial cell suspension was centrifuged at 4000 rpm for 15 min at 4°C; the cell pellet was then resuspended in lysis buffer (Tris 25mM, NaCl 100mM, and 5mM Imidazole, pH 7.0) and lysed by sonication on ice for 3 mins (10s on and 40s off) (Misonix S-4000; Farmingdale, NY). After the centrifugation at 14,000rpm for 15 mins at 4°C, the supernatant was subjected to the binding resin composed of agarose beads derivatized with a tetradentate chelation moiety and loaded with divalent cobalt ions (Thermo Fisher Scientific, MA). After the loading of supernatants to the resin, the resin was washed with washing buffer (Tris 25mM, NaCl 100mM, and 30mM Imidazole, pH 7.0) to remove weakly bound contaminants with 5 times the volume of resin, and then the elution buffer (Tris 25mM, NaCl 100mM, and 250mM Imidazole, pH 7.0) was added. To remove any metal ions, 1/10 volume of 0.5M EDTA solution (pH 8.0) was added to

the final eluted proteins. To remove excess imidazole from purified protein solutions and exchange buffers for further functional studies, the final samples were dialyzed against 1X PBS buffer at 4 °C for 24 h using Spectrum™ Laboratories Spectra/Por™ 2 12–14 Standard RC dry dialysis kits (Thermo Fisher Scientific, MA). The purity of protein in each step was confirmed by SDS-PAGE gel (Mini-PROTEAN TGX, Bio-Rad Laboratories, CA) stained with SimplyBlue solution (Thermo Fisher Scientific, MA).

3.2.4.3 Surface plasmon resonance

With the purified aPDL1-FN3 protein, we can study the binding kinetics of them to PDL1 using surface plasmon resonance (SPR). Specifically, we used a BIAcore T200 (GE Healthcare) at 25 °C. In the SPR, the CM5 sensor chips which enable the immobilization of PDL1 were used for evaluating the specific binding affinity of the FN3 proteins to PDL1. In addition, the specificity of FN3 to PDL1 can be examined by SPR using other protein-immobilized surfaces such as PD1 and PDL2, which should not bind to the purified FN3. We characterized the binding affinity of our FN3 proteins to PDL1 using the interaction between protein G and Fc (**Figure 18**).

In detail, the series S sensor chip CM5 (GE healthcare) was normalized using 70% glycerol. Protein G was immobilized in flow paths 1 and 2 of the CM5 chip, using NHS/EDC coupling. A solution of 0.5M EDC/1M NHS was injected at 5 µl/min for 7 minutes to activate the chip surface. 200 µg/ml of protein G in 10 mM sodium acetate buffer (pH 4) was injected at 5 µl/min for 30 seconds to obtain a final RU (response unit)

of around 600. Next, 1M ethanolamine was injected at 5 $\mu\text{l}/\text{min}$ for 10 minutes to inactivate the chip surface. In this way, the chip was securely immobilized with protein G.

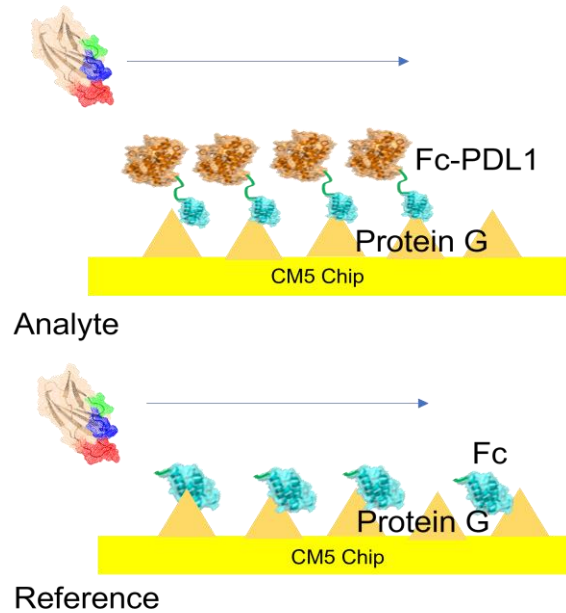


Figure 18: Schematic showing the structures of SPR for binding kinetics. After the immobilized protein G on the CM5 gold chip, Fc is used as a reference, and Fc-PDL1 is used as an analyte. FN3 is flowed over the chip for its binding kinetics to PDL1 by the subtraction of reference signal from that of an analyte.

To characterize the binding affinity of FN3 to PDL1, the Fc-tagged version was used and as a control, only Fc protein was used. Briefly, on flow path 1, we injected Fc protein at a flow rate of 30 $\mu\text{l}/\text{min}$ for 20 seconds, and on flow path 2, we injected Fc-tagged PDL1 (Fc-PDL1) at a flow rate of 30 $\mu\text{l}/\text{min}$ for 20 seconds. Our protein samples were injected over immobilized Fc-PDL1 and Fc simultaneously on both flow paths at a flow rate of 30 $\mu\text{l}/\text{min}$ at 25 $^{\circ}\text{C}$ for 3 minutes, and the response in resonance units was

recorded for 180 seconds. Protein samples were replaced with running buffer (1X PBS) for 600 seconds for dissociation. After each experiment, the chip surface was regenerated with 10 mM glycine-HCl (pH 1.5) for 30 seconds to remove bound molecules before the next measurement. After injection of serially diluted protein samples in running buffer and subtraction of the signal of flow path 1, the final SPR sensorgrams were obtained. The sensorgrams were analyzed using a 1:1 Langmuir binding model in BIAevaluation software (GE Healthcare).

3.3 Results and discussion

3.3.1 Optimizing panning system against PDL1

Successful panning requires the conformational integrity of target protein, which necessitates additional interaction to immobilize the protein in solution. To capture the PDL1 target, we use the specific interaction between protein G and the Fc region of an antibody. For example, PDL1 protein which is fused with the Fc domain (Fc-PDL1) can be captured by protein G-coated magnetic beads through the interaction between the protein G and the Fc portion. In this way, we can fully expose our target protein to the FN3-displaying phages, providing more extensive binding interaction between Fc-PDL1 and FN3.

To prevent any potential binding to the Fc fusion tag, we firstly screened our FN3 phage library against Fc-captured protein G magnetic beads and collected unbound phages. Then, these unbound phages were screened against Fc-PDL1-captured protein G

magnetic beads. After washing steps to remove weakly or non-specifically bound phages, only specifically and strongly bound phages were eluted. After the amplification of the phages, two more rounds of selection were used and optimized. The successful enrichment for PDL1-binding was confirmed by paper-based ELISA (**Figure 19**). After the second round of panning, more *E. coli* clones infected by phages exhibited the ability to bind to PDL1. Bigger and stronger dots signify stronger binding to PDL1.

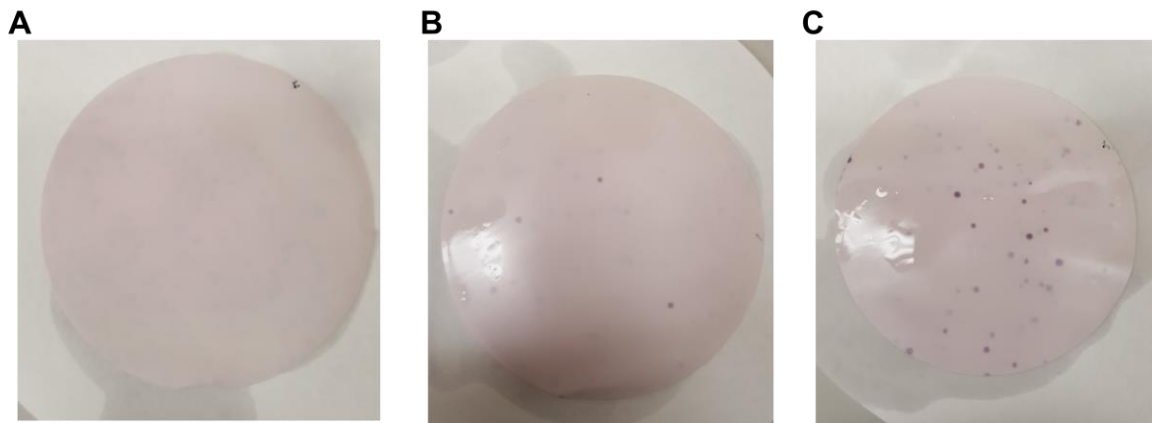


Figure 19: Paper-based ELISA showing the successful enrichment and panning against PDL1. Each paper is transferred from (A) naïve phages before panning, (B) the eluted phage after the first round of panning, and (C) the eluted phage after the second round of panning.

3.3.2 Discovering FN3 sequences that bind to PDL1

After the last round of panning, six candidates out of fifty were selected, and their clones were identified by Sanger sequencing as well as characterized for their binding affinity to PDL1 by phage ELISA (**Figure 20**).

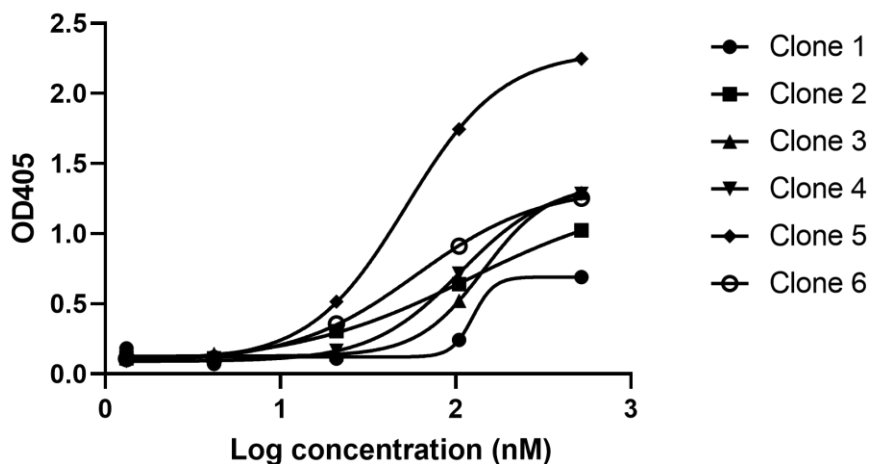


Figure 20: Phage ELISA of six sequences from naïve libraries. The final eluted phages are isolated for single clones, genes are extracted for sequencing, and phages are used for phage ELISA for the characterization of their binding affinity to PD-L1.

Among these candidates, one promising FN3 sequence (Clone 4) was selected for its sequence for further affinity maturation. **Table 8** describes the approximate binding affinity measured by phage ELISA and corresponding DNA sequences. Since we obtained several unique DNA sequences, we utilized this information to design second-generation libraries for affinity maturation.

Table 8: The sequences and binding affinities of six clones

Clone	K _D	BC loops	DE loop	FG loop
1	130 nM	AVT	TGKS	GWSHPRSM
2	120 nM	VVT	MRFV	RGTGRRAW
3	140 nM	AVT	GGSK	TYWMVVAS
4	100 nM	AVT	TRIV	SGRRTMHY
5	50 nM	VVT	TRFV	YRQMGVGVW
6	60 nM	AVT	TGSK	PMMLGRTL

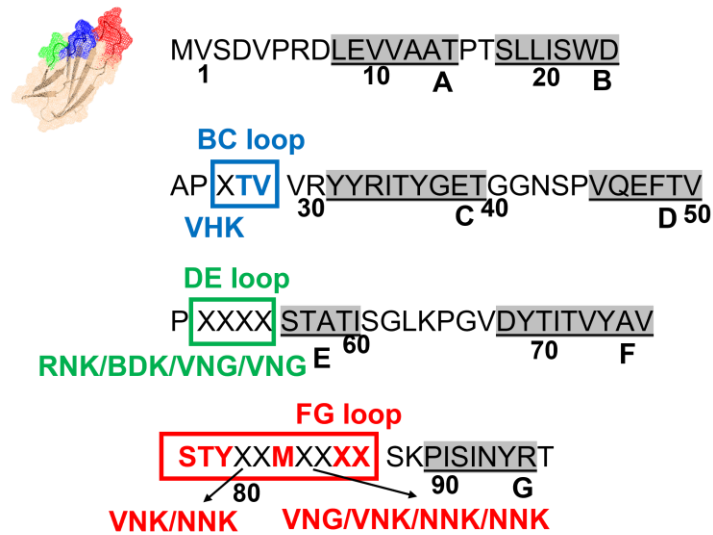


Figure 21: Synthetic gene-coding for second-generation libraries.

The sequences of three loop regions for second-generation libraries were designed as follows; 1) the sequence of BC loop region was defined as XVT where X covered hydrophobic residues like alanine and valine; 2) the sequence of DE loop region was defined as XXXX which covered degenerate codons in order, RNK/BDK/VNG/VNG, to cover the sequences of all binders from the previously eluted phages; 3) the sequence of FG loop region was based on that of clone 5 with the addition of two randomized positions for tighter binding. We included methionine residue in the middle of the sequences because all sequences exhibit methionine in their binding surfaces. Other residues were designed to encode the sequences of all binders from the previously eluted phages. **Figure 21** illustrates the FN3 gene sequences for the construction of second-generation libraries

3.3.3 Affinity maturation

Using the constructed second-generation libraries, three rounds of panning against PDL1 were performed with more stringent conditions with buffers containing fetal bovine serum. This buffer removes the potential binding of FN3 to serum proteins, further improving the specific binding of FN3 to PDL1.

After the last round of panning from second-generation libraries, two methods of sequencing were used: Sanger sequencing and next-generation sequencing. Although Sanger sequencing is labor-intensive, while preparing the DNA for sequencing of individual clones, corresponding FN3-displaying phages can be simultaneously produced by the infection of helper phages. This allows us to measure the binding affinity of each FN3-displaying phage using ELISA and to match each FN3 sequence with its approximate binding affinity. On the other hand, next-generation sequencing can provide us with more sequences that could be undiscovered from the Sanger sequencing due to its limited number of clones covered. To cover the depth of sequences and analyze their population, next-generation sequencing was utilized (Miseq, Illumina from Duke GCB).

Among five candidates selected for phage ELISA (**Figure 22**) and Sanger sequencing, the most promising FN3 sequence was hit 2, which showed the strongest binding affinity to PDL1. This sequence was also the most populated sequence from the

results of next-generation sequencing. Thus, the sequence of hit 2 was finally chosen for protein expression.

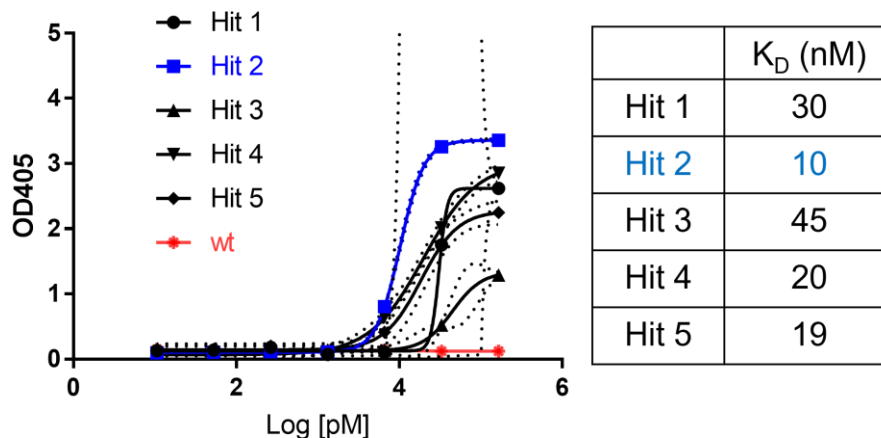


Figure 22: Phage ELISA of final five hits for their binding affinity to PDL1 and their sequences. The final eluted phages are isolated for single clones, the genes of five hits are extracted for sequencing, and phages are used for phage ELISA for binding affinity to PD-L1. The hit 2 sequence is also the most populated sequence from next-generation sequencing.

3.3.4 Characterization of PDL1-binding FN3 protein

The DNA fragment encoding both the PDL1-binding FN3 (hit 2), as well as a histidine tag, was synthesized, and this gene was incorporated into the pET24 *E. coli* expression vector using Gibson assembly. Insertion of the correct sequence was confirmed, and this plasmid was transformed into BL21 (DE3) *E. coli* competent cells for protein expression. After the induction of IPTG and periplasmic extraction, the soluble FN3 proteins were purified by IMAC. IMAC allows the his-tag-fused FN3 to be bound and eluted, providing highly purified FN3 proteins, as confirmed by SDS-PAGE (**Figure 23**).

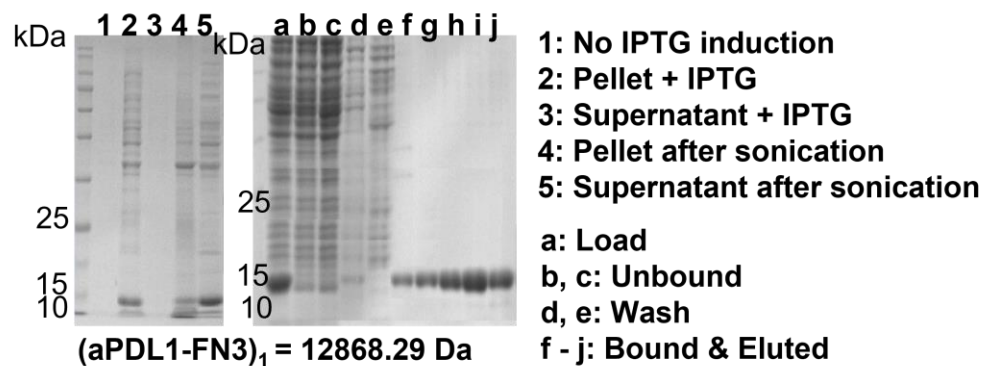


Figure 23: SDS-PAGE showing the successful expression (left) and purification (right) of His-tag-fused FN3 (12.87kDa). The FN3 is produced by the addition of IPTG (+) and is soluble after sonication. IMAC purifies FN3 proteins.

SPR was used for the characterization of the binding kinetic of FN3 to human and murine PDL1 as well as its specificity to PDL1 as compared to PD1, PDL2, EGFR, and HER2 (**Figure 24**). Our PDL1-binding FN3 (aPDL1-FN3) did not show any significant binding affinity to PD1, PDL2, EGFR, and HER2. The binding kinetics of FN3 was evaluated and fitted in the 1:1 Langmuir model, resulting in FN3 dissociation constants (K_D) of 16 nM for human PDL1 and 36 nM for murine PDL1. **Table 9** illustrates the detailed binding kinetics profiles of aPDL1-FN3 to human and murine PDL1. Altogether, this data demonstrates the specific binding of aPDL1-FN3 to PDL1 and the potential of aPDL1-FN3 as a PDL1 antagonist.

Table 9: The binding kinetics of aPDL1-FN3

Target	k_{on} (on-rate, 1/Ms)	k_{off} (off-rate, 1/s)	K_D (nM)
Human PDL1	1.61E5	2.61E-3	16.2
Mouse PDL1	5.01E4	1.83E-3	36.4

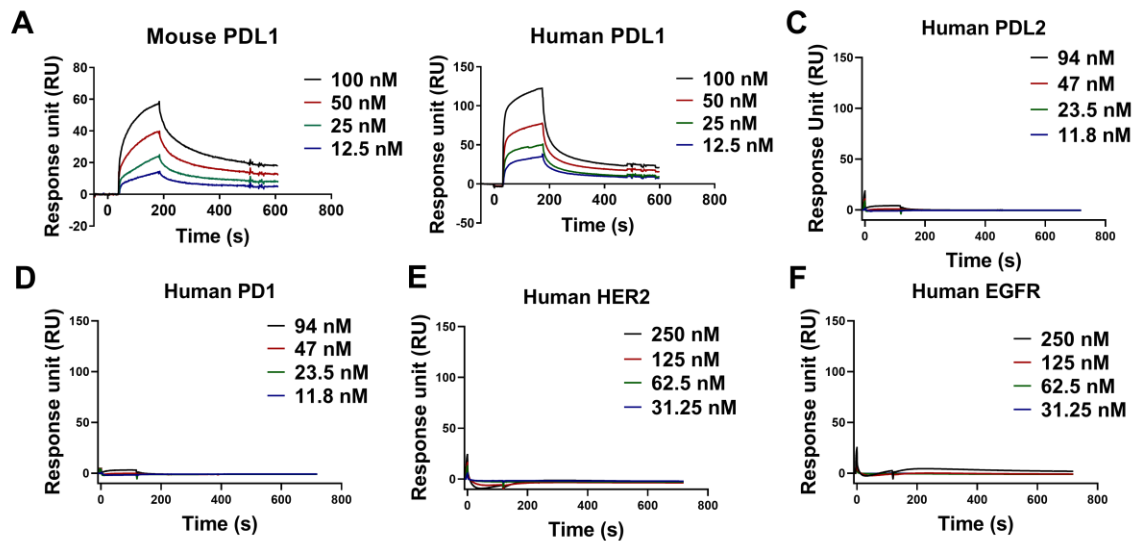


Figure 24: The binding kinetic profiles of the FN3 by the SPR: with the immobilized (A) mouse PDL1, (B) human PDL1, (C) human PDL2, (D) human PD1, (E) human HER2, and (F) human EGFR. Each concentration is shown and indicated by different types of color.

3.4 Conclusion and future directions

To discover FN3 proteins that bind to a target, we extensively utilize an M13 phage display system. Using the constructed naïve libraries described previously, we screened them against PDL1 that is overexpressed by cancer cells for their escape from the immune system. As a binder to PDL1, FN3 can antagonize the interaction of PDL1 to PD1, inducing cancer-specific immunity. Thus, this chapter aims to discover PDL1-binding FN3 sequences.

Here, the isolation of FN3 mutants that bind to PDL1 and their enrichments was confirmed by a paper-based ELISA. Using phage ELISA and Sanger sequencing, PDL1-binding FN3 sequences were successfully discovered and used for the basis of second-

generation libraries for affinity maturation. The second-generation libraries were constructed and screened more stringently against PDL1. The final phages were subjected to phage ELISA, Sanger sequencing, and next-generation sequencing. All these results suggest a promising FN3 sequence whose binding affinity is around 10 nM, as measured by phage ELISA. This FN3 sequence is introduced to the *E. coli* expression vector, and the aPDL1-FN3 protein is produced, purified, and analyzed by SPR. This aPDL1-FN3 protein shows specific binding to human and mouse PDL1.

Using this optimized screening method, we can further expand our target to different immune checkpoints (130). In the future, we can develop more robust methods for screening and analyzing hit sequences based on the results of this chapter. It is encouraged to perform an affinity maturation step to select the best binders to a new target for three reasons: 1) it is hard to obtain the strongest binder using the sparse sampling of the sequence space as well as hard randomization using NNK codons; 2) using the clones from this first library, however, provides a good structural basis for the second-generation libraries where all three loops can make a significant contribution to binding; 3) the introduction of desired binding functions can be readily achieved without concerns about the bias from stringent conditions. Since the panning from affinity maturation step already begins with sequences that have binding affinity to a target, more stringent designs of negative and positive panning improve specific binding affinity.

We can also further improve the currently developed aPDL1-FN3 in terms of PDL1 binding affinity, specificity, and stability. We believe that this protein retains the global folding structure of FN3, showing that this protein can accommodate and tolerate many mutations in the three loops. Although the stability of aPDL1-FN3 is lower than that of the wild-type FN3 protein, aPDL1-FN3 can tolerate chemical denaturation and reversible folding. To further improve this protein, computational methods (162) and/or phage display can be utilized.

4. Optimizing the valency of aPDL1-FN3

4.1 Introduction and motivation

Despite the sub-nanomolar affinity of aPDL1-FN3, many biological situations require more elaborate and strong binding affinities where monovalent affinity may not be sufficient to accomplish the desired therapeutic effect. In nature, multiple copies of ligands are involved in their molecular recognition (163). For example, antibodies have bivalency to achieve a picomolar range of binding affinity (164), and virus particles contain large copy numbers of proteins to bind to host cells (165). This multivalent interaction is characterized by its avidity and enhances the individual binding affinity, allowing it to be stronger and tighter (166). Thus, to design a drug that can compete with antibody therapeutics and multivalent biological interactions, we create multivalent versions of aPDL1-FN3 proteins. Since multivalent presentation is hypothesized to possess avidity effects, multivalent aPDL1-FN3 proteins should exhibit improved binding affinity, potency, and efficacy. In this chapter, the valency of aPDL1-FN3 proteins is optimized in terms of their PDL1 binding affinity and potency to inhibit the interaction between PDL1 and PD1.

4.1.1 Modularity and multivalency

An advantage of using the FN3 scaffold protein is its modularity: the ability to readily assemble more than two other proteins to exhibit desired architectures and functions. Because of their minimal size and structural plasticity, FN3 scaffold proteins

can contain a multiplicity of their domains to facilitate specific interactions from multiple partners (80). As a result, the assembled complexes have emergent properties. Such modular design and concerted binding interactions can allow for proteins to effectively sense their targets and transduce their downstream molecules in a well-controlled manner (167). The ability to use a modular FN3 protein is especially valuable as they are small and hence very efficient at targeting tissue uptake and penetration.

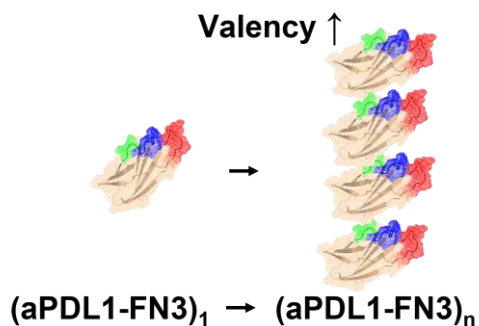


Figure 25: Schematic for the construction of aPDL1-FN3 oligomers. aPDL1-FN3 proteins are linearly repeated for multivalent presentation.

Specifically, in our drug design, owing to the modularity of FN3, aPDL1-FN3 can be oligomerized using genetic tandem repeats, and unlike bivalent antibodies, the number of valencies is not restricted (**Figure 25**). Thus, when engineered multivalently, aPDL1-FN3 oligomers change the dose-responses of the PDL1-activated pathway, improve their threshold sensitivity, and serve potent PDL1 inhibitors.

4.1.2 Multivalency and therapeutic effects

To determine the therapeutic effects of a drug, we consider two factors: 1) potency which refers to the concentration of drug required to generate a certain therapeutic effect; 2) efficacy which refers to a maximum therapeutic response that can be achieved by a drug. We believe that the multivalent presentation of aPDL1-FN3 would improve its potency compared to that of its monovalent version due to its avidity. As demonstrated by many scientists, avidity effects determine the potency and efficacy of drugs (168-170). For example, multivalent formats of antibody-like domains in self-assembled nanoparticles can reduce the critical concentration of cluster formation, improving their neutralization potency and capacity compared to a full bivalent antibody (165, 171).

The structural plasticity and stability of FN3, combined with recent advances in protein engineering enable us to increase the number of aPDL1-FN3 proteins in the multimer, thus increasing its avidity effects. This enhanced avidity can further improve the overall binding affinity to PDL1 and its antagonizing potency.

4.2 Materials and methods

4.2.1 Construction of (aPDL1-FN3)_n

(aPDL1-FN3)_n domains were oligomerized where the valency (n) of aPDL1-FN3 was systematically varied from 1 to 5. Flexible (Gly₄Ser)₃ peptide linkers were used to tether these proteins to one another. To construct the genes encoding these sequences,

several dsDNA fragments were designed to possess 15 to 18 complementary base pairs between each other. They were then synthesized by Integrated DNA Technologies (Coralville, IA). Fragments for different constructs were assembled and cloned by Gibson assembly into the pET24 vector. All genes encode a Histidine-tag (His₈) on the C-terminus for purification. After successful gene assembly was confirmed by Sanger sequencing, the correct plasmid was transformed into the BL21(DE3) expression strain of *E. coli* (New England Biolabs, MA). Aliquots of the DNA stocks were stored at -20 °C and transformed cell stocks were stored with glycerol at -80 °C.

4.2.2 Expression and purification of (aPDL1-FN3)_n

The (aPDL1-FN3)_n proteins were expressed in BL21(DE3) *E. coli* using autoclaved 2xYT media (16 g of tryptone, 10 g of yeast extract, 5 g of NaCl, and pH 7.0 in 1 L of distilled H₂O). From frozen glycerol stocks, small starters (50 ml) were grown overnight and used to inoculate 6 of 1 L flasks containing 2xYT media supplemented with kanamycin (45 µg/ml). After the flasks were incubated in a shaker at 37 °C and 200 rpm for 3 hours, the final concentration of 0.5 mM of IPTG (Gold Biotechnology) was added per flask. Then, all flasks were incubated in a shaker at 18 °C and 200 rpm for 24 hours.

The FN3 protein was purified by IMAC. Briefly, the bacterial cell suspension was centrifuged at 4000 rpm for 15 min at 4 °C; the cell pellet was then resuspended in lysis buffer (Tris 25mM, NaCl 100mM, and 5mM Imidazole, pH 7.0) and lysed by sonication on ice for 3 mins (10s on and 40s off) (Misonix S-4000; Farmingdale, NY). After

centrifugation at 14,000 rpm for 15 mins at 4 °C, the supernatant was subjected to binding resin composed of agarose beads derivatized with a tetradentate chelation moiety and loaded with divalent cobalt ions (Thermo Fisher Scientific, MA). After loading of supernatants to the resin, the resin was washed with washing buffer (Tris 25 mM, NaCl 100 mM, and 30 mM Imidazole, pH 7.0) to remove weakly bound contaminants with 5 times the volume of resin, and then eluted with elution buffer (Tris 25 mM, NaCl 100 mM, and 250 mM Imidazole, pH 7.0). To remove any metal ions, 1/10 volume of 0.5 M EDTA solution (pH 8.0) was also added to the final eluted proteins. To remove excess imidazole from purified protein solutions and exchange buffers for further functional studies, the final samples were dialyzed against 1X PBS buffer at 4 °C for 24 h). The purity of each protein was confirmed by SDS-PAGE gel (Mini-PROTEAN TGX, Bio-Rad Laboratories, CA) stained with SimplyBlue solution (Thermo Fisher Scientific, MA).

4.2.3 Biophysical characterization

4.2.3.1 Mass spectrometry

To confirm the molecular weight of (aPDL1-FN3)_n proteins, we used matrix-assisted laser desorption/ionization-time of flight mass spectrometry (MALDI-TOF MS). Specifically, we used a Bruker Autoflex Speed LRF MALDI-TOF (Bruker Daltonik GmbH, Bremen, Germany) equipped with an Nd/YAG laser (355 nm). The instrument was calibrated against an aldolase (Sigma Aldrich, Mw = 39,211.28 Da) or apomyoglobin

(Sigma Aldrich, Mw = 16,952.27) standard. Samples for MALDI-TOF-MS analysis were prepared by mixing 1 μ L of purified protein with 9 μ L of an α -cyano-4-hydroxycinnamic acid matrix (a saturated solution was prepared by suspending 10 mg of the matrix in 500 μ L H₂O + 0.3% TFA and 500 μ L acetonitrile + 0.3% TFA). Afterward, 1 μ L of this mixture was deposited onto a polished steel sample plate and dried in air at room temperature.

4.2.3.2 Dynamic light scattering

Dynamic light scattering (DLS) measurements of proteins were performed using a Wyatt DynaPro temperature-controlled instrument (Wyatt Technology, Santa Barbara, CA), with 10 acquisitions collected at room temperature. Samples for the DLS system were prepared in 1X PBS and filtered through Whatman Anotop sterile syringe filters (0.2 μ m; GE healthcare, PA) into a black 96 well plate (Corning®). The data points presented for this characterization represent the mean of R_h of the sample, illustrating the polydispersity.

4.2.3.3 Surface plasmon resonance

We used a Biacore T200 SPR instrument. First, the series S sensor chip CM5 (GE healthcare) was normalized using 70% glycerol. Protein G was immobilized in flow paths 1 and 2 of the CM5 chip, using NHS/EDC coupling. A solution of 0.5 M EDC/1M NHS was injected at 5 μ l/min for 7 minutes to activate the chip surface. 200 μ g/ml of protein G in 10 mM sodium acetate buffer (pH 4.0) was injected at 5 μ l/min for 30

seconds to obtain a final RU (response unit) of around 800. Next, 1 M ethanolamine was injected at 5 μ l/min for 10 minutes to inactivate the chip surface. To characterize the binding affinity of FN3 to PDL1, the Fc-tagged version was used and as a control, only Fc protein was used. Briefly, on flow path 1, we injected Fc protein at a flow rate of 30 μ l/min for 20 seconds and on flow path 2, we injected Fc-tagged PDL1 (Fc-PDL1) at a flow rate of 30 μ l/min for 20 seconds. Our protein samples were injected over immobilized Fc-PDL1 and Fc simultaneously on both flow paths at a flow rate of 30 μ l/min at 25 °C for 3 mins. Then, protein samples were replaced with running buffer (1X PBS) for 5 mins for dissociation. After each experiment, the chip surface was regenerated with 10 mM glycine-HCl (pH 1.5) for 30 secs. After injection of serially diluted protein samples in running buffer and subtraction of the signal of flow path 1, the final SPR sensorgrams were obtained and analyzed using a 1:1 Langmuir binding model in BIAevaluation software (GE Healthcare).

4.2.3.4 Fluorescent labeling and confirmation

To fluorescently label proteins, 1 mg of AlexaFluor488-NHS ester was dissolved in 100 μ l DMSO. The N-terminal amine of proteins was labeled with AlexaFluor488-NHS ester by incubating 20 - 100 μ M protein with ten molar equivalents of dye, rotating for 1 hour at room temperature in sodium phosphate buffer, pH 6.0. Excess unlabeled dye was removed with a Zeba desalting spin column, extensive dialysis, or centrifugal

ultrafiltration (Amicon™ Ultra-15, 10kDa MWCO). The purity of labeled proteins was assessed by size exclusion chromatography.

For size exclusion chromatography analysis of the purity of fluorescently labeled proteins, a Shodex OHPak SB-804 HQ column (New York, NY) was used with an isocratic flow of 0.5 ml/min of 1X PBS. We used Shimadzu's high-performance liquid chromatography system (Shimadzu Scientific Instruments, Columbia, MD). HPLC-grade solvents were purchased from VWR International (Radnor, PA). All buffers and samples were prepared in 1X PBS and filtered through 0.2 µm.

4.2.4 *In vitro* characterization

4.2.4.1 PD1/PDL1 blockade assay

CHO TCR/hPDL1 cells were prepared in their growth media (Ham's F12 supplemented with 10 % FBS). First, cells were washed with 1X DPBS, trypsinized with 0.25 % trypsin/EDTA, and harvested by centrifugation at 250 g for 5 mins. The cell pellet was resuspended in warm media and the cells were counted with a hemocytometer after 1:1 dilution into 0.4 % Trypan blue solution (Thermo Fisher Scientific, MA). The cell density was adjusted to 4×10^5 cells/ml by the addition of warm media, and the cell suspension was transferred to a sterile reagent reservoir. Using a multichannel pipette, 100 µl of cells were added to each well of 96-well flat, white clear-bottom assay plates (Corning®). The plate was incubated in a 37 °C, 5 % CO₂ incubator overnight.

To prepare protein samples in an assay buffer (RPMI 1640 supplemented with 1% FBS), a sterile clear bottom 96-well plate was prepared. In the case of 2.5-fold dilution, 250 μ l of proteins were added to the first well, and 150 μ l of assay buffer was added to other wells. The 100 μ l of proteins from the first well was transferred to the 150 μ l of assay buffer and gently mixed. This step was repeated until a sufficient range of concentration was covered. These protein samples were added to the plate coated with CHO TCR/hPDL1 cells.

Jurkat/PD1 cells were prepared, and the cell density was adjusted to 1.25×10^6 cells/ml by the addition of assay buffer. Using a multichannel pipette, 40 μ l of cells were added to each well of the plate coated with CHO TCR/hPDL1 cells followed by the addition of protein samples. The plate was incubated again in a 37 °C, 5% CO₂ incubator for 6-8 hours.

Since protein samples effectively antagonize the interaction between CHO TCR/hPDL1 cells and Jurkat/PD1 cells, TCR activation induces the luminescence of the NFAT pathway (**Figure 26**). After taking out the plate and equilibrating it to room temperature for 10 mins, 80 μ l of Bio-Glo™ reagents (Promega, WI) was added to each well. In 10-30 mins, the luminescence signal was measured by a multimode plate reader (Tecan).

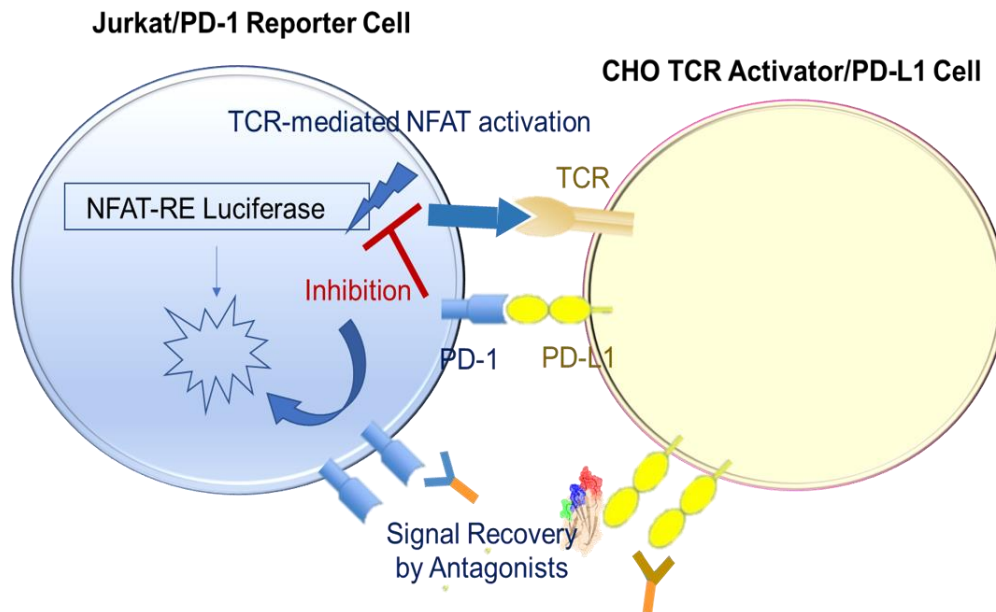


Figure 26: Representation of the PD1/PDL1 blockade assay. This consists of two genetically engineered cell lines, Jurkat/PD1 reporter cell and CHO TCR/PDL1 cells. When co-cultured, PD1/PDL1 interaction inhibits TCR-mediated luminescence via activation of the NFAT pathway. When this interaction is disrupted by the aPDL1-FN3 or antibodies, TCR activation induces luminescence that can be readily detected.

4.2.4.2 Flow cytometry

Overnight cultures of CHO-hPDL1 cells were prepared for flow cytometry. First, cells were trypsinized with 0.25% trypsin/EDTA and harvested by centrifugation at 500g for 3 mins. The cell pellet was resuspended in 1X PBS and the cells were counted with a hemocytometer after 1:1 dilution into 0.4% Trypan blue solution (Thermo Fisher Scientific, MA) The cell density was adjusted to 2×10^6 cells/ml by the addition of blocking buffer (5% rat serum, 5% mouse serum, 1% CD16/32 (clone 93, eBioscience, San Diego, CA). Then, the cells were incubated with fluorescently labeled proteins by gently mixing 190 μ l of the cell suspension and 10 μ l of proteins at the final concentration of 1

μM of proteins. The mixture of cells and proteins was incubated at $37\text{ }^{\circ}\text{C}$ for 1 hour. After incubation, cells were collected, washed 3 times with 0.2ml of 1XPBS with 1%BSA on ice, and adjusted to a final cell concentration of 1×10^5 cells/ml for flow analysis. Live cells were analyzed for population fluorescence on a BD Accuri C6 (BD Biosciences, CA).

4.2.4.3 3D spheroids and confocal imaging

Overnight cultures of CT26.WT cells were prepared and accurately counted for producing aggregates of 3D tumor spheroids. To ease the process, we used AggreWell™-800 24-well plates (Stemcell Technologies, Canada), as described in the manufacturer's manual. Briefly, wells were pretreated with 500 μl of anti-adherence rinsing solution, the plate was centrifuged at 1300 g for 5 mins, and the plate was carefully rinsed with warm media (RPMI 1640 supplemented with 10% FBS) to remove any bubbles. After aspiration of all rinsing media, 1.2×10^6 cells were added to each well (4000 cells per microwell), and warm media was added to sufficiently adjust the volume to 2 ml per well. The plate was centrifugated at 100 g for 5 mins to capture cells in microwells and observed under a microscope to verify the cells were evenly distributed among the microwells. Over 10 days of incubation at $37\text{ }^{\circ}\text{C}$, 50% of media was carefully changed every other day. In 10 days, spheroids were harvested using a 37 μm reversible strainer (Stemcell Technologies, Canada). Using this strainer, the aggregates remained on the filter during the harvest, and single cells flowed through. After washing three times, the strainer was inverted, and the addition of warm media eluted spheroids.

The spheroids were placed on a 12-well plate and incubated with fluorescently labeled 1 μ M of proteins and 1 μ M of Hoechst (Thermo Fisher Scientific, MA) for nucleus staining. The mixture of spheroids and proteins was incubated at 37 °C for 1 hour. After incubation, 3D spheroids were collected and washed 3 times with 0.05ml of 1X PBS with 10% FBS. The spheroids were placed in a 35 mm glass bottom petri dish and imaged with the Andor Dragonfly Spinning Disk confocal microscope using a 40X oil immersion objective. The fluorescence signal from Alexa 488 was acquired using a 488 nm laser with a 525/50 nm bandpass filter while Hoechst fluorescence was captured using a 405 nm laser with a 450/50 nm bandpass filter. A Z-stack of the spheroid was acquired, and the center slice(s) were processed for analysis.

4.3 Results and discussion

4.3.1 Qualitative characterization of (aPDL1-FN3)_n constructs with gel electrophoresis

We hypothesized that creating linear tandem repeats of aPDL1-FN3 hit (Hit 2) would increase their PDL1 affinity due to their increased valency. To study this, we cloned, expressed, and purified (aPDL1-FN3)₁ through (aPDL1-FN3)₅ with flexible (Gly4Ser)₃ peptide linkers between monomers to enable each monomer to engage a PDL1 receptor on the tumor cell surface. An agarose gel of double-digested expression vectors confirmed the successful insertion of different numbers of FN3 gene repeats into a pET 24 expression vector (**Figure 27**).

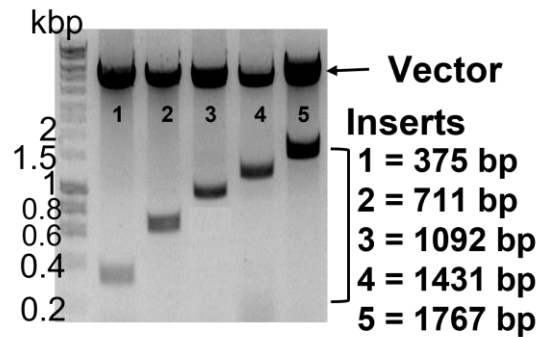


Figure 27: Agarose gel image of the genes of aPDL1-FN3 oligomers. This image confirms the correct sizes of aPDL1-FN3 genes ranging from mono-valent to penta-valent that were introduced to the expression vector.

We used the *E. coli* expression system to express tandem repeats of aPDL1-FN3 protein ranging from mono-valency to penta-valency. After bacterial cell expression, we purified (aPDL1-FN3)_n oligomers using the interaction between their His-tag at the C-terminal and metal ions such as nickel and cobalt. After the purification of (aPDL1-FN3)_n oligomers by the IMAC, we confirm their purity using sodium dodecyl sulfate-polyacrylamide gel electrophoresis (SDS-PAGE), followed by Simply blue staining. The stained SDS-PAGE image of purified multivalent aPDL1-FN3 proteins exhibited a single band with no other visible contaminants (**Figure 28A**).

Also, to confirm the complete expression of aPDL1-FN3 oligomers, we used a trans-blot turbo transfer system (Bio-Rad Laboratories, CA). Briefly, proteins on the gel were transferred to a membrane, and the membrane was blocked for 10 mins using an Everyblot blocker buffer (Bio-Rad Laboratories, CA) and incubated with an anti-His-tag antibody conjugated with alkaline phosphatase (Bio-Rad laboratories, CA) for 1 hour

with gentle shaking at room temperature. After washing 3 times with 1X PBS supplemented with 0.1% tween 20, the addition of NBT/BCIP stock solution resulted in an insoluble, purple-colored band, indicating that His-tags were present on those bands. A western blot image confirmed the complete expression of proteins by His-tags without any truncation (**Figure 28B**).

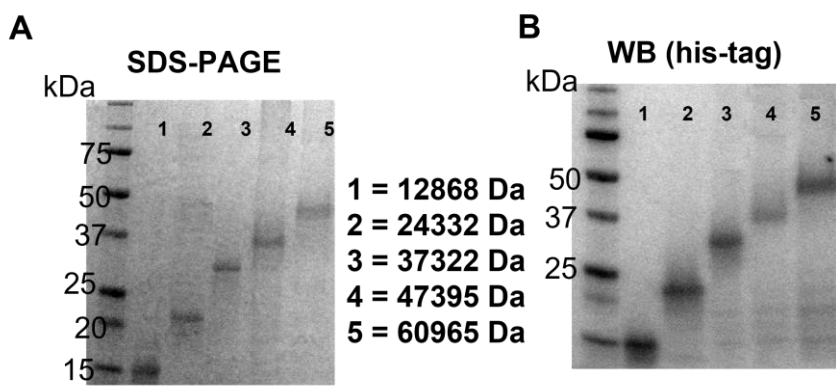


Figure 28: SDS-PAGE (A) and WB (B) images of multivalent (aPDL1-FN3)_n proteins. These confirm the full-length expression and successful purification of multivalent (aPDL1-FN3)_n proteins as they have a His₈-tag at their C-terminus.

4.3.2 Biophysical characterization of (aPDL1-FN3)_n

To confirm the correct molecular weights of purified aPDL1-FN3 oligomers, we decided to use matrix-assisted laser desorption/ionization-time of flight (MALDI-TOF) mass spectrometry. This is because MALDI is a soft ionization technique that usually causes minimal to no fragmentation of analytes and allows the molecular ions of analytes to be readily identified even in mixtures of biopolymers (172). Thus, MALDI allows our proteins to be ionized as [protein + H]⁺ and/or [protein + 2H]²⁺ without any

fragmentation (173). These ionized proteins travel to a detector, which measures their times for travel. This data results in the determination of the ratio of protein molecular mass to charge. We successfully obtained the molecular mass of aPDL1-FN3 oligomers and confirmed their correct sizes (Figure 29).

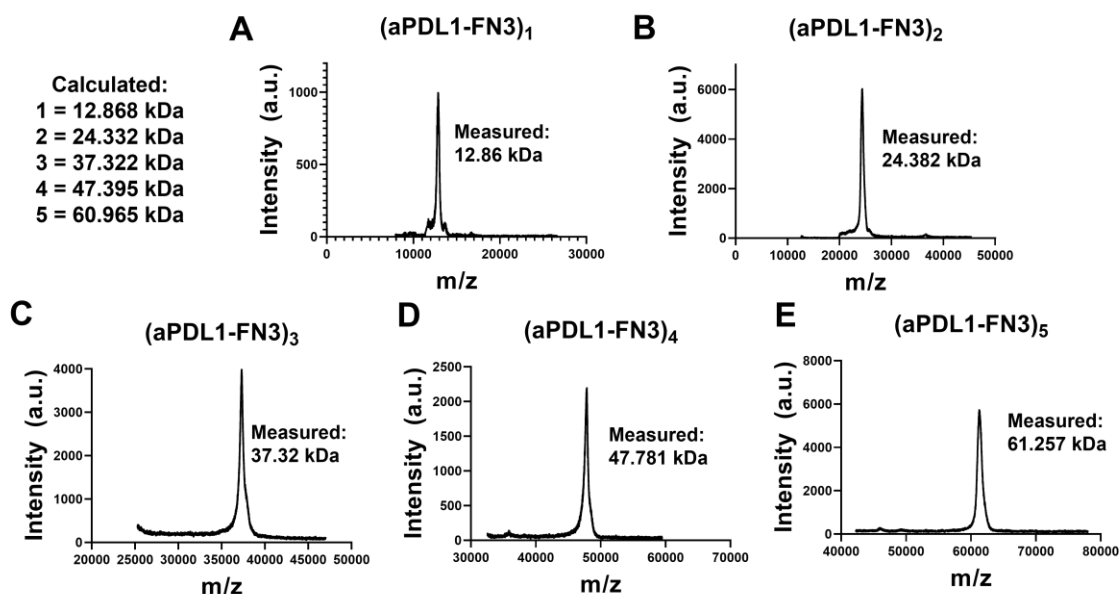


Figure 29: Purified (aPDL1-FN3)_n proteins are characterized for their molecular weights: (A) (aPDL1-FN3)₁, (B) (aPDL1-FN3)₂, (C) (aPDL1-FN3)₃, (D) (aPDL1-FN3)₄, and (E) (aPDL1-FN3)₅ are all confirmed for their correct sizes. The calculated molecular weights are tabulated next to panel (A) and the experimentally measured MWs are shown in each panel and agree the calculated MWs within the error of the technique.

Since multivalency presentation can cause aggregation or instability of proteins, we also analyzed their hydrodynamic radius (R_h) using dynamic light scattering (DLS). Fortunately, we did not detect any significant aggregation of these proteins (Figure 30).

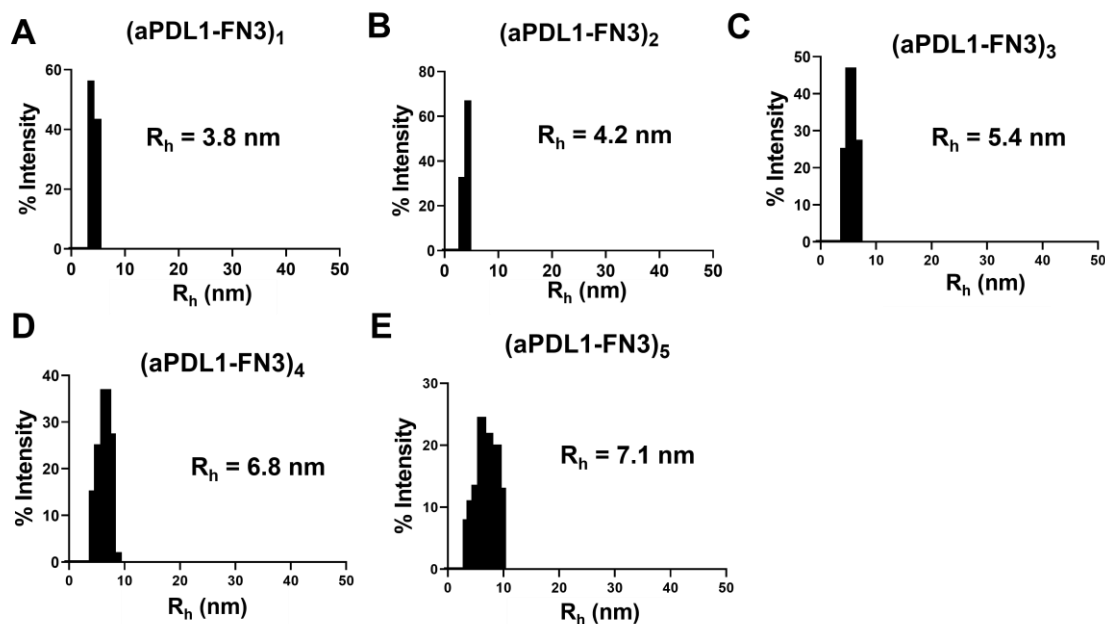


Figure 30: Purified (aPDL1-FN3)_n proteins are characterized for their hydrodynamic radius (R_h): (A) (aPDL1-FN3)₁, (B) (aPDL1-FN3)₂, (C) (aPDL1-FN3)₃, (D) (aPDL1-FN3)₄, and (E) (aPDL1-FN3)₅. All constructs have R_h 's consistent with their size and no construct showed any significant aggregation or micelle formation. The measured R_h are shown in each panel.

4.3.3 Characterization of the binding kinetics of (aPDL1-FN3)_n

We analyzed the binding kinetics of purified (aPDL1-FN3)_n oligomers to human and murine PDL1 using SPR. The data suggest that the binding affinity for PDL1 increases with increasing valency from 1 to 4. Specifically, the off-rate of the tetramer becomes very slow (**Figure 31**). The very slow off-rate is desirable for drug candidates because slower dissociation results in a longer residence time.

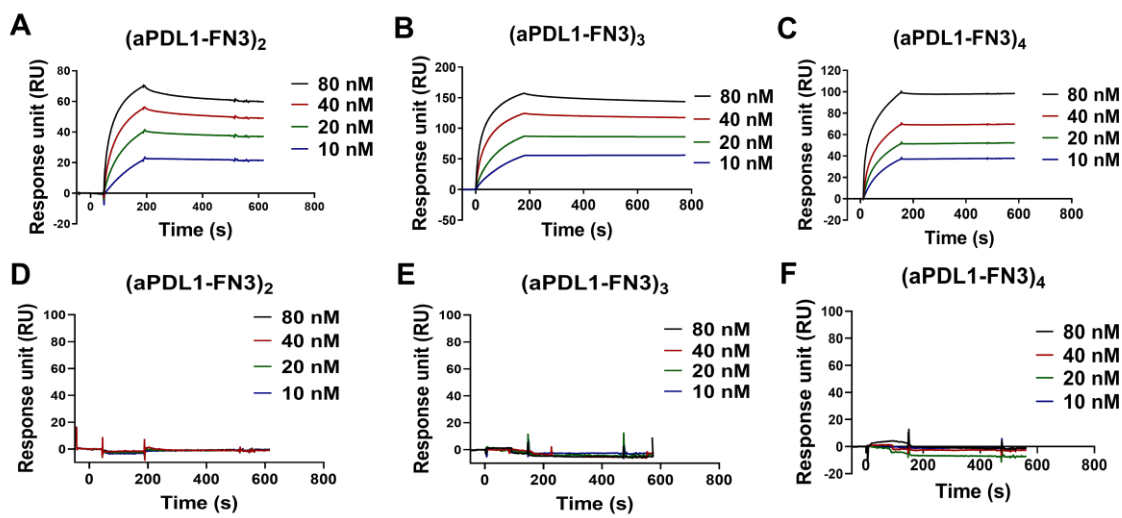


Figure 31: SPR sensorgrams of (aPDL1-FN3)_n oligomers. The (aPDL1-FN3)₂, (aPDL1-FN3)₃, and (aPDL1-FN3)₄, show binding to human PDL1 (A, B, C), and lack of binding to human PD1 (D, E, F). Increased valency slows their off-rates (k_{off}), and significantly increases their K_D .

The aPDL1-FN3 tetramer, (aPDL1-FN3)₄, has a remarkably high binding affinity for PDL1, with a K_D of 94 pM for human PDL1. The (aPDL1-FN3)₄ shows no off-target binding to human PD1 or human PDL2. **Table 10** describes the details of binding kinetic profiles of (aPDL1-FN3)_n proteins.

Table 10: The binding kinetics of (aPDL1-FN3)_n oligomers

Construct	k_{on} (on-rate, 1/Ms)	k_{off} (off-rate, 1/s)	K_D (nM)
(aPDL1-FN3) ₂	1.27E5	1.83E-4	1.44
(aPDL1-FN3) ₃	2.18E5	9.74E-5	0.45
(aPDL1-FN3) ₄	2.51E5	2.35E-5	0.094

4.3.4 Characterization after fluorescence conjugation

Next, we used the primary amine group on the N-terminus of proteins as the site of conjugation for fluorescent dyes. We specifically chose to use Alexafluor488 because

this dye molecule is stable and the conjugation of this dye to our proteins does not cause significant aggregation or micelle formation. Because the engineered loop regions of aPDL1-FN3 proteins contain lysine residues that could be hampered by this conjugation, we optimized the reaction conditions for Alexafluor488 conjugation. We performed pilot reactions, varying the length of reaction time (30 mins, 1 hour, and 3 hours), the molar ratio of protein to fluorescent dyes (1:5, 1:10, and 1:15), and the pH of buffer (6.0, 6.5, and 7.0). From this experiment, we determined that 1 hour with a molar ratio of 1:10 is a suitable condition for high efficiency. We chose to maintain the pH of a buffer as 6.0 because in general, lower pH levels are kinetically favorable for N-terminus conjugation over lysine conjugation due to their different pI values.

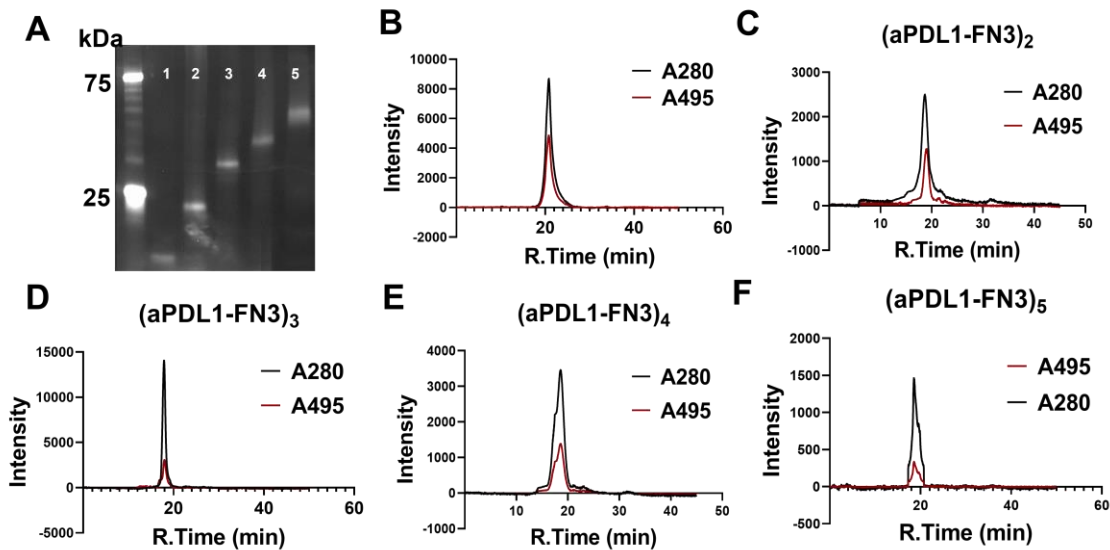


Figure 32: Characterization of Alexafluor488-conjugated (aPDL1-FN3)_n proteins. (A) SDS-PAGE fluorescence image shows (aPDL1-FN3)_n labeled with Alexafluor488 fluorescent dye. (B-F) SEC-HPLC of (aPDL1-FN3)_n (n = 1-5 in panels B-F) show

colocalized peaks at A280 (protein) and A495 (fluorescent dye), indicating that the proteins were successfully fluorescently labeled.

Using this optimized condition, we successfully conjugated the (aPDL1-FN3)_n oligomers with Alexafluor488 dyes. We confirmed the successful reaction and purity of our conjugated proteins using SDS-PAGE as well as size exclusion chromatography (SEC) (**Figure 32**). In SEC, due to the characteristic absorbance of Alexafluor488 dyes at 495 nm for its maximum excitation and that of protein at 280 nm, their co-localized peaks indicate that proteins are successfully conjugated with Alexafluor488 dyes.

4.3.5 Characterization of the potency of (aPDL1-FN3)_n

Although (aPDL1-FN3)_n proteins have a strong binding affinity to PDL1, for their therapeutic efficacy, their binding to PDL1 should effectively antagonize the interaction between PD1 and PDL1. To characterize this inhibitory interaction, we decided to utilize in vitro PD1/PDL1 blockade assay. This assay is comprised of two genetically engineered cell lines, Jurkat/PD1 reporter cells and CHO TCR/PDL1 cells. When co-cultured, the PD1 on Jurkat cells and PDL1 on CHO cells are bound, preventing TCR from being activated, resulting in no luminescence activation. However, if anti-PDL1 binders are present and successfully antagonize this interaction, TCR is activated inducing luminescence signals that can be detected by a plate reader. Using the serial dilution of (aPDL1-FN3)_n proteins, we can characterize their potency, determined by the IC₅₀ values of this assay.

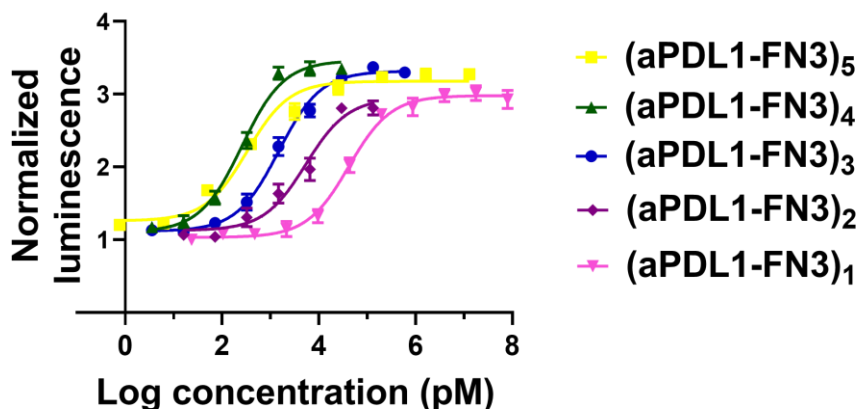


Figure 33: A PDL1 blockade assay was used to characterize the IC₅₀ values of (aPDL1-FN3)_n proteins (n=1-5).

Table 11: The IC₅₀ of (aPDL1-FN3)_n oligomers

Construct	IC ₅₀ [nM]
(aPDL1-FN3) ₁	30.3 ~ 57.6
(aPDL1-FN3) ₂	2.69 ~ 10.4
(aPDL1-FN3) ₃	0.97 ~ 1.84
(aPDL1-FN3) ₄	0.19 ~ 0.36
(aPDL1-FN3) ₅	0.21 ~ 0.52

According to the results of this assay, the potency of (aPDL1-FN3)_n proteins increases with increasing valency from 1 to 5 and is specifically saturated with the tetramer (**Figure 33**). (aPDL1-FN3)₄ shows high antagonism of the PD1/PDL1 interaction in this *in vitro* assay, with a half-maximal inhibitory concentration (IC₅₀) of around 260 pM. **Table 11** summarizes the IC₅₀ of (aPDL1-FN3)_n oligomers. These results are competitive with those of an FDA-approved monoclonal antibody that binds PDL1,

atezolizumab, which has a K_D of 433 pM for human PDL1 and 134 pM for murine PDL1, and an IC_{50} of 140 pM.

4.3.6 Quantifying the effect of multivalency on *in vitro* PDL1-binding with flow cytometry

We next validated the *in vitro* PDL1-binding of (aPDL1-FN3)_n proteins using genetically engineered CHO-hPDL1 cell lines that stably express human PDL1 receptors on their cellular membranes. This cell line is very useful for evaluating the *in vitro* PDL1-binding of (aPDL1-FN3)_n. It is also useful for determining the valency most optimal for saturating all receptors on the cellular level since all cells express the PDL1 receptor.

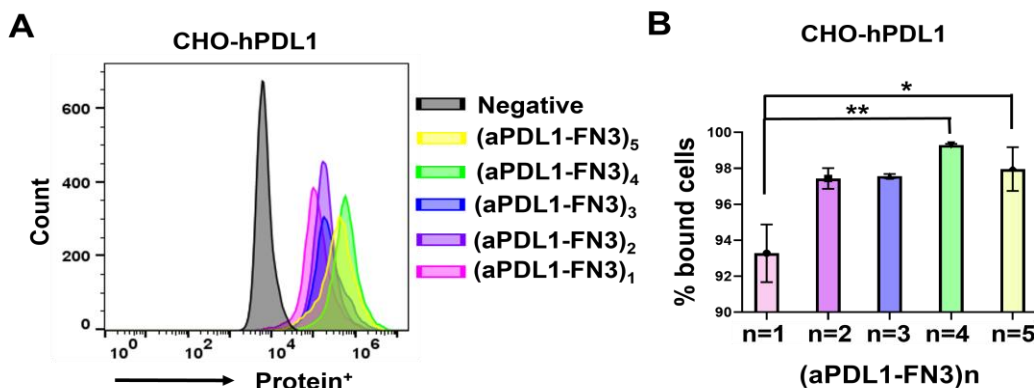


Figure 34: Flow cytometry was performed using CHO-hPDL1 cells to characterize the *in vitro* PDL1 binding of (aPDL1-FN3)_n proteins (n=1-5). (A) All proteins successfully bind to hPDL1 receptors on CHO cells. (B) Higher valency leads to the increased number of cells that were bound by. (aPDL1-FN3)₄ and (aPDL1-FN3)₅ proteins significantly bind to more CHO-hPDL1 cells than (aPDL1-FN3)₁ protein (* $p < 0.05$, ** $p < 0.005$, one-way ANOVA). Based on the neutralization cell reporter assay and flow cytometry, (aPDL1-FN3)₄ was chosen for the fusion with ELP.

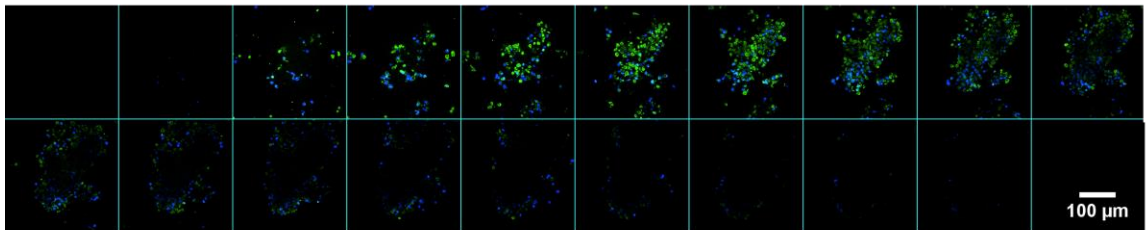
For this, we used the fluorescently labeled (aPDL1-FN3)_n proteins, incubated them with CHO-hPDL1 cell lines, and analyzed cell populations for fluorescence by flow cytometry (**Figure 34**). The data demonstrate that the percentage of cells bound to PDL1 increases as the valency increases from 1 to 5, and saturates with the tetramer. This result is well-matched with a PDL1 blockade assay, suggesting that (aPDL1-FN3)₄ protein is the most optimal candidate for the fusion with biopolymer before *in vivo* testing.

4.3.7 *In vitro* characterization of tumor spheroids uptake and penetration

To evaluate the effect of multivalency on PDL1-binding on a 3D level, we generated a tumor spheroid model using cancer cell lines. We specifically chose the CT26.WT cell line because this cell line has PDL1-binding and has been proven to form a 3D spheroid model using various methods (174, 175). To generate a CT26-specific spheroid model, we utilized an aggregation method based on the hanging drop method (174). In this method, a cell suspension is positioned in the U-shaped bottom of a microwell in a plate, using centrifugation. This force is similar to the force of gravity, and the cells spontaneously form cellular aggregates, giving rise to a single spheroid. This method produces a large number of spheroids with manageable control of their sizes. To ensure that cells are assembled into spheroids in environments that govern cell-cell and cell-extracellular matrix (ECM) interactions, cell aggregates are continuously supplemented with growth media under close monitoring and maintained for 10 days to

provide sufficient time for cells to proliferate, aggregate, and differentiate. Using this method, spheroids have a diameter of 200 μm or more, usually with a spherical shape, and exhibit three zones of cell populations: 1) an internal zone is filled with necrotic cells due to their low accessibility of nutrients and oxygen and high accumulation of waste and debris; 2) a middle zone contains quiescent cells; 3) an external zone includes the most vibrant cells that are proliferating and migrating. These different populations and ECM recapitulate many characteristics of in vivo tumor models. Thus, these features make spheroids a promising model for studying the effect of multivalency on tumor uptake and penetration.

A: Monomer



B: Tetramer

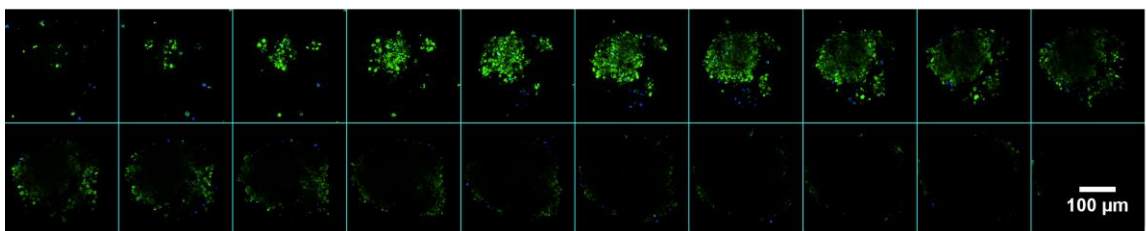


Figure 35: Montage of Z-stack images of (A) (aPDL1-FN3)₁ and (B) (aPDL1-FN3)₄ proteins. (aPDL1-FN3)₄ protein more evenly binds to PDL1 than (aPDL1-FN3)₁ protein. Hoechst is labeled blue, and protein is labeled green. The scale bar is shown on the bottom right.

To validate the choice of (aPDL1-FN3)₄ for the next step, we compared the specific PDL1-binding of (aPDL1-FN3)₄ with (aPDL1-FN3)₁ protein. For this, we used the fluorescently labeled (aPDL1-FN3)₁ and (aPDL1-FN3)₄ proteins, incubated them with CT26-spheroids, stained with Hoechst for nuclear staining, and imaged the spheroids for the specificity of PDL1-binding. The result (**Figure 35**) shows that (aPDL1-FN3)₄ has a more even distribution of PDL1-binding as compared to (aPDL1-FN3)₁. This result suggests that higher valencies require lower concentration to saturate receptors on 3D spheroid models as well as on 2D cells.

4.4 Conclusion and future directions

In this chapter, using the discovered aPDL1-FN3 sequence from phage display, we modulated the affinity and valency of aPDL1-FN3 proteins by creating a set of modular (aPDL1-FN3)_n domains where the valency (n) of the FN3 domains was systematically varied from 1 to 5. The multivalent (aPDL1-FN3)_n proteins were successfully cloned, produced in *E. coli*, and purified by IMAC. Purified (aPDL1-FN3)_n proteins were characterized for their biophysical properties, including their molecular weights, hydrodynamic radius, aggregation or micelle formation after fluorescence conjugation, and specific binding affinity to PDL1. Owing to the multivalency presentation and avidity effects, higher valency enhanced PDL1-specific binding affinity by around ~170-fold, into the picomolar regime, reducing its dissociation rate. Also, increased valency greatly improves its antagonistic interaction between PD1 and PDL1

by around ~160-fold, characterized by their IC₅₀. Importantly, a PDL1 blockade assay and flow cytometry show that specific PDL1 binding is saturated with the tetra-valency of (aPDL1-FN3)₄. Thus, we chose (aPDL1-FN3)₄ for the recombinant fusion with biopolymers before *in vivo* evaluation.

With the methods and principles described in this chapter, we successfully demonstrated a proof-of-concept platform where multivalency can be optimized for therapeutic purposes. Although we specifically chose (aPDL1-FN3)₄ for this thesis, different valencies and orientations can be explored for various applications (154). For example, for diagnostic tools, a very slow off-rate is not desired, but a faster on-rate and off-rate are more favorable to avoid any toxicities. We believe this platform can be robustly utilized for optimizing diagnostic agents or therapeutic binders that are multi-specific or multi-valent.

5. Developing the fusion between (aPDL1-FN3)₄ and ELP

5.1 Introduction and motivation

Small binding scaffolds are advantageous due to their small sizes. However, because of these small sizes, they are rapidly cleared by glomerular filtration, thus suffering a very short serum half-life (176). This restricts their use as therapeutics by themselves and always requires further conjugation with biopolymers (177). Thus, the criteria for the choice of biopolymers would be as follows: 1) extending serum half-life; 2) imparting stealth properties; 3) increasing solubility and stability; 4) sustained release formulation. All these criteria would increase the accumulation of target tissue *in vivo* while reducing off-target effects and maintaining a continuous level of drug concentration for therapeutic efficacy. One promising solution that fulfills all of these criteria is the genetic fusion of elastin-like polypeptide (ELP).

5.1.1 Recombinant fusion with ELP

The short serum half-life of oligomers of the FN3 domain potentially reduces their uptake by solid tumors. To improve the plasma circulation duration of rapidly excreted peptide and protein drugs, we have previously developed a genetically encoded delivery system that involves the fusion of a protein-drug to an ELP (96).

ELP is not only biodegradable, non-toxic, and non-inflammatory, but also very versatile. It can be readily prepared in different formulations, including soluble unimers, (unassembled chains), micellular nanoparticles, and macroscale coacervates (178). This is

because ELP exhibits reversible lower critical solution temperature (LCST) phase-transition behavior. By modulating the length and the hydrophobicity of ELP, it can be optimized for the most suitable delivery formats (179). The relationship between the sequence properties of ELPs and LCST behavior has been extensively studied, allowing us to rationally engineer ELP-based platforms for various applications (180, 181). Previously, we have shown that the hydrophobic drug conjugation to ELP triggers its self-assembly into nanoparticles that significantly extends the pharmacokinetics of a native drug (182, 183). Also, the ELP system enables us to develop an injectable depot formulation (95), which is useful for the delivery of immune checkpoint inhibitors.

5.1.2 Sustained and localized release of ELP

As a fusion partner of (aPDL1-FN3)₄, we specifically chose to use ELP as an injectable depot-forming module. This depot formulation is desired because this format can provide sustained and localized delivery of anti-PDL1 drugs with enhanced pharmacokinetics and bioavailability. The LCST behavior of ELP can be tuned to form an insoluble coacervate upon heating above a critical transition temperature (T_t) (184). Thus, the T_t can be precisely optimized between room temperature (25 °C) and body temperature (37 °C) such that the fusion with ELP and drug can be injected as a solution and transitioned into a depot upon injection *in vivo*. As this ELP depot is continuously diluted from the boundary, the fusion ELP-drug is slowly released into circulation (92, 185, 186).

We have previously shown that a fusion of glucagon-like peptide (GLP1) to ELP can be subcutaneously injected through a narrow-gauge needle into diabetic mice (91). It creates a depot that continuously releases the drug and controls blood glucose levels for up to 10 days (92). This 10-day duration of glucose control is better than that provided by two FDA-approved sustained-release technologies: Trulicity, an Fc fusion of GLP-1, and Bydureon, a degradable microsphere formulation. These results also show that an ELP depot can exceed the performance of an antibody-based drug.

Combining an immune checkpoint inhibitor with an ELP has not yet been previously explored and requires thorough optimization. Using the optimized (aPDL1-FN3)₄ protein, we designed a genetic fusion method to produce sets of (aPDL1-FN3)₄-ELP proteins (**Figure 36**). The goal of this work is to endow (aPDL1-FN3)₄ with the reversible phase transition behavior of ELPs for sustained and localized delivery.

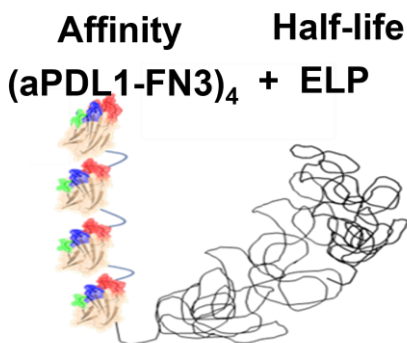


Figure 36: The schematic shows the modular design of (aPDL1-FN3)₄ fused with ELP. ELP protein was chosen to improve the serum half-life of the drug. ELP was fused to the C-terminus of (aPDL1-FN3)₄.

5.2 Materials and methods

5.2.1 Construct design and synthesis

Because ELPs contain highly repetitive genes, PCR-based traditional methods for genetic fusion are not possible. Thus, to fuse the protein with ELP, we commonly use plasmid reconstruction by recursive directional ligation (PRe-RDL) (**Figure 37**) (187). Briefly, we used two plasmids: one contained the ELP construct, and the other contained the (aPDL1-FN3)₄ construct. Then, for a C-terminus fusion of ELP, (aPDL1-FN3)₄-encoding plasmid was cleaved by Bgl1 and Acu1 while ELP-encoding plasmid was cleaved by Bgl1 and BseR1. After ligating these two halves, we reconstructed a final plasmid that encodes the fusion protein between (aPDL1-FN3)₄ and ELP. The successful fusion was confirmed by Sanger sequencing, and the final plasmid was transformed into the BL21(DE3) expression strain of *E. coli* (New England Biolabs, MA). Aliquots of the DNA stocks were stored at -20 °C and transformed cell stocks with glycerol were stored at -80 °C.

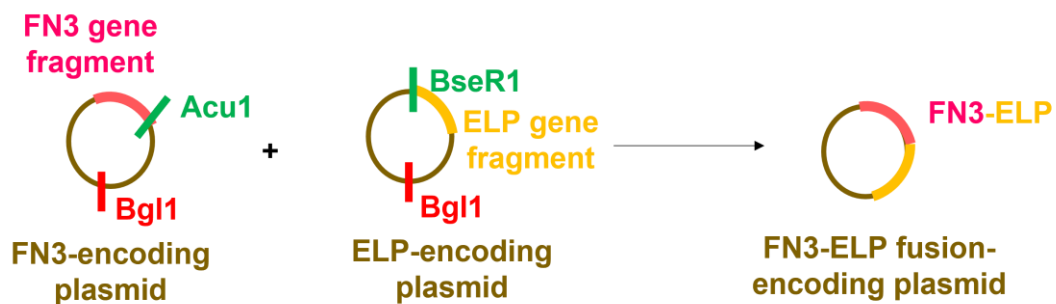


Figure 37: The schematic shows a plasmid reconstruction for FN3-ELP fusion by recursive directional ligation (PRe-RDL).

5.2.2 Protein expression and purification

The (aPDL1-FN3)₄-ELP proteins were expressed in BL21(DE3) *E. coli* using autoclaved 2xYT media (16 g of tryptone, 10 g of yeast extract, 5 g of NaCl, and pH 7.0 in 1 L of distilled H₂O). From the frozen glycerol stocks, small starters (50 ml) were grown overnight and used to inoculate 6 of 1 L flasks of 2xYT media supplemented with kanamycin (45 µg/ml). After the flasks were incubated in a shaker at 37 °C and 200 rpm for 3 hours, the final concentration of 0.5 mM of IPTG (Gold Biotechnology) was added per flask. Then, all flasks were incubated in a shaker at 18 °C and 200 rpm for 24 hours. Cells were harvested by centrifugation at 4,000 rpm and 4 °C for 15 mins, and the cells were resuspended in the phosphate buffer. 1 L cells were resuspended in 80 ml of buffer.

Because the fusion with ELP endows its reversible phase transition behavior to the fusion protein, we can readily purify (aPDL1-FN3)₄-ELP using inverse transition cycling (ITC) (188, 189). After sonicating the resuspended cell pellets, the cell lysate was centrifuged at 4 °C (below the T_t) to remove insoluble cell fragments. The supernatant was then heated at 37 °C with a high concentration of ammonium sulfates to trigger the phase transition of ELP fusion proteins. This suspension was then centrifuged at 37 °C to form a pellet by ELP fusion protein at the bottom of the centrifuge tube, along with aggregated contaminants. This pellet was then dissolved by the addition of low salt buffer (1X PBS) and incubated at 4 °C. These steps were repeated 2-3 times until the fusion protein was highly pure, confirmed by SDS-PAGE.

5.2.3 Biophysical characterization

5.2.3.1 Dynamic light scattering

Dynamic light scattering (DLS) measurements of proteins were performed using a Wyatt DynaPro temperature-controlled instrument (Wyatt Technology, Santa Barbara, CA), with 10 acquisitions collected at both 25 °C and 37 °C. Samples for the DLS system were prepared in 1X PBS and filtered through Whatman Anotop sterile syringe filters (0.2 µm; GE healthcare, PA) into a black 96 well plate (Corning®). The data points presented for this characterization represent the mean of R_h of the sample, illustrating the polydispersity.

5.2.3.2 UV/vis spectroscopy

Temperature-triggered phase separation was characterized by UV-vis spectrophotometry (Cary 300 Bio Agilent). Briefly, serial diluted ELP fusion proteins (1-100 µM in PBS) was heated from 25 °C to 50 °C at a rate of 1 °C/min, and the optical density at 350 nm (OD 350 nm) was measured. As the temperature was increased towards the T_t (solution-to-coacervate), the OD_{350 nm} increased rapidly, indicating the coacervation of ELP-fused proteins and the formation of micron-size aggregates.

5.2.3.3 Surface plasmon resonance

We use a Biacore T200 SPR instrument. First, the series S sensor chip CM5 (GE healthcare) was normalized using 70% glycerol. Protein G was immobilized in flow paths 1 and 2 of the CM5 chip, using NHS/EDC coupling. A solution of 0.5M EDC/1M

NHS was injected at 5 $\mu\text{l}/\text{min}$ for 7 minutes to activate the chip surface. 200 $\mu\text{g}/\text{ml}$ of protein G in 10 mM sodium acetate buffer (pH 4.0) was injected at 5 $\mu\text{l}/\text{min}$ for 30 seconds to obtain a final RU (response unit) of around 800. Next, 1M ethanolamine was injected at 5 $\mu\text{l}/\text{min}$ for 10 minutes to inactivate the chip surface. To characterize the binding affinity of FN3 to PDL1, the Fc-tagged version was used and as a control, only Fc protein was used. Briefly, on flow path 1, we injected Fc protein at a flow rate of 30 $\mu\text{l}/\text{min}$ for 20 seconds, and on flow path 2, we injected Fc-tagged PDL1 (Fc-PDL1) at a flow rate of 30 $\mu\text{l}/\text{min}$ for 20 seconds. Our protein samples were injected over immobilized Fc-PDL1 and Fc simultaneously on both flow paths at a flow rate of 30 $\mu\text{l}/\text{min}$ at 25 $^{\circ}\text{C}$ for 3 mins. Then, protein samples were replaced with running buffer (1X PBS) for 5 mins for dissociation. After each experiment, the chip surface was regenerated with 10 mM glycine-HCl (pH 1.5) for 30 secs. After injection of serially diluted protein samples in running buffer and subtraction of the signal of flow path 1, the final SPR sensorgrams were obtained and analyzed using a 1:1 Langmuir binding model in BIAevaluation software (GE Healthcare).

5.2.3.4 Fluorescent dye labeling and confirmation

To fluorescently label proteins, 1 mg of AlexaFluor488-NHS ester was dissolved in 100 μl DMSO. The N-terminal amine of proteins was labeled with AlexaFluor488-NHS ester by incubating 20 - 100 μM protein with ten molar equivalents of dye, rotating for 1 hour at room temperature in sodium phosphate buffer, pH 6.0. Excess unlabeled

dye was removed with a Zeba desalting spin column, extensive dialysis, or centrifugal ultrafiltration (Amicon™ Ultra-15, 10kDa MWCO). The purity of labeled proteins was assessed by size exclusion chromatography.

For size exclusion chromatography analysis of the purity of fluorescently labeled proteins, a Shodex OHPak SB-804 HQ column (New York, NY) was used with an isocratic flow of 0.5 ml/min of 1X PBS. We use Shimadzu's high-performance liquid chromatography system (Shimadzu Scientific Instruments, Columbia, MD). HPLC-grade solvents were purchased from VWR International (Radnor, PA). All buffers and samples were prepared in 1X PBS and filtered through 0.2 µm.

5.2.4 *In vitro* characterization

5.2.4.1 Cell culture

CT26.WT cells were purchased from ATCC. These cells were cultured at 37 °C with 5% CO₂ in RPMI1640 (ATCC modification, A1049101, Gibco) supplemented with 10% fetal bovine serum (FBS) and penicillin/ streptomycin. MC38 cells were purchased from Kerfast and cultured at 37 °C with 5% CO₂ in Dulbecco's modified MEM with 10% FBS, 2mM glutamine, 0.1 mM nonessential amino acids, 1 mM sodium pyruvate, 10 mM HEPES, 50µg/ml gentamycin sulfate, and penicillin/streptomycin. B16.F10 cells were cultured at 37 °C with 5% CO₂ in Dulbecco's modified MEM with 10% fetal bovine serum, 4 mM L-glutamine, 4500 mg/L glucose, 1 mM sodium pyruvate, and 1500 mg/L sodium bicarbonate. CHO-hPDL1 cells were purchased from Promega and cultured at

37 °C with 5% CO₂ in Ham's F12 media with 10% FBS, 200 µg/ml hygromycin, and 250µg/ml G-418 sulfate solution. Jurkat-PD1 cells were purchased from Promega and cultured at 37 °C with 5% CO₂ in RPMI1640 media with 10% FBS, 0.1 mM nonessential amino acids, 1 mM sodium pyruvate, 200 µg/ml hygromycin, and 500µg/ml G-418 sulfate solution.

5.2.4.2 PD1/PDL1 blockade assay

CHO TCR/hPDL1 cells were prepared in Ham's F12 supplemented with 10% FBS. First, cells were washed with 1X DPBS, trypsinized with 0.25% trypsin/EDTA, and harvested by centrifugation at 250g for 5 mins. The cell pellet was resuspended in warm media and the cells were counted with a hemocytometer after 1:1 dilution into 0.4% Trypan blue solution (Thermo Fisher Scientific, MA). The cell density was adjusted to 4×10^5 cells/ml by the addition of warm media, and the cell suspension was transferred to a sterile reagent reservoir. Using a multichannel pipette, 100 µl of cells were added to each well of a 96-well flat, white clear-bottom assay plate (Corning®). The plate was incubated in a 37 °C, 5% CO₂ incubator overnight.

To prepare protein samples in an assay buffer (RPMI 1640 supplemented with 1% FBS), a sterile clear bottom 96-well plate was prepared. In the case of 2.5-fold dilution, 250 µl of proteins were added to the first well, and 150 µl of assay buffer was added to other wells. The 100 µl of proteins from the first well was transferred to the 150 µl of assay buffer and gently mixed. This step was repeated until a sufficient range of

concentration was covered. These protein samples were added to the plate coated with CHO TCR/hPDL1 cells.

Jurkat/PD1 cells were prepared, and the cell density was adjusted to 1.25×10^6 cells/ml by the addition of assay buffer. Using a multichannel pipette, 40 μ l of cells were added to each well of the plate coated with CHO TCR/hPDL1 cells followed by the addition of protein samples. The plate was incubated again in a 37 °C, 5% CO₂ incubator for 6-8 hours.

Since protein samples effectively antagonize the interaction between CHO TCR/hPDL1 cells and Jurkat/PD1 cells, TCR activation induces the luminescence of the NFAT pathway. After taking out the plate and equilibrating it to room temperature for 10 mins, 80 μ l of Bio-Glo™ reagents (Promega, WI) was added to each well. In 10-30 mins, the luminescence signal was measured by a multimode plate reader (Tecan).

5.2.4.3 Flow cytometry

Overnight cultures of mammalian cells (CHO-hPDL1, Jurkat-PD1, CT26.WT, and MC38 cells) were prepared for flow cytometry. First cells were trypsinized with 0.25% trypsin/EDTA and harvested by centrifugation at 500g for 3 mins. The cell pellet was resuspended in 1X PBS and the cells were counted with a hemocytometer after 1:1 dilution into 0.4% Trypan blue solution (Thermo Fisher Scientific, MA) The cell density was adjusted to 2×10^6 cells/ml by the addition of blocking buffer (5% rat serum, 5% mouse serum, 1% CD16/32 (clone 93, eBioscience, San Diego, CA). Then, the cells were

incubated with fluorescently labeled proteins by gently mixing 190 μl of the cell suspension and 10 μl of proteins at a final concentration of 1 μM of proteins. The mixture of cells and proteins was incubated at 37 °C for 1 hour. After incubation, cells were collected, washed 3 times with 0.2ml of 1XPBS with 1%BSA on ice, and adjusted to a final cell concentration of 1×10^5 cells/ml for flow analysis. Live cells populations were analyzed for fluorescence on a BD Accuri C6 (BD Biosciences, CA).

5.2.4.4 3D spheroids and confocal imaging

Overnight cultures of CT26.WT cells were prepared and accurately counted for producing aggregates of 3D tumor spheroids. To ease the process, we used AggreWell™-800 24-well plates (Stemcell Technologies, Canada), as described in the manufacturer's manual. Briefly, wells were pretreated with 500 μl of anti-adherence rinsing solution, the plate was centrifuged at 1300 g for 5 mins, and the plate was carefully rinsed with warm media (RPMI 1640 supplemented with 10% FBS) to remove any bubbles. After aspiration of all rinsing media, 1.2×10^6 cells were added to each well (4000 cells per microwell), and warm media was added to sufficiently adjust the volume of 2 ml per well. The plate was centrifugated at 100 g for 5 mins to capture cells in microwells and observed under a microscope to verify the cells were evenly distributed among the microwells. Over 10 days of incubation at 37 °C, 50% of media was carefully changed every other day. In 10 days, spheroids were harvested using a 37 μm reversible strainer (Stemcell Technologies, Canada). Using this strainer, the aggregates remain on

the filter during the harvest, and single cells flow through. After washing three times, the strainer was inverted, and the addition of warm media eluted the spheroids.

The spheroids were placed on a 12-well plate and incubated with fluorescently labeled 1 μM of proteins and 1 μM of Hoechst (Thermo Fisher Scientific, MA) for nucleus staining. The mixture of spheroids and proteins was incubated at 37 °C for 6 hours. After incubation, 3D spheroids were collected and washed 3 times with 0.05ml of 1X PBS with 10% FBS. The spheroids were placed in a 35 mm glass bottom petri dish and imaged under Andor Dragonfly Spinning Disk confocal microscope using a 40X oil immersion objective. Fluorescence signal from Alexa 488 was acquired using a 488 nm laser and a 525/50 nm bandpass filter while Hoechst fluorescence was captured using a 405 nm laser with a 450/50 nm bandpass filter. A Z-stack of the spheroid was acquired, and the center slice(s) were processed for analysis.

Images were then analyzed in ImageJ according to the method described by Thurber and Wittrup. Briefly, the 'hot' pixels due to bulk antibody, noise, and autofluorescence were reduced using the despeckle function. A threshold was set to eliminate background signal and autofluorescence and the pixels above the threshold were captured in a binary mask. Heterogeneity in receptor expression results in areas saturated with the constructs but with intensity values below the set threshold. These areas (holes) were then filled by a series of erosion and dilation of pixels. This method was automated to avoid and process differences between images. The sample front and

outer perimeter were then traced manually for each image and penetration depths were measured. Three spheroids were analyzed for each sample and at least 30 measurements were performed per image. Statistical significance between the observed mean penetration depth was analyzed by one-way ANOVA.

5.2.5 *In vivo* studies

5.2.5.1 Pharmacokinetics

Pharmacokinetics were measured using Alexafluor488-labeled proteins. To remove any unreacted fluorophores, extensive dialysis and ultrafiltration were used in PBS. Before *in vivo* injection, all fluorescently labeled proteins were confirmed by the SEC/HPLC, and their endotoxin levels were ensured to be under 0.25 EU/ml. Balb/c female mice (The Jackson Laboratory) were administered with 67 nmol/kg BW of Alexafluor488-labeled proteins via either an intraperitoneal (*i.p.*) injection or intravenous (*i.v.*) injection via tail vein. 10 µl blood samples were collected from the tail vein in microcentrifuge tubes with 100 µl of heparin at certain time points. The concentration of fluorescently labeled protein in the blood was measured by a fluorescence plate reader (Tecan). Under identical conditions, the serial dilutions of proteins for *in vivo* injections were measured and used for a standard curve. Then, blood concentration time-course data was analyzed with a standard two-compartment PK model for *i.v.* and non-compartmental model for *i.p.* PK data to ascertain the pharmacokinetic parameters.

Pharmacokinetic parameters were analyzed as follows. The elimination half-life ($t_{1/2, \text{Elim}}$) was calculated from the slope of the linear regression fit to the elimination portion of the log concentration vs. time curve. For *i.p.* data, the elimination half-life was calculated by calculating the slope of the time points after C_{max} (maximum serum concentration). t_{max} for *i.p.* PK data was determined as the time required to reach C_{max} . The area under the curve (AUC) was calculated by GraphPad Prism 9 software (La Jolla, CA) using the trapezoidal rule. The serum concentration at $t=0$ (C_0), for the *i.v.* data was extrapolated by fitting a linear line through the early time points (45 s–4h range). The volume of distribution (V_D) which reflects the degree of extravascular tissues and organ distribution of polypeptide, was calculated as $VD = (\text{Dose injected } i.v.)/(C_0)$. The clearance of proteins from systemic circulation (CL), was calculated as $(\text{dose} \times F)/\text{AUC}$ where F (bioavailability) = 1 for *i.v.* bolus injection. All pharmacokinetic parameters were reported as mean \pm SEM.

5.2.5.2 Efficacy

All animal experiments were performed under protocols approved by the Duke Institutional Animal Care and Use Committee (IACUC).

B16.F10 model: C57bl/6 mice (The Jackson Laboratory, male, 6–10 weeks old) were shaved and subcutaneously inoculated on the right flank with 1×10^5 B16.F10 melanoma cells. Mice were treated on days 4, 7, and 10 (post-inoculation) with one of the following: an equivalent volume of PBS, (NonsenseFN3)₄-ELP, (aPDL1-FN3)₄-ELP, anti-

mousePDL1 antibody (clone number: 10F.9G2, Bioxcell), and atezolizumab-based anti-PDL1 antibody (Invivogen). Each dose for treatment was 67 nmol/kg BW, an equimolar dose of 10 mg/kg BW of antibody.

CT26.WT model: Balb/c mice (The Jackson Laboratory, female, 6–10 weeks old) were shaved and subcutaneously inoculated on the right flank with 1×10^5 CT26.WT cells. When tumor volumes reach $\sim 70 \text{ mm}^3$, mice were treated 3 times 3 days apart with one of the following: an equivalent volume of PBS, (aPDL1-FN3)₄-ELP, anti-mouse PDL1 antibody (clone number: 10F.9G2, Bioxcell), and atezolizumab-based anti-PDL1 antibody (Invivogen). Each dose was 67 nmol/kg BW, the same as 10 mg/kg BW of antibody.

MC38 model: C57bl/6 mice (The Jackson Laboratory, male and female, 6–10 weeks old) were shaved and inoculated subcutaneously on the right flank with 1×10^5 MC38 cells. Using MC38 cells, we studied two different conditions for the initiation of treatments: 1) When tumor volumes reach $\sim 70 \text{ mm}^3$, mice were treated 3 times 3 days apart with one of the following: an equivalent volume of PBS, (aPDL1-FN3)₄-ELP, anti-mousePDL1 antibody (clone number: 10F.9G2, Bioxcell), and atezolizumab-based anti-PDL1 antibody (Invivogen). Each dose was 67 nmol/kg BW, same as 10 mg/kg BW of antibody; 2) Mice were treated on days 4, 7, and 10 (post-inoculation) with one of the following: an equivalent volume of PBS, (NonsenseFN3)₄-ELP, (aPDL1-FN3)₄-ELP, anti-mousePDL1 antibody (clone number: 10F.9G2, Bioxcell), and atezolizumab-based anti-

PDL1 antibody (Invivogen). Each dose was 67 nmol/kg BW. In this study, we had tumor-free survivors for treatment groups. Thus, those mice were used for tumor-reinoculation to study if mice develop systemic anti-tumor immunities.

For all inoculations, cells were suspended in DPBS at a concentration appropriate for a 50 μ l injection. Mice were sacrificed if they appeared moribund or lost > 15% of their baseline body weight, or if the tumor volumes exceeded 2000 mm³. Tumor volumes were calculated using the formula: Volume (mm³) = length \times width² \times 0.52. Mice were randomized to treatment groups using the list randomizer from random.org.

5.2.5.3 Rechallenge

With the mice surviving from the first tumor inoculation, we decided to re-inoculate the same number (10^5) of tumor cells (MC38) at the same location (right flank). We used naïve mice without receiving treatments before as a control. At day 85 post-inoculation, survivors were shaved, and *s.c.* inoculated with the 10^5 of MC38. Their body weights and tumor sizes were monitored. Mice surviving from this re-inoculation were subjected to second re-inoculation with the same number of cells but at the opposite location (left flank). On day 170 post-inoculation, survivors were shaved, and *s.c.* inoculated on the left flank with the 10^5 of MC38. Their body weights and tumor sizes were monitored. Tumor dimensions (length and width) were measured every other day, and tumor volumes were calculated using the formula described above.

5.2.5.4 Biodistribution

Organ distribution of (NonsenseFN3)₄-ELP, (aPDL1-FN3)₄-ELP, and anti-PDL1 antibodies were determined by radiolabeling a tyrosine residue of the proteins with ¹²⁵I, as previously described (186, 190, 191). Briefly, 200 µl of proteins at 100 µM was added to a pre-coated IODO-Gen tube with 2 mCi [¹²⁵I]Na on ice and incubated for 15 min. The reaction mixture was purified by a ZebaSpin desalting column (Thermo Fisher Scientific). Balb/c mice (The Jackson Laboratory) were shaved and subcutaneously inoculated with 1 × 10⁵ CT26.WT cells. Then, mice were placed on 0.4 wt% potassium iodide water to block radionuclide accumulation in the thyroid. After around 7 days, tumor volumes reached ~70mm³. Then, mice were randomly divided (n = 5 per group). Each mouse was weighed before injection and received treatments based on their weights. Each treatment involved the intraperitoneal injection of 4 µCi ¹²⁵I equivalents of 67 nmol/kg BW of proteins, and we performed a total of three injections two days apart. Two days after the last injection, whole organs were harvested and the concentration of proteins in each organ was determined by measuring ¹²⁵I activity with an automated gamma counter (LKB-Wallac) in counts per minute (CPM). Simultaneously, under identical conditions, serial dilutions of ¹²⁵I labeled proteins used for injections were measured to create a standard curve. Then, using this standard curve, CPM was converted to the percent injected dose (%ID), and then the %ID was normalized against the weight of the organ to calculate %ID/g of tissue.

5.2.5.5 Immunomodulation profiles

Balb/c mice were shaved s.c. inoculated with 10^5 of CT26.WT cells and when tumor volume reached 70mm^3 , mice were treated with an equivalent volume of PBS, (NonsenseFN3)₄-ELP, (aPDL1-FN3)₄-ELP and anti-PDL1 antibody (Bioxcell) three times two days apart. Each dose was 67 nmol/kg BW. After two days from the last injection of drugs, mice were sacrificed and tumors were harvested, processed, and analyzed for tumor-infiltrating lymphocytes. **Figure 38** illustrates the overview of this experiment.

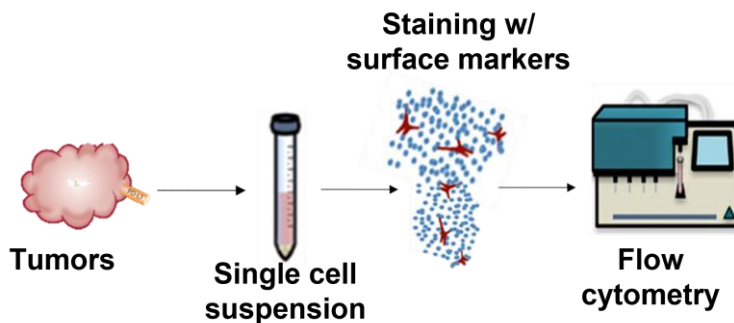


Figure 38: The schematic shows the methodology. Tumor tissues are harvested and digested with DNase I and Collagenase IV at 37°C for 1 h. The cells are filtered through a strainer, yielding a single cell suspension. After staining with various surface markers, the fluorescence intensity of the cells was measured by flow cytometry to identify the immune cells that reside in the tumor tissue.

Briefly, tumors were mechanically dissociated and then enzymatically degraded for 60 min at 37°C in HBSS buffer containing 5 mg/mL collagenase type I (Gibco, Grand Island, NY) and 0.2 mg/mL DNAase I (Roche, Indianapolis, IN) supplemented with 5% FBS. The solution was diluted in PBS and passed through $70\ \mu\text{m}$ strainers. Cells were then pelleted by centrifugation and resuspended in ACK red cell lysis buffer (Quality

Biological, Gaithersburg, MD) for 10 min, after which the solution was diluted with PBS. Cells were pelleted and counted by Trypan blue exclusion. One million cells were used for antibody staining. Zombie Live/Dead Aqua stain (Biolegend, San Diego, CA) was applied for 30 min. Cells were then blocked (5% rat serum, 5% mouse serum, 1% CD16/32 (clone 93, eBioscience, San Diego, CA)) in FACS buffer (PBS with 3% FBS and 30 μ M EDTA) for 30 min. Cells were then stained antibodies for 30 min, washed 3 times with PBS, and then fixed with 0.4% paraformaldehyde in PBS. Antibody clone and fluorophore information can be found in Appendix A.

5.3 Results and discussion

5.3.1 Depot vs Soluble ELP for (aPDL1-FN3)₄ fusion

5.3.1.1 (aPDL1-FN3)₄-ELP_{depot} is tuned for transition temperature below 37°C

We created two different ELP fusion protein therapeutics by fusing (aPDL1-FN3)₄ to two types of ELP: (1) soluble ELP (ELP_{soluble}) that remains soluble at body temperature (37°C) because its transition temperature at 100 μ M is around 50 °C. The ELP_{soluble} consists of 120 repeats of the VPGXG pentamer, where X is 90% Ala and 10% Val; (2) our optimized depot-forming ELP (ELP_{depot}) that forms a depot below body temperature (37°C), because its transition temperature at 100 μ M is 31°C. The ELP_{depot} consists of 120 repeats of the VPGXG pentamer, where X is 20% Ala and 80% Val. The (aPDL1-FN3)₄ was fused to the N- or C-terminus of the ELP (**Figure 39**).

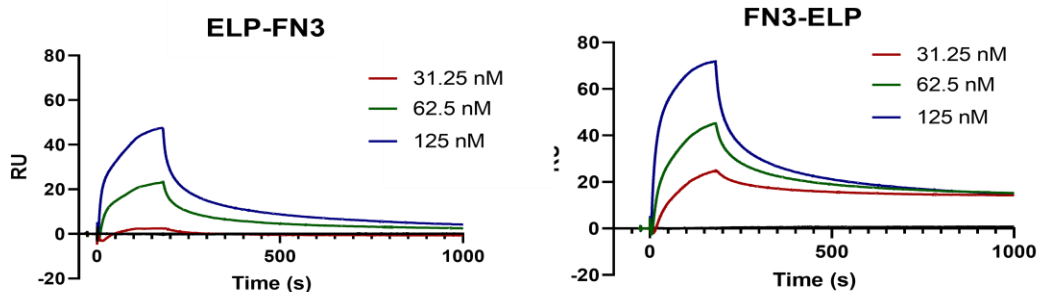


Figure 39: SPR determines the C-terminus fusion of ELP. FN3-ELP has a faster on-rate and slower off-rate than ELP-FN3.

Using SPR, we found that the ELP-(aPDL1-FN3)₄ fusion had a much slower on-rate and a faster off-rate than the oppositely oriented (aPDL1-FN3)₄-ELP fusion. We, therefore, decided to continue solely with the (aPDL1-FN3)₄-ELP fusion.

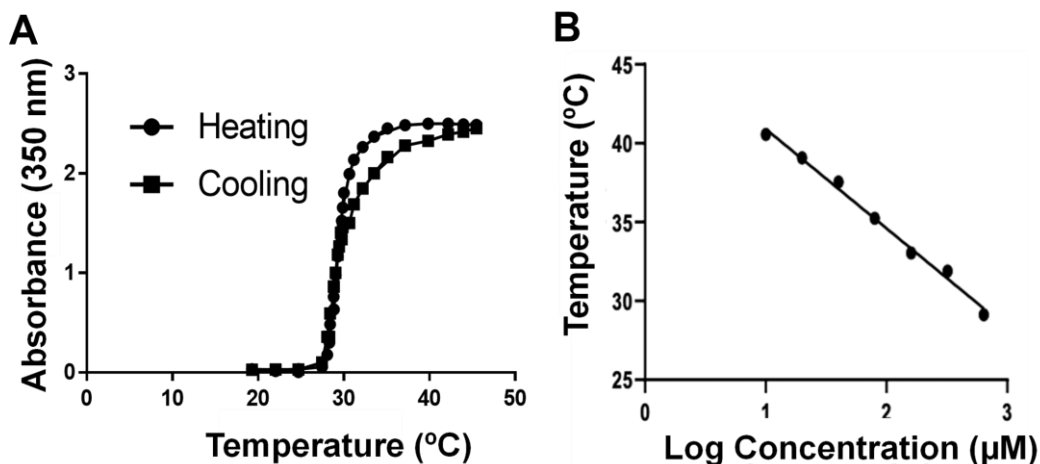


Figure 40: (aPDL1-FN3)₄-ELP_{depot} is tuned for Tt below 37 °C. (A) Optical turbidity as a function of temperature for a heating cycle (circles) and cooling cycle (squares). The Tt is 31 °C as defined by the inflection point of the curve. (B) Tt of (aPDL1-FN3)₄-ELP_{depot} as a function of concentration.

Both (aPDL1-FN3)₄-ELP_{depot} and (aPDL1-FN3)₄-ELP_{soluble} show reversible LCST phase transition behavior which enables them to rapidly transition from a soluble state

to an insoluble coacervate with the addition of heat, and there is no significant hysteresis between heating and cooling cycles (Figure 40A). The concentration-dependent Tt of (aPDL1-FN3)₄-ELP_{depot} varies from 28°C to 40°C, over the range of 6–500 μM, which spans the likely range of injection concentration (Figure 40B).

5.3.1.2 (aPDL1-FN3)₄-ELP_{depot} shows strong PDL1 antagonism

To examine how (aPDL1-FN3)₄-ELP_{depot} retains its PDL1 antagonism despite the fusion with ELP, we used a PDL1 blockade assay. The result shows that (aPDL1-FN3)₄-ELP_{depot} remains strong antagonists of both human and murine PDL1, with an IC₅₀ of 250 pM, close to 140 pM IC₅₀ of anti-PDL1 antibody controls (Figure 41).

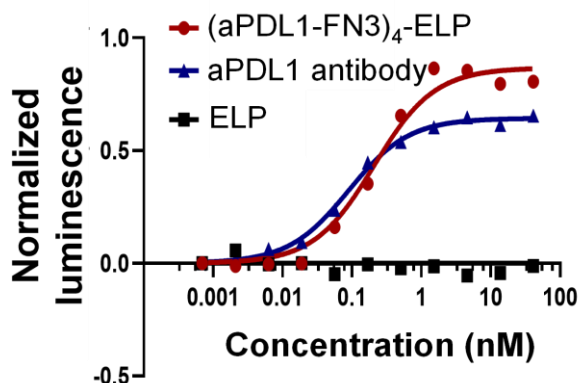


Figure 41: PDL1 blockade assay shows that (aPDL1-FN3)₄-ELP_{depot} antagonizes PDL1 signaling, with an IC₅₀ of 250 pM.

5.3.1.3 (aPDL1-FN3)₄-ELP_{soluble} shows better *in vivo* tumor efficacy than (aPDL1-FN3)₄-ELP_{depot} at their equimolar doses

With both (aPDL1-FN3)₄-ELP_{depot} and (aPDL1-FN3)₄-ELP_{soluble} constructs, we studied *in vivo* efficacy to determine whether a depot formulation has advantages for

tumor regression efficacy. Because PDL1 antagonist-based immunotherapy necessitates intact *in vivo* immunity, we chose to utilize a CT26 syngeneic colorectal cancer model in Balb/c mice. On day 0, mice were subcutaneously (*s.c.*) injected in the right flank with 10^5 CT26 cells. When tumor volume reached 80 - 100mm³, mice were injected *s.c.* with (aPDL1-FN3)₄-ELP_{depot} or (aPDL1-FN3)₄-ELP_{soluble} at equimolar doses or with vehicle control (PBS). From the tumor growth curves and survival rates, (aPDL1-FN3)₄-ELP_{soluble} shows better *in vivo* tumor efficacy than (aPDL1-FN3)₄-ELP_{depot} (p<0.05; **Figure 42A** and **42B**).

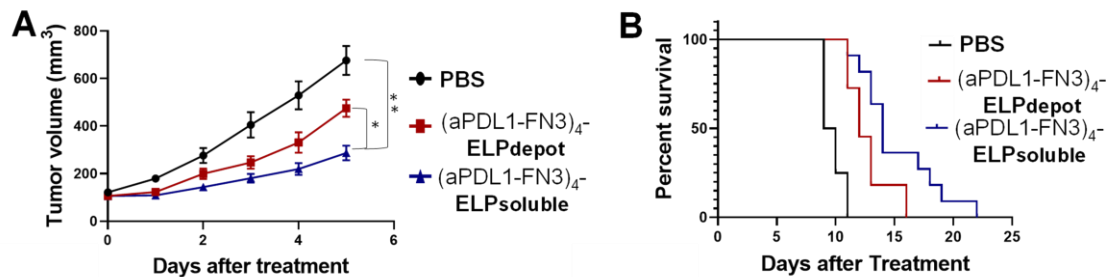


Figure 42: *In vivo* anti-cancer efficacy in a CT26 syngeneic mouse model. 10^5 of CT26 colon cancer cells were implanted *s.c.* in Balb/c mice, and tumors were allowed to grow to 80~100 mm³. Mice were then treated (day 0) *s.c.* with PBS, (aPDL1-FN3)₄-ELP_{soluble} or (aPDL1-FN3)₄-ELP_{depot} (n = 8–10 mice). (A) The primary tumor growth curve and (B) survival plot indicate tumor growth inhibition for mice one time treated with the fusion protein. With the same administration route, (aPDL1-FN3)₄-ELP_{soluble} shows better efficacy than (aPDL1-FN3)₄-ELP_{depot} (p<0.05). Data and error bars represent mean ± SEM. *p<0.05, **p<0.005

Next, to investigate if the localized delivery of protein therapeutics has advantages over systemic delivery, we injected (aPDL1-FN3)₄-ELP_{depot} intratumorally (*i.t.*) in the same mice model. When the tumor volume reached 80 - 100mm³, mice were

injected with either (aPDL1-FN3)₄-ELP_{depot} (*s.c.* or *i.t.*) or (aPDL1-FN3)₄-ELP_{soluble} (*s.c.* or intraperitoneally (*i.p.*)) at equimolar doses. To maximize their therapeutic efficacy, we treated each drug three times, three days apart. This frequency of drug injection was determined based on the previous tumor growth curve; after a single injection of drug (day 0), tumor growth grew again 4 days later. With multiple injections and different delivery formats, the systemic delivery of (aPDL1-FN3)₄-ELP_{soluble} shows better efficacy than the localized and systemic delivery of (aPDL1-FN3)₄-ELP_{depot} (**Figure 43A and 43B**). We, therefore, decided to continue solely with the (aPDL1-FN3)₄-ELP_{soluble} fusion, and its term is referred to (aPDL1-FN3)₄-ELP. Also, we decided to use *i.p.* injection for the preclinical study to match the administration routes of anti-PDL1 antibodies, enabling us to directly compare *in vivo* activities between (aPDL1-FN3)₄-ELP and anti-PDL1 antibodies.

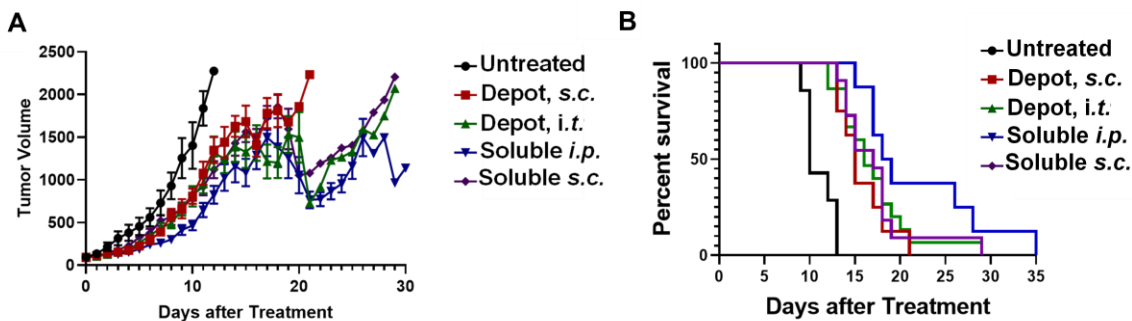


Figure 43: *In vivo* efficacy with three injections in CT26 model. Mice are treated 3 times 3 days apart (day 0, 3, and 6) with one of the following: 1) *s.c.* (aPDL1-FN3)₄-ELP_{soluble}; 2) *i.p.* (aPDL1-FN3)₄-ELP_{soluble}; 3) *s.c.* (aPDL1-FN3)₄-ELP_{depot}; and 4) *i.t.* (aPDL1-FN3)₄-ELP_{depot}. The (aPDL1-FN3)₄-ELP_{soluble} shows the best efficacy among these groups. (A) Primary tumor growth curve and (B) survival plot showed significant tumor growth inhibition for mice 3 times treated with (aPDL1-FN3)₄-ELP.

Tumor growth curves were analyzed by two-way ANOVA and Tukey's test and survival data by log-rank test. Data and error bars represent mean \pm SEM.

5.3.2 Qualitative characterization with gel electrophoresis

To create an experimental control that does not possess PDL1-binding for our protein therapeutics, (NonsenseFN3)₄-ELP was synthesized. This scaffold has the same ELP with (aPDL1-FN3)₄-ELP, whose sequences are 120 repeats of VPGXG where X is comprised of 90% alanine and 10% valine. However, the (NonsenseFN3)₄ domain does not have PDL1-binding because its BC, DE, and FG loop regions are changed to (Gly_nSer)_n linkers. Thus, (NonsenseFN3)₄-ELP is a perfect scaffold control for us to examine the effect of PDL1-binding on *in vitro* and *in vivo* characterization.

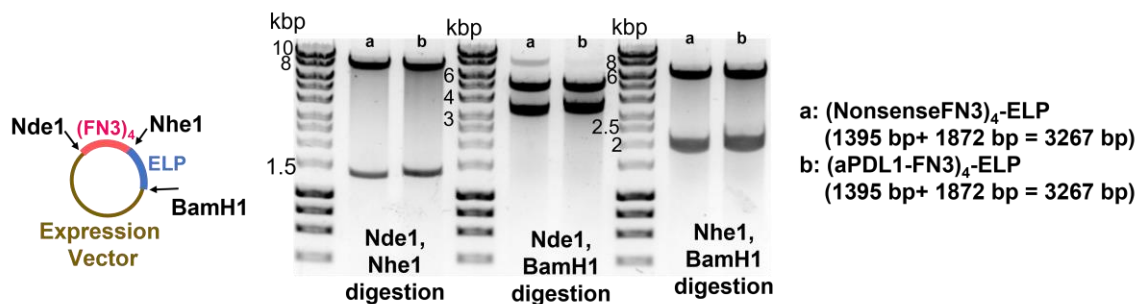


Figure 44: Characterization of fusion proteins using an agarose gel. DNA agarose gel of restriction digests confirms the successful insertion of (Nonbinding)₄-ELP and (aPDL1-FN3)₄-ELP genes into a pET-24 expression vector.

We used PRe-RDL to produce both (NonsenseFN3)₄-ELP and (aPDL1-FN3)₄-ELP (187). To confirm their genetic fusion using agarose gel, we utilized three restriction enzyme sites embedding in their sequences: Nde1 at the 5' of FN3 gene fragments, Nhe1 at the junction between FN3 and ELP fragments, and BamH1 at the C' of ELP gene

fragments. An agarose gel of double-digested expression vectors confirmed the successful insertion of constructs for (NonsenseFN3)₄-ELP and (aPDL1-FN3)₄-ELP into a pET 24 expression vector (**Figure 44**).

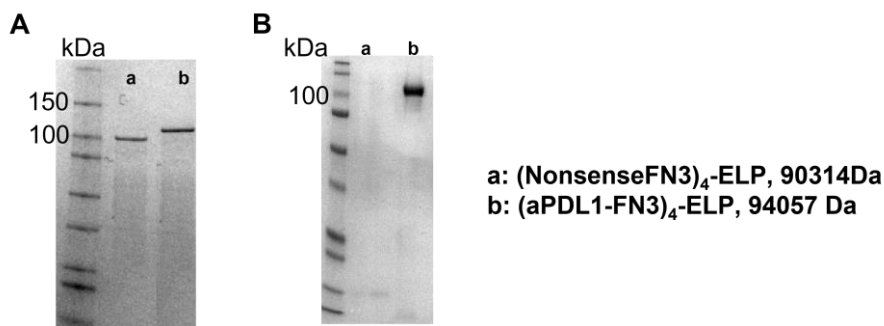


Figure 45: Characterization of fusion proteins using SDS-PAGE and WB. (A) SDS-PAGE confirms the correct size of fusion proteins. The calculated sizes are shown. (B) Western blot of native gels showed that (aPDL1-FN3)₄-ELP are detected by PDL1 protein. This confirmed that (aPDL1-FN3)₄-ELP binds PDL1 whereas (NonsenseFN3)₄-ELP does not.

We used the *E. coli* expression system to express (NonsenseFN3)₄-ELP and (aPDL1-FN3)₄-ELP. After bacterial cell expression, we purified both (NonsenseFN3)₄-ELP and (aPDL1-FN3)₄-ELP proteins using ITC. Then, the purity of these proteins was confirmed by SDS-PAGE (**Figure 45A**). Also, to ensure only (aPDL1-FN3)₄-ELP has PDL1-binding, we utilize a western blot method. Briefly, purified proteins were separated in the native gel electrophoresis system. Then, the gel was transferred to a membrane, incubated at room temperature with blocking buffer for 15 mins, with Fc-PDL1 for 1 hour, and with AP-conjugated anti-Fc antibody for 1 hour. After washing 3 times using 1X PBS with 0.1% tween 20, NBT/BCIP solution was added to the membrane, resulting in an insoluble, purple-colored band indicating the binding affinity

to PDL1. Using this system, we successfully confirmed that (aPDL1-FN3)₄-ELP has PDL1-binding while (NonsenseFN3)₄-ELP does not (Figure 45B).

5.3.3 Biophysical characterization of (aPDL1-FN3)₄-ELP

With the purified (aPDL1-FN3)₄-ELP protein, we characterized its biophysical properties: 1) hydrodynamic radius (R_h) was measured by DLS to confirm if ELP fusion causes any significant aggregation or micelles formation; 2) the purity was confirmed by analytical SEC-HPLC; 3) reversible phase transition behavior was studied using UV/vis spectrophotometry. Since a phase transition behavior is temperature-dependent and exhibits a visual change in its turbidity, the optical density of the protein sample is measured at the wavelength of 350 nm as a function of solution temperature.

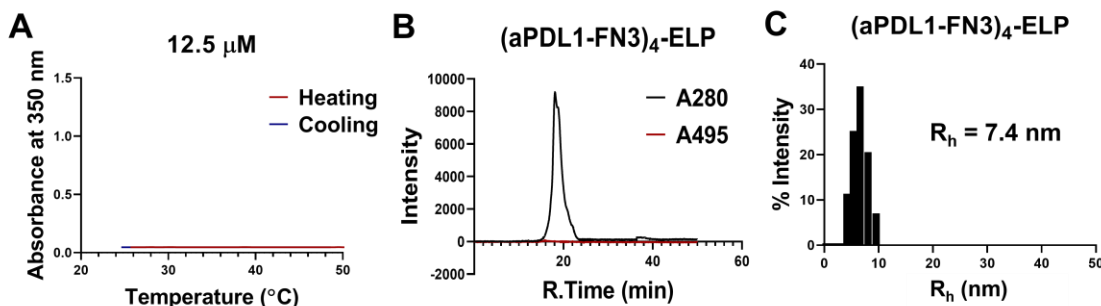


Figure 46: Biophysical characterization of (aPDL1-FN3)₄-ELP fusion protein. (A) UV/vis spectrophotometry shows that (aPDL1-FN3)₄-ELP remains soluble at body temperature. (B) SEC-HPLC shows that (aPDL1-FN3)₄-ELP is highly pure. (C) DLS shows that (aPDL1-FN3)₄-ELP is a unimer without micelles formation or aggregation.

Figure 46 illustrates the biophysical characterization of the (aPDL1-FN3)₄-ELP construct. Since this construct has soluble ELP, UV/vis spectrophotometry at 350 nm showed that (aPDL1-FN3)₄-ELP does not show LCST behavior at body temperature (37

°C) at a concentration of 12.5 μM that is used for *in vivo* injection in animal experiments. SEC-HPLC showed that purified (aPDL1-FN3)₄-ELP is >95% pure. Finally, DLS showed that (aPDL1-FN3)₄-ELP is a unimer with an R_h of 7.4 nm and that no larger aggregates were observed.

5.3.4 Characterization of the binding kinetics of (aPDL1-FN3)₄-ELP

With the purified (aPDL1-FN3)₄-ELP protein, we utilized SPR to analyze its specific binding to PDL1 as well as to characterize its binding kinetics to human and murine PDL1. The data suggest that (aPDL1-FN3)₄-ELP exhibits the ability to bind to human PDL1 and murine PDL1 and does not bind to human PD1 and human PDL2 (Figure 47).

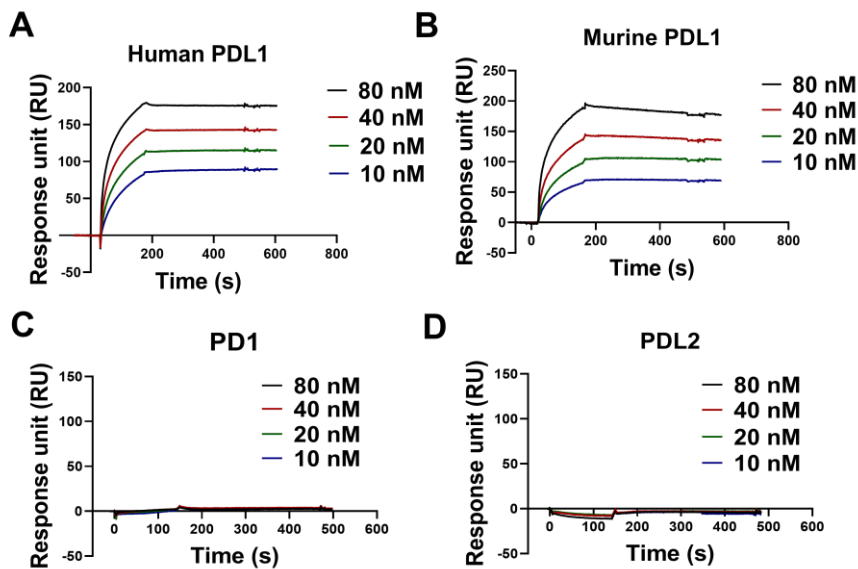


Figure 47: Characterization of the specific PDL1 binding kinetics of (aPDL1-FN3)₄-ELP using SPR. The SPR sensorgrams of (aPDL1-FN3)₄-ELP showing binding to human PDL1 and murine PDL1, and lack of binding to human PD1 and human PDL2.

Also, the binding kinetics of (aPDL1-FN3)₄-ELP is 136 pM for human PDL1 and 225 pM for murine PDL1. This result indicates that the fusion with ELP successfully endows the LCST behavior of ELP without significantly changing the properties of (aPDL1-FN3)₄ protein. Despite the ELP fusion, (aPDL1-FN3)₄-ELP retains its specific PDL1 binding.

5.3.5 Characterization after fluorescence conjugation

Next, we used the primary amine group on the N-terminus of (aPDL1-FN3)₄-ELP as the site of conjugation for Alexafluor488 dyes. We utilized the identical method and conditions for the conjugation of aPDL1-FN3 oligomers as described in the previous chapter. Using this condition and method, we successfully conjugated the (aPDL1-FN3)₄-ELP proteins with Alexafluor488 dyes. We confirmed the successful reaction and purity of our conjugated proteins using SDS-PAGE as well as size exclusion chromatography (SEC) (Figure 48A and 48B).

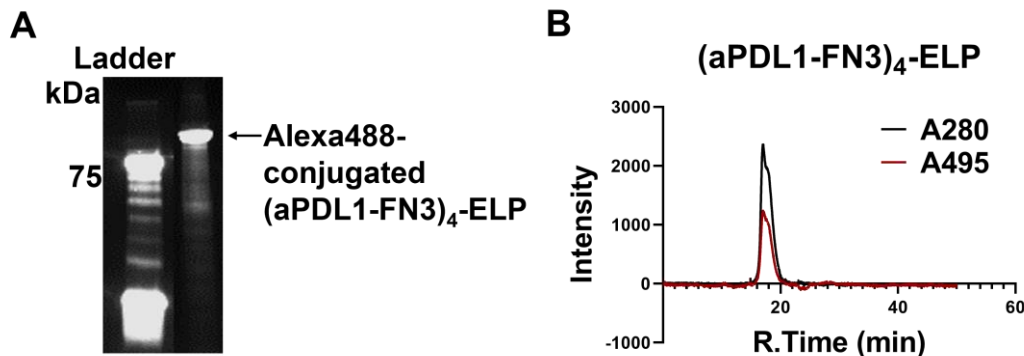


Figure 48: Successful conjugation of (aPDL1-FN3)₄-ELP with Alexafluor488. (A) Fluorescence image of SDS-PAGE shows (aPDL1-FN3)₄-ELP labeled with Alexafluor488 fluorescent dye. (B) SEC-HPLC of (aPDL1-FN3)₄-ELP shows

colocalized peaks with absorbance at 280 nm (protein) and 495 nm (fluorescent dye), indicating the protein was successfully labeled with Alexafluor488.

In SEC-HPLC, due to the characteristic absorbance of Alexafluor488 dyes at 495 nm for its maximum excitation and that of protein at 280 nm, their co-localized peaks indicate that (aPDL1-FN3)₄-ELP construct is successfully conjugated with Alexafluor488 dyes.

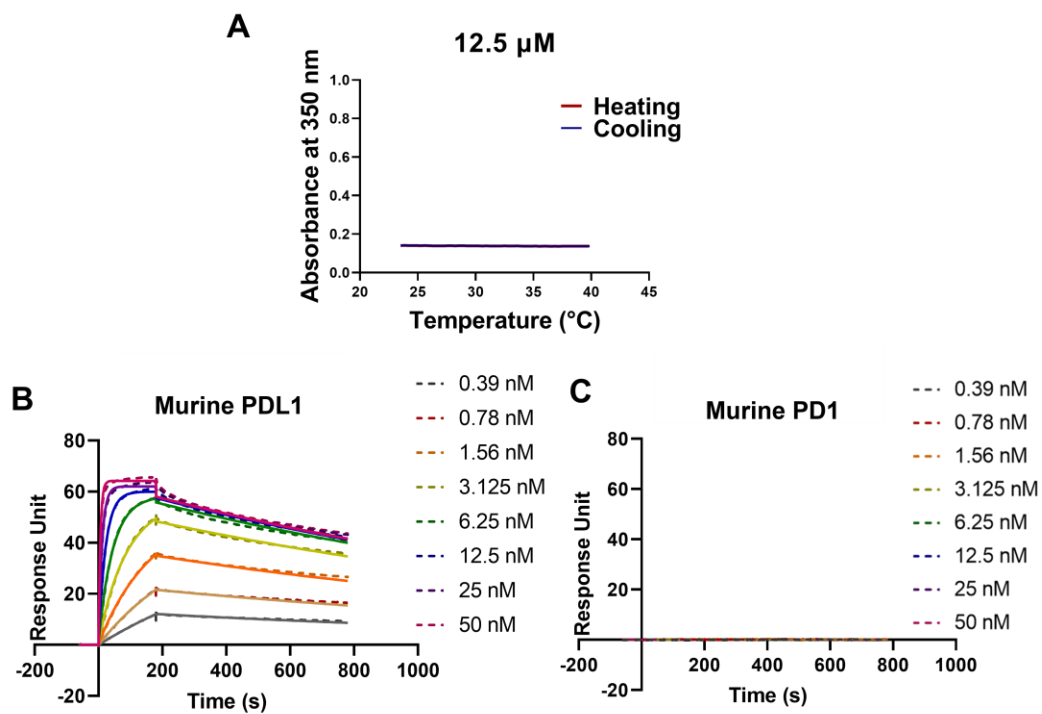


Figure 49: Biophysical characterization of (aPDL1-FN3)₄-ELP conjugated with Alexafluor488. (A) UV-vis absorbance at 350 nm of 12.5 μM solution of (aPDL1-FN3)₄-ELP in 1X PBS buffer. The baseline absorbance shows that the fusion protein does not undergo an LCST phase transition between 20-40 $^{\circ}\text{C}$, suggesting that it will remain soluble upon *in vivo* concentration at this injection concentration. (B-C) SPR sensorgrams of fluorescence-conjugated (aPDL1-FN3)₄-ELP binding to murine PDL1 (B) and murine PD1 (C). The SPR data show that (aPDL1-FN3)₄-ELP binds strongly to murine PDL1 but does not bind to murine PD1.

We also confirmed that the conjugation of Alexafluor488 dyes did not significantly change the biophysical properties of (aPDL1-FN3)₄-ELP using UV/vis spectrophotometry (Figure 49A) and SPR (Figure 49B and 49C). After the conjugation, (aPDL1-FN3)₄-ELP maintains its ELP properties. Specifically, (aPDL1-FN3)₄-ELP remains soluble at a concentration of 12.5 μM that is used for *in vivo* injection in animal experiments. Also, Alexafluor488-labeled (aPDL1-FN3)₄-ELP retains (aPDL1-FN3)₄ properties: strong and specific PDL1 binding.

5.3.6 Characterization of the potency of (aPDL1-FN3)₄-ELP

To characterize the PDL1 antagonism of (aPDL1-FN3)₄-ELP, we used two assays: 1) *in vitro* PD1/PDL1 blockade assay as described in the previous chapter; 2) AlphaLISA PD1/PDL1 blockade assay.

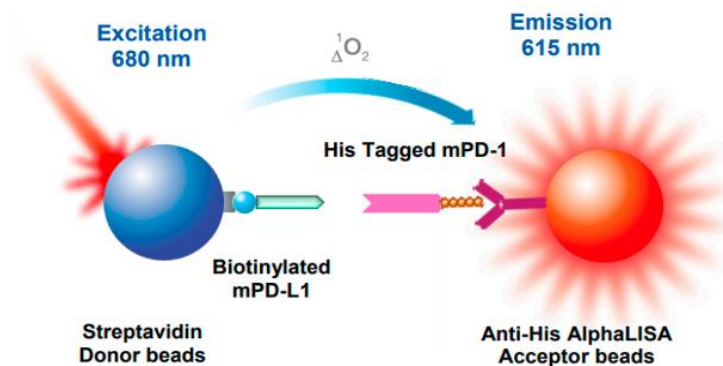


Figure 50: Schematic showing the mechanism of AlphaLISA assay for mouse PDL1 antagonism. While a biotinylated mouse PDL1 is captured by streptavidin-coated donor beads, his-tagged mouse PD1 is captured by anti-His acceptor beads. When mouse PD1 and mouse PDL1 bind together, the donor beads excite acceptor beads, releasing a light emission at 615 nm. However, when (aPDL1-FN3)₄-ELP antagonizes mouse PDL1, this energy transfer is prohibited without releasing light.

We specifically chose AlphaLISA because it allows us to characterize the potency of (aPDL1-FN3)₄-ELP against mouse PDL1. In the AlphaLISA mouse PDL1 assay (**Figure 50**), while a biotinylated mouse PDL1 binds to streptavidin-coated Alpha donor beads, his-tagged mouse PD1 is bound by anti-6X-His AlphaLISA acceptor beads.

When PD1 binds to PDL1, donor beads and acceptor beads come into proximity to each other. The excitation of the Donor beads releases singlet oxygen molecules, promoting a cascade of energy transfer in the acceptor beads. This transfer results in light emission at 615 nm. Thus, once the PDL1 antagonist exists and antagonizes the interaction between PD1 and PDL1, this energy transfer is prohibited, and no light is released at 615nm.

Using the serial dilution of (aPDL1-FN3)₄-ELP and (NonsenseFN3)₄-ELP proteins, we characterized their potency compared to those of anti-PDL1 antibodies. According to the results of this assay (**Figure 51**), while (NonsenseFN3)₄-ELP did not show any PDL1 antagonism, (aPDL1-FN3)₄-ELP successfully antagonized the interaction between PD1 and PDL1. This demonstrates the specific PDL1 binding and antagonism from the engineered loop regions of aPDL1-FN3. Also, the IC₅₀ of (aPDL1-FN3)₄-ELP is around 242 pM for mouse PDL1 and 506 pM for human PDL1. These values are competitive with those of anti-PDL1 antibodies whose IC₅₀ values are around 120-140 pM for mouse PDL1 and 227 pM for human PDL1.

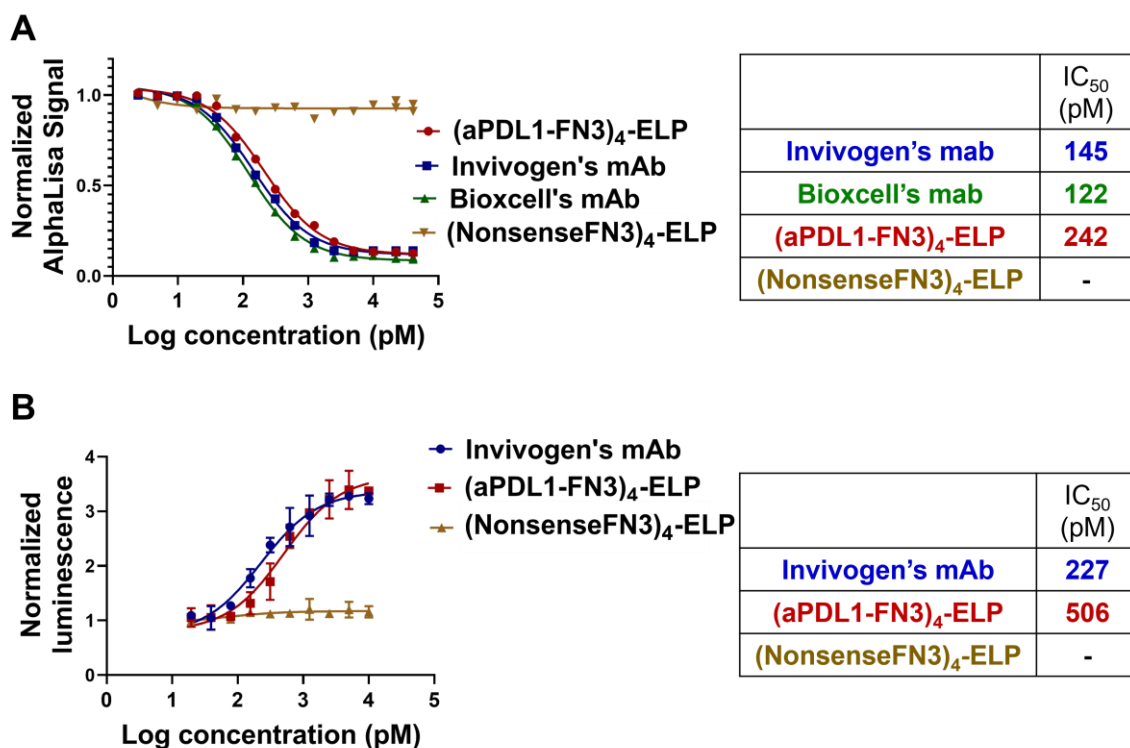


Figure 51: Characterization of IC₅₀ of (aPDL1-FN3)₄-ELP as compared to anti-PDL1 antibodies. The IC₅₀ values are quantified by a curve-fit of the dose-response curves in both (A) AlphaLISA and (B) *in vitro* PDL1 blockade assay and are listed in the adjacent table. While (NonsenseFN3)₄-ELP did not show any PDL1 antagonism, (aPDL1-FN3)₄-ELP showed similar picomolar IC₅₀ values with anti-PDL1 antibodies from Invivogen's and Bioxcell's.

We also performed AlphaLISA using the (aPDL1-FN3)₄-ELP conjugated with either iodine- or Alexafluor488- molecules (**Figure 52**). This study is to ensure that after conjugation, (aPDL1-FN3)₄-ELP maintains its strong mouse PDL1 antagonism before *in vivo* studies. We successfully confirmed that Alexafluor488-conjugated, iodine-conjugated versions retain their strong PDL1 antagonism as much as unconjugated (aPDL1-FN3)₄-ELP. The iodine-conjugated (aPDL1-FN3)₄-ELP has the lowest IC₅₀ of

around 2 nM because tyrosine residue used for the conjugation contributes to the binding pocket in the FG loop of aPDL1-FN3.

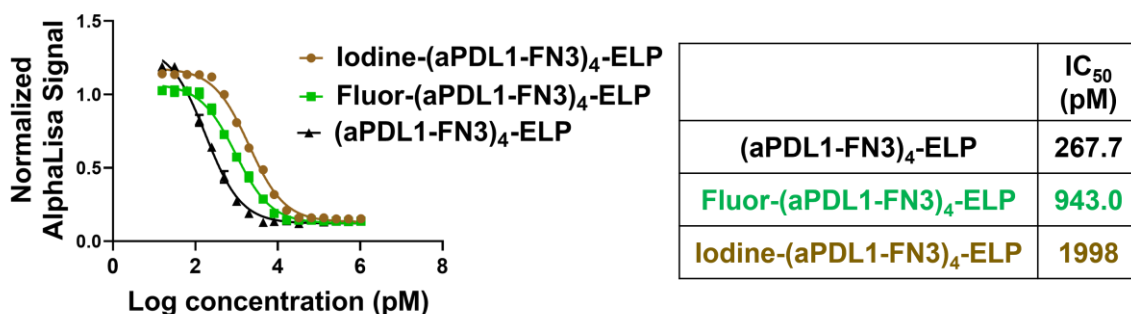


Figure 52: AlphaLISA for murine PDL1 binding showing the normalized AlphaLISA signal as a function of protein concentration of the Alexafluor488- conjugated, iodine-conjugated, and unconjugated (aPDL1-FN3)₄-ELP. The curves were fit to calculate the IC₅₀ for PDL1 antagonism, which are shown in the adjacent table.

5.3.7 *In vitro* quantifying specific PDL1-binding of (aPDL1-FN3)₄-ELP with flow cytometry

We next validated the *in vitro* PDL1-binding of (aPDL1-FN3)₄-ELP using four different cell lines: 1) genetically engineered Jurkat-PD1 cell lines that do not have any PDL1 expression. This cell line is useful to evaluate if (aPDL1-FN3)₄-ELP proteins exhibit any non-specific binding for PD1 receptors; 2) genetically engineered CHO-hPDL1 cell lines that stably express human PDL1 receptors on their cellular membranes. This cell line is very useful to validate the *in vitro* PDL1-binding of (aPDL1-FN3)₄-ELP and determine if (aPDL1-FN3)₄-ELP can saturate all PDL1 receptors at the cellular level because all cells express the PDL1 receptor; 3) CT26.WT colon cancer cell lines that are known for PDL1 expression and used for anti-PDL1 therapy in the preclinical model; 4)

MC38 colon cancer cell lines that are utilized the most for *in vivo* anti-PDL1 therapy. Using these two cancer cell lines, we can confirm the PDL1 expression levels of each and decide if these candidates are suitable for *in vivo* testing in the future.

For this study, we used the fluorescently labeled (aPDL1-FN3)₄-ELP and (NonsenseFN3)₄-ELP, incubated them with these four cell lines that have a range of PDL1 expression levels, and analyzed these cell populations for fluorescence by flow cytometry. First, (aPDL1-FN3)_n proteins and their ELP fusion proteins did not bind to Jurkat cells expressing PD1 (**Figure 53**). This indicates a lack of PD1 binding of aPDL1-FN3.

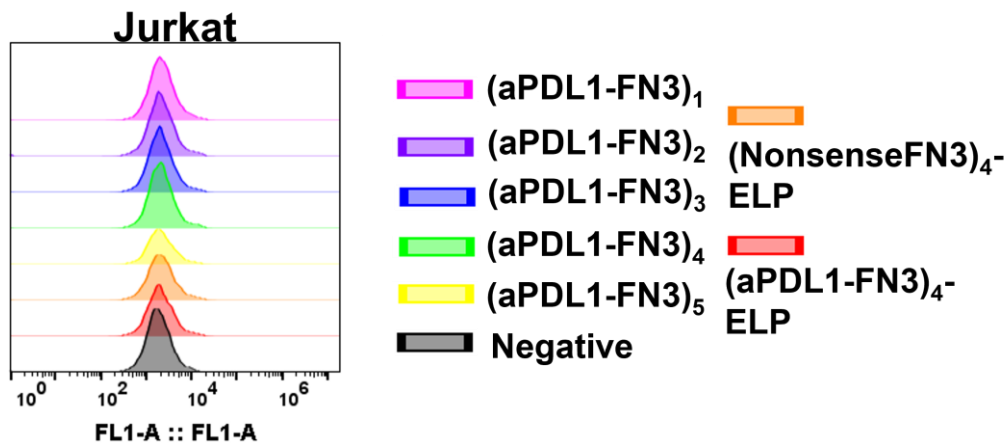


Figure 53: Flow cytometry data analysis using Jurkat/PD1 cells. Flow cytometry histograms of (aPDL1-FN3)_n proteins and their ELP fusion proteins to Jurkat cells that express PD1 show a lack of binding of the FN3 to PD1.

With CHO cells that stably express human PDL1 receptors, around 95% of (aPDL1-FN3)₄-ELP successfully bound to PDL1 on these cells, while (NonsenseFN3)₄-ELP did not bind to PDL1 (**Figure 54**). This result indicates that (aPDL1-FN3)₄-ELP

almost saturates PDL1 receptors due to their valency and potency, and their specific PDL1-binding is because of the aPDL1-FN3 domain, not the scaffold.

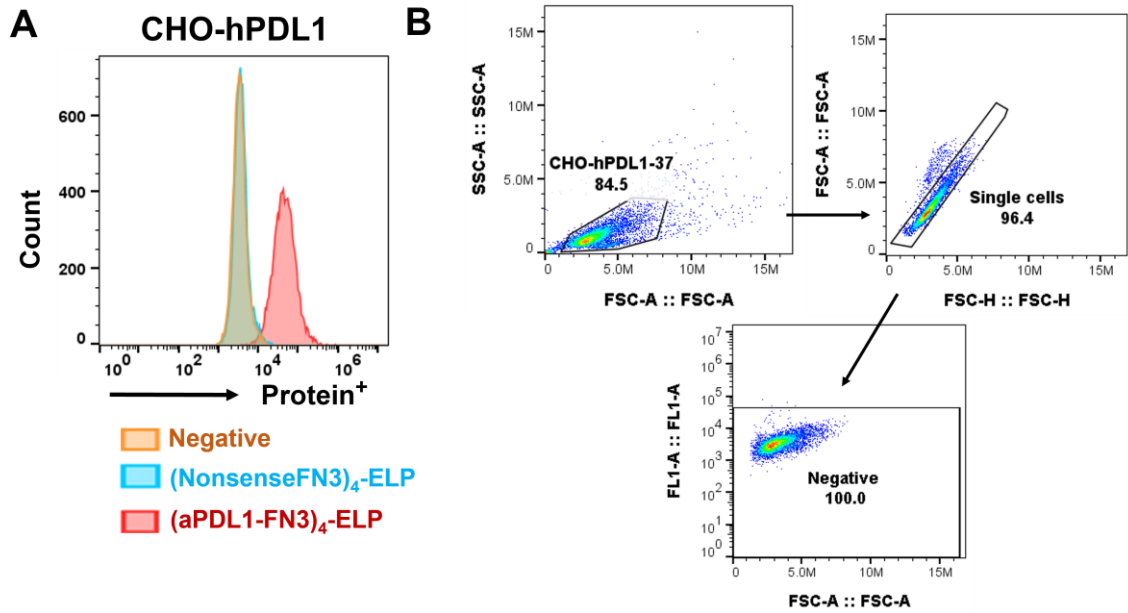


Figure 54: Flow cytometry data analysis using CHO-hPDL1 cells. (A) While (NonsenseFN3)₄-ELP protein does not bind to hPDL1 receptors on CHO cells, (aPDL1-FN3)₄-ELP binds, retaining their PDL1 binding after the fusion. (B) The gating strategy is used for the quantification of proteins bound to CHO cells that express hPDL1 (CHO-hPDL1). Each gating strategy is referred to as CHO cells, followed by single cells and fluorescence population. The percentage of cells for each gating is indicated in the panels. First, 84.5% of cells are chosen as live CHO cells. Then, 96.4 % of single cells are selected. In this sample, 100% of cells exhibit no fluorescence.

With CT26.WT and MC38 cancer cell lines, we quantified the PDL1 expression level using the binding capability of fluorescently conjugated (aPDL1-FN3)₄-ELP (Figure 55). In CT26.WT cells, around 62% cells were bound by (aPDL1-FN3)₄-ELP while in MC38 cells, approximately 58% cells were bound by (aPDL1-FN3)₄-ELP. Because of stable expression, CHO-hPDL1 cells exhibit a significantly greater fraction of cells

number of percentages. CHO-hPDL1 cells have a significantly greater fraction around 95%— that are bound by (aPDL1-FN3)₄-ELP than CT26.WT or MC38 cells (*p<0.05, **p<0.005, one-way ANOVA test).

5.3.8 *In vitro* characterization of 3D tumor spheroids uptake and penetration of (aPDL1-FN3)₄-ELP

To evaluate the tumor penetration and uptake of (aPDL1-FN3)₄-ELP as compared to those of anti-PDL1 antibodies, we utilized CT26.WT-based tumor 3D spheroid models as previously described. After seeding CT26.WT cells, cell aggregates were maintained for 10 days to allow them to assemble into spheroids governing cell-ECM interactions. Then, using the spheroids with a diameter larger than around 200 μm, Alexafluor488-conjugated-(aPDL1-FN3)₄-ELP, (NonsenseFN3)₄-ELP, and anti-PDL1 antibodies were incubated for the final concentration of 1 μM for 1 hour at 37 °C. Simultaneously, Hoechst solution was also incubated for nucleus staining. After washing, spheroids were placed in a 35 mm glass bottom petri dish and imaged by Andor dragonfly spinning disk confocal microscopy. The processed Z-stack images are illustrated in the following figures: (NonsenseFN3)₄-ELP (**Figure 56**), (aPDL1-FN3)₄-ELP (**Figure 57**), Bioxcell's anti-PDL1 antibody (**Figure 58**), and Invivogen's anti-PDL1 antibody (**Figure 59**).

According to the montage of Z-stack images, (NonsenseFN3)₄-ELP did not have significant binding to CT26 spheroids, while (aPDL1-FN3)₄-ELP exhibited PDL1-targeted tumor uptake and penetration. Compared to the images of anti-PDL1 antibodies, (aPDL1-FN3)₄-ELP has a more uniform distribution inside the spheroids and deeper penetration. However, antibodies remain in more peripheral areas of spheroids.

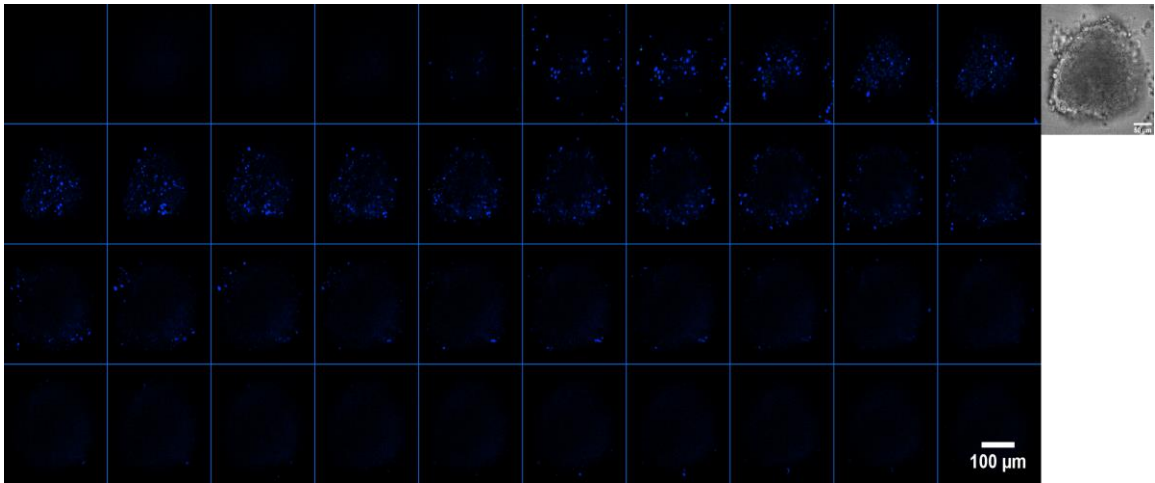


Figure 56: Montage of Z-stack images of (NonsenseFN3)₄-ELP using CT26 spheroids. The DIC image is shown in the top right. Hoechst is labeled blue, and protein is labeled green. The scale bar is shown on the bottom right.

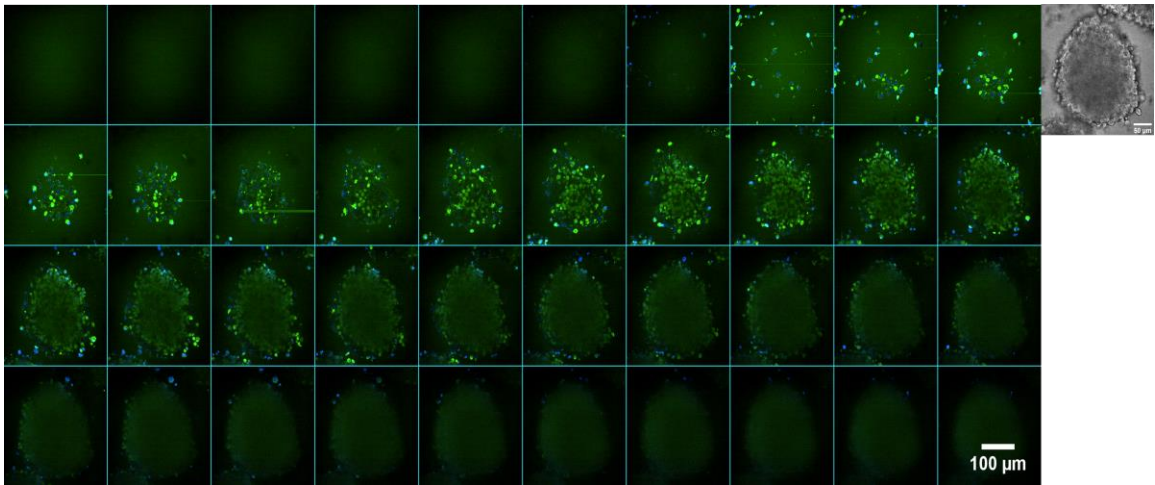


Figure 57: Montage of Z-stack images of (aPDL1-FN3)₄-ELP using CT26 spheroids. The DIC image is shown in the top right. Hoechst is labeled blue, and protein is labeled green. The scale bar is shown on the bottom right.

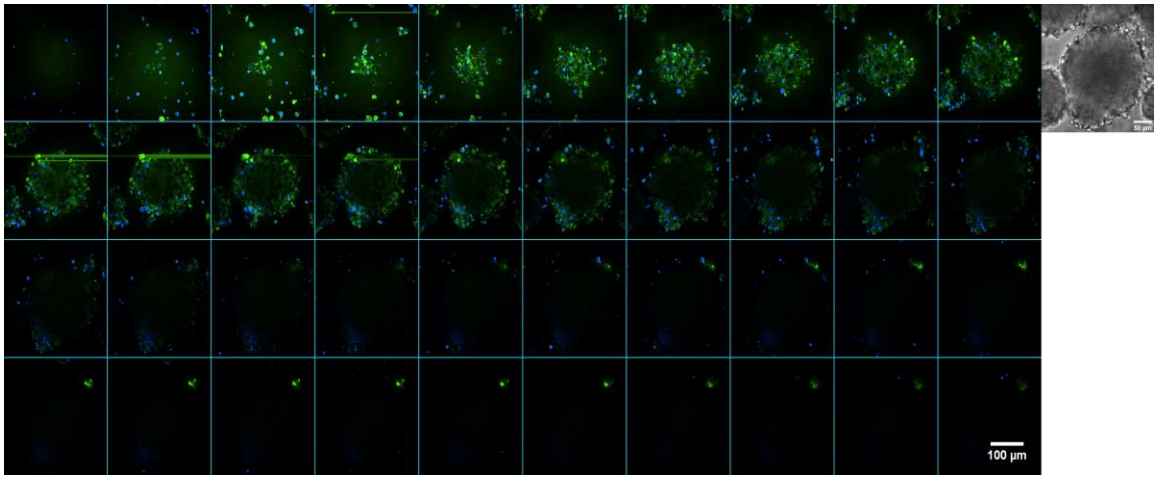


Figure 58: Montage of Z-stack images of Bioxcell's anti-PDL1 antibody using CT26 spheroids. The DIC image is shown in the top right. Hoechst is labeled blue, and protein is labeled green. The scale bar is shown on the bottom right.

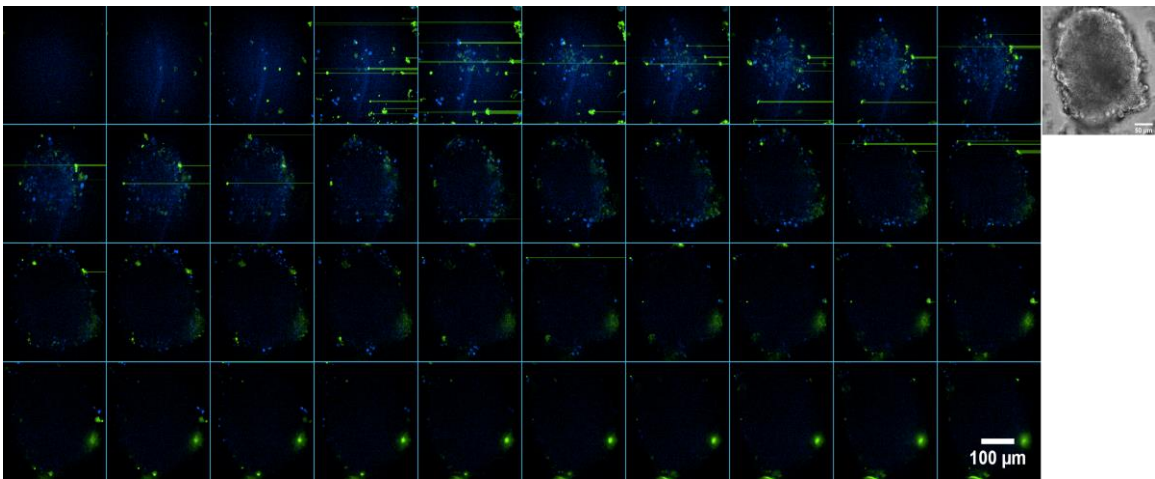


Figure 59: Montage of Z-stack images of Invivogen's anti-PDL1 antibody using CT26 spheroids. The DIC image is shown in the top right. Hoechst is labeled blue, and protein is labeled green. The scale bar is shown on the bottom right.

Based on these images, we also calculated the penetration depth for each sample (Figure 60). While Invivogen's and Bioxcell's anti-PDL1 antibodies have an average of 33.5 μm or 20.8 μm for the depth of penetration respectively, (aPDL1-FN3)₄-ELP exhibits

62.4 μm . This result indicates that $(\text{aPDL1-FN3})_4\text{-ELP}$ penetrates 3D tumor spheroids around 2-3 significantly deeper than anti-PDL1 antibodies. This better penetration and tumor uptake could be because of the smaller size, tetravalency, and modularity of $(\text{aPDL1-FN3})_4\text{-ELP}$ protein therapeutics.

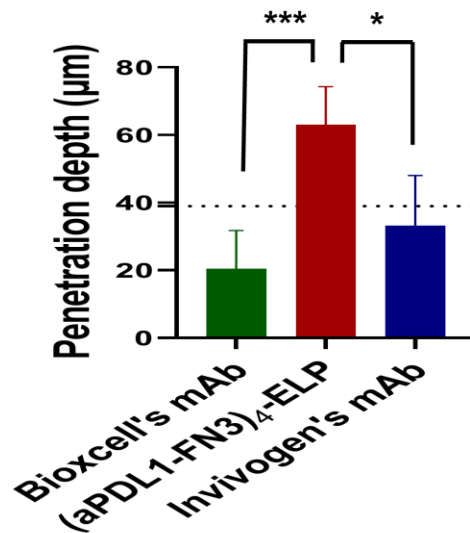


Figure 60: Tumor penetration depth for $(\text{aPDL1-FN3})_4\text{-ELP}$ and anti-PDL1 antibodies. $(\text{aPDL1-FN3})_4\text{-ELP}$ exhibits 2-3 times deeper penetration of tumor than antibodies using CT26 spheroids (* $p < 0.05$, * $p < 0.005$, one-way ANOVA and Tukey's test).**

5.3.9 Pharmacokinetics of $(\text{aPDL1-FN3})_4\text{-ELP}$

We studied the effect of the genetic fusion of ELP on half-life and cumulative plasma exposure after either *i.p.* or intravenous (*i.v.*) administrations in Balb/c mice. We performed a single *i.p.* injection of either fluorescently labeled $(\text{aPDL1-FN3})_4$ or $(\text{aPDL1-FN3})_4\text{-ELP}$, or a single *i.v.* injection of fluorescently labeled $(\text{aPDL1-FN3})_4\text{-ELP}$. At time points from 15 seconds to 120 hours, we collected blood from the tail veins of mice and measured fluorescence intensity in plasma. The concentration of $(\text{aPDL1-FN3})_4$ and

(aPDL1-FN3)₄-ELP in plasma at various time points were then calculated using a standard curve that relates fluorescence intensity to their protein concentration. Then, the concentration of proteins in plasma was plotted as a function of time (Figure 61).

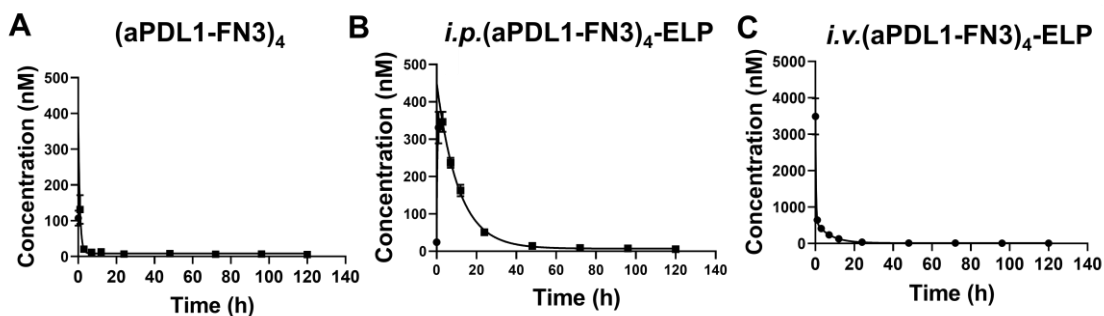


Figure 61: Pharmacokinetics show circulating proteins in plasma as a function of time following a single injection of (A) *i.p.* (aPDL1-FN3)₄, (B) *i.p.* (aPDL1-FN3)₄-ELP, and (C) *i.v.* (aPDL1-FN3)₄-ELP.

To determine the PK parameters shown in Table 12, we used the PK solver program (192). The *i.p.* data were fit to a non-compartmental model while the *i.v.* data were fit to a two-compartment model. Fusion to an ELP increased the protein's elimination half-life from 1.6 hours to approximately 11 hours, providing a 6-fold improvement in the serum half-life of the anti-PDL1 drug. This prolonged the effectiveness of the drugs in plasma. According to preclinical data of anti-PDL1 antibodies (193), the minimum effective concentration of antibodies for their therapeutic effects is 40 nM. Above this minimum effective concentration, the fusion with ELP maintained effectiveness in plasma for 28.5h, compared to 2.2 h for the (aPDL1-FN3)₄ alone. The fusion with ELP also prevented burst release and promoted slow release into

the systemic circulation, as evidenced by the 2.6-fold lower C_{\max} value and 2.8-fold longer t_{\max} value — defined as the time it takes for a drug to reach its C_{\max} . This release profile is beneficial for drug delivery as it prevents wasted drugs, better maintains plasma drug concentration within the therapeutic window, and minimizes side effects. This minimization in burst release is also reflected in the total cumulative blood exposure of the drug, measured by the area under the plasma concentration versus time curve (AUC). The 5730 nM·h AUC of (aPDL1-FN3)₄-ELP is 4.8 times greater than the 1193 nM·h AUC of (aPDL1-FN3)₄. The bioavailability of *i.p.* injection for (aPDL1-FN3)₄-ELP was 76.5%. Using this bioavailability (F), we calculated the clearance of the protein from systemic circulation (CL) with the formula, dose · F/AUC. The CL of (aPDL1-FN3)₄ is 4.30 ml/h/kg while the CL of (aPDL1-FN3)₄-ELP is 0.895 ml/h/kg, which is 48-fold slower. All these parameters show the significant enhancement of pharmacokinetics due to the fusion with ELP.

Table 12: Pharmacokinetics parameters

	<i>i.p.</i> (aPDL1-FN3) ₄	<i>i.p.</i> (aPDL1-FN3) ₄ -ELP	<i>i.v.</i> (aPDL1-FN3) ₄ -ELP
$t_{\text{elim, 1/2}}$	1.598 ± 0.263 h	10.58 ± 0.91 h	5.09 ± 0.13 h
$t_{>40\text{nM}}$	2.182 ± 0.352 h	28.5 ± 2.3 h	21.7 ± 2.1 h
C_{max}	131.7 ± 12.41 nM	346.6 ± 29.19 nM	3527 ± 155.6 nM
t_{max}	1.07 ± 0.32 h	3.048 ± 2.616 h	~ 0 h
C_0	106.8±24.90 nM	20.37 ± 29.67 nM	3527 ± 155.6 nM
CL	4.30 ml/h/kg	0.895 ml/h/kg	8.943 ml/h/kg
AUC _{inf}	1193 ± 138 nM·h	5730 ± 344 nM·h	7492 ± 642 nM·h
F (%)	-	76.5 %	100 %

To compare the pharmacokinetics of (aPDL1-FN3)₄-ELP with those of anti-PDL1 antibodies, we *i.p.* administered fluorescently conjugated (aPDL1-FN3)₄-ELP or anti-PDL1 antibodies in Balb/c mice. After a single injection of an equimolar dose of 67 nmol/kg, blood samples were collected at various time points between 15 seconds to 7 days. Using a standard curve, the concentration of protein in plasma was plotted as a function of time.

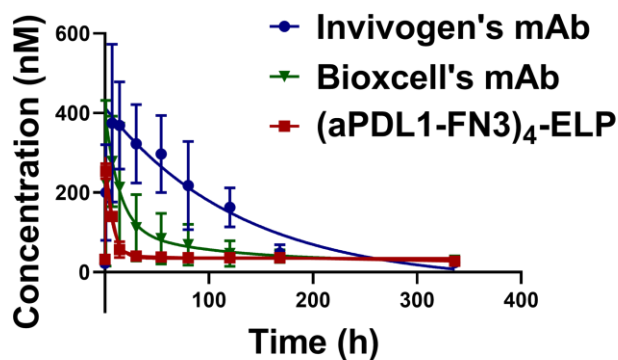


Figure 62: Pharmacokinetics of (aPDL1-FN3)₄-ELP and anti-PDL1 antibodies. The protein concentration in plasma was plotted as a function of time following a single *i.p.* injection of (aPDL1-FN3)₄-ELP, Invivogen's anti-PDL1 antibodies, and Bioxcell's anti-PDL1 antibodies.

After the data was fit to a non-compartmental model, we quantified the PK parameters of (aPDL1-FN3)₄-ELP as well as anti-PDL1 antibodies shown in **Table 13**. Although (aPDL1-FN3)₄-ELP increases the protein's elimination half-life due to the fusion with ELP, anti-PDL1 antibodies exhibit a much longer serum half-life: Bioxcell's anti-PDL1 antibodies show around 7 times that of (aPDL1-FN3)₄-ELP and Invivogen's anti-PDL1 antibodies show around 10 times that of (aPDL1-FN3)₄-ELP. Especially, IgG1-

based Invivogen's mAb has around 4-5 days of serum half-life while IgG2-based Bioxcell's mAb has around 3 days of serum half-life. We believe that this difference is mainly due to the different types of isotypes. We believe that this difference is mainly due to the different types of isotypes contributing to pharmacokinetics (194, 195).

Table 13: Pharmacokinetics parameters as compared to anti-PDL1 antibodies

	<i>i.p.</i> (aPDL1-FN3) ₄ -ELP	<i>i.p.</i> Bioxcell's mAb	<i>i.p.</i> Invivogen's mAb
$t_{elim, 1/2}$	9.381±3.206 h	74.01±3.42 h	107.4±9.479 h
$t_{>40nM}$	27.3± 3.41 h	177.7± 11.24 h	251.7±45.47 h
C_{max}	255.3±8.67 nM	278.5±68.66 nM	371.3±57.92 nM
t_{max}	2.525±0.447 h	7.151±1.43 h	9.321±2.319 h
C_0	28.06±9.202 nM	30.16±69.35 nM	21.40±54.75 nM
AUC_{inf}	13291±853.3 nM·h	20608±4183 nM·h	43281±5698 nM·h

5.3.10 Evaluating *in vivo* efficacy of (aPDL1-FN3)₄-ELP

5.3.10.1 Primary tumor growth

Having shown improved pharmacokinetics of (aPDL1-FN3)₄-ELP, we next examined the therapeutic effect of (aPDL1-FN3)₄-ELP on antitumor immune responses and compared its efficacy with those of anti-PDL1 antibodies. We chose to utilize two different anti-PDL1 antibodies for thorough comparisons: (1) anti-mouse PDL1 antibody (clone number: 10F.9G2, Bioxcell) that has been commonly used for *in vivo* research (196-199); (2) atezolizumab-based anti-PDL1 antibody (Invivogen) that features a PDL1-binding Fab region equivalent to that of the FDA-approved atezolizumab drug. The Fc region of atezolizumab is a fully-humanized IgG1 that contains an N298A mutation to

restrict both antibody-dependent cytotoxicity (ADCC) and complement-dependent cytotoxicity (CDC) (200, 201). To utilize this property of atezolizumab in preclinical mice studies, Invivogen's anti-PDL1 antibody has murine IgG1 with D265A exhibiting no ADCC and low CDC. We believe the use of both antibodies' controls would enable us to gauge the efficacy of our fusion drug compared to current standard treatments. We evaluated the *in vivo* anti-tumor efficacy of (aPDL1-FN3)₄-ELP using the following immunocompetent mouse models, which are known to respond to anti-PDL1 checkpoint blockade: (1) B16.F10 (ATCC CRL-6475) *s.c.* melanoma model in male C57Bl/6 mice; (2) MC38 *s.c.* colon cancer model in male and female C57bl/6 mice; and (3) CT26 (CT26.WT, ATCC CRL-2638) *s.c.* colon cancer model in male and female Balb/c mice.

B16.F10 melanoma model: On day 0, male C57bl/6 mice were inoculated *s.c.* with 10⁵ of B16.F10 cells. On days 4, 7, and 10, mice were treated three times with one of the following treatment groups: (i) PBS control; (ii) (NonsenseFN3)₄-ELP scaffold control; (iii) (aPDL1-FN3)₄-ELP drug; (iv) Bioxcell's anti-PDL1 antibody; and (v) Invivogen's anti-PDL1 antibody. Each drug administration was *i.p.* at a dose of 67 nmol/kg, the same conditions for atezolizumab in preclinical studies. In this tumor regression study (**Figure 63**), all treatment groups slowed tumor growth, compared with the no-treatment control groups ($p < 0.05$). Notably, (NonsenseFN3)₄-ELP had no therapeutic effect on the overall tumor growth, compared to the PBS group, suggesting that the anti-tumor efficacy of

(aPDL1-FN3)₄-ELP was induced by its PDL1 antagonistic effect, not by the protein scaffold. Also, we did not detect any significant toxicities after treatments.

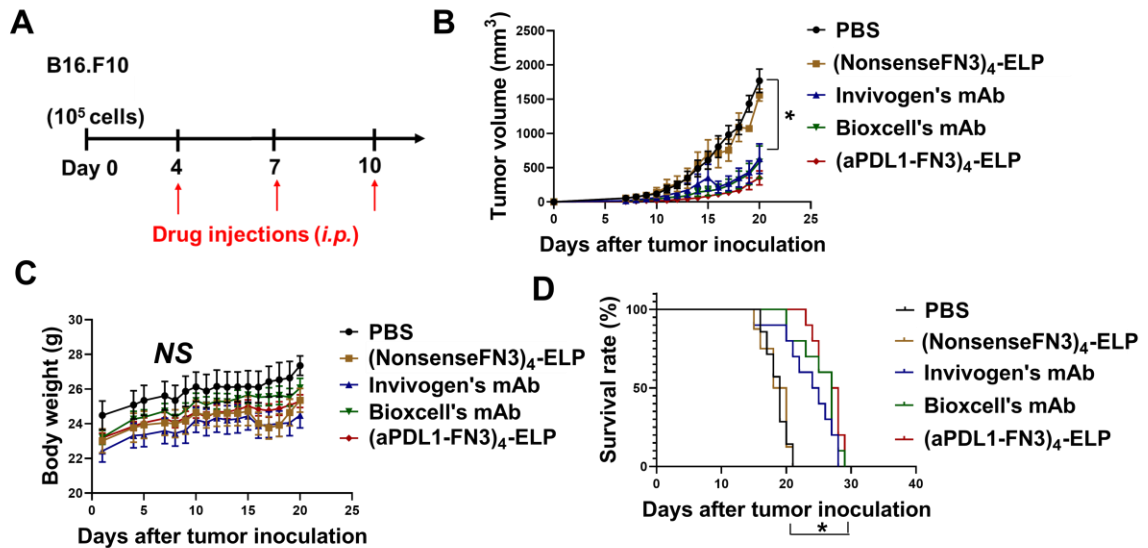


Figure 63: *In vivo* anti-cancer efficacy in a B16.F10 syngeneic mouse model. (A) The schematic shows the dosing schedule. 10⁵ of B16.F10 melanoma cells were implanted s.c. in C57bl/6 mice (day 0). On days 4, 7, and 10, mice were treated *i.p.* with PBS, (NonsenseFN3)₄-ELP, (aPDL1-FN3)₄-ELP, Invivogen's anti-PDL1 mAb, or Bioxcell's anti-PDL1 mAb. We chose a sample size of n = 5-8 mice. Mice were given three injections three days apart with a dose of 67 nmol/kg per injection. Panels (B-C) show results for the B16.F10 model: primary tumor growth curve (B), body weight (C), and survival plot (D) and demonstrate tumor growth inhibition for mice treated with anti-PDL1 antagonists (*p<0.05).

MC38 colon cancer model: A total of 10⁵ MC38 cells were inoculated s.c. in male and female C57bl/6 mice and allowed to grow to the size of 70 ~ 90 mm³. Mice were then treated on day 0 with one of the following treatment groups: (i) PBS control; (ii) (aPDL1-FN3)₄-ELP; (iii) Bioxcell's anti-PDL1 antibody; or (iv) Invivogen's anti-PDL1 antibody. In this study, we did not include (NonsenseFN3)₄-ELP control because we already

confirmed that this protein exhibited no therapeutic efficacy. The treatment schedule and dose are identical as described above: three *i.p.* injections three days apart with each dose of 67 nmol/kg. Results from the MC38 tumor regression study (Figure 64B) showed that (aPDL1-FN3)₄-ELP significantly slowed primary tumor growth, compared with PBS ($p < 0.005$) and two anti-PDL1 antibodies ($p < 0.05$). (aPDL1-FN3)₄-ELP also improved overall survival ($p < 0.05$, log-rank) than PBS and Bioxcell's anti-PDL1 antibody (Figure 64D). Moreover, (aPDL1-FN3)₄-ELP exhibited no overt signs of toxicity and weight loss (Figure 64C).

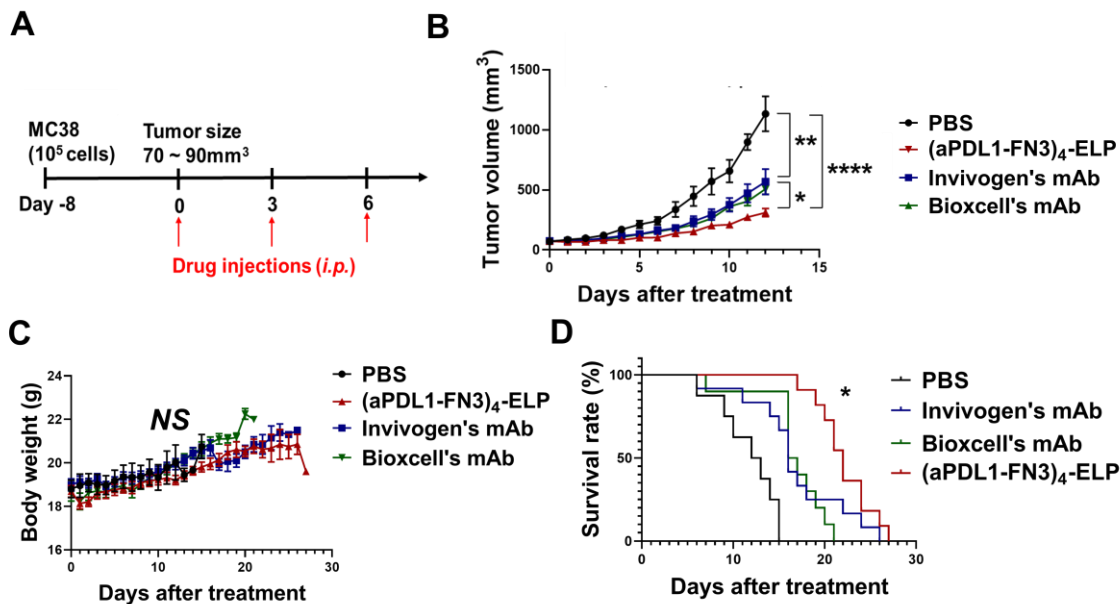


Figure 64: *In vivo* anti-cancer in an MC38 syngeneic mouse model. (A) The schematic shows the dosing schedule of this study. 10⁵ of MC38 colorectal cancer cells were implanted *s.c.* in C57bl/6 mice. After tumors were allowed to grow to 70~90 mm³, mice were then treated (day 0) *i.p.* with PBS, (aPDL1-FN3)₄-ELP, or anti-PDL1 mAbs (n = 8–12 mice) with a total of three injections three days apart at a dose of 67 nmol/kg. Primary tumor growth curves (B), body weights (C), and survival plots (D) show significant tumor growth inhibition for mice treated with (aPDL1-FN3)₄-ELP

compared to PBS ($p < 0.005$) or anti-PDL1 antibody ($p < 0.05$). Overall, (aPDL1-FN3)₄-ELP shows improved survival than PBS and Bioxcell's anti-PDL1 antibody ($p < 0.05$, log-rank).

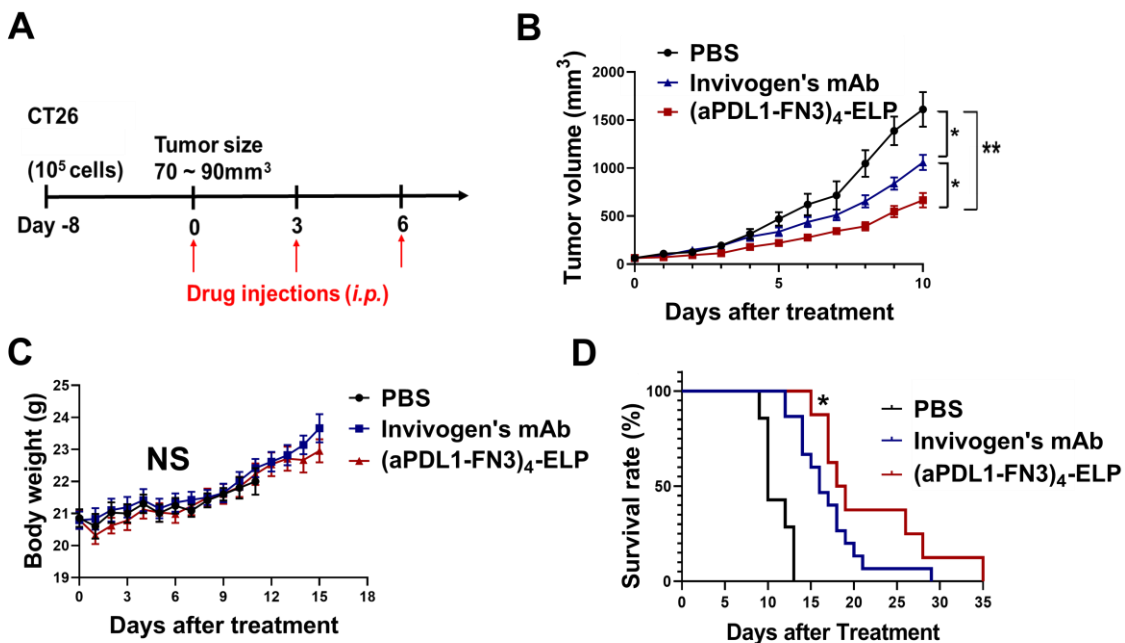


Figure 65: *In vivo* anti-cancer efficacy in a CT26.WT syngeneic mouse model. (A) The schematic shows the dosing schedule of this study. 10⁵ of CT26 colorectal cancer cells were implanted *s.c.* in female Balb/c mice. Tumors were allowed to grow to 70~90 mm³ over 8 days. Mice were then treated (day 0) *i.p.* with PBS, (aPDL1-FN3)₄-ELP, or anti-PDL1 mAb ($n = 8-12$ mice) with a total of three injections three days apart at a dose of 67 nmol/kg. Primary tumor growth curves (B), body weights (C), and survival plots (D) show significant tumor growth inhibition for mice treated with (aPDL1-FN3)₄-ELP compared to PBS ($p < 0.005$) or anti-PDL1 antibody ($p < 0.05$). Overall, (aPDL1-FN3)₄-ELP shows improved survival than PBS and anti-PDL1 antibody ($p < 0.05$, log-rank).

CT26.WT colon cancer: To investigate the therapeutic potential of (aPDL1-FN3)₄-ELP on different mice strains, we chose to use the CT26 model. Female Balb/c mice were injected *s.c.* in the right flank with CT26. When the tumor size reached 70 ~ 90 mm³, mice were injected *i.p.* with PBS, (aPDL1-FN3)₄-ELP or Invivogen's anti-PDL1 antibody. All

treatment conditions are identified as described above. The (aPDL1-FN3)₄-ELP significantly reduced primary tumor growth relative to PBS (p<0.005), and Invivogen's anti-PDL1 antibody (p<0.05) (**Figure 65B**), and improved overall survival (p<0.05, log-rank) (**Figure 65D**). These results indicate that (aPDL1-FN3)₄-ELP has possible therapeutic advantages over the existing anti-PDL1 antibodies in terms of tumor growth inhibition. The treatment triggered no significant body weight decrease (**Figure 65C**).

5.3.10.2 Tumor rechallenge

In recent experiments that we carried out to maximize the therapeutic efficacy of (aPDL1-FN3)₄-ELP as well as anti-PDL1 antibodies, we started treatments based on the days of inoculation, rather than the tumor sizes. All conditions of these treatments (groups, dose, and schedule) were the same as in the previous B16.F10 mice model study.

In this study (**Figure 66**), while all PBS and (NonsenseFN3)₄-ELP groups continued to grow tumors, (aPDL1-FN3)₄-ELP and two anti-PDL1 antibodies treatments resulted in surviving mice: 11 mice for (aPDL1-FN3)₄-ELP; 9 mice for Bioxcell's anti-PDL1 antibody; and 9 mice for Invivogen's anti-PDL1 antibody. All treatments did not exhibit overt toxicities.

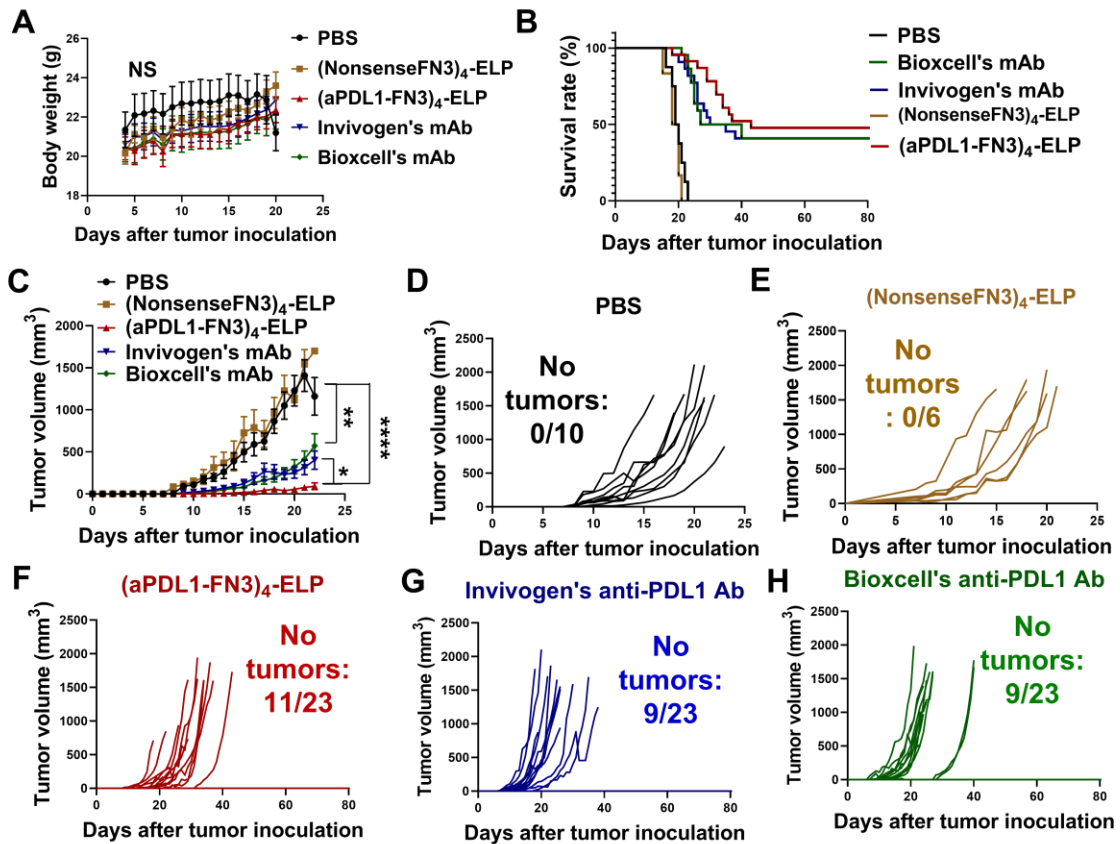


Figure 66: *In vivo* anti-cancer efficacy in an MC38 syngeneic mouse model showing some tumor-free mice. (A) Treatments did not exhibit overt toxicities. (B) The survival plot shows that treatment groups have 9-11 surviving mice. (C) Treatments delayed or inhibited the initiation of primary tumor growth. (D-H) Individual tumor growth curves. 10^5 of MC38 colon cancer cells were implanted *s.c.* in male and female C57bl/6 mice (day 0). On days 4, 7, and 10, mice were treated *i.p.* with (D) PBS, (E) (NonsenseFN3)₄-ELP, (F) (aPDL1-FN3)₄-ELP, (G) InvivoGen's or (H) Bioxcell's anti-PDL1 antibodies. Tumor growth curves were analyzed by two-way ANOVA and Tukey's test, and survival data were analyzed by log-rank test. Data and error bars represent mean \pm SEM. * $p < 0.05$, ** $p < 0.005$, **** $p < 0.0001$

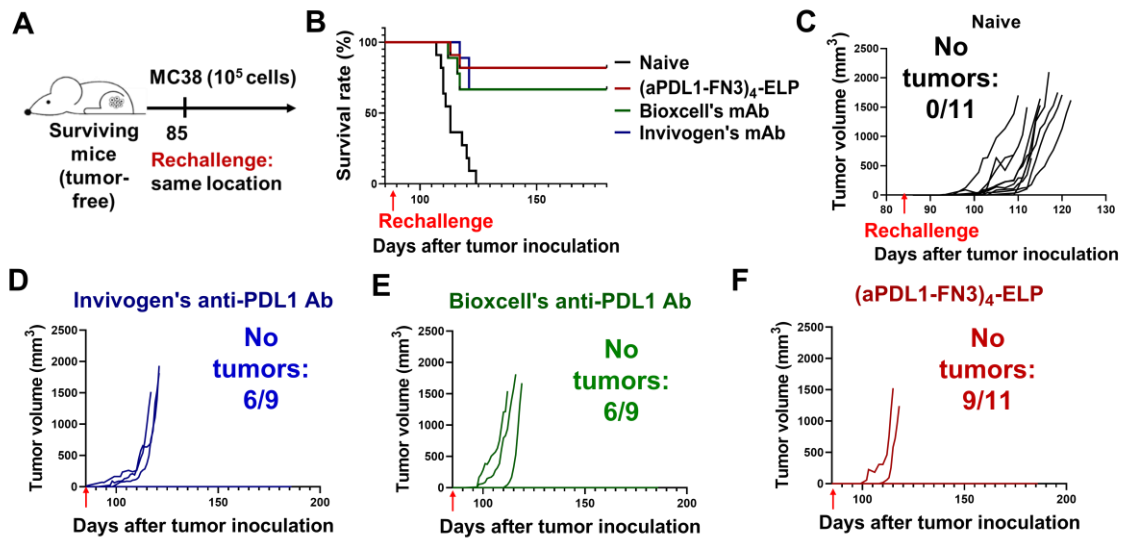


Figure 67: *In vivo* rechallenge experiment in an MC38 syngeneic mouse model. (A) The schematic shows the dosing schedule of this study. (B) The survival plot shows that (aPDL1-FN3)₄-ELP groups had 9 mice surviving from the re-challenge (81%), and each mAb group had 6 surviving mice from the re-challenge (67%). (C-F) Individual tumor growth curves of mice that were previously treated with (C) none, (D) Invivogen's mAb, (E) Bioxcell's mAb, and (E) (aPDL1-FN3)₄-ELP, after tumor re-inoculation. Survival data were analyzed by log-rank test.

The (aPDL1-FN3)₄-ELP groups had 11 surviving mice and antibody groups had 9 surviving mice that were used for the rechallenge experiment in **Figure 67**. On day 85 after the initial tumor inoculation, surviving mice were reinoculated with the same number (10⁵) of MC38 cells at the same location (right flank) as the original primary tumor. As a control for the treatment groups, we used mice that did not receive any drugs before. On day 170 after reinoculation, the (aPDL1-FN3)₄-ELP groups had 9 mice surviving from the re-challenge (81%), and each mAb group had 6 surviving mice from the re-challenge (67%). These results show that (aPDL1-FN3)₄-ELP successfully induces systemic activation of anti-tumor immunity and immunological memory.

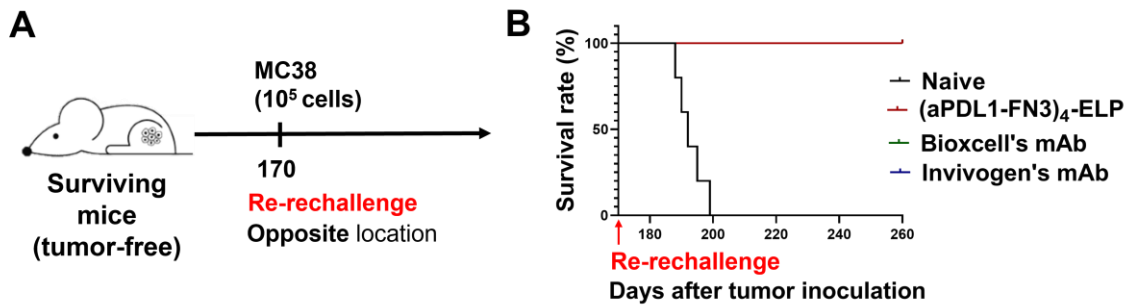


Figure 68: *In vivo* re-challenge experiment in an MC38 syngeneic mouse model. (A) The schematic shows the dosing schedule of this study. (B) The survival plot shows that all 9 mice in (aPDL1-FN3)₄-ELP groups (100%) and all 6 mice in each mAb group (100%) prevented tumor recurrence while all 5 naïve control mice grew tumors.

With these survivors, we re-inoculated the same number (10⁵) of MC38 cells, but at the opposite location (left flank). The opposite site is a more stringent condition to demonstrate the systemic anti-tumor immunity from the treatments of anti-PDL1 drugs. On day 170 after the initial tumor inoculation, we used mice that were tumor-free survivors after treatments and naïve mice as a control for re-inoculation and monitored their tumor growths and body weights (**Figure 68**). While all control mice continued to grow tumors, all treatment groups (100%) did not show any tumor growths for 3 months. This indicates that (aPDL1-FN3)₄-ELP systematically activates anti-tumor immunity and induces immunological memory against tumor recurrence.

5.3.11 *In vivo* biodistribution of (aPDL1-FN3)₄-ELP

Next, we evaluated the effect of specific PDL1-binding to organ distribution using (aPDL1-FN3)₄-ELP protein and its control, (Nonsense)₄-ELP, as compared to two

anti-PDL1 antibodies from Invivogen and Bioxcell. To achieve this, we radiolabeled a tyrosine residue of protein constructs with ^{125}I , as previously described (92, 191).

For this study, we used female Balb/c mice (n=5 per group) and inoculated 10^5 of CT26.WT cells. Upon reaching a tumor size of 70 ~ 90 mm^3 , mice were weighed and *i.p.* injected with 4 μCi ^{125}I equivalent of 67 nmol/kg of following constructs for three times two days apart: (i) (NonsenseFN3)₄-ELP scaffold control; (ii) (aPDL1-FN3)₄-ELP; (iii) Bioxcell's anti-PDL1 antibody; or (iv) Invivogen's anti-PDL1 antibody. On day 8 after the initial treatment, whole organs were harvested and the protein concentrations in each organ were measured for their ^{125}I activities using a gamma counter. ^{125}I -labeled protein samples used for injections were serially diluted and measured under identical conditions with organs to create a standard curve. The raw data of activities in CPM was converted to the percent injected dose (%ID) using the standard curve and normalized against the weight of organs (%ID/g).

According to organ distribution data (**Figure 69A**), (aPDL1-FN3)₄-ELP and (NonsenseFN3)₄-ELP show similar uptake of normal organs, except tumors where PDL1 receptors are overexpressed. This indicates that specific PDL1-binding promotes tumor binding and accumulation. Compared to anti-PDL1 antibodies, (aPDL1-FN3)₄-ELP shows lower accumulation in the organs of the heart, lung, liver, kidney, and pancreas, except for muscle and brain. These organs have higher concentrations of anti-PDL1 antibodies because of their higher concentration in blood. Thus, for (aPDL1-FN3)₄-ELP,

no long-term accumulation for normal organs is observed because (aPDL1-FN3)₄-ELP has a faster serum half-life than anti-PDL1 antibodies which contributes to faster clearance in the body. The interesting fact is despite the short serum half-life of (aPDL1-FN3)₄-ELP, (aPDL1-FN3)₄-ELP maintains the competitive tumor uptake compared to anti-PDL1 antibodies (**Figure 69B**).

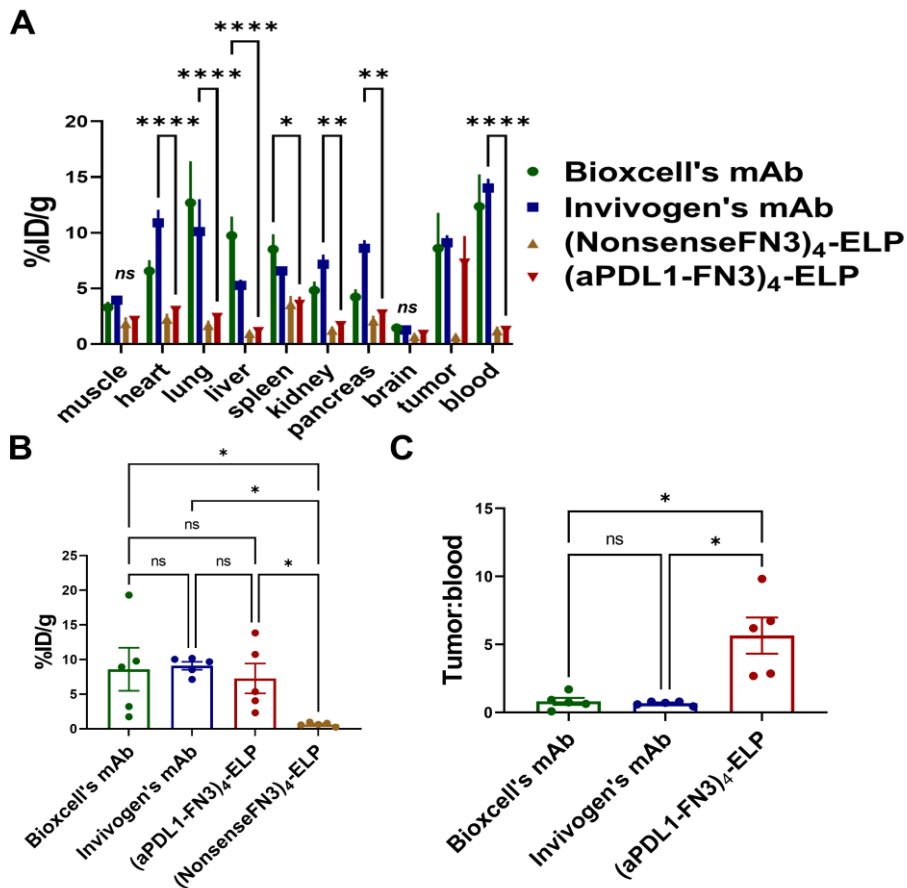


Figure 69: Biodistribution profiles of (aPDL1-FN3)₄-ELP compared to anti-PDL1 antibodies and (NonsenseFN3)₄-ELP scaffold control. (A) Organ distribution profiles including tumor, blood, and other healthy organs, were analyzed by two-way ANOVA and Tukey's test. (B) Tumor organ profile is analyzed by Kruskal-Wallis test. Anti-PDL1 drugs showed similar tumor uptake as compared to non-biner control ($p < 0.05$). (C) The ratio of tumor to blood is analyzed by the Kruskal-Wallis test.

(aPDL1-FN3)₄-ELP has a significantly better ratio of tumor uptake to blood compared to anti-PDL1 antibodies (p<0.05). Data and error bars represent mean ± SEM. *p<0.05, **p<0.005, **p<0.0001**

To explain this contrast more effectively, we quantified the ratio of protein concentrations in tumors to those in the blood (**Figure 69C**). This data shows that (aPDL1-FN3)₄-ELP has a significantly higher tumor accumulation with respect to blood compared to anti-PDL1 antibodies. This sharp contrast could be beneficial over both synthetic polymers like PEG that are non-biodegradable and antibodies that could be localized in normal organs for weeks.

The relative lack of accumulation of (aPDL1-FN3)₄-ELP in healthy tissue with a desired high tumor accumulation suggests that prolonged serum half-life is not the sole purpose of therapeutics development. To optimize a delicate balance between higher tumor uptake and accumulation and lower uptake of healthy organs, we should carefully design therapeutics considering their effective pharmacokinetics and efficient penetration and retention, controlled by various characteristics such as molecular weight, affinity, and valency.

5.3.12 Tumor immunomodulation profiles of (aPDL1-FN3)₄-ELP

Having observed at least slightly better anti-tumor efficacy of (aPDL1-FN3)₄-ELP compared to those of anti-PDL1 antibodies, we seek to explain the possible advantages of using (aPDL1-FN3)₄-ELP over anti-PDL1 antibodies. To achieve this, we studied the immunomodulation profile of tumor-infiltrating lymphocytes using the CT26 mouse

model as described above. Upon reaching a tumor size of 70 ~ 90 mm³, mice were injected *i.p.* with one of four treatment groups: (i) PBS control; (ii) (NonsenseFN3)₄-ELP; (iii) (aPDL1-FN3)₄-ELP; (iv) and Bioxcell's anti-PDL1 antibody.

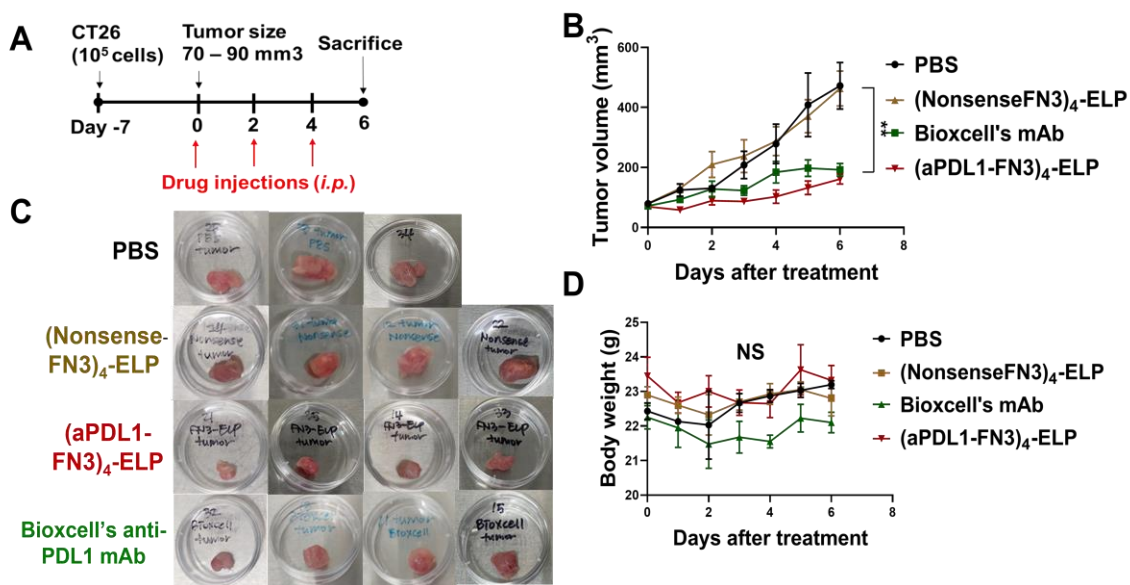


Figure 70: Tumor immunomodulation profile study using a CT26 mouse model. (A) The schematic shows the schedule of this study. 10⁵ CT26 cells were inoculated *s.c.* into Balb/c mice, and at day 7 or 8, once the tumor volume reached 70–90 mm³ in size, tumors were injected *i.p.* three times, two days apart, at a dose of 67 nmol/kg (n = 3-4) of the following treatments: PBS, Bioxcell's anti-PDL1 mAb, (NonsenseFN3)₄-ELP and (aPDL1-FN3)₄-ELP. **(B)** Tumor growth curves as a function of time post-inoculation. **(C)** Photographs of tumors after harvest and before processing. Treatment groups had smaller tumors compared to control groups — (NonsenseFN3)₄-ELP and PBS. **(D)** No significant body weight change was observed between the treatment and control groups. Data and error bars represent mean ± SEM. *p<0.05, **p<0.005, ***p<0.0001

To maximize the therapeutic differences, we maintained similar treatment conditions in the previous studies: three injections two days apart with each dose of 67 nmol/kg. Two days after the last third injection, mice were humanely euthanized, and their tumors were harvested. Then tumors were mechanically dissociated and

enzymatically degraded for 1 hour at 37 °C in HBSS buffer containing 5 mg/mL Collagenase Type I and 0.2 mg/mL DNAase I supplemented with 5% FBS. This solution was diluted in PBS and passed through 70 µm strainers. Cells were then pelleted by centrifugation and resuspended in ACK red cell lysis buffer for 10 min at room temperature, after which the solution was diluted with PBS. Cells were pelleted and counted by Trypan blue exclusion. A total of 10⁶ cells were used for antibody staining. Zombie Live/Dead Aqua stain was applied for 30 min. Cells were then blocked (5% rat serum, 5% mouse serum, 1% CD16/32) in FACS buffer (PBS with 3% FBS and 30 µM EDTA) for 30 min. Cells were then stained with antibodies for 30 min for their surface markers (CD45, CD11b, CD3, CD4, CD8), washed 2 times with PBS, and then fixed with 0.4% paraformaldehyde in PBS. **Figure 70** illustrates the effects of treatments on tumor size and growth.

Using flow cytometry, we gated cell population for tumor cells, single cells, and fluorescence against CD45 followed by either CD11b for myeloid-derived suppressor cells (MDSCs), CD3/CD8 for CD8⁺ T cells, or CD3/CD4 for CD4⁺ T cells (**Figure 71A**).

Then, we analyzed the ratio of CD8⁺ T cells to myeloid-derived suppressor cells (MDSCs) or the ratio of CD4⁺ T cells to MDSCs in the tumor. The normalization against MDSCs is required because drug treatments would increase the absolute number of immune cells. To characterize the phenotyping of tumor-infiltrating immune cells without the bias from drug injection, the relatively increased number of cells should be

calculated: for anti-PDL1 therapy, CD8⁺ T cells are normalized against either T_{reg} cells or MDSCs.

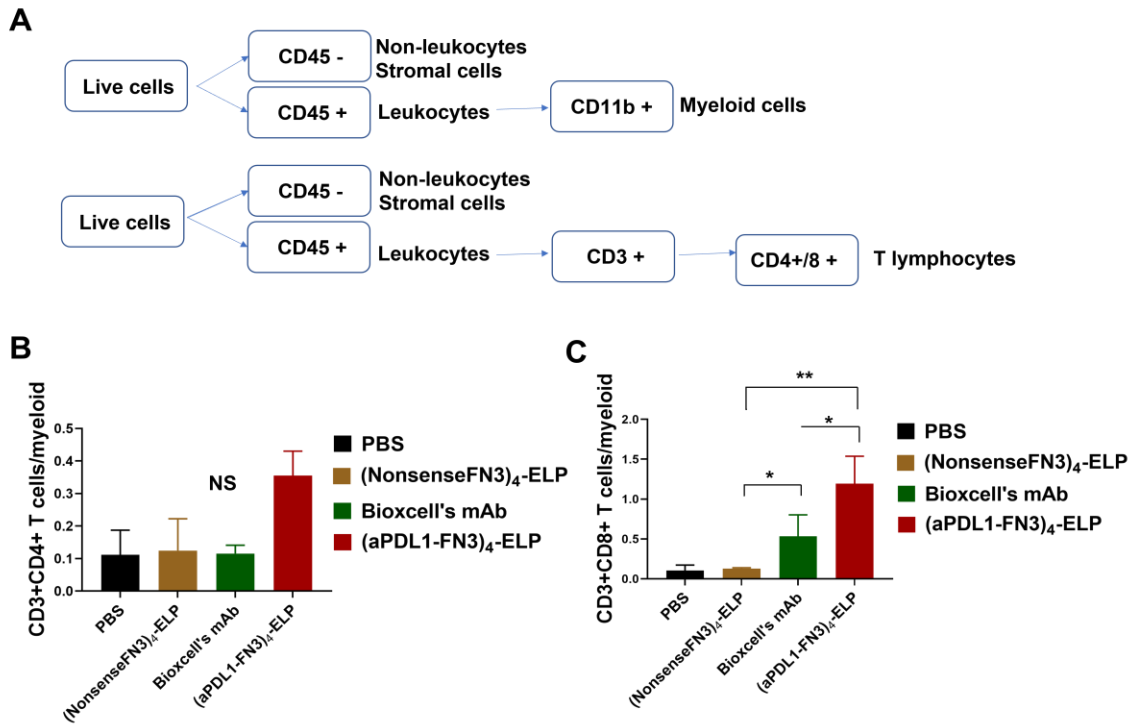


Figure 71: Flow cytometry data analysis for quantification of tumor-infiltrating T lymphocytes. (A) shows the gating strategy for flow cytometry. First, only live cells were chosen for analysis. CD45⁺ gating was applied to identify immune cells, CD11b⁺ was used to characterize myeloid cells as a reference while CD3⁺CD4⁺ or CD3⁺CD8⁺ were used for T lymphocytes. (B) The quantification of CD3⁺CD4⁺ T lymphocytes shows no significant difference between treatment groups. (C) The quantification of CD3⁺CD8⁺ T lymphocytes shows that (aPDL1-FN3)₄-ELP significantly increases intratumoral infiltration of CD3⁺CD8⁺ T cells relative to non-treatment (p<0.005) and Bioxcell's mAb (p<0.05). Data were analyzed by one-way ANOVA. Data and error bars represent mean ± SEM. *p<0.05, **p<0.005.

According to the result of tumor immunomodulation profile, while all groups show the similar ratio of CD4⁺ T cells to CD11b⁺ MDSCs (**Figure 71B**), (aPDL1-FN3)₄-ELP has a significantly higher ratio of CD8⁺ T cells to CD11b⁺ MDSCs in tumors than

that of Bioxcell's anti-PDL1 antibody (**Figure 71C**). This demonstrates that (aPDL1-FN3)₄-ELP exhibited more efficient infiltration of CD8⁺ T cells into tumor tissues. This may explain why (aPDL1-FN3)₄-ELP has at least slightly better anti-tumor efficacy than current standard anti-PDL1 antibodies in MC38 and CT26 models.

5.4 Conclusion and future directions

After optimizing the valency of (aPDL1-FN3)₄, we genetically fused it to ELP proteins for enhanced pharmacokinetics as well as sustained and localized delivery. We created two different types of (aPDL1-FN3)₄-ELP proteins: the depot-forming fusion whose T_t is between 25°C and 37°C and the soluble fusion whose T_t is above 50°C. Unfortunately, depot-forming (aPDL1-FN3)₄-ELP protein exhibits much worse *in vivo* efficacy in a CT26 syngeneic mouse model than soluble (aPDL1-FN3)₄-ELP protein at their equimolar doses. This can be possibly explained by three reasons: 1) depot-forming (aPDL1-FN3)₄-ELP has inherently low bioavailability due to its format, and the low concentration in plasma might not be sufficient to induce systemic anti-tumor immunity on time; 2) the hydrophobicity of depot-forming ELP somehow causes low *in vivo* bioactivity. Although we confirmed that ELP has reversible transition behavior, during its *in vivo* release, the bioactivity of ELP fusion protein can be damaged; 3) slow release is not a suitable delivery format for cancer immunotherapy. Unlike metabolic diseases such as type II diabetes that favor sustained release, clinically, anti-PDL1 therapy uses high dose injections (1000 mg IV over 1 hour) to saturate PDL1 receptors on circulating

immune cells in the blood. This requirement has proven significant for clinical therapeutic efficacy because otherwise immune cells are not effectively activated for anti-tumor immunity. Thus, we decided to continue to only use the soluble format of (aPDL1-FN3)₄-ELP fusion protein.

To thoroughly characterize (aPDL1-FN3)₄-ELP, we created a scaffold control that does not have specific PDL1 binding, (NonsenseFN3)₄-ELP. This protein does not have engineered BC, DE, and FG loop regions for PDL1-binding. We successfully cloned, recombinantly synthesized, and purified (aPDL1-FN3)₄-ELP and (NonsenseFN3)₄-ELP by inverse transition cycling, a non-chromatographic method that exploits their phase-transition behavior. Purified (aPDL1-FN3)₄-ELP and (NonsenseFN3)₄-ELP proteins were characterized for their biophysical properties, including their LCST behaviors, hydrodynamic radius, any aggregation or micelle formation after fluorescence conjugation, and specific binding affinity to PDL1. Despite the fusion with ELP, (aPDL1-FN3)₄-ELP retains its strong and specific PDL1 binding and antagonism in the picomolar regime similar to anti-PDL1 antibodies.

We confirmed *in vivo* efficacy of (aPDL1-FN3)₄-ELP using three syngeneic mice models: B16.F10 melanoma and MC38 and CT26 colorectal cancers. Especially for the MC38 and CT26 model, (aPDL1-FN3)₄-ELP shows at least a slightly better therapeutic efficacy than anti-PDL1 antibodies. To explain this, we performed three experiments: organ distribution profiles, tumor uptake and penetration using 3D spheroids, and

tumor-infiltrating immunomodulation profiles. All results show that (aPDL1-FN3)₄-ELP has significantly better tumor uptake and penetration than anti-PDL1 antibodies, although (aPDL1-FN3)₄-ELP has a shorter plasma half-life than anti-PDL1 antibodies. This is because the modularity of (aPDL1-FN3)₄-ELP enables this drug to possess higher valency (tetra-valency) while maintaining smaller molecular weight and similar PDL1 binding affinity. These characteristics allow (aPDL1-FN3)₄-ELP to have a desired tumor uptake and penetration with significantly lower distribution to healthy tissues. This interesting result suggests that (aPDL1-FN3)₄-ELP could potentially reduce the toxic side effects of common antibody-based immune checkpoints such as pneumonitis (inflammation in the lungs), diarrhea, rashes, itchiness, hormone imbalances, and kidney infections. In this chapter, we successfully developed the (aPDL1-FN3)₄-ELP drug as an alternative to anti-PDL1 antibodies.

6. Developing the fusion between (aPDL1-FN3)₄ and ABD

6.1 Introduction and motivation

6.1.1 Recombinant fusion with ABD

Albumin-binding domain (ABD) is a small protein comprised of 46 amino acid residues from streptococcal protein G (100). The fusion with ABD is a common strategy to extend the half-lives of scaffold proteins and exploit FcRn-mediated recycling (99). Previously, ABD protein has been extensively engineered and modified for affinity maturation to sub-picomolar binding affinity to human albumin as well as for deimmunization to remove T cell epitopes. Recently, the fusion between affibody molecule and ABD successfully enhanced the pharmacokinetic profiles in humans in clinical trials (NCT02690142) (202). Besides affibodies, many scaffold proteins, including anticalins and antibody fragments, have been fused to the ABD to extend their half-lives, and the effect of fusion with ABD has been confirmed in animal models (101, 102). In this chapter, we create a fusion protein between the optimized (aPDL1-FN3)₄ and the albumin-binding domain (ABD), replacing the fusion with ELP from the previous chapter. This fusion protein is referred to as (aPDL1-FN3)₄-ABD.

In a modular protein platform, ABD is another half-life module that can be used to enhance pharmacokinetics owing to its binding ability to albumin (**Figure 72**). Since albumin is abundant in plasma, upon *in vivo* injection of (aPDL1-FN3)₄-ABD, the fused ABD protein binds to albumin circulating in the blood while the (aPDL1-FN3)₄ protein

targets and antagonizes PDL1. Particularly, the function of ABD-binding increases the plasma half-life of (aPDL1-FN3)₄-ABD, while the function of PDL1-binding allows for the uptake and penetration by PDL1-overexpressed tumors. The combined binding functions would induce anti-tumor immunity until (aPDL1-FN3)₄-ABD proteins are biodegraded in the body.

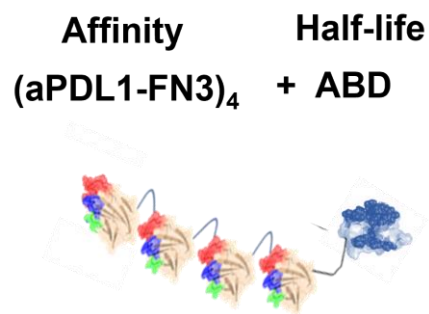


Figure 72: Schematic for the construction of (aPDL1-FN3)₄-ABD protein. The optimized tetra-avalency of (aPDL1-FN3) is genetically fused to ABD for enhanced pharmacokinetics.

Among the many ABD derivatives, we specifically chose a deimmunized ABD protein (ABD094) because this version would reduce the immunogenicity of protein drugs (100). This is especially useful for cancer immunotherapy, as it recruits the immune system to fight cancer. The sequence of ABD094 is shown in Appendix B. ABD094 has shown very weak to non-immunogenic responses in T cell proliferation assays.

6.1.2 Advantages over the fusion with ELP

As a half-life module for (aPDL1-FN3)₄ drug delivery, ABD can be more advantageous over ELP in two ways: 1) longer serum half-life; 2) smaller molecular weight. Owing to the small molecular weight of ABD, the fusion with ABD would not significantly increase the apparent molecular weight of the drug, and this molecular weight (~50kDa) is around half that of the ELP fusion, (aPDL1-FN3)₄-ELP (~95kDa). The smaller size of (aPDL1-FN3)₄-ABD would potentially increase the tumor uptake and penetration compared to (aPDL1-FN3)₄-ELP and especially anti-PDL1 antibodies. While maintaining the most compact anti-PDL1 drug molecule, (aPDL1-FN3)₄-ABD could show a longer serum half-life than (aPDL1-FN3)₄-ELP. This reasoning is based on previous results of our laboratory, where a longer serum half-life is observed for ABD compared to ELP (103, 203).

We have previously developed ABD-coated nanoparticles that contain a defined number of covalently conjugated drug molecules in the core and that bind endogenous serum albumin with high affinity on the corona. In a canine model, which is more correlated with human outcomes compared to mouse models, ABD-coated nanoparticles (ABDN-Dox) have been shown to have a significantly greater plasma half-life and plasma exposure than ELP-based nanoparticles (CP-Dox) (103). Also, in a mouse model, ABDN-Dox has been shown to have a much lower accumulation in the liver and spleen than CP-Dox (103). It has also been shown to accumulate in tumors to a great extent,

resulting in a wider therapeutic window for ABDN-Dox than CP-Dox (203). Altogether, these results show great potential for ABD fusion in its clinical translation, as it may help improve pharmacokinetics, lower toxicities, and enhance tumor uptake and penetration.

6.2 Materials and methods

6.2.1 Construct design and synthesis

The (aPDL1-FN3)₄ domain was genetically fused with the ABD domain. We created three different fusion proteins depending on the linker used to tether protein to one another: 1) a flexible (Gly₄Ser)₂ peptide linker was inserted; 2) an ELP linker (VPGAG)₁₀ was inserted; 3) two linkers, including an ELP linker (VPGAG)₁₀ and a rigid helical linker ((KEAAA)₃KELAA)₂ were inserted. To construct the genes encoding these sequences, several dsDNA fragments were designed to possess 15 to 18 complementary base pairs and synthesized by Integrated DNA Technologies (Coralville, IA). Fragments for each construct were assembled and cloned by Gibson assembly into the pET24 vector. All genes encode a Histidine-tag (His₈) on the C-terminus of the (aPDL1-FN3)₄-ABD gene for convenient purification. After successful gene assembly was confirmed by Sanger sequencing, the correct plasmid was transformed into the BL21(DE3) expression strain of *E. coli* (New England Biolabs, MA). Aliquots of the DNA stocks were stored at -20 °C and transformed cell stocks with glycerol were stored at -80 °C.

6.2.2 Protein expression and purification

The (aPDL1-FN3)₄-ABD proteins were expressed in BL21(DE3) *E. coli* using autoclaved 2xYT media (16 g of tryptone, 10 g of yeast extract, 5 g of NaCl, and pH 7.0 in 1L of distilled H₂O). From the frozen glycerol stocks, small starters (50 ml) were grown overnight and used to inoculate 6 of 1 L flasks of 2xYT media supplemented with kanamycin (45 µg/ml). After the flasks were incubated in a shaker at 37 °C and 200 rpm for 3 hours, a final concentration of 0.5mM of IPTG (Gold Biotechnology) was added per flask. Then, all flasks were incubated in a shaker at 18 °C and 200 rpm for 24 hours.

Most of (aPDL1-FN3)₄-ABD proteins should be denatured for purification by the IMAC. Briefly, the bacterial cell suspension was centrifuged at 4000 rpm for 15 min at 4°C; the cell pellet was then resuspended in lysis buffer (Tris 25 mM, NaCl 100 mM, 6 M Urea, and 5mM Imidazole, pH 6.5) and lysed by sonication on ice for 3 mins (10s on and 40s off) (Misonix S-4000; Farmingdale, NY). After centrifugation at 14,000rpm for 15 mins at 4°C, the supernatant was subjected to a binding resin composed of agarose beads derivatized with a tetradentate chelation moiety and loaded with divalent cobalt ions (Thermo Fisher Scientific, MA). After the loading of supernatants to the resin, the resin was washed with washing buffer (Tris 25 mM, NaCl 100 mM, 6 M Urea, and 30 mM Imidazole, pH 6.5) at 5 times the volume of resin to remove weakly bound contaminants with. Then, the elution buffer (Tris 25 mM, NaCl 100 mM, 6 M Urea, and 250 mM Imidazole, pH 6.5) was added. To remove any metal ions, 1/10 volume of 0.5M

EDTA solution (pH 8.0) was added to the final eluted proteins. To remove excess imidazole from purified protein solutions and exchange buffers for further functional studies, the final samples were dialyzed against 1X PBS buffer at 4 °C for 24 h. The purity of each protein was confirmed by SDS-PAGE gel (Mini-PROTEAN TGX, Bio-Rad Laboratories, CA) stained with SimplyBlue solution (Thermo Fisher Scientific, MA).

6.2.3 Biophysical characterization

6.2.3.1 Mass spectrometry

To confirm the molecular weight of (aPDL1-FN3)₄-ABD protein, we used matrix-assisted laser desorption/ionization-time of flight mass spectrometry (MALDI-TOF MS)

Specifically, we used a Bruker Autoflex Speed LRF MALDI-TOF (Bruker Daltonik GmbH, Bremen, Germany) equipped with an Nd/YAG laser (355 nm). The instrument was calibrated against an aldolase (Sigma Aldrich, Mw = 39,211.28 Da) or apomyoglobin (Sigma Aldrich, Mw = 16,952.27) standard. Samples for MALDI-TOF-MS analysis were prepared by mixing 1 µL of purified protein with 9 µL of an α -cyano-4-hydroxycinnamic acid matrix (a saturated solution was prepared by suspending 10 mg of the matrix in 500 µL H₂O + 0.3% TFA and 500 µL acetonitrile + 0.3% TFA). Afterward, 1 µL of this mixture was deposited onto a polished steel sample plate and dried in air at room temperature.

6.2.3.2 Dynamic light scattering

Dynamic light scattering (DLS) measurements of proteins were performed using a Wyatt DynaPro temperature-controlled instrument (Wyatt Technology, Santa Barbara, CA), with 10 acquisitions collected at room temperature. Samples for the DLS system were prepared in 1X PBS and filtered through Whatman Anotop sterile syringe filters (0.2 μm ; GE healthcare, PA) into a black 96 well plate (Corning). The data points presented for this characterization represent the mean of R_n .

6.2.3.3 Surface plasmon resonance

We used a Biacore T200 SPR. First, the series S sensor chip CM5 (GE healthcare) was normalized using 70% glycerol. Flow path 1 was used as a reference without immobilizing anything. Flow path 2, human PDL1 was immobilized using NHS/EDC coupling to characterize PDL1 binding. For the analysis of albumin-binding, human albumin was immobilized in flow path 3, and mouse albumin was immobilized in flow path 4 using the same NHS/EDC coupling. A solution of 0.5M EDC/1M NHS was injected at 5 $\mu\text{l}/\text{min}$ for 7 minutes to activate the chip surface. 200 $\mu\text{g}/\text{ml}$ of protein G in 10 mM sodium acetate buffer (pH 4.0) was injected at 5 $\mu\text{l}/\text{min}$ for 30 seconds to obtain a final RU (response unit) of around 800-1000. Next, 1M ethanolamine was injected at 5 $\mu\text{l}/\text{min}$ for 10 minutes to inactivate the chip surface. Our protein samples were injected over immobilized target proteins simultaneously on all flow paths at a flow rate of 30 $\mu\text{l}/\text{min}$ at 25 $^{\circ}\text{C}$ for 3 mins. Then, protein samples were replaced with running buffer (1X

PBS) for 5 mins for dissociation. After each experiment, the chip surface was regenerated with 10 mM glycine-HCl (pH 1.5) for 30 secs. After injection of serially diluted protein samples in running buffer and subtraction of the signal of flow path 1, the final SPR sensorgrams were obtained and analyzed using a 1:1 Langmuir binding model in BIAevaluation software (GE Healthcare).

6.2.4 *In vitro* potency

CHO TCR/hPDL1 cells were prepared in their growth media (Ham's F12 supplemented with 10% FBS). First, cells were washed with 1X DPBS, trypsinized with 0.25% trypsin/EDTA, and harvested by centrifugation at 250g for 5 mins. The cell pellet was resuspended in warm media and the cells were counted with a hemocytometer after 1:1 dilution into 0.4% Trypan blue solution (Thermo Fisher Scientific, MA). The cell density was adjusted to 4×10^5 cells/ml by the addition of warm media, and the cell suspension was transferred to a sterile reagent reservoir. Using a multichannel pipette, 100 μ l of cells were added to each well of 96-well flat, white clear-bottom assay plates (Corning). The plates were incubated in a 37 °C, 5% CO₂ incubator overnight.

We prepared protein samples in two assay buffers to confirm if ABD-binding affects PDL1-binding: 1) RPMI 1640 without FBS; 2) RPMI 1640 supplemented with 10% FBS. In the case of 2.5-fold dilution, 250 μ l of proteins were added to the first well of a sterile clear bottom 96-well plate, and 150 μ l of assay buffer was added to other wells. 100 μ l of proteins from the first well was transferred to the 150 μ l of assay buffer and

gently mixed. This step was repeated until a sufficient range of concentration was covered. These protein samples were added to the plate coated with CHO TCR/hPDL1 cells.

Jurkat/PD1 cells were prepared, and the cell density was adjusted to 1.25×10^6 cells/ml by the addition of assay buffer. Using a multichannel pipette, 40 μ l of cells were added to each well of the plate coated with CHO TCR/hPDL1 cells followed by the addition of protein samples. The plate was incubated again in a 37 °C, 5% CO₂ incubator for 6-8 hours.

Since protein samples effectively antagonize the interaction between CHO TCR/hPDL1 cells and Jurkat/PD1 cells, TCR activation induces the luminescence of the NFAT pathway. After taking out the plate and equilibrating it to room temperature for 10 mins, 80 μ l of Bio-Glo™ reagents (Promega, WI) was added to each well. After 10-30 mins, the luminescence signal was measured by a multimode plate reader (Tecan).

6.3 Results and discussion

6.3.1 Qualitative characterization with gel electrophoresis

We hypothesized that the length and flexibility of linkers between (aPDL1-FN3)₄ and ABD proteins affect their binding affinity towards PDL1 and/or ABD. Thus, we created three different (aPDL1-FN3)₄-ABD proteins depending on the linkers used to fuse these proteins: 1) a flexible (Gly₄Ser)₂ peptide linker was used, and this fusion is referred to as (aPDL1-FN3)₄-GS-ABD; 2) an ELP linker (VPGAG)₁₀ was inserted, and this

fusion is referred as (aPDL1-FN3)₄-ELP-ABD; 3) two linkers, including an ELP linker (VPGAG)₁₀ and a rigid helical linker ((KEAAA)₃KELAA)₂ was used, and this fusion is referred as (aPDL1-FN3)₄-EH-ABD. The helical linker was additionally chosen to improve the albumin binding affinity of (aPDL1-FN3)₄-EH-ABD upon the fusion.

We used the *E. coli* expression system to express all three (aPDL1-FN3)₄-ABD proteins. After bacterial cell expression, we denatured and purified (aPDL1-FN3)₄-ABD proteins using IMAC. We confirmed their purity using sodium dodecyl sulfate-polyacrylamide gel electrophoresis (SDS-PAGE), followed by Simply blue staining. The stained SDS-PAGE image of purified multivalent aPDL1-FN3 proteins exhibited a single band with no other visible contaminants (**Figure 73**).

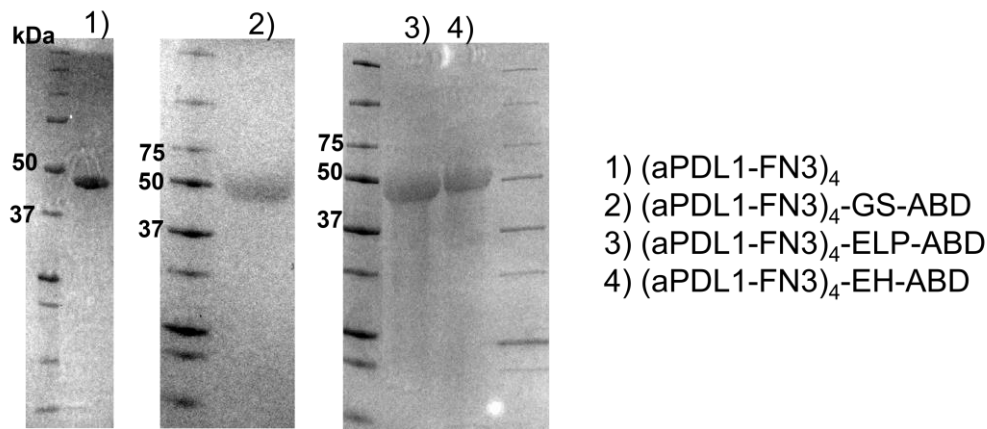


Figure 73: SDS-PAGE images of (aPDL1-FN3)₄-ABD proteins. These images confirm the successful expression and purification of (aPDL1-FN3)₄-ABD proteins.

6.3.2 Biophysical characterization

To confirm the correct molecular weights of purified (aPDL1-FN3)₄-ABD proteins, we decided to use MALDI-TOF mass spectrometry. MALDI is a soft ionization

technique to generate ionized proteins without causing fragmentation of proteins. Also, MALDI is well-tolerable to mixtures of biopolymers in buffer solution. After MALDI, the ionized proteins travel to a detector, and the detector measures their times for travel, resulting in the calculation of the ratio of protein molecular mass to charge. We successfully obtained the molecular mass of (aPDL1-FN3)₄-GS-ABD, (aPDL1-FN3)₄-ELP-ABD, and (aPDL1-FN3)₄-EH-ABD proteins and confirmed their correct sizes (**Figure 74**).

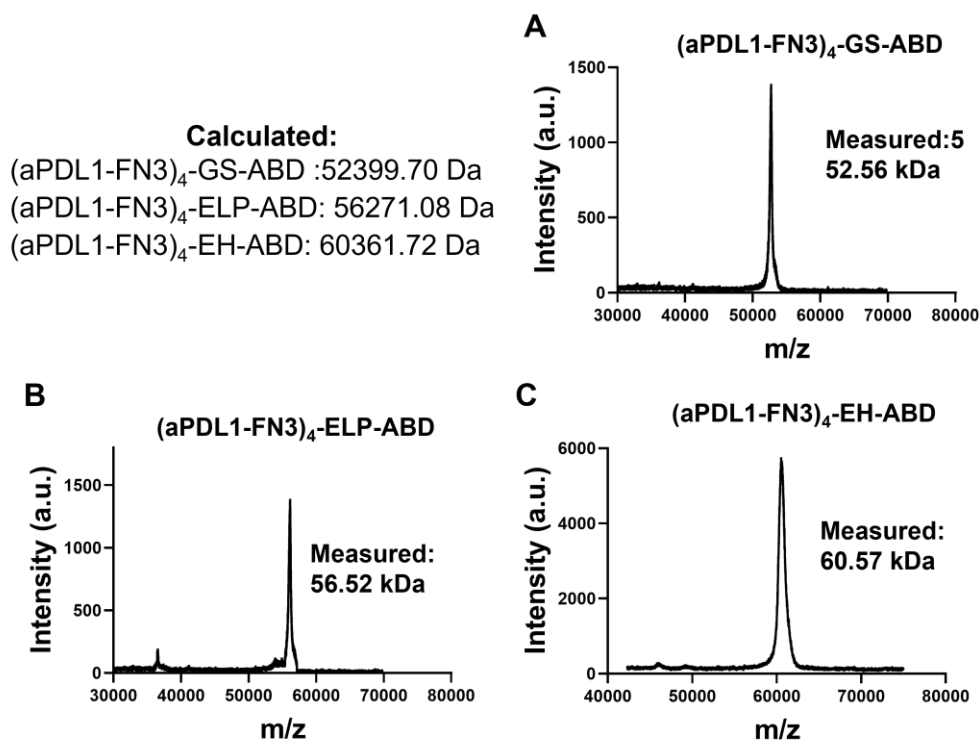


Figure 74: Purified (aPDL1-FN3)₄-ABD proteins are characterized for their molecular weights: (A) (aPDL1-FN3)₄-GS-ABD, (B) (aPDL1-FN3)₄-ELP-ABD, and (C) (aPDL1-FN3)₄-EH-ABD proteins are all confirmed for their correct sizes. The calculated molecular weights are tabulated next to panel (A) and the experimentally measured MWs are shown in each panel and agree the calculated MWs within the error of the technique.

Also, since the fusion with ABD can cause aggregation or instability of proteins, we analyzed their hydrodynamic radius (R_h) using dynamic light scattering (DLS). Fortunately, we did not detect any significant aggregation of the following proteins: (aPDL1-FN3)₄-GS-ABD, (aPDL1-FN3)₄-ELP-ABD, and (aPDL1-FN3)₄-EH-ABD (**Figure 75**).

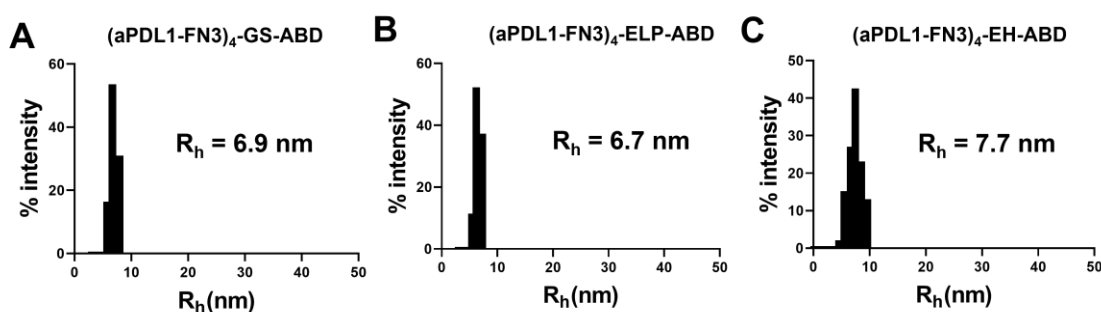


Figure 75: Purified (aPDL1-FN3)₄-ABD proteins are characterized for their hydrodynamic radius (R_h): (A) (aPDL1-FN3)₄-GS-ABD, (B) (aPDL1-FN3)₄-ELP-ABD, and (C) (aPDL1-FN3)₄-EH-ABD. All constructs have R_h 's consistent with their size and no construct showed any significant aggregation or micelle formation. The measured R_h are shown in each panel.

6.3.3 PDL1 antagonism

Using the serial dilution of (aPDL1-FN3)₄-GS-ABD, (aPDL1-FN3)₄-ELP-ABD, and (aPDL1-FN3)₄-EH-ABD proteins, we characterized their potency and compared them to decide which linker is the most optimal for ABD fusion. According to the results of this assay (**Figure 76**), while all three proteins successfully antagonized the interaction between PD1 and PDL1, the (aPDL1-FN3)₄-EH-ABD exhibits the highest potency in terms of IC_{50} as compared to that of (aPDL1-FN3)₄-GS-ABD and (aPDL1-FN3)₄-ELP-ABD (**Table 14**). This result shows that the combination of two linkers, ELP, and helical

linkers, is the most appropriate for the fusion with ABD to maintain specific PDL1 binding and the highest PDL1 antagonism.

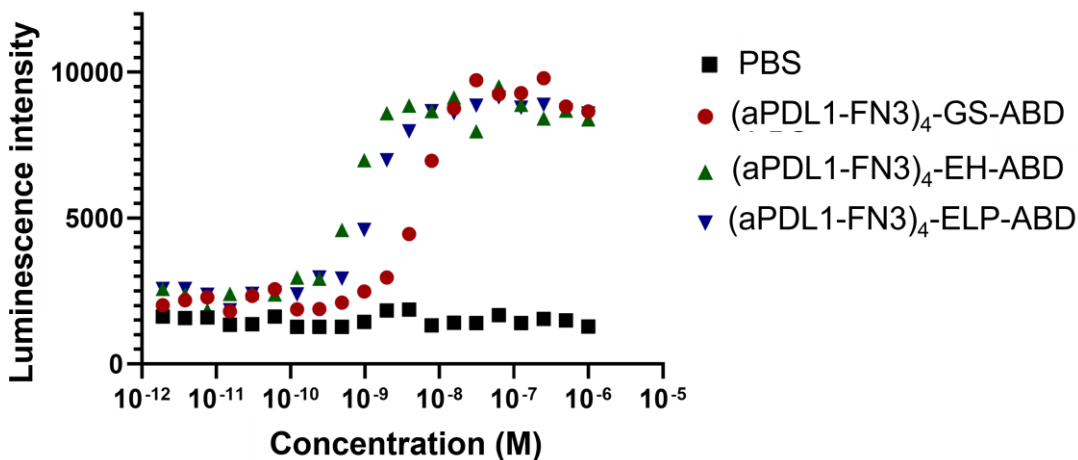


Figure 76: Characterization of the PDL1 antagonism of (aPDL1-FN3)₄-ABD proteins using *in vitro* PDL1 blockade assay. The (aPDL1-FN3)₄-EH-ABD protein shows the highest potency for PDL1 antagonism.

Table 14: The IC₅₀ of (aPDL1-FN3)₄-ABD proteins

Construct	IC ₅₀ [nM]
(aPDL1-FN3) ₄ -GS-ABD	30.3
(aPDL1-FN3) ₄ -ELP-ABD	2.69
(aPDL1-FN3) ₄ -EH-ABD	0.97

6.3.4 Binding affinity to PDL1 and albumin

With the most optimal (aPDL1-FN3)₄-EH-ABD protein, we utilized SPR to analyze its specific binding to PDL1 as well as specific binding to albumin. The data suggest that (aPDL1-FN3)₄-EH-ABD exhibits the ability to bind to PDL1 from humans and mice as well as serum albumin from humans and mice (Figure 77).

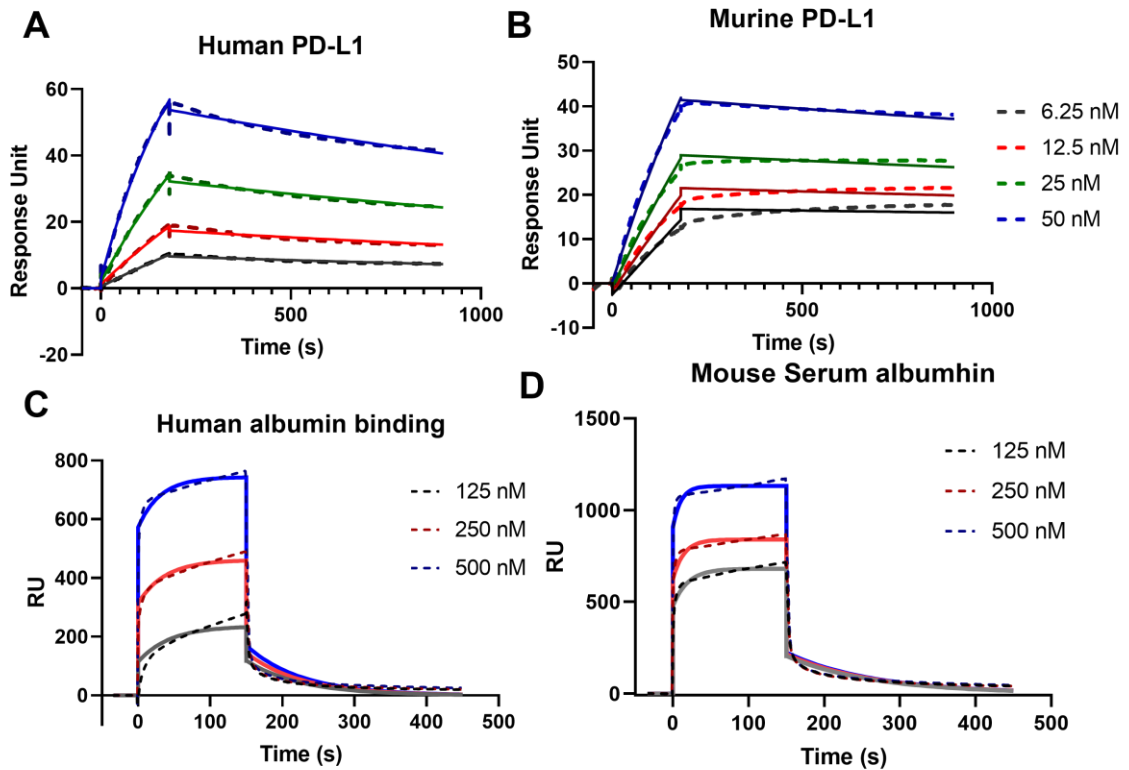


Figure 77: Characterization of the specific PDL1 and albumin binding kinetics of (aPDL1-FN3)₄-EH-ABD using SPR. The SPR sensorgrams of (aPDL1-FN3)₄-EH-ABD show specific binding to human and murine PDL1 (A, B) as well as human and murine albumin (C, D).

Specifically, the binding kinetics of (aPDL1-FN3)₄-EH-ABD is 1.1 nM for human PDL1, 2.5 nM for murine PDL1, 560 nM for human serum albumin, and 890 nM for murine serum albumin. This result indicates that the fusion with ABD successfully endows the binding ability to ABD without significantly changing the properties of (aPDL1-FN3)₄ protein. Despite the ABD fusion, (aPDL1-FN3)₄ retains its specific PDL1 binding.

Table 15: The binding kinetics of (aPDL1-FN3)₄-EH-ABD

Target	k _{on} [1/Ms]	k _{off} [1/s]	K _D [nM]
Human PDL1	1.67E5	1.87E-4	1.1
Murine PDL1	1.37E5	3.42E-4	2.5
Human ABD	2.22E5	1.26E-2	560
Murine ABD	3.12E5	2.79E-2	890

6.4 Conclusion and future directions

In this chapter, we genetically fused the (aPDL1-FN3)₄ protein, which was optimized for PDL1 binding, to the deimmunized variant of the ABD protein. The ABD protein is used as an alternative to the ELP half-life module because ABD can potentially enhance pharmacokinetics compared to ELP, as it has a smaller drug size which should result in higher tumor uptake and penetration. To optimize the length and selection of linkers for ABD fusion, we created three (aPDL1-FN3)₄-ABD proteins by inserting three different linkers between (aPDL1-FN3)₄ and ABD proteins: 1) (aPDL1-FN3)₄-GS-ABD with a flexible (Gly₄Ser)₂ peptide linker; 2) (aPDL1-FN3)₄-ELP-ABD with an ELP linker (VPGAG)₁₀; 3) (aPDL1-FN3)₄-EH-ABD with an ELP linker (VPGAG)₁₀ as well as a rigid helical linker ((KEAAA)₃KELAA)₂ for enhanced albumin binding.

We successfully cloned, produced, and purified (aPDL1-FN3)₄-ABD proteins by IMAC. Purified (aPDL1-FN3)₄-ABD proteins were characterized for their biophysical properties, including their molecular weights, hydrodynamic radius, and specific PDL1 antagonism. Despite the fusion with ABD, (aPDL1-FN3)₄-ABD retains its strong and specific PDL1 antagonism in the sub-nanomolar range. After careful characterization, we

chose (aPDL1-FN3)₄-EH-ABD for future studies because its potency is the highest, as demonstrated by the characterization of binding affinity to PDL1 and serum albumin from both humans and mice using SPR. The (aPDL1-FN3)₄-EH-ABD protein shows strong and specific binding affinity to PDL1 as well as serum albumin.

The (aPDL1-FN3)₄-EH-ABD has a molecular weight of around ~60kDa, which is only 40% of that of antibody and 60% of that of (aPDL1-FN3)₄-ELP. Since (aPDL1-FN3)₄-ELP exhibits better tumor uptake and penetration using CT26 cancer spheroids, we expect that smaller (aPDL1-FN3)₄-EH-ABD would potentially show even higher tumor uptake and penetration. This can be beneficial for further *in vivo* therapeutic efficacy and biodistribution studies. Although we have not studied these characteristics in the preclinical setting, hypothetically, aPDL1-FN3)₄-EH-ABD has promising potential for increasing serum half-life, tumor uptake, and tumor penetration. In this chapter, we successfully show the potential of the (aPDL1-FN3)₄-EH-ABD drug as an alternative to anti-PDL1 antibodies and (aPDL1-FN3)₄-ELP.

7. Concluding remarks

7.1 Summary of works

This thesis research has produced a modular platform for the development of anti-PDL1 protein therapeutics in cancer immunotherapy. This modular protein therapeutics platform is comprised of two different modules that can be optimized for their functions respectively: 1) affinity module used to specifically bind to PDL1; 2) half-life module used to enhance the pharmacokinetics of the anti-PDL1 drug.

For the affinity module, we used an FN3 scaffold protein that is compact, structurally stable, and readily engineered in the sequence of its three loops to bind to PDL1. We specifically chose to utilize the most well-established M13 filamentous phage display system to develop anti-PDL1 FN3 proteins, as described in Chapter 2. This allowed us to successfully discover several candidates of anti-PDL1 FN3 proteins in the sub-nanomolar ranges of PDL1 affinity. After affinity maturation of these candidates, we finally obtained the sequence of an optimal candidate, the anti-PDL1 FN3 protein (aPDL1-FN3). Using this sequence, we genetically cloned, successfully expressed in the *E. coli* system, and purified (aPDL1-FN3) protein by IMAC, as described in Chapter 3. To tune the affinity module for its PDL1-binding affinity, we created (aPDL1-FN3) oligomers ranging in valency from mono-valency to penta-valency, as described in Chapter 4. After thorough characterization of (aPDL1-FN3)_n oligomers, the tetra-valent version, (aPDL1-FN3)₄ is finally selected because the tetramer saturates PDL1 receptors

on the cellular level resulting in strong PDL1 antagonism and specific PDL1 binding, as measured by flow cytometry and an *in vitro* PDL1 blockade assay

We decide to genetically fuse the optimal (aPDL1-FN3)₄ protein to a half-life module for enhanced pharmacokinetics. In this thesis, we utilized two different half-life modules: 1) elastin-like polypeptides (ELP) which exhibits reversible phase transition behaviors and can be engineered for sustained and localized delivery by modulating its genetic code, as described in Chapter 5; 2) albumin-binding domain (ABD) which has a very small size, promising for tumor penetration and uptake and shows longer serum half-life than ELP, as described in Chapter 6.

We invested our efforts in optimizing ELPs for sustained and localized delivery. The depot-forming (aPDL1-FN3)₄-ELP proteins were engineered to form an insoluble coacervate between room temperature and body temperature such that upon *in vivo* injection, (aPDL1-FN3)₄-ELP can be slowly released. However, this delivery format did not show *in vivo* therapeutic efficacy as promising as the soluble (aPDL1-FN3)₄-ELP protein which did not transition at physiological temperatures. Thus, we continued further studies only with the soluble version of (aPDL1-FN3)₄-ELP. We confirmed that (aPDL1-FN3)₄-ELP exhibited *in vivo* therapeutic efficacy in three different cancer models: 1) B16.F10 melanoma; 2) MC38 colorectal cancer; 3) CT26 colorectal cancer. Especially, (aPDL1-FN3)₄-ELP showed at least slightly better efficacy than those of anti-PDL1 antibodies in MC38 and CT26 cancer models. For MC38, (aPDL1-FN3)₄-ELP systemically

induced anti-tumor immunity, preventing tumor recurrence from rechallenge. In addition, the biodistribution of (aPDL1-FN3)₄-ELP showed that (aPDL1-FN3)₄-ELP has a lower accumulation in normal organs, including lung, liver, kidney, than those of anti-PDL1 antibodies, but has a similar level of tumor accumulation. Given that anti-PDL1 antibodies have much longer serum half-lives than that of (aPDL1-FN3)₄-ELP, this observation indicates that (aPDL1-FN3)₄-ELP possesses the higher ratio of tumor uptake to blood, as compared to those of anti-PDL1 antibodies. This result implies lower toxicity and better tumor uptake and penetration of (aPDL1-FN3)₄-ELP, suggesting a great potential for clinical translation.

Next, we utilized the deimmunized variant of ABD as another half-life module. We optimized the linker (EH) for the fusion with ABD, which is composed of a disordered ELP-based linker for sufficient spacing and a rigid helical linker for improved albumin binding. Despite the fusion with ABD, (aPDL1-FN3)₄-EH-ABD continues to show specific PDL1 binding and strong PDL1 antagonism while maintaining albumin-binding. These characteristics are desired for future *in vivo* studies for two reasons: 1) ABD has shown a longer serum half-life than ELP. Upon *in vivo* injection, (aPDL1-FN3)₄-EH-ABD binds to serum albumin circulating in the blood until (aPDL1-FN3)₄-EH-ABD is uptaken by PDL1-overexpressing tumors; 2) the smaller size of (aPDL1-FN3)₄-EH-ABD compared to (aPDL1-FN3)₄-ELP can potentially show improved tumor uptake and penetration. Altogether, we successfully develop the

modular protein therapeutics, (aPDL1-FN3)₄-ELP and (aPDL1-FN3)₄-EH-ABD, as an alternative to anti-PDL1 antibodies in cancer immunotherapy.

7.2 Future directions

This thesis research suggests the great potential of modular protein therapeutics as an alternative protein drug to monoclonal antibodies for cancer immunotherapy. This work is conceptually innovative in its modular design as it decouples “form” from “function”. Traditionally, a monoclonal antibody has been used as a cornerstone of modern cancer therapy for three important functional reasons: 1) an antibody can be generated against virtually any protein so that an antibody-drug that binds a target of interest can be developed on demand; 2) antibodies have high affinity, and 3) antibodies have a long half-life upon systemic administration because their ~150 kDa size is above the renal filtration limit and because of FcRn recycling. However, the major limitation of antibodies is precisely that their form and function are coupled, driven by millions of years of evolution. Opportunities to further evolve and improve the highly conserved and structurally inflexible scaffold of IgG’s—the class of antibody most commonly used as drugs—are approaching an asymptote.

This thesis research suggests a promising modular design that is simple, generic, modular, and flexible. We can identify unique FN3 variants that bind virtually any protein target of interest by panning our FN3 phage display library; we can tune their affinity by making linear oligomers that are connected by flexible peptide linkers; we

can create bispecific and trispecific drugs by simply arranging copies of different FN3 variants along the linear backbone, and we can tune their pharmacokinetics by fusing to a soluble ELP or ABD. Finally, we can potentially solve the problem of the limited penetration and uptake of antibodies into solid tumors in our design by embedding higher valency and decreasing the size of our fusion protein drugs. Based on this work, we can expand our modular platform to different targets in cancer therapeutics and diagnostics.

Appendix A

Table 16: The reagents and materials used in this thesis

Materials	Company
Gibson assembly master mix	Synthetic Genomics
HiFi PCR premix	Takara
M1307 helper phage	New England Biolabs
ER2738 competent cells	Lucigen
Kanamycin sulfate	EMD Millipore
Tetracycline hydrochloride	Sigma-Aldrich
Carbenicillin Disodium Salt	Thermo Fisher Scientific
Electroporation cuvette	Bio-Rad Laboratories
Protein G-coated magnetic beads	New England Biolabs
6-tube magnetic separation rack	New England Biolabs
Fc protein (hIgG1)	R&D systems
Fc fused human PDL1	R&D systems
Fc fused mouse PDL1	R&D systems
Corning® Maxisorp 96-well plate	Thermo Fisher Scientific
EveryBlot Blocking Buffer	Bio-Rad Laboratories
Whatman® nitrocellulose membrane filters	Millipore-sigma
Protein G	Sigma-Aldrich
Fc fused human PD1	R&D systems
Fc fused human PDL2	R&D systems
NBT/BCIP solutoin	Thermo Fisher Scientific
pNPP solution	Sigma-Aldrich
Ultrapure glycerol	Thermo Fisher Scientific
3M sodium acetate pH 5.2	Thermo Fisher Scientific
Molecular grade ethanol	Thermo Fisher Scientific
Molecular grade water	Thermo Fisher Scientific
BL21 competent cells	New England Biolabs
EB5a competent cells	New England Biolabs
IPTG	Gold Biotechnology
HisPur™ Cobalt Resin	Thermo Fisher Scientific
Ammonium sulfate	Sigma-Aldrich
Imidazole	Sigma-Aldrich
Urea	Sigma-Aldrich

PEG-8000	Sigma-Aldrich
0.5M EDTA, pH 8.0	Thermo Fisher Scientific
1X PBS tablet	EMD Millipore
SpectraPor® Float-A-Lyzer	Thermo Fisher Scientific
Pierce high-capacity endotoxin removal resin	Thermo Fisher Scientific
Amicon™ Ultra-15 Centrifugal Filter Units	Millipore-sigma
Millex™ syringe filter	Millipore-sigma
CM5 chip	GE healthcare
Bio-Glo™ Luciferase Assay System	Promega
Mouse PDL1 AlphaLISA	Perkin Elmer
HyClone® ultrapure water	Cytiva
Endo-free NaOH	Sigma-Aldrich
Sodium phosphate dibasic, endotoxin-tested	VWR
Sodium dihydrogen phosphate monohydrate, endotoxin-tested	VWR
NHS ester Alexafluor488	Thermo Fisher Scientific
Deuterated DMSO	Sigma-Aldrich
Zeba™ spin column	Thermo Fisher Scientific
Pierce™ Iodination Tubes	Thermo Fisher Scientific
Heparin sodium salt from porcine intestinal mucosa	Sigma-Aldrich
ACK lysis buffer	Thermo Fisher Scientific
AggreWell-800	Stemcell Technologies
37 µm reversible strainer	Stemcell Technologies
Corning® 70 µm strainer	BD Biosciences
SimplyBlue™ SafeStain	Thermo Fisher Scientific
Albumin from mouse serum	Sigma-Aldrich
Albumin from human serum	Sigma-Aldrich

Table 17: The recipes for buffers and media used in this thesis

Materials	Composition
LB	10 g/L tryptone, 5 g/L yeast extract, and 10 g/L NaCl; pH 7.0; autoclave

2xYT	16 g/L tryptone, 10 g/L yeast extract, and 5 g/L NaCl; pH 7.0; autoclave
PEG/NaCl (5X)	200 g/L PEG-8000, 150 g/L NaCl; autoclave
pH 1.5 Glycine buffer	10 mM glycine HCl; pH 1.5; sterile filtered
Neutralization buffer	0.1M Tris base; pH 8; sterile filtered
AP-staining buffer	100 mM NaCl, 5mM MgCl ₂ , and 100 mM Tris; pH 9.5; sterile filtered
Fluorescent dye conjugation buffer	0.367 g/L Na ₂ HPO ₄ ·7H ₂ O, 1.191 g/L NaH ₂ PO ₄ ·H ₂ O; pH 6.0; sterile filtered
SDS-PAGE buffer	0.025 M Tris HCl, 0.192 M Glycine and 0.1% (w/v) Sodium Dodecyl Sulfate (SDS); pH 8.3
Native-PAGE buffer	0.025 M Tris HCl and 0.192 M Glycine; pH 8.3

Table 18: The antibodies used in this thesis

Materials	Clone number	Company
PE/Cy7 anti-CD3e	clone 145-2C11	BD Biosciences
FITC anti-CD8a	clone 53-6.7	BD Biosciences
APC anti-CD4	clone RM4-5	BD Biosciences
APC-Cy7 anti-CD11b	clone M1/70	eBioscience
Qdot605 anti-CD45	clone 30-F11	eBioscience
Anti-MS CD16/CD32	2.4G2	Stemcell
Anti-Fc (human IgG1)	M1308A10	BioLegend
AP-conjugated anti-Fc	Polyclonal	abcam
Anti-M13 (pVIII)	RL-ph2	Invitrogen
Anti-Histag	AD1.1.10	Bio-Rad Laboratories
AP-conjugated anti-Histag	AD1.1.10	Bio-Rad Laboratories
Anti-PDL1 antibody	10F.9G2	Bioxcell
Anti-PDL1 antibody	Atezolizumab-based	Invivogen

Table 19: The reagents for cell cultures

Materials	Company
FBS	Gibco™ Thermo Fisher Scientific
0.25% Trypsin-EDTA	Gibco™ Thermo Fisher Scientific
1x DPBS	Gibco™ Thermo Fisher Scientific
Trypan blue solution	Gibco™ Thermo Fisher Scientific
G-418 solution	Gibco™ Thermo Fisher Scientific
Pen/strep	Gibco™ Thermo Fisher Scientific
MEM Non-Essential Amino Acids Solution	Gibco™ Thermo Fisher Scientific
Sodium pyruvate	Gibco™ Thermo Fisher Scientific
Gentamicin	Gibco™ Thermo Fisher Scientific
Zombie Live/Dead	BioLegend
Hoechst 33342 Solution (20 mM)	Thermo Fisher Scientific
BSA	Sigma-Aldrich

Appendix B

Table 20: The sequences of all protein constructs used in this thesis

Constructs	AA sequence
(aPDL1-FN3) ₁	MVSDVPRDLEVVAATPTSLLISWDAPVVTVRYYRITYGETGG NSPVQEFTVPTRFVSTATISGLKPGVDYTITVYAVSTYRQMGV GWSKPISINYRTGGGGSGGGGSGGGGSASHHHHHHHH
(aPDL1-FN3) ₂	MVSDVPRDLEVVAATPTSLLISWDAPVVTVRYYRITYGETGG NSPVQEFTVPTRFVSTATISGLKPGVDYTITVYAVSTYRQMGV GWSKPISINYRTGGGGSGGGGSGGGGSMVSDVPRDLEVVA TPTSLLISWDAPVVTVRYYRITYGETGGNSPVQEFTVPTRFVS TATISGLKPGVDYTITVYAVSTYRQMGVGWSKPISINYRTGG GGSGGGGSGGGGSASHHHHHHHH
(aPDL1-FN3) ₃	MVSDVPRDLEVVAATPTSLLISWDAPVVTVRYYRITYGETGG NSPVQEFTVPTRFVSTATISGLKPGVDYTITVYAVSTYRQMGV GWSKPISINYRTGGGGSGGGGSMVSDVPRDLEVVA SMVSDVPRDLEVVAATPTSLLISWDAPVVTVRYYRITYGETG GNSPVQEFTVPTRFVSTATISGLKPGVDYTITVYAVSTYRQMG VGWSKPISINYRTGGGGSGGGGSGGGGSMVSDVPRDLEVVA ATPTSLLISWDAPVVTVRYYRITYGETGGNSPVQEFTVPTRFV STATISGLKPGVDYTITVYAVSTYRQMGVGWSKPISINYRT GGGGSGGGGSGGGGSASHHHHHHHH
(aPDL1-FN3) ₄	MVSDVPRDLEVVAATPTSLLISWDAPVVTVRYYRITYGETGG NSPVQEFTVPTRFVSTATISGLKPGVDYTITVYAVSTYRQMGV GWSKPISINYRTGGGGSGGGGSGGGGSMVSDVPRDLEVVA TPTSLLISWDAPVVTVRYYRITYGETGGNSPVQEFTVPTRFVS TATISGLKPGVDYTITVYAVSTYRQMGVGWSKPISINYRTGG GGSGGGGSGGGGSMVSDVPRDLEVVAATPTSLLISWDAPV TVRYYRITYGETGGNSPVQEFTVPTRFVSTATISGLKPGVDYTI TVYAVSTYRQMGVGWSKPISINYRTGGGGSGGGGSGGGGSM VSDVPRDLEVVAATPTSLLISWDAPVVTVRYYRITYGETGGN SPVQEFTVPTRFVSTATISGLKPGVDYTITVYAVSTYRQMGV GWSKPISINYRTGGGGSGGGGSASHHHHHHHH
(aPDL1-FN3) ₅	MVSDVPRDLEVVAATPTSLLISWDAPVVTVRYYRITYGETGG NSPVQEFTVPTRFVSTATISGLKPGVDYTITVYAVSTYRQMGV GWSKPISINYRTGGGGSGGGGSGGGGSMVSDVPRDLEVVA TPTSLLISWDAPVVTVRYYRITYGETGGNSPVQEFTVPTRFVS TATISGLKPGVDYTITVYAVSTYRQMGVGWSKPISINYRTGG

	GGSGGGGSGGGGSMVSDVPRDLEVVAATPTSLLISWDAPVV TVRYRITYGETGGNSPVQEFTVPTRFVSTATISGLKPGVDYTI TVYAVSTYRQMGVGWSKPISINYRTGGGGSGAFDQLAPLVI NYRTGGGGSGGGGSGGGGSMVSDVPRDLEVVAATPTSLLIS WDAPVVTVRYRITYGETGGNSPVQEFTVPTRFVSTATISGLK PGVDYTITVYAVSTYRQMGVGWSKPISINYRTGGGGSGGGG SGGGGSMVSDVPRDLEVVAATPTSLLISWDAPVVTVRYRIT YGETGGNSPVQEFTVPTRFVSTATISGLKPGVDYTITVYAVST YRQMGVGWSKPISINYRTGGGGSGGGGSASHHHHHHHH
(aPDL1-FN3) ₄ -ELP	MVSDVPRDLEVVAATPTSLLISWDAPVVTVRYRITYGETGG NSPVQEFTVPTRFVSTATISGLKPGVDYTITVYAVSTYRQMGV GWSKPISINYRTGGGGSGGGGSGGGGSMVSDVPRDLEVVA TPTSLLISWDAPVVTVRYRITYGETGGNSPVQEFTVPTRFVS TATISGLKPGVDYTITVYAVSTYRQMGVGWSKPISINYRTGGG GSGGGGSGGGGSMVSDVPRDLEVVAATPTSLLISWDAPVVT VRYRITYGETGGNSPVQEFTVPTRFVSTATISGLKPGVDYTIT VYAVSTYRQMGVGWSKPISINYRTGGGGSGGGGSGGGGSMV SDVPRDLEVVAATPTSLLISWDAPVVTVRYRITYGETGGNSP VQEFTVPTRFVSTATISGLKPGVDYTITVYAVSTYRQMGVGW SKPISINYRTGGGGSGGGGSGGGGSASGVGVPGVGVPGAGV PGAGVPGAGVPGAGVPGAGVPGAGVPGAGVPGAGVPGAG VPGVGVPGAGVPGAGVPGAGVPGAGVPGAGVPGAGVPGA GVPGAGVPGAGVPGVGVPGAGVPGAGVPGAGVPGAGVPG AGVPGAGVPGAGVPGAGVPGAGVPGVGVPGAGVPGAGVP GAGVPGAGVPGAGVPGAGVPGAGVPGAGVPGAGVPGVGV PGAGVPGAGVPGAGVPGAGVPGAGVPGAGVPGAGVPGAG VPGAGVPGVGVPGAGVPGAGVPGAGVPGAGVPGAGVPGA GVPGAGVPGAGVPGAGVPGVGVPGAGVPGAGVPGAGVPG AGVPGAGVPGAGVPGAGVPGAGVPGAGVPGAGVPGAGVP GAGVPGAGVPGAGVPGAGVPGAGVPGAGVPGAGVPGAGV PGVGVPGAGVPGAGVPGAGVPGAGVPGAGVPGAGVPGAG VPGAGVPGAGVPGVGVPGAGVPGAGVPGAGVPGAGVPGA GVPGAGVPGAGVPGAGVPGAGVPGVGVPGAGVPGAGVPG AGVPGAGVPGAGVPGAGVPGAGVPGAGVPGAGVPGAGVP GAGVPGVGVPGAGVPGAGVPGAGVPGAGVPGAGVPGAGV PGAGVPGAGVPGAGVPGY
(NonsenseFN3) ₄ -ELP	MVSDVPRDLEVVAATPTSLLISWDAPVGGGSRYYRITYGETGG NSPVQEFTVPTGGGSTATISGLKPGVDYTITVYAGGGGSGGG GGGSPISINYRTGGGGSGGGGSGGGGSMVSDVPRDLEVVAAT PTSLLISWDAPVGGGSRYYRITYGETGGNSPVQEFTVPTGGGS

	TATISGLKPGVDYTITVYAGGGGSGGGGSGGGSPISINYRTGGG GSGGGGSGGGGSMVSDVPRDLEVVAATPTSLLISWDAPVGG GSRYYRITYGETGGNSPVQEFTVPTGGGSTATISGLKPGVDYTI TVYAGGGGSGGGGSGGGSPISINYRTGGGGSGGGGSGGGGSM VSDVPRDLEVVAATPTSLLISWDAPVGGGSRYYRITYGETGG NSPVQEFTVPTGGGSTATISGLKPGVDYTITVYAGGGGSGGG SGGGSPISINYRTGGGGSGGGGSGGGGSASGVGVPVGVPGA GVPGAGVPGAGVPGAGVPGAGVPGAGVPGAGVPGAGVPG AGVPGVGVPGAGVPGAGVPGAGVPGAGVPGAGVPGAGVPG GAGVPGAGVPGAGVPGVGVPGAGVPGAGVPGAGVPGAGV PGAGVPGAGVPGAGVPGAGVPGAGVPGVGVPGAGVPGAG VPGAGVPGAGVPGAGVPGAGVPGAGVPGAGVPGAGVPGV GVPGAGVPGAGVPGAGVPGAGVPGAGVPGAGVPGAGVPG AGVPGAGVPGVGVPGAGVPGAGVPGAGVPGAGVPGAGVPG GAGVPGAGVPGAGVPGAGVPGVGVPGAGVPGAGVPGAGV PGAGVPGAGVPGAGVPGAGVPGAGVPGAGVPGVGVPGAG VPGAGVPGAGVPGAGVPGAGVPGAGVPGAGVPGAGVPGA GVPGVGVPGAGVPGAGVPGAGVPGAGVPGAGVPGAGVPG AGVPGAGVPGAGVPGVGVPGAGVPGAGVPGAGVPGAGVPG GAGVPGAGVPGAGVPGAGVPGAGVPGVGVPGAGVPGAGV PGAGVPGAGVPGAGVPGAGVPGAGVPGAGVPGAGVPGAG VPGAGVPGVGVPGAGVPGAGVPGAGVPGAGVPGAGVPGA GVPGAGVPGAGVPGAGVPGY
ABD-094	LAEAKEANAELDSYGVSDFYKRLIDKAKTVEGVEALKD AILAALP
(aPDL1-FN3) ₄ - GS-ABD	MVSDVPRDLEVVAATPTSLLISWDAPVVTVRYRITYGETGG NSPVQEFTVPTRFVSTATISGLKPGVDYTITVYAVSTYRQMGV GWSKPISINYRTGGGGSGGGGSGGGGSMVSDVPRDLEVVA TPTSLLISWDAPVVTVRYRITYGETGGNSPVQEFTVPTRFVST ATISGLKPGVDYTITVYAVSTYRQMGVGWSKPISINYRTGGGG SGGGGSGGGGSMVSDVPRDLEVVAATPTSLLISWDAPVVTVR YRITYGETGGNSPVQEFTVPTRFVSTATISGLKPGVDYTITVY AVSTYRQMGVGWSKPISINYRTGGGGSGGGGSGGGGSMVS DVPRDLEVVAATPTSLLISWDAPVVTVRYRITYGETGGNSP VQEFTVPTRFVSTATISGLKPGVDYTITVYAVSTYRQMGVGW SKPISINYRTGGGGSGGGGSASGLAEAKEANAELDSYGV SDFYKRLIDKAKTVEGVEALKDAILAALPGHHHHHHHHH
(aPDL1-FN3) ₄ - ELP-ABD	MVSDVPRDLEVVAATPTSLLISWDAPVVTVRYRITYGETGG NSPVQEFTVPTRFVSTATISGLKPGVDYTITVYAVSTYRQMGV GWSKPISINYRTGGGGSGGGGSGGGGSMVSDVPRDLEVVA

	<p>TPTSLLISWDAPVVTVRYRITYGETGGNSPVQEFTVPTRFVST ATISGLKPGVDYTITVYAVSTYRQMGVGWSKPISINYRTGGGG SGGGGSGGGGSMVSDVPRDLEVVAATPTSLLISWDAPVVTVR YYRITYGETGGNSPVQEFTVPTRFVSTATISGLKPGVDYTITVY AVSTYRQMGVGWSKPISINYRTGGGGSGGGGSGGGGSMVSD VPRDLEVVAATPTSLLISWDAPVVTVRYRITYGETGGNSPVQ EFTVPTRFVSTATISGLKPGVDYTITVYAVSTYRQMGVGWSKP ISINYRTGGGGGSGGGGSASGGVPGAGVPGAGVPGAGVPGA GVPGAGVPGAGVPGAGVPGAGVPGAGVPGAGVPGAGLAEAKEAA NAELDSYGVSDFYKRLIDKAKTVEGVEALKDAILAALPGHH HHHHHH</p>
<p>(aPDL1-FN3)₄- EH-ABD</p>	<p>MVSDVPRDLEVVAATPTSLLISWDAPVVTVRYRITYGETGG NSPVQEFTVPTRFVSTATISGLKPGVDYTITVYAVSTYRQMGV GWSKPISINYRTGGGGSGGGGSGGGGSMVSDVPRDLEVVA TPTSLLISWDAPVVTVRYRITYGETGGNSPVQEFTVPTRFVST ATISGLKPGVDYTITVYAVSTYRQMGVGWSKPISINYRTGGGG SGGGGSGGGGSMVSDVPRDLEVVAATPTSLLISWDAPVVTVR YYRITYGETGGNSPVQEFTVPTRFVSTATISGLKPGVDYTITVY AVSTYRQMGVGWSKPISINYRTGGGGSGGGGSGGGGSMVSD VPRDLEVVAATPTSLLISWDAPVVTVRYRITYGETGGNSPVQ EFTVPTRFVSTATISGLKPGVDYTITVYAVSTYRQMGVGWSKP ISINYRTGGGGGSGGGGSASGGVPGAGVPGAGVPGAGVPGA GVPGAGVPGAGVPGAGVPGAGVPGAGVPGAGVPGAGGKKEAAK EAAAKEAAKELAAKEAAAKEAAAKEAAAKEAAKELAAGLAEA KEAANAELDSYGVSDFYKRLIDKAKTVEGVEALKDAILAALP GHHHHHHHH</p>

References

1. A. M. Scott, J. D. Wolchok, L. J. Old, Antibody therapy of cancer. *Nature Reviews Cancer* **12**, 278 (2012).
2. A. Mullard, FDA approves 100th monoclonal antibody product. *Nat Rev Drug Discov* **20**, 491-495 (2021).
3. H. Kaplon, J. M. Reichert, Antibodies to watch in 2021. *mAbs* **13**, 1860476 (2021).
4. R.-M. Lu *et al.*, Development of therapeutic antibodies for the treatment of diseases. *Journal of Biomedical Science* **27**, 1 (2020).
5. N. S. Lipman, L. R. Jackson, L. J. Trudel, F. Weis-Garcia, Monoclonal Versus Polyclonal Antibodies: Distinguishing Characteristics, Applications, and Information Resources. *ILAR Journal* **46**, 258-268 (2005).
6. M. L. Chiu, G. L. Gilliland, Engineering antibody therapeutics. *Current Opinion in Structural Biology* **38**, 163-173 (2016).
7. H. Shim, Bispecific Antibodies and Antibody-Drug Conjugates for Cancer Therapy: Technological Considerations. *Biomolecules* **10**, 360 (2020).
8. U. Brinkmann, R. E. Kontermann, The making of bispecific antibodies. *mAbs* **9**, 182-212 (2017).
9. E. Havrdova, D. Horakova, I. Kovarova, Alemtuzumab in the treatment of multiple sclerosis: key clinical trial results and considerations for use. *Therapeutic advances in neurological disorders* **8**, 31-45 (2015).
10. L. A. Raedler, Opdivo (Nivolumab): Second PD-1 Inhibitor Receives FDA Approval for Unresectable or Metastatic Melanoma. *American health & drug benefits* **8**, 180-183 (2015).
11. Y. Y. Syed, Durvalumab: First Global Approval. *Drugs* **77**, 1369-1376 (2017).
12. C. Krasner, R. M. Joyce, Zevalin: 90yttrium labeled anti-CD20 (ibritumomab tiuxetan), a new treatment for non-Hodgkin's lymphoma. *Curr Pharm Biotechnol* **2**, 341-349 (2001).

13. A. M. Bradley, M. Devine, D. DeRemer, Brentuximab vedotin: an anti-CD30 antibody-drug conjugate. *Am J Health Syst Pharm* **70**, 589-597 (2013).
14. N. Jain *et al.*, Loncastuximab tesirine, an anti-CD19 antibody-drug conjugate, in relapsed/refractory B-cell acute lymphoblastic leukemia. *Blood advances* **4**, 449-457 (2020).
15. L. M. Hoffman, L. Gore, Blinatumomab, a Bi-Specific Anti-CD19/CD3 BiTE(®) Antibody for the Treatment of Acute Lymphoblastic Leukemia: Perspectives and Current Pediatric Applications. *Frontiers in oncology* **4**, 63-63 (2014).
16. M. L. Chiu, D. R. Goulet, A. Teplyakov, G. L. Gilliland, Antibody Structure and Function: The Basis for Engineering Therapeutics. *Antibodies (Basel, Switzerland)* **8**, 55 (2019).
17. K. Miller *et al.*, Design, Construction, and In Vitro Analyses of Multivalent Antibodies. *The Journal of Immunology* **170**, 4854-4861 (2003).
18. G. Vidarsson, G. Dekkers, T. Rispens, IgG Subclasses and Allotypes: From Structure to Effector Functions. *Frontiers in Immunology* **5**, (2014).
19. J. M. Reichert, Probabilities of success for antibody therapeutics. *mAbs* **1**, 387-389 (2009).
20. J. Davda *et al.*, Immunogenicity of immunomodulatory, antibody-based, oncology therapeutics. *Journal for ImmunoTherapy of Cancer* **7**, 105 (2019).
21. M. R. Dreher *et al.*, Tumor Vascular Permeability, Accumulation, and Penetration of Macromolecular Drug Carriers. *JNCI: Journal of the National Cancer Institute* **98**, 335-344 (2006).
22. Q. Wang *et al.*, Design and Production of Bispecific Antibodies. *Antibodies (Basel)* **8**, (2019).
23. G. P. Adams *et al.*, High Affinity Restricts the Localization and Tumor Penetration of Single-Chain Fv Antibody Molecules. *Cancer Research* **61**, 4750-4755 (2001).

24. J. K. H. Liu, The history of monoclonal antibody development – Progress, remaining challenges and future innovations. *Annals of Medicine and Surgery* **3**, 113-116 (2014).
25. M. Gebauer, A. Skerra, Engineered protein scaffolds as next-generation antibody therapeutics. *Current Opinion in Chemical Biology* **13**, 245-255 (2009).
26. T. Wurch, A. Pierré, S. Depil, Novel protein scaffolds as emerging therapeutic proteins: from discovery to clinical proof-of-concept. *Trends in Biotechnology* **30**, 575-582 (2012).
27. S. I. Rudnick, G. P. Adams, Affinity and avidity in antibody-based tumor targeting. *Cancer biotherapy & radiopharmaceuticals* **24**, 155-161 (2009).
28. M. Bruning *et al.*, The intracellular Ig fold: a robust protein scaffold for the engineering of molecular recognition. *Protein Engineering, Design and Selection* **25**, 205-212 (2012).
29. R. Vazquez-Lombardi *et al.*, Challenges and opportunities for non-antibody scaffold drugs. *Drug Discovery Today* **20**, 1271-1283 (2015).
30. F. Khodabakhsh *et al.*, Development of a novel nano-sized anti-VEGFA nanobody with enhanced physicochemical and pharmacokinetic properties. *Artificial Cells, Nanomedicine, and Biotechnology* **46**, 1402-1414 (2018).
31. X. Ji *et al.*, Neutralization of TNF α in tumor with a novel nanobody potentiates paclitaxel-therapy and inhibits metastasis in breast cancer. *Cancer Letters* **386**, 24-34 (2017).
32. A. Krasniqi *et al.*, Theranostic Radiolabeled Anti-CD20 sdAb for Targeted Radionuclide Therapy of Non-Hodgkin Lymphoma. *Molecular Cancer Therapeutics* **16**, 2828 (2017).
33. C. H. Kang *et al.*, Identification of Potent CD19 scFv for CAR T Cells through scFv Screening with NK/T-Cell Line. *Int J Mol Sci* **21**, (2020).
34. E. Y. Yang, K. Shah, Nanobodies: Next Generation of Cancer Diagnostics and Therapeutics. *Frontiers in Oncology* **10**, (2020).

35. J. Chen, B. Wang, Y. Wu, Structural Characterization and Function Prediction of Immunoglobulin-like Fold in Cell Adhesion and Cell Signaling. *Journal of chemical information and modeling* **58**, 532-542 (2018).
36. D. M. Halaby, A. Poupon, J. P. Mornon, The immunoglobulin fold family: sequence analysis and 3D structure comparisons. *Protein Engineering, Design and Selection* **12**, 563-571 (1999).
37. Z. A. Ahmad *et al.*, scFv Antibody: Principles and Clinical Application. *Clinical and Developmental Immunology* **2012**, 15 (2012).
38. P. Bannas, J. Hambach, F. Koch-Nolte, Nanobodies and Nanobody-Based Human Heavy Chain Antibodies As Antitumor Therapeutics. *Frontiers in immunology* **8**, 1603-1603 (2017).
39. C. Hamers-Casterman *et al.*, Naturally occurring antibodies devoid of light chains. *Nature* **363**, 446-448 (1993).
40. C. U. Zajc *et al.*, Driving CARs with alternative navigation tools - the potential of engineered binding scaffolds. *Febs j* **288**, 2103-2118 (2021).
41. M. Scully *et al.*, Caplacizumab Treatment for Acquired Thrombotic Thrombocytopenic Purpura. *New England Journal of Medicine* **380**, 335-346 (2019).
42. F. Peyvandi *et al.*, Caplacizumab for Acquired Thrombotic Thrombocytopenic Purpura. *New England Journal of Medicine* **374**, 511-522 (2016).
43. R. Simeon, Z. Chen, In vitro-engineered non-antibody protein therapeutics. *Protein & Cell* **9**, 3-14 (2018).
44. M. S. Bajaj *et al.*, Engineering kunitz domain 1 (KD1) of human tissue factor pathway inhibitor-2 to selectively inhibit fibrinolysis: properties of KD1-L17R variant. *The Journal of biological chemistry* **286**, 4329-4340 (2011).
45. H.-J. Lee, J. J. Zheng, PDZ domains and their binding partners: structure, specificity, and modification. *Cell Communication and Signaling* **8**, 8 (2010).
46. F. Y. Frejd, K.-T. Kim, Affibody molecules as engineered protein drugs. *Experimental & Molecular Medicine* **49**, e306-e306 (2017).

47. C. Rothe, A. Skerra, Anticalin(®) Proteins as Therapeutic Agents in Human Diseases. *BioDrugs : clinical immunotherapeutics, biopharmaceuticals and gene therapy* **32**, 233-243 (2018).
48. D. Steiner, P. Forrer, A. Plückthun, Efficient selection of DARPins with sub-nanomolar affinities using SRP phage display. *J Mol Biol* **382**, 1211-1227 (2008).
49. B. B. Kohnehrouz, A. Talischian, A. Dehnad, S. Nayeri, Novel Recombinant Traceable c-Met Antagonist-Avimer Antibody Mimetic Obtained by Bacterial Expression Analysis. *Avicenna Journal of Medical Biotechnology* **10**, 9+ (2018).
50. M. Friedman *et al.*, Phage display selection of Affibody molecules with specific binding to the extracellular domain of the epidermal growth factor receptor. *Protein Engineering Design and Selection* **20**, 189-199 (2007).
51. J. Wojcik *et al.*, A potent and highly specific FN3 monobody inhibitor of the Abl SH2 domain. *Nat Struct Mol Biol* **17**, 519-527 (2010).
52. M. Gebauer, A. Skerra, Anticalins small engineered binding proteins based on the lipocalin scaffold. *Methods Enzymol* **503**, 157-188 (2012).
53. L. Renders *et al.*, First-in-human Phase I studies of PRS-080#22, a hepcidin antagonist, in healthy volunteers and patients with chronic kidney disease undergoing hemodialysis. *PloS one* **14**, e0212023-e0212023 (2019).
54. A. M. Hohlbaum *et al.*, Sustained plasma hepcidin suppression and iron elevation by Anticalin-derived hepcidin antagonist in cynomolgus monkey. *British journal of pharmacology* **175**, 1054-1065 (2018).
55. H. K. Binz, M. T. Stumpp, P. Forrer, P. Amstutz, A. Plückthun, Designing repeat proteins: well-expressed, soluble and stable proteins from combinatorial libraries of consensus ankyrin repeat proteins. *J Mol Biol* **332**, 489-503 (2003).
56. E. H. Souied *et al.*, Treatment of Exudative Age-Related Macular Degeneration with a Designed Ankyrin Repeat Protein that Binds Vascular Endothelial Growth Factor: a Phase I/II Study. *American Journal of Ophthalmology* **158**, 724-732.e722 (2014).

57. R. M. Hussain, C. Y. Weng, C. C. Wykoff, R. A. Gandhi, S. M. Hariprasad, Abicipar pegol for neovascular age-related macular degeneration. *Expert Opin Biol Ther* **20**, 999-1008 (2020).
58. R. Garuti *et al.*, The Modular Adaptor Protein Autosomal Recessive Hypercholesterolemia (ARH) Promotes Low Density Lipoprotein Receptor Clustering into Clathrin-coated Pits. *Journal of Biological Chemistry* **280**, 40996-41004 (2005).
59. T.-H. Heo, J. Wahler, N. Suh, Potential therapeutic implications of IL-6/IL-6R/gp130-targeting agents in breast cancer. *Oncotarget* **7**, 15460-15473 (2016).
60. D. Lipovšek, Adnectins: engineered target-binding protein therapeutics. *Protein Engineering, Design and Selection* **24**, 3-9 (2011).
61. S. A. Jacobs *et al.*, Design of novel FN3 domains with high stability by a consensus sequence approach. *Protein Engineering, Design and Selection* **25**, 107-117 (2012).
62. A. Koide, C. W. Bailey, X. Huang, S. Koide, The fibronectin type III domain as a scaffold for novel binding proteins¹¹Edited by J. Wells. *Journal of Molecular Biology* **284**, 1141-1151 (1998).
63. K. Gorman, J. McGinnis, B. Kay, Generating FN3-Based Affinity Reagents Through Phage Display. *Current Protocols in Chemical Biology* **10**, e39 (2018).
64. S. Koide, A. Koide, D. Lipovšek, in *Methods in Enzymology*, K. D. Wittrup, G. L. Verdine, Eds. (Academic Press, 2012), vol. 503, pp. 135-156.
65. G. Kamalinia, B. J. Grindel, T. T. Takahashi, S. W. Millward, R. W. Roberts, Directing evolution of novel ligands by mRNA display. *Chem Soc Rev* **50**, 9055-9103 (2021).
66. B. J. Hackel, A. Kapila, K. Dane Wittrup, Picomolar Affinity Fibronectin Domains Engineered Utilizing Loop Length Diversity, Recursive Mutagenesis, and Loop Shuffling. *Journal of Molecular Biology* **381**, 1238-1252 (2008).
67. D. J. Leahy, W. A. Hendrickson, I. Aukhil, H. P. Erickson, Structure of a fibronectin type III domain from tenascin phased by MAD analysis of the selenomethionyl protein. *Science* **258**, 987-991 (1992).

68. A. Koide, J. Wojcik, R. N. Gilbreth, R. J. Hoey, S. Koide, Teaching an old scaffold new tricks: Monobodies constructed using alternative surfaces of the FN3 scaffold. *Journal of Molecular Biology* **415**, 393-405 (2012).
69. S. P. Dineen *et al.*, The Adnectin CT-322 is a novel VEGF receptor 2 inhibitor that decreases tumor burden in an orthotopic mouse model of pancreatic cancer. *BMC Cancer* **8**, 352 (2008).
70. D. Schiff *et al.*, Phase 2 study of CT-322, a targeted biologic inhibitor of VEGFR-2 based on a domain of human fibronectin, in recurrent glioblastoma. *Investigational New Drugs* **33**, 247-253 (2015).
71. R. Berger *et al.*, Phase I Safety and Pharmacokinetic Study of CT-011, a Humanized Antibody Interacting with PD-1, in Patients with Advanced Hematologic Malignancies. *American Association for Cancer Research* **14**, 3044-3051 (2008).
72. T. Mitchell *et al.*, Pharmacologic Profile of the Adnectin BMS-962476, a Small Protein Biologic Alternative to PCSK9 Antibodies for Low-Density Lipoprotein Lowering. *Journal of Pharmacology and Experimental Therapeutics* **350**, 412 (2014).
73. A. Stein Evan *et al.*, LDL CHOLESTEROL REDUCTION WITH BMS-962476, AN ADNECTIN INHIBITOR OF PCSK9: RESULTS OF A SINGLE ASCENDING DOSE STUDY. *Journal of the American College of Cardiology* **63**, A1372-A1372 (2014).
74. M. Madireddi *et al.*, P.14 - BMS-986089 is a high affinity anti-myostatin adnectin that increases muscle volume in three preclinical species. *Neuromuscular Disorders* **26**, S94-S95 (2016).
75. P. G. Chandler, A. M. Buckle, Development and Differentiation in Monobodies Based on the Fibronectin Type 3 Domain. *Cells* **9**, 610 (2020).
76. V. Ramamurthy *et al.*, Structures of Adnectin/Protein Complexes Reveal an Expanded Binding Footprint. *Structure* **20**, 259-269 (2012).
77. E. Karatan *et al.*, Molecular Recognition Properties of FN3 Monobodies that Bind the Src SH3 Domain. *Chemistry & Biology* **11**, 835-844 (2004).

78. R. N. Gilbreth, B. M. Chacko, L. Grinberg, J. S. Swers, M. Baca, Stabilization of the third fibronectin type III domain of human tenascin-C through minimal mutation and rational design. *Protein Engineering, Design and Selection* **27**, 411-418 (2014).
79. C. Q. Pan, M. Sudol, M. Sheetz, B. C. Low, Modularity and functional plasticity of scaffold proteins as p(l)acemakers in cell signaling. *Cellular Signalling* **24**, 2143-2165 (2012).
80. J. S. Swers *et al.*, Multivalent Scaffold Proteins as Superagonists of TRAIL Receptor 2–Induced Apoptosis. *Molecular Cancer Therapeutics* **12**, 1235-1244 (2013).
81. A. Ruggiero *et al.*, Paradoxical glomerular filtration of carbon nanotubes. *Proceedings of the National Academy of Sciences* **107**, 12369-12374 (2010).
82. W. Hassouneh, S. R. MacEwan, A. Chilkoti, Fusions of elastin-like polypeptides to pharmaceutical proteins. *Methods in enzymology* **502**, 215-237 (2012).
83. A. Bandyopadhyay, S. K. Chowdhury, S. Dey, J. C. Moses, B. B. Mandal, Silk: A Promising Biomaterial Opening New Vistas Towards Affordable Healthcare Solutions. *Journal of the Indian Institute of Science* **99**, 445-487 (2019).
84. M. Meyer, Processing of collagen based biomaterials and the resulting materials properties. *BioMedical Engineering OnLine* **18**, 24 (2019).
85. G. Qin, X. Hu, P. Cebe, D. L. Kaplan, Mechanism of resilin elasticity. *Nature Communications* **3**, 1003 (2012).
86. A. Chilkoti, M. R. Dreher, D. E. Meyer, D. Raucher, Targeted drug delivery by thermally responsive polymers. *Advanced Drug Delivery Reviews* **54**, 613-630 (2002).
87. J. R. McDaniel, D. C. Radford, A. Chilkoti, A Unified Model for De Novo Design of Elastin-like Polypeptides with Tunable Inverse Transition Temperatures. *Biomacromolecules* **14**, 2866-2872 (2013).
88. S. Cho, S. Dong, K. N. Parent, M. Chen, Immune-tolerant elastin-like polypeptides (iTEPs) and their application as CTL vaccine carriers. *Journal of drug targeting* **24**, 328-339 (2016).

89. R. S. Ingle, W. Tao, J. N. Tripathy, H. S. Gill, Synthesis and Immunogenicity Assessment of Elastin-Like Polypeptide-M2e Construct as an Influenza Antigen. *Nano LIFE* **4**, 1450004-1450004 (2014).
90. S. Roberts, M. Dzuricky, A. Chilkoti, Elastin-like polypeptides as models of intrinsically disordered proteins. *FEBS Letters* **589**, 2477-2486 (2015).
91. M. Amiram, K. M. Luginbuhl, X. Li, M. N. Feinglos, A. Chilkoti, Injectable protease-operated depots of glucagon-like peptide-1 provide extended and tunable glucose control. *Proceedings of the National Academy of Sciences* **110**, 2792-2797 (2013).
92. K. M. Luginbuhl *et al.*, One-week glucose control via zero-order release kinetics from an injectable depot of glucagon-like peptide-1 fused to a thermosensitive biopolymer. *Nature biomedical engineering* **1**, 0078 (2017).
93. T. Christensen, W. Hassouneh, K. Trabbic-Carlson, A. Chilkoti, Predicting Transition Temperatures of Elastin-Like Polypeptide Fusion Proteins. *Biomacromolecules* **14**, 1514-1519 (2013).
94. M. Amiram, K. M. Luginbuhl, X. Li, M. N. Feinglos, A. Chilkoti, A depot-forming glucagon-like peptide-1 fusion protein reduces blood glucose for five days with a single injection. *Journal of controlled release : official journal of the Controlled Release Society* **172**, 10.1016/j.jconrel.2013.1007.1021 (2013).
95. C. A. Gilroy, S. Roberts, A. Chilkoti, Fusion of fibroblast growth factor 21 to a thermally responsive biopolymer forms an injectable depot with sustained anti-diabetic action. *Journal of controlled release : official journal of the Controlled Release Society* **277**, 154-164 (2018).
96. S. R. MacEwan, A. Chilkoti, Elastin-like polypeptides: Biomedical applications of tunable biopolymers. *Peptide Science* **94**, 60-77 (2010).
97. F. Kratz, Albumin as a drug carrier: design of prodrugs, drug conjugates and nanoparticles. *J Control Release* **132**, 171-183 (2008).
98. M. S. Dennis *et al.*, Albumin binding as a general strategy for improving the pharmacokinetics of proteins. *J Biol Chem* **277**, 35035-35043 (2002).

99. J. Nilvebrant, S. Hober, The albumin-binding domain as a scaffold for protein engineering. *Computational and structural biotechnology journal* **6**, e201303009-e201303009 (2013).
100. S. A. Jacobs *et al.*, Fusion to a highly stable consensus albumin binding domain allows for tunable pharmacokinetics. *Protein Engineering, Design and Selection* **28**, 385-393 (2015).
101. E. Adabi, F. Saebi, A. Moradi Hasan-Abad, L. Teimoori-Toolabi, G. A. Kardar, Evaluation of an Albumin-Binding Domain Protein Fused to Recombinant Human IL-2 and Its Effects on the Bioactivity and Serum Half-Life of the Cytokine. *Iranian biomedical journal* **21**, 77-83 (2017).
102. M. Siegemund *et al.*, Pharmacokinetic Engineering of OX40-Blocking Anticalin Proteins Using Monomeric Plasma Half-Life Extension Domains. *Frontiers in Pharmacology* **12**, (2021).
103. P. Yousefpour *et al.*, Genetically Encoding Albumin Binding into Chemotherapeutic-loaded Polypeptide Nanoparticles Enhances Their Antitumor Efficacy. *Nano Letters* **18**, 7784-7793 (2018).
104. F. Sha, G. Salzman, A. Gupta, S. Koide, Monobodies and other synthetic binding proteins for expanding protein science. *Protein science : a publication of the Protein Society* **26**, 910-924 (2017).
105. C. Dantas-Barbosa, M. de Macedo Brigido, A. Q. Maranhao, Antibody Phage Display Libraries: Contributions to Oncology. *International Journal of Molecular Sciences* **13**, 5420 (2012).
106. C. M. Hammers, J. R. Stanley, Antibody Phage Display: Technique and Applications. *J Invest Dermatol* **134**, e17 (2014).
107. F. Festa, J. Steel, X. Bian, J. Labaer, High-throughput cloning and expression library creation for functional proteomics. *PROTEOMICS* **13**, 1381-1399 (2013).
108. M. A. Alfaleh *et al.*, Phage Display Derived Monoclonal Antibodies: From Bench to Bedside. *Frontiers in Immunology* **11**, (2020).
109. E. Beghetto, N. Gargano, Lambda-display: a powerful tool for antigen discovery. *Molecules (Basel, Switzerland)* **16**, 3089-3105 (2011).

110. J. Nicastro, K. Sheldon, R. A. Slavcev, Bacteriophage lambda display systems: developments and applications. *Appl Microbiol Biotechnol* **98**, 2853-2866 (2014).
111. G. P. Smith, Filamentous fusion phage: novel expression vectors that display cloned antigens on the virion surface. *Science* **228**, 1315-1317 (1985).
112. D. A. Marvin, Filamentous phage structure, infection and assembly. *Current Opinion in Structural Biology* **8**, 150-158 (1998).
113. W.-J. Chung, D.-Y. Lee, S. Y. Yoo, Chemical modulation of M13 bacteriophage and its functional opportunities for nanomedicine. *International journal of nanomedicine* **9**, 5825-5836 (2014).
114. P. Passaretti, I. Khan, T. R. Dafforn, P. Goldberg Oppenheimer, Improvements in the production of purified M13 bacteriophage bio-nanoparticle. *Scientific Reports* **10**, 18538 (2020).
115. T. Sawada, Filamentous virus-based soft materials based on controlled assembly through liquid crystalline formation. *Polymer Journal* **49**, 639-647 (2017).
116. V. A. Petrenko, V. J. Vodyanoy, Phage display for detection of biological threat agents. *Journal of Microbiological Methods* **53**, 253-262 (2003).
117. N. B. Adey, B. K. Kay, Identification of calmodulin-binding peptide consensus sequences from a phage-displayed random peptide library. *Gene* **169**, 133-134 (1996).
118. G. P. Smith, J. K. Scott, in *Methods in Enzymology*. (Academic Press, 1993), vol. 217, pp. 228-257.
119. J. McCafferty, A. D. Griffiths, G. Winter, D. J. Chiswell, Phage antibodies: filamentous phage displaying antibody variable domains. *Nature* **348**, 552-554 (1990).
120. C. F. Barbas, 3rd, A. S. Kang, R. A. Lerner, S. J. Benkovic, Assembly of combinatorial antibody libraries on phage surfaces: the gene III site. *Proc Natl Acad Sci U S A* **88**, 7978-7982 (1991).
121. F. Breitling, S. Dübel, T. Seehaus, I. Klewinghaus, M. Little, A surface expression vector for antibody screening. *Gene* **104**, 147-153 (1991).

122. D. O'Connell, B. Becerril, A. Roy-Burman, M. Daws, J. D. Marks, Phage versus Phagemid Libraries for Generation of Human Monoclonal Antibodies. *Journal of Molecular Biology* **321**, 49-56 (2002).
123. J. Rakonjac, G. Jovanovic, P. Model, Filamentous phage infection-mediated gene expression: construction and propagation of the gIII deletion mutant helper phage R408d3. *Gene* **198**, 99-103 (1997).
124. L. Chasteen, J. Ayriss, P. Pavlik, A. R. M. Bradbury, Eliminating helper phage from phage display. *Nucleic acids research* **34**, e145-e145 (2006).
125. S. F. Parmley, G. P. Smith, Antibody-selectable filamentous fd phage vectors: affinity purification of target genes. *Gene* **73**, 305-318 (1988).
126. J. H. Lee *et al.*, Production of tunable nanomaterials using hierarchically assembled bacteriophages. *Nature Protocols* **12**, 1999-2013 (2017).
127. S. Branston, E. Stanley, E. Keshavarz-Moore, J. Ward, Precipitation of filamentous bacteriophages for their selective recovery in primary purification. *Biotechnology Progress* **28**, 129-136 (2012).
128. J. D. Twomey, B. Zhang, Cancer Immunotherapy Update: FDA-Approved Checkpoint Inhibitors and Companion Diagnostics. *The AAPS journal* **23**, 39-39 (2021).
129. V. K. Anagnostou, J. R. Brahmer, Cancer Immunotherapy: A Future Paradigm Shift in the Treatment of Non-Small Cell Lung Cancer. *Clinical Cancer Research* **21**, 976-984 (2015).
130. L. Milling, Y. Zhang, D. J. Irvine, Delivering safer immunotherapies for cancer. *Advanced Drug Delivery Reviews* **114**, 79-101 (2017).
131. R. J. Greenwald, G. J. Freeman, A. H. Sharpe, THE B7 FAMILY REVISITED. *Annual Review of Immunology* **23**, 515-548 (2004).
132. W. Zou, L. Chen, Inhibitory B7-family molecules in the tumour microenvironment. *Nature Reviews Immunology* **8**, 467-477 (2008).
133. Y. Iwai, J. Hamanishi, K. Chamoto, T. Honjo, Cancer immunotherapies targeting the PD-1 signaling pathway. *Journal of Biomedical Science* **24**, 26 (2017).

134. J.-F. Brunet *et al.*, A new member of the immunoglobulin superfamily – CTLA-4. *Nature* **328**, 267-270 (1987).
135. L. H. Camacho, CTLA-4 blockade with ipilimumab: biology, safety, efficacy, and future considerations. *Cancer medicine* **4**, 661-672 (2015).
136. M. Reck *et al.*, Pembrolizumab versus Chemotherapy for PD-L1–Positive Non–Small-Cell Lung Cancer. *New England Journal of Medicine* **375**, 1823-1833 (2016).
137. A. Naing *et al.*, Phase 2 study of pembrolizumab in patients with advanced rare cancers. *Journal for ImmunoTherapy of Cancer* **8**, e000347 (2020).
138. H. T. Lee, S. H. Lee, Y.-S. Heo, Molecular Interactions of Antibody Drugs Targeting PD-1, PD-L1, and CTLA-4 in Immuno-Oncology. *Molecules (Basel, Switzerland)* **24**, 1190 (2019).
139. F. S. Hodi *et al.*, Improved survival with ipilimumab in patients with metastatic melanoma. *N Engl J Med* **363**, 711-723 (2010).
140. C. Robert *et al.*, Pembrolizumab versus Ipilimumab in Advanced Melanoma. *New England Journal of Medicine* **372**, 2521-2532 (2015).
141. Y. Choi *et al.*, T-cell agonists in cancer immunotherapy. *Journal for ImmunoTherapy of Cancer* **8**, e000966 (2020).
142. S. N. Linch, M. J. McNamara, W. L. Redmond, OX40 Agonists and Combination Immunotherapy: Putting the Pedal to the Metal. *Frontiers in Oncology* **5**, (2015).
143. T. Bartkowiak, M. A. Curran, 4-1BB Agonists: Multi-Potent Potentiators of Tumor Immunity. *Frontiers in Oncology* **5**, (2015).
144. S. Qin *et al.*, Novel immune checkpoint targets: moving beyond PD-1 and CTLA-4. *Molecular Cancer* **18**, 155 (2019).
145. F. Arce Vargas *et al.*, Fc Effector Function Contributes to the Activity of Human Anti-CTLA-4 Antibodies. *Cancer cell* **33**, 649-663.e644 (2018).
146. D. Ha *et al.*, Differential control of human Treg and effector T cells in tumor immunity by Fc-engineered anti-CTLA-4 antibody. *Proc Natl Acad Sci U S A* **116**, 609-618 (2019).

147. X. Chen, X. Song, K. Li, T. Zhang, Fc γ R-Binding Is an Important Functional Attribute for Immune Checkpoint Antibodies in Cancer Immunotherapy. *Frontiers in immunology* **10**, 292-292 (2019).
148. J. R. McDaniel, D. J. Callahan, A. Chilkoti, Drug delivery to solid tumors by elastin-like polypeptides. *Advanced drug delivery reviews* **62**, 1456-1467 (2010).
149. S. Li *et al.*, Nanobody against PDL1. *Biotechnology Letters* **42**, 727-736 (2020).
150. L. Jing *et al.*, Screening and production of an affibody inhibiting the interaction of the PD-1/PD-L1 immune checkpoint. *Protein Expression and Purification* **166**, 105520 (2020).
151. T. S. Stutvoet *et al.*, Molecular Imaging of PD-L1 Expression and Dynamics with the Adnectin-Based PET Tracer (18)F-BMS-986192. *J Nucl Med* **61**, 1839-1844 (2020).
152. S. Watanabe *et al.*, Biodistribution and radiation dosimetry of the novel hypoxia PET probe [18F]DiFA and comparison with [18F]FMISO. *EJNMMI Research* **9**, 60 (2019).
153. F. Zhang *et al.*, Structural basis of a novel PD-L1 nanobody for immune checkpoint blockade. *Cell Discovery* **3**, 17004 (2017).
154. R. L. Maute *et al.*, Engineering high-affinity PD-1 variants for optimized immunotherapy and immuno-PET imaging. *Proceedings of the National Academy of Sciences* **112**, E6506 (2015).
155. D. J. Rubins *et al.*, In Vivo Evaluation and Dosimetry Estimate for a High Affinity Affibody PET Tracer Targeting PD-L1. *Molecular Imaging and Biology* **23**, 241-249 (2021).
156. A. Basran, E. Stanley, Abstract 3776: Generation and formatting of an Affimer[®] biotherapeutic for the inhibition of the PD-L1/PD-1 pathway: Proof of concept in mouse. *Cancer Research* **78**, 3776 (2018).
157. A. Basran *et al.*, Abstract 4108: Preclinical evaluation of half-life extended Affimer[®] biotherapeutics targeting the PD-L1 pathway. *Cancer Research* **79**, 4108 (2019).

158. D. J. Donnelly *et al.*, Synthesis and Biologic Evaluation of a Novel ¹⁸F-Labeled Adnectin as a PET Radioligand for Imaging PD-L1 Expression. *Journal of Nuclear Medicine* **59**, 529 (2018).
159. A. Natarajan *et al.*, A Novel Engineered Small Protein for Positron Emission Tomography Imaging of Human Programmed Death Ligand-1: Validation in Mouse Models and Human Cancer Tissues. *Clinical Cancer Research* **25**, 1774 (2019).
160. T. Vanhercke, C. Ampe, L. Tirry, P. Denolf, Rescue and in situ selection and evaluation (RISE): a method for high-throughput panning of phage display libraries. *J Biomol Screen* **10**, 108-117 (2005).
161. K. Kato *et al.*, Model for the complex between protein G and an antibody Fc fragment in solution. *Structure* **3**, 79-85 (1995).
162. T. Kadonosono *et al.*, Design Strategy to Create Antibody Mimetics Harboring Immobilised Complementarity Determining Region Peptides for Practical Use. *Scientific Reports* **10**, 891 (2020).
163. M. Mammen, S. K. Choi, G. M. Whitesides, Polyvalent Interactions in Biological Systems: Implications for Design and Use of Multivalent Ligands and Inhibitors. *Angew Chem Int Ed Engl* **37**, 2754-2794 (1998).
164. P. Holliger, T. Prospero, G. Winter, "Diabodies": small bivalent and bispecific antibody fragments. *Proceedings of the National Academy of Sciences* **90**, 6444 (1993).
165. E. Rujas *et al.*, Multivalency transforms SARS-CoV-2 antibodies into ultrapotent neutralizers. *Nature Communications* **12**, 3661 (2021).
166. D. Vance, J. Martin, S. Patke, R. S. Kane, The design of polyvalent scaffolds for targeted delivery. *Adv Drug Deliv Rev* **61**, 931-939 (2009).
167. T. Curk, J. Dobnikar, D. Frenkel, Optimal multivalent targeting of membranes with many distinct receptors. *Proceedings of the National Academy of Sciences* **114**, 7210-7215 (2017).
168. Á. M. Cuesta, N. Sainz-Pastor, J. Bonet, B. Oliva, L. Álvarez-Vallina, Multivalent antibodies: when design surpasses evolution. *Trends in Biotechnology* **28**, 355-362 (2010).

169. N. Nuñez-Prado *et al.*, The coming of age of engineered multivalent antibodies. *Drug Discovery Today* **20**, 588-594 (2015).
170. A. Goel *et al.*, Genetically Engineered Tetravalent Single-Chain Fv of the Pancarcinoma Monoclonal Antibody CC49: Improved Biodistribution and Potential for Therapeutic Application. *Cancer Research* **60**, 6964 (2000).
171. C. K. Thota, D. J. Mikolajczak, C. Roth, B. Kokschi, Enhancing Antimicrobial Peptide Potency through Multivalent Presentation on Coiled-Coil Nanofibrils. *ACS Medicinal Chemistry Letters* **12**, 67-73 (2021).
172. M. Welker, E. R. B. Moore, Applications of whole-cell matrix-assisted laser-desorption/ionization time-of-flight mass spectrometry in systematic microbiology. *Systematic and Applied Microbiology* **34**, 2-11 (2011).
173. C. Fenselau, P. A. Demirev, Characterization of intact microorganisms by MALDI mass spectrometry. *Mass Spectrometry Reviews* **20**, 157-171 (2001)
174. M. Valcárcel *et al.*, Three-dimensional growth as multicellular spheroid activates the proangiogenic phenotype of colorectal carcinoma cells via LFA-1-dependent VEGF: implications on hepatic micrometastasis. *Journal of translational medicine* **6**, 57-57 (2008).
175. J. E. Perez, I. Nagle, C. Wilhelm, Magnetic molding of tumor spheroids: emerging model for cancer screening. *Biofabrication*, (2020).
176. A. Orlova, H. Wällberg, S. Stone-Elander, V. Tolmachev, On the Selection of a Tracer for PET Imaging of HER2-Expressing Tumors: Direct Comparison of a ¹²⁴I-Labeled Affibody Molecule and Trastuzumab in a Murine Xenograft Model. *Journal of Nuclear Medicine* **50**, 417-425 (2009).
177. Y. Qi, A. Chilkoti, Protein-polymer conjugation-moving beyond PEGylation. *Current opinion in chemical biology* **28**, 181-193 (2015).
178. S. Saha, S. Banskota, S. Roberts, N. Kirmani, A. Chilkoti, Engineering the Architecture of Elastin-Like Polypeptides: From Unimers to Hierarchical Self-Assembly. *Advanced Therapeutics* **3**, 1900164 (2020).

179. D. E. Meyer, A. Chilkoti, Quantification of the Effects of Chain Length and Concentration on the Thermal Behavior of Elastin-like Polypeptides. *Biomacromolecules* **5**, 846-851 (2004).
180. J. L. Schaal *et al.*, Injectable polypeptide micelles that form radiation crosslinked hydrogels in situ for intratumoral radiotherapy. *Journal of controlled release : official journal of the Controlled Release Society* **228**, 58-66 (2016).
181. S. Banskota, P. Yousefpour, N. Kirmani, X. Li, A. Chilkoti, Long circulating genetically encoded intrinsically disordered zwitterionic polypeptides for drug delivery. *Biomaterials* **192**, 475-485 (2019).
182. E. M. Mastria *et al.*, Doxorubicin-conjugated polypeptide nanoparticles inhibit metastasis in two murine models of carcinoma. *Journal of controlled release : official journal of the Controlled Release Society* **208**, 52-58 (2015).
183. E. M. Mastria *et al.*, Nanoparticle formulation improves doxorubicin efficacy by enhancing host antitumor immunity. *Journal of Controlled Release* **269**, 364-373 (2018).
184. B. C. Dash *et al.*, Tunable elastin-like polypeptide hollow sphere as a high payload and controlled delivery gene depot. *Journal of Controlled Release* **152**, 382-392 (2011).
185. C. A. Gilroy *et al.*, Sustained release of a GLP-1 and FGF21 dual agonist from an injectable depot protects mice from obesity and hyperglycemia. *Science Advances* **6**, eaaz9890.
186. W. Liu *et al.*, Injectable intratumoral depot of thermally responsive polypeptide-radiionuclide conjugates delays tumor progression in a mouse model. *Journal of controlled release : official journal of the Controlled Release Society* **144**, 2-9 (2010).
187. J. R. McDaniel, J. A. MacKay, F. G. Quiroz, A. Chilkoti, Recursive Directional Ligation by Plasmid Reconstruction Allows Rapid and Seamless Cloning of Oligomeric Genes. *Biomacromolecules* **11**, 944-952 (2010).
188. J. J. Bellucci, M. Amiram, J. Bhattacharyya, D. McCafferty, A. Chilkoti, Three-in-One Chromatography-Free Purification, Tag Removal, and Site-Specific Modification of Recombinant Fusion Proteins Using Sortase A and Elastin-like Polypeptides. *Angewandte Chemie International Edition* **52**, 3703-3708 (2013).

189. D. E. Meyer, A. Chilkoti, Purification of recombinant proteins by fusion with thermally-responsive polypeptides. *Nature Biotechnology* **17**, 1112-1115 (1999).
190. W. Liu *et al.*, Tumor accumulation, degradation and pharmacokinetics of elastin-like polypeptides in nude mice. *Journal of Controlled Release* **116**, 170-178 (2006).
191. W. Liu, M. R. Dreher, D. C. Chow, M. R. Zalutsky, A. Chilkoti, Tracking the in vivo fate of recombinant polypeptides by isotopic labeling. *Journal of Controlled Release* **114**, 184-192 (2006).
192. Y. Zhang, M. Huo, J. Zhou, S. Xie, PKSolver: An add-in program for pharmacokinetic and pharmacodynamic data analysis in Microsoft Excel. *Comput Methods Programs Biomed* **99**, 306-314 (2010).
193. I. Genentech, "A phase I, open-label, dose-escalation study of the safety and pharmacokinetics of Atezolizumab (MPDL3280A) administered intravenously as a single agent to patients with locally advanced or metastatic solid tumors or hematologic malignancies."
194. P. Vieira, K. Rajewsky, The half-lives of serum immunoglobulins in adult mice. *Eur J Immunol* **18**, 313-316 (1988).
195. J. V. Peppard, E. Orlans, The biological half-lives of four rat immunoglobulin isotypes. *Immunology* **40**, 683-686 (1980).
196. A. M. Paterson *et al.*, The programmed death-1 ligand 1:B7-1 pathway restrains diabetogenic effector T cells in vivo. *Journal of immunology (Baltimore, Md. : 1950)* **187**, 1097-1105 (2011).
197. R. Stewart *et al.*, Identification and Characterization of MEDI4736, an Antagonistic Anti-PD-L1 Monoclonal Antibody. *Cancer Immunology Research* **3**, 1052 (2015).
198. H. Lin *et al.*, Host expression of PD-L1 determines efficacy of PD-L1 pathway blockade-mediated tumor regression. *J Clin Invest* **128**, 1708 (2018).
199. M. J. Eppihimer *et al.*, Expression and regulation of the PD-L1 immunoinhibitory molecule on microvascular endothelial cells. *Microcirculation (New York, N.Y. : 1994)* **9**, 133-145 (2002).

200. R. S. Herbst *et al.*, Predictive correlates of response to the anti-PD-L1 antibody MPDL3280A in cancer patients. *Nature* **515**, 563 (2014).
201. R. Deng *et al.*, Preclinical pharmacokinetics, pharmacodynamics, tissue distribution, and tumor penetration of anti-PD-L1 monoclonal antibody, an immune checkpoint inhibitor. *mAbs* **8**, 593-603 (2016).
202. M. Altai *et al.*, Influence of Molecular Design on the Targeting Properties of ABD-Fused Mono- and Bi-Valent Anti-HER3 Affibody Therapeutic Constructs. *Cells* **7**, (2018).
203. P. Yousefpour *et al.*, Conjugate of Doxorubicin to Albumin-Binding Peptide Outperforms Aldoxorubicin. *Small* **15**, 1804452 (2019).

Biography

Junseon Min received her Bachelor of Science in Bioengineering from UNIST in February 2013. In February 2015, Junseon received her Master of Science in Biomedical Sciences from UNIST. In August 2015, Junseon started her doctoral research in Biomedical Engineering at Duke University. While in graduate school, Junseon learned phage display from the Cold Spring Harbor Laboratory Course and received two scholarships, the Helmsley Scholarship and the National Institute of General Medical Sciences (NIGMS) Scholarship. In 2016-2017, Junseon was a recipient of the James H. McElhaney fellowship. Her work in the research group of Dr. Ashutosh Chilkoti was used as a base for proposing research grants from the National Institute of Health (NIH). Along with her colleagues in the Chilkoti group, she authored and contributed to the following publications.

- Weber, P.; Dzuricky, M.; **Min, J.**; Jenkins, I.; Chilkoti, A., Concentration-Independent Multivalent Targeting of Cancer Cells by Genetically Encoded Core-Crosslinked Elastin/Resilin-like Polypeptide Micelles. *Biomacromolecules*. 2021; 22 (10), 4347-4356.
- Wang, J.; **Min, J.**; Eghtesadi, SA.; Kane, R.; Chilkoti, A., Quantitative Study of the Interaction of Multivalent Ligand-Modified Nanoparticles with Breast Cancer Cells with Tunable Receptor Density. *ACS Nano*. 2020; 14 (1), 372-383.